

Photonic integrated circuits for shaped pulse laser systems

Citation for published version (APA):

Tahvili, M. S. (2013). *Photonic integrated circuits for shaped pulse laser systems*. [Phd Thesis 1 (Research TU/e / Graduation TU/e), Electrical Engineering]. Technische Universiteit Eindhoven. <https://doi.org/10.6100/IR755280>

DOI:

[10.6100/IR755280](https://doi.org/10.6100/IR755280)

Document status and date:

Published: 01/01/2013

Document Version:

Publisher's PDF, also known as Version of Record (includes final page, issue and volume numbers)

Please check the document version of this publication:

- A submitted manuscript is the version of the article upon submission and before peer-review. There can be important differences between the submitted version and the official published version of record. People interested in the research are advised to contact the author for the final version of the publication, or visit the DOI to the publisher's website.
- The final author version and the galley proof are versions of the publication after peer review.
- The final published version features the final layout of the paper including the volume, issue and page numbers.

[Link to publication](#)

General rights

Copyright and moral rights for the publications made accessible in the public portal are retained by the authors and/or other copyright owners and it is a condition of accessing publications that users recognise and abide by the legal requirements associated with these rights.

- Users may download and print one copy of any publication from the public portal for the purpose of private study or research.
- You may not further distribute the material or use it for any profit-making activity or commercial gain
- You may freely distribute the URL identifying the publication in the public portal.

If the publication is distributed under the terms of Article 25fa of the Dutch Copyright Act, indicated by the "Taverne" license above, please follow below link for the End User Agreement:

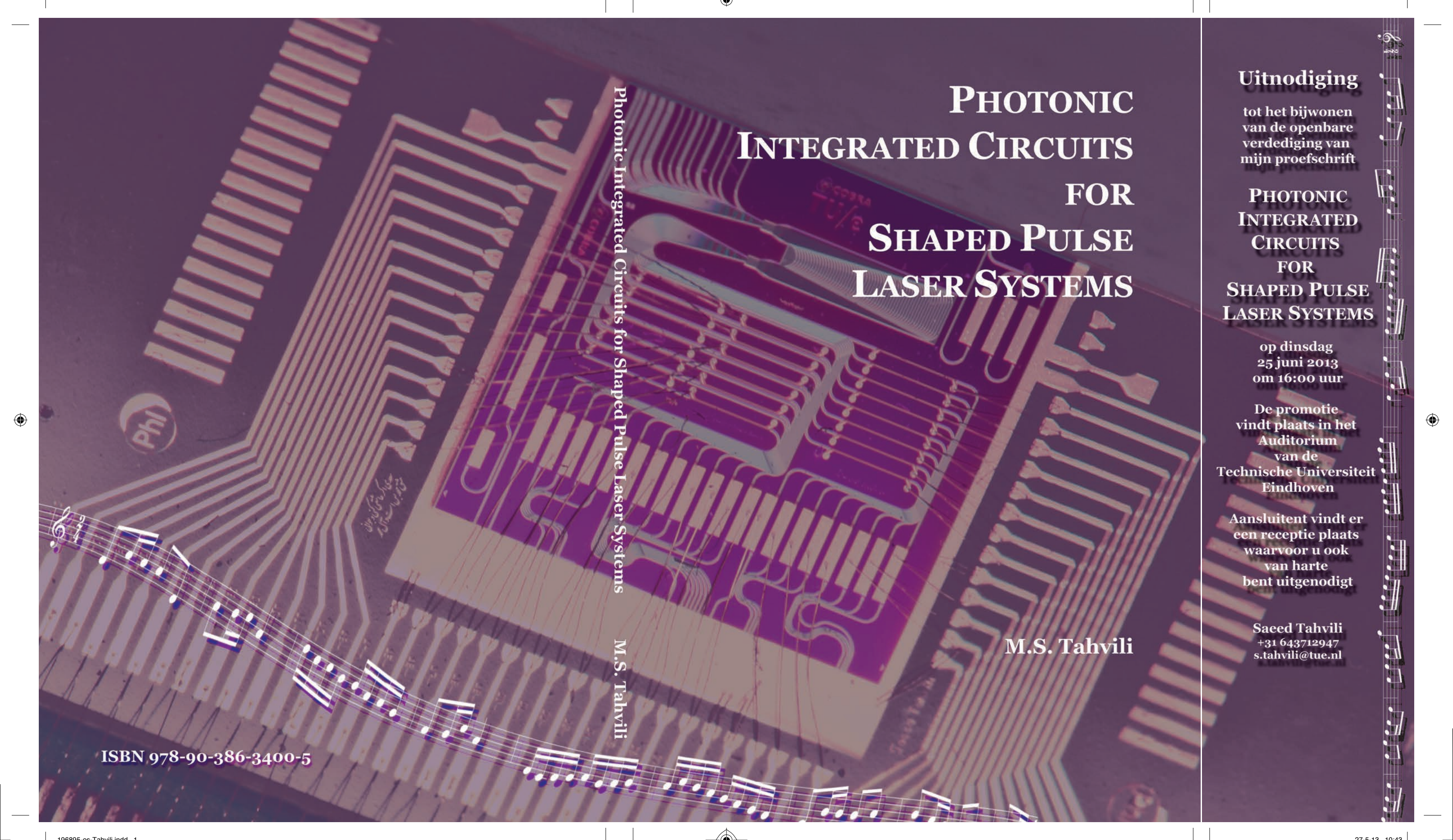
www.tue.nl/taverne

Take down policy

If you believe that this document breaches copyright please contact us at:

openaccess@tue.nl

providing details and we will investigate your claim.



PHOTONIC INTEGRATED CIRCUITS FOR SHAPED PULSE LASER SYSTEMS

Photonic Integrated Circuits for Shaped Pulse Laser Systems

M.S. Tahvili

M.S. Tahvili

Uitnodiging

tot het bijwonen
van de openbare
verdediging van
mijn proefschrift

PHOTONIC INTEGRATED CIRCUITS FOR SHAPED PULSE LASER SYSTEMS

op dinsdag
25 juni 2013
om 16:00 uur

De promotie
vindt plaats in het
Auditorium
van de
Technische Universiteit
Eindhoven

Aansluitend vindt er
een receptie plaats
waarvoor u ook
van harte
bent uitgenodigd

Saeed Tahvili
+31 643712947
s.tahvili@tue.nl

ISBN 978-90-386-3400-5

PHOTONIC INTEGRATED CIRCUITS FOR SHAPED PULSE LASER SYSTEMS

PROEFSCHRIFT

ter verkrijging van de graad van doctor aan de
Technische Universiteit Eindhoven, op gezag van de
rector magnificus, prof.dr.ir. C.J. van Duijn, voor een
commissie aangewezen door het College voor
Promoties in het openbaar te verdedigen
op dinsdag 25 juni 2013 om 16.00 uur

door

Mohammad Saeed Tahvili

geboren te Shiraz, Iran

Dit proefschrift is goedgekeurd door de promotor:

prof.dr.ir. M.K. Smit

Copromotor:

dr. E.A.J.M. Bente

The research presented in this thesis was supported by the IOP Photonic Devices program managed by Agentschap NL and Technologiestichting STW under grant number IPD083346, by the Joint European Platform for InP-based Photonic Integrated Components and Circuits (JePPiX) and by the European FP7 project EuroPIC under grant agreement NMP 228839.

Copyright © 2013 M.S. Tahvili

Printed in The Netherlands

A catalogue record is available from the Eindhoven University of Technology Library

Tahvili, Mohammad Saeed

Photonic Integrated Circuits for Shaped Pulse Laser Systems / by Mohammad Saeed Tahvili. –Eindhoven : Technische Universiteit Eindhoven, 2013.

Proefschrift. – ISBN: 978-90-386-3400-5

NUR 959

Trefw.: halfgeleiderlasers / geïntegreerde optica / 3-5 verbindingen / quantum-dots
Subject headings: semiconductor lasers / integrated optics / III-V semiconductors / quantum-dots / optical pulse shaping / optical pulse compression

To my parents,
and to my wife

Contents

Contents	i
1 Introduction	1
1.1. Photonic integrated circuits for shaped pulse laser systems	2
1.2. Outline of thesis	4
References	6
2 Dual-wavelength InAs/InP(100) Quantum Dot Mode-locked Lasers	9
2.1. Introduction	9
2.2. Passively mode-locked 10GHz laser	11
2.3. Dual-wavelength operation at 10GHz	13
2.3.1 Optical spectra	13
2.3.2 Verification of ML in both mode groups	15
2.4. Hybrid mode-locking	15
2.4.1 RF locking range	16
2.4.2 Evaluation of chirp	17
2.5. 3GHz mode-locked laser	18
2.5.1 Passive mode-locking	18
2.5.2 Hybrid mode-locking	20
2.5.3 Chirp evaluation under hybrid mode-locking	22
2.6. Self mode-locked 4.5GHz QD laser	23
2.7. Summary and Discussion	24
2.7.1 Spectral Splitting: dual-wavelength ML	24
2.7.2 Chirped pulse generation	25
References	27
3 Extended Cavity InP/InGaAsP Integrated Mode-locked Ring Laser	31
3.1. Introduction	31
3.2. Device design and operation	32
3.3. Directional control of power	35
References	37
4 Optical Pulse Shaping: Overview and Design of an InP Integrated Device.....	39
4.1. Fourier transform pulse shaping	39
4.1.1. FT pulse shaping using fixed masks	41
4.1.2. FT pulse shaping using programmable spatial light modulators	42
4.1.2.1. Liquid crystal SLM	42
4.1.2.2. Acousto-optic SLM	44

4.2. Other pulse shaping techniques	44
4.2.1. All-fiber pulse shaper.....	45
4.2.2. Acousto-optic programmable dispersive filters	45
4.2.3. Direct space to time pulse shaping.....	46
4.3. Control strategies for programmable pulse shaping.....	47
4.4. Line-by-line vs. group-of-lines pulse shaping	48
4.5. Integrated optical pulse shaper devices.....	51
4.5.1. Integrated spectral de-/multiplexer	52
4.6. Design of an InP-based monolithically integrated pulse shaper	53
4.6.1. AWG: spectral de-/multiplexer.....	54
4.6.2. Modulation speed of phase and amplitude.....	54
4.6.3. Phase-only or amplitude-and-phase pulse shaping	55
4.6.4. Layout.....	55
4.6.5. Final design.....	55
References	57
5 Full Calibration and Characterization of the InP-based Optical Pulse Shaper..	63
5.1. Device realization	63
5.1.1. Device mounting and cooling	64
5.2. Description of the calibration method.....	66
5.2.1. Measurement of a complex transfer function: the channel response	68
5.2.2. Mathematical description the mask function: the effect of control signals..	69
5.3. Experimental implementation of the calibration method.....	70
5.3.1. Measurement of the channel response in reference state	70
5.3.2. Effect of control signals.....	73
5.3.2.1. PM: Phase tuning and induced excess loss	74
5.3.2.2. SOA: Optical gain and induced phase change	78
5.4. Verification of the channel characterization method	80
5.4.1. Verification of the channel characterization method - SIMBA technique ...	80
5.4.2. Demonstration of the control signal calibration.....	81
References	82
6 Modeling Performance of the Integrated Pulse Shaper Device	85
6.1. Description of the pulse shaper model.....	85
6.1.1. Input and output pulse shapes	86
6.1.2. Device model components.....	87
6.1.3. Calculation of control signals	88
6.2. Group-of-lines shaping: 10GHz input.....	89
6.2.1. Waveguide dispersion.....	89
6.2.2. AWG channel dispersion	91
6.3. Line-by-line shaping: 50GHz input	94
6.3.1. Phase and amplitude shaping.....	95
References	96
7 Demonstration of Chirp Compensation for Optical Pulse Compression.....	97
7.1. Introduction.....	97
7.2. Design and fabrication	98
7.2.1 Generic integration technology.....	98
7.2.2 Device design and characterization.....	98

7.3. Demonstration of chirp compensation	101
7.4. Conclusions	104
References	104
8 Design and Components of a Hybrid Integrated Optical Pulse Shaper	105
8.1. Hybrid integration scheme	106
8.1.1. Waveguide pitch	107
8.1.2. Optical mode size	107
8.1.3. Tilted waveguides	109
8.2. TriPleX device: spectral de-/multiplexer	111
8.2.1. Ring resonator	112
8.2.2. Interleaver filter	114
8.2.3. Tunable coupler	116
8.2.4. Device design	116
8.3. Experimental characterization of the TriPleX device	119
8.3.1. Slicer stages	120
8.3.2. Loss measurement	121
8.3.3. Wavelength tuning	123
8.3.4. Operating multiple channels	124
8.4. InP device: phase modulator array	126
8.4.1. Layer stack modification	127
8.4.2. Waveguide geometry	128
8.4.3. Characterization of SSCs	129
8.5. Summary and conclusions	132
References	133
A1 Stepped Heterodyne Technique for Complex Spectrum Analysis	135
References	137
List of Abbreviations	138
Photonic Integrated Circuits for Shaped Pulse Laser Systems	140
Acknowledgements	142
List of Publications	145
Journal publications	145
International conferences	145
Local Conferences and Events	147
Curriculum vitae	149

CHAPTER 1

Introduction

The invention of lasers has significantly influenced the human life. Lasers are the key enabling components for a diverse range of applications from the high-tech fiber optic communication systems, precise surgical instruments and heavy industrial machinery, to end-user products such as hand held pointers, barcode scanners and optical data storage devices. Interestingly enough, the first working laser in 1960 [1] generated pulses of light rather than a continuous wave. Since then, several techniques, such as Q-switching and mode-locking have been developed for stable generation of ever shorter optical pulses.

Optical pulse shaping is complementary to the subject of optical pulse generation. Pulse compression is probably the most widely credited case of pulse shaping which dates back almost 30 years [2], [3]. That is just after the invention of the colliding pulse mode-locked (ML) dye lasers [4]. Solid-state laser sources were developed in the 1990s [5] and offered several advantages over organic dye lasers, including higher output power level and more importantly stability which facilitated a wider use of femtosecond (fs) lasers [6]. This led to a rapid progress in the field of ultrafast optics and advanced the applications of ultrafast laser systems. In recent years, the fiber-based ultrashort pulse laser technology has reached a mature state of development. Bench-top fs fiber lasers rely on the fiber-optic technology and are in practice more robust in comparison to solid-state lasers which have free-space optical elements.

The availability of ultrafast pulses has triggered many research areas and applications including extremely stable optical frequency comb generation [7], [8], highly accurate metrology [9–11] and coherent control of quantum and nonlinear processes [12], [13]. However, the cost of current laser systems is relatively high and the related optical components are complex and bulky. This has hindered the widespread deployment of fs laser systems and limited the applications to well-controlled laboratory environments.

The work presented in this thesis focuses on development of miniaturized shaped pulse laser systems based on photonic integrated circuits. This thesis addresses three important issues of an integrated shaped pulse laser system, namely pulse generation, laser source stabilization and shaping of optical pulses. Photonic integration is the enabling technology to build active and passive optical devices and circuits which provide complex functionalities on a photonic chip. This technology has the potential to promote the practical and widespread utility of compact, robust and cost-effective ultrafast laser systems.

1.1. Photonic integrated circuits for shaped pulse laser systems

Fig.1.1 presents a schematic drawing of a typical ultrafast laser system. Such a system consists of a time/frequency stabilized ML laser which generates a repetitive train of optical pulses, an optical amplifier to reach sufficient power and a pulse compressor to achieve short optical pulses. For several applications, specific pulse shaping is required as well. Pulse shaping is generally achieved through manipulation of the phase and/or amplitude of the spectral components, i.e. the evenly spaced narrow lines which constitute the frequency spectrum of the pulse train. An ultrafast laser system which incorporates the pulse shaper capability is referred to as a shaped pulse laser system.

In order to build a fully integrated ultrafast laser system, the first step is to realize the constituent elements of the system. These elements include the pulse source, the amplifier and the pulse shaper. This work mainly focuses on the subject of pulse generation using semiconductor ML lasers as well as the optical pulse shaping. These subjects are very different in essence, but complement for realizing an integrated shaped pulse laser system. This thesis therefore consists of two main parts. The first part is comprised of chapters 2 and 3 in which investigations on the pulse generation using semiconductor ML laser diodes (MLLDs) is reported upon.

Semiconductor MLLDs have shown promising performance [14], [15]. They are already in use as high-speed sources in fiber-optic communication systems [16] and have received much attention in different fields of research such as frequency comb generation [17–19] and biomedical imaging [20]. However, the overall performance of MLLDs is deficient in terms of coherent optical bandwidth and power levels as compared to the state of the art of other technologies which are currently employed. We have considered the issue of available optical bandwidth by investigating MLLDs based on the InAs/InP(100) quantum dot (QD) gain material. This material is compatible with the InP/InGaAsP integration technology and provides an optical bandwidth which is larger than the bulk or quantum well gain media. The unique pulse properties of Fabry-Pérot QD MLLDs and their stabilization through the hybrid ML technique are discussed in chapter 2 for a number of devices with different repetition rates.

A strong approach to enhance the performance of MLLDs and to overcome some issues that disturb the conventional all-active two-section devices is to implement advanced laser cavity designs. For instance, the extended-cavity design is particularly important to reduce the self-phase modulation effects from the gain section. Furthermore, intra-cavity spectral filters may be used to increase the coherent bandwidth [21] or to achieve new ML regimes [22]. To realize monolithically integrated short pulse laser systems, active-passive integration is a requirement for any photonic fabrication platform to be used, since such technology allows the integration of active and passive components on

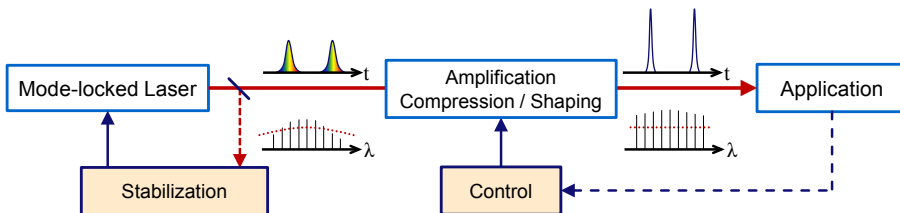


Fig.1.1. Schematic illustration of an ultrafast laser system with pulse shaping capability.

a single chip. In chapter 3, we present an extended cavity ML ring laser with an asymmetric design which enables directional control of the optical power. It is an example of how active-passive integration opens up possibilities for devices.

The second part of the thesis consists of chapter 4–8 which deal with integrated pulse shaper devices. Pulse shaping has a major role in an ultrafast laser system. A brief overview of the pulse shaping techniques which are currently in use is given in chapter 4. The possibility of a broader utilization of integrated fs laser systems calls for further development of the integration technology, which in turn boosts the application of such integrated devices. This is generally known as ‘market pull’ and this has so far led to the development of application-oriented photonic integration fabrication platforms. Such platforms are usually optimized for high performance of a certain range of products. This implies that the costs involved in the development of application-oriented technologies are only justified for products which cover a large market.

An alternative approach which has recently attracted much attention is the generic foundry model [23]. The generic model is based on the development and standardization of certain optical elements to serve as the basic building blocks (BBs) of the platform. The BBs can be combined to realize complex optical circuits with advanced functionalities. Using standardized BBs enables a significant reduction in the design effort and allows for sharing the costs of a single fabrication run between multiple users/designs. The design for a monolithically integrated pulse shaper, which has been fabricated in an InP-based generic foundry platform, is presented in chapter 4. Chapter 5 is dedicated to the characterization and the full calibration of the integrated device. In this chapter the calibration procedure and experimental methods are explained in detail. Chapter 6 presents a model to simulate the effect on an optical pulse which passes through the pulse shaper device using the actual calibration data. This modeling of the pulse shaper gives insight into the performance of the integrated device and demonstrates how the control signals can be calculated to achieve specific output pulse properties given an input pulse shape.

Monolithic integration [23–25] provides the greatest simplicity and reliability benefits when consolidating optical components into a single device. In chapter 7, we show the functionality of the realized integrated InP-based device by demonstration of chirp compensation for the optical pulses generated by a quantum-dash MLLD.

In recent years, heterogeneous/hybrid integration platforms have attracted attention. Heterogeneous integration [26–28] particularly involves integration of III-V semiconductors onto silicon-on-insulator substrates or silicon chips. On the other hand, hybrid integration [29–31] is generally based on assembling multiple photonic chips and components together to form a compound optical module. Assembly of optical devices is in itself a technological challenge; however, the hybrid integration has the advantage that the capabilities of different optical platforms may be merged. In chapter 8, we explore the possibility of realizing a hybrid integrated pulse shaper which combines a TriPleX spectral de-/multiplexer and an InP phase modulator array. In this scheme, the TriPleX device provides a low-loss platform for fabrication of a spectral de-/multiplexer with individually tunable channels. An important advantage of the hybrid integration scheme in case of an optical pulse shaper is that light pulses with at least two orders of magnitude higher peak power can be transported in the TriPleX waveguides (compared to InP/InGaAsP waveguides).

1.2. Outline of thesis

The outline of the chapters in the thesis that follow this brief introductory chapter is described in more detail below.

Chapter 2 presents an investigation of passive and hybrid mode-locking in Fabry-Pérot type two-section InAs/InP(100) quantum dot lasers. These devices show dual wavelength operation. Over the whole current and voltage range for mode-locking of these lasers, the optical output spectra show two distinct lobes. The two lobes provide a coherent bandwidth and are verified to lead to two synchronized optical pulses. The generated optical pulses are elongated in time due to a chirp which shows opposite signs over the two spectral lobes. Self-induced mode-locking in the single-section laser shows that the dual-wavelength spectra correspond to emission from ground state. In the hybrid mode-locking regime, a map of the locking range is presented by measuring the values of timing jitter for several values of power and frequency of the external electrical modulating signal. An overview of the behavior of InAs/InP(100) quantum dot mode-locked lasers was obtained and a systematic trend in the behavior of the lasers was discovered and presented as the conclusion.

The contents of this chapter have been published separately as:

M. S. Tahvili, L. Du, M. J. R. Heck, R. Nötzel, M. K. Smit, and E. A. J. M. Bente, “Dual-wavelength passive and hybrid mode-locking of 3, 4.5 and 10 GHz InAs/InP(100) quantum dot lasers,” *Optics Express*, vol. 20, no. 7, p. 8117, Mar. 2012.

Chapter 3 concerns a passively mode-locked InP/InGaAsP multiple quantum well semiconductor extended cavity ring laser. The laser operates at 20GHz repetition rate and around 1575nm wavelength. The device has been realized using the active-passive integration technology in the COBRA photonic integration platform (within the framework of JePPIX). We demonstrate that the relative positioning of the amplifier and absorber in a monolithically integrated ring laser can be used to control the balance of power between counter-propagating fields in the mode-locked state. This result is a demonstration of the enhancements possible to MLLs using active-passive integration technology.

The contents of this chapter appear partly in:

M.S. Tahvili, Y. Barbarin, X.J.M. Leijtens, T. de Vries, E. Smalbrugge, J. Bolk, H.P.M.M. Ambrosius, M.K. Smit, and E.A.J.M. Bente, “Directional control of optical power in integrated InP/InGaAsP extended cavity mode-locked ring lasers,” *Optics Letters*, vol. 36, no. 13, p. 2462, Jun. 2011.

Chapter 4 provides an overview of the most widely employed optical pulse shaper systems. We explain the basic principle of the pulse shaping technique which has been used in this thesis and give some information on different practical aspects of the pulse shaper devices. An overview of integrated pulse shapers and relevant applications are given as well. We conclude the chapter by presenting the design of an ultracompact InP-based monolithically integrated optical pulse shaper which is made according to the fabrication technology platform of Oclaro Inc. and with a focus on the

application in highly accurate metrology and Coherent Anti-Stokes Raman Spectroscopy (CARS) microscopy.

Chapter 5 is dedicated to the characterization and calibration of the monolithically integrated optical pulse shaper. The chip has been realized in an InP-based generic photonic foundry process within the framework of EuroPIC and integrates a 20-channel arrayed waveguide grating with 20 phase modulators and 20 SOAs. We present the theoretical and experimental procedure for full calibration of the device. This calibration leads to a mathematical description of the pulse shaper. Details of the experiments and measurement setups are given.

The content of this chapter is in preparation for publication in the IEEE Photonics Journal with the following title: “*Complete calibration of an InP-based monolithically integrated optical pulse shaper*”.

Chapter 6 presents a model to simulate the effect on an optical pulse which passes through our pulse-shaper device with its 20 channels at 50GHz spacing using the actual calibration data. The first goal of this modeling of the pulse shaper is to give insight into the performance of the integrated device and to simulate the effect of practical issues which disturb the pulse shaping performance. The second goal is to use the model to demonstrate how the required control signals can be calculated in order to achieve specific output pulse properties given an input pulse shape.

Chapter 7 focuses on the demonstration of dispersion compensation for highly chirped optical pulses by employing the integrated optical pulse shaper which is presented in chapter 5. The chip is operated at optimized conditions to compensate the chirp of a passively mode-locked quantum dash laser source. The pulses from the laser source are sent through the pulse shaper and then characterized in the time domain using the stepped heterodyne technique. The results show a nearly flat chirp profile over the duration of the optical pulse, and suppressed trailing features owing to chirp compensation which lead to a reduction of a factor of two in pulse width.

The contents of this chapter appear partly in:

S. Tahvili, S. Latkowski, B. Smalbrugge, X.J.M. Leijtens, P.J. Williams, M.J. Wale, J. Parra-Cetina, R. Maldonado-Basilio, P. Landais, M.K. Smit, and E.A.J.M. Bente, “*InP-Based Integrated Optical Pulse Shaper: Demonstration of Chirp Compensation,*” IEEE Photonics Technology Letters, vol. 25, no. 5, pp. 450–453, Mar. 2013.

Chapter 8 deals with the investigation into the possibility of realizing a hybrid integrated pulse shaper which combines the capabilities of the InP and TriPleX technology platforms. This scheme is particularly interesting because of the possibility of achieving fast phase/amplitude manipulation in InP while realizing a low-loss multi channel TriPleX spectral de-/multiplexer in which each channel is individually tunable. Our approach is to first describe the design criteria for building the hybrid system and define the coupling interface between the TriPleX and InP chips. We then focus on the design and characterization of the devices independently. The

designs are explained in detail and experimental results are given. The TriPleX device is an integrated tunable 24 channel demultiplexer. The InP device integrates a dense array of spot size converters (SSCs) with phase modulators. We explain the detailed design procedure and present characterization of SSCs. We then draw conclusions on this technological approach.

References

- [1] T. H. Maiman, "Stimulated Optical Radiation in Ruby," *Nature*, vol. 187, no. 4736, pp. 493–494, Aug. 1960.
- [2] C. V. Shank, "Compression of femtosecond optical pulses," *Applied Physics Letters*, vol. 40, no. 9, p. 761, 1982.
- [3] J. G. Fujimoto, a. M. Weiner, and E. P. Ippen, "Generation and measurement of optical pulses as short as 16 fs," *Applied Physics Letters*, vol. 44, no. 9, p. 832, 1984.
- [4] C. V. S. R.L. Fork, B.I. Greene, "Generation of Optical pulses Shorter than 0.1psec by Colliding pulse Mode Locking," *Applied Physics Letters*, vol. 38, no. 9, pp. 671–673, 1981.
- [5] W. Sibbett, A. A. Lagatsky, and C. T. A. Brown, "The development and application of femtosecond laser systems," *Optics Express*, vol. 20, no. 7, p. 6989, Mar. 2012.
- [6] J. Ye and S. T. Cundiff, Eds., "front matter," Boston: Kluwer Academic Publishers, 2005.
- [7] J. Hall, "Nobel Lecture: Defining and measuring optical frequencies," *Reviews of Modern Physics*, vol. 78, no. 4, pp. 1279–1295, Nov. 2006.
- [8] T. W. Hänsch, "Einstein Lecture – Passion for precision," *Annalen der Physik*, vol. 15, no. 9, pp. 627–652, Sep. 2006.
- [9] T. Udem, R. Holzwarth, and T. W. Hänsch, "Optical frequency metrology.," *Nature*, vol. 416, no. 6877, pp. 233–7, Mar. 2002.
- [10] T.-A. Liu, N. R. Newbury, and I. Coddington, "Sub-micron absolute distance measurements in sub-millisecond times with dual free-running femtosecond Er fiber-lasers.," *Optics express*, vol. 19, no. 19, pp. 18501–9, Sep. 2011.
- [11] K.-N. Joo, Y. Kim, and S.-W. Kim, "Distance measurements by combined method based on a femtosecond pulse laser.," *Optics express*, vol. 16, no. 24, pp. 19799–806, Nov. 2008.
- [12] P. Nuernberger, G. Vogt, T. Brixner, and G. Gerber, "Femtosecond quantum control of molecular dynamics in the condensed phase," *Physical chemistry chemical physics:PCCP*, vol. 9, no. 20, pp. 2470–97, May 2007.
- [13] S. Postma, A. C. W. van Rhijn, J. P. Korterik, P. Gross, J. L. Herek, and H. L. Offerhaus, "Application of spectral phase shaping to high resolution CARS spectroscopy," *Optics Express*, vol. 16, no. 11, p. 7985, May 2008.
- [14] E. A. Avrutin, J. H. Marsh, and E. L. Portnoi, "Monolithic and multi-GigaHertz mode-locked semiconductor lasers: Constructions, experiments, models and applications," *IEE Proceedings - Optoelectronics*, vol. 147, no. 4, pp. 251–278, 2000.
- [15] K. a Williams, M. G. Thompson, and I. H. White, "Long-wavelength monolithic mode-locked diode lasers," *New Journal of Physics*, vol. 6, pp. 179–179, Nov. 2004.
- [16] R. Kaiser and B. Huttli, "Monolithic 40-GHz Mode-Locked MQW DBR Lasers for High-Speed Optical Communication Systems," *IEEE Journal of Selected Topics in Quantum Electronics*, vol. 13, no. 1, pp. 125–135, 2007.
- [17] P. J. Delfyett, S. Gee, H. Izadpanah, S. Ozharar, F. Quinlan, and T. Yilmaz, "Optical frequency combs from semiconductor lasers and applications in ultrawideband signal

- processing and communications,” *Journal of Lightwave Technology*, vol. 24, no. 7, pp. 2701–2719, Jul. 2006.
- [18] K. W. Holman, D. J. Jones, J. Ye, and E. P. Ippen, “Orthogonal control of the frequency comb dynamics of a mode-locked laser diode,” *Optics letters*, vol. 28, no. 23, pp. 2405–7, Dec. 2003.
- [19] T. J. Pinkert, E. J. Salumbides, M. S. Tahvili, W. Ubachs, E. A. J. M. Bente, and K. S. E. Eikema, “Frequency comb generation by CW laser injection into a quantum-dot mode-locked laser,” *Optics Express*, vol. 20, no. 19, p. 21357, Sep. 2012.
- [20] H. Guo, K. Sato, K. Takashima, and H. Yokoyama, “Two-photon Bio-imaging with a Mode-locked Semiconductor Laser,” pp. 3–5, 2006.
- [21] J. S. Parker, A. Bhardwaj, P. R. a. Binetti, Y.-J. Hung, and L. a. Coldren, “Monolithically Integrated Gain-Flattened Ring Mode-Locked Laser for Comb-Line Generation,” *IEEE Photonics Technology Letters*, vol. 24, no. 2, pp. 131–133, Jan. 2012.
- [22] M. J. R. Heck and J. E. Bowers, “Integrated Fourier-Domain Mode-Locked Lasers: Analysis of a Novel Coherent Comb Laser,” *IEEE Journal of Selected Topics in Quantum Electronics*, vol. 18, no. 1, pp. 201–209, Jan. 2012.
- [23] M. Smit et al., “Generic foundry model for InP-based photonics,” *IET Optoelectronics*, vol. 5, no. 5, p. 187, 2011.
- [24] M. Smit, J. van der Tol, and M. Hill, “Moore’s law in photonics,” *Laser & Photonics Reviews*, vol. 6, no. 1, pp. 1–13, Jan. 2012.
- [25] J. J. G. . van der Tol, Y. S. Oei, U. Khalique, R. Notzel, and M. K. Smit, “InP-based photonic circuits: Comparison of monolithic integration techniques,” *Progress in Quantum Electronics*, vol. 34, no. 4, pp. 135–172, Jul. 2010.
- [26] G. Roelkens et al., “III-V/silicon photonics for on-chip and intra-chip optical interconnects,” *Laser & Photonics Reviews*, vol. 4, no. 6, pp. 751–779, Nov. 2010.
- [27] J. van der Tol et al., “Photonic integration in indium-phosphide membranes on silicon,” *IET Optoelectronics*, vol. 5, no. 5, p. 218, 2011.
- [28] D. Liang, G. Roelkens, R. Baets, and J. E. Bowers, “Hybrid Integrated Platforms for Silicon Photonics,” *Materials*, vol. 3, no. 3, pp. 1782–1802, Mar. 2010.
- [29] G. Maxwell et al., “Hybrid integration of monolithic semiconductor optical amplifier arrays using passive assembly,” *Proceedings Electronic Components and Technology, 2005. ECTC '05.*, vol. 2, pp. 1349–1352, 2005.
- [30] A. Poustie, “Hybrid integration for advanced photonic devices,” 2008, vol. 7135, pp. 713502–713502–10.
- [31] G. T. Kanellos et al., “All-Optical 3R Burst-Mode Reception at 40 Gb/s Using Four Integrated MZI Switches,” *Journal of Lightwave Technology*, vol. 25, no. 1, pp. 184–192, Jan. 2007.

CHAPTER 2

Dual-wavelength InAs/InP(100) Quantum Dot Mode-locked Lasers

In this chapter, an investigation of passive and hybrid mode-locking in Fabry-Pérot type two-section InAs/InP(100) quantum dot lasers are presented. Devices show dual wavelength operation. Over the whole current and voltage range for mode-locking of these lasers, the optical output spectra show two distinct lobes. The two lobes provide a coherent bandwidth and are verified to lead to two synchronized optical pulses. The generated optical pulses are elongated in time due to a chirp which shows opposite signs over the two spectral lobes. Self-induced mode-locking in the single-section laser shows that the dual-wavelength spectra correspond to emission from ground state. In the hybrid mode-locking regime, a map of locking range is presented by measuring the values of timing jitter for several values of power and frequency of the external electrical modulating signal. An overview of the systematic behavior of InAs/InP(100) quantum dot mode-locked lasers is presented as conclusion.

2.1. Introduction

More than 15 years of research on semiconductor quantum dots (QDs) has revealed distinctive properties of such material for incorporation as active medium in semiconductor optical amplifiers (SOAs) and lasers. So far, a major part of the research on QDs has been dedicated to InGaAs/GaAs material systems which emit in the wavelength range of 1.0-1.3 μm . Progress in growth of InAs self assembled QDs [1] and quantum dashes [2] on InP substrate has allowed research on features of such quantum structures in the 1.5 μm telecommunication window. At the COBRA Research Institute, optically active materials based on InAs QDs on n-type (100) InP substrate have been developed which provide peak gain in the wavelength range of 1.5 μm to 1.8 μm [3]. This brings the interesting properties of QDs to the wavelength region which is attractive not only for fiber optic communications but also for novel applications such as integrated tunable lasers for gas sensing and optical coherence tomography [4]. QDs show low spontaneous emission levels and a broad gain spectrum. The wide gain bandwidth is in principle an ideal feature for optical pulse generation. In case of InGaAs/GaAs QD-based mode-locked (ML) lasers, there has been much progress since the first demonstration of a 7.4GHz passively mode-locked QD laser in 2001 [5].

Several research groups in recent years have studied and achieved sub-ps pulse generation [6], high peak power and Fourier limited pulse generation (see for example [7] and references therein). QDs and Q-dash material offer the widest available bandwidth from ML devices in comparison with bulk or quantum well material. Recently, we have investigated ML operation in lasers incorporating InAs/InP(100) QD gain material.

We have previously reported on highly chirped ML operation in Fabry-Pérot type InAs/InP(100) QD lasers over a wide range of operating parameters. Such devices generate elongated pulses with a relatively wide, i.e. 8nm, optical bandwidth [8,9]. Our observations have demonstrated operating regimes that have outputs which look similar to FM locking [10] and our devices show different ML properties in comparison with InGaAs/GaAs QD-based lasers. On the other hand, the ML behavior in our devices has similar properties as observed in single-section InAs/InP Q-dash ML lasers [11]. The aim of this chapter is to compare the performance of devices with different repetition rates and roundtrip losses and point out the relationship between the results. This will help with work aimed at understanding the origin of the observed dynamics in the lasers.

In this chapter, we consider an aspect of mode-locking in InAs/InP QD lasers which is the occurrence of stable dual-wavelength ML operation. The dual-wavelength short pulse operation is in itself interesting for applications such as optical generation of THz signals or CARS experiments on rotational states in molecules. We will present detailed characterization of a 4mm-long two-section laser which has 10GHz repetition frequency and investigate the region of ML in terms of operating parameters in section 2. In section 3, we show that over the whole range of ML, the optical spectrum consists of two spectral lobes. We confirm the fact that both spectral lobes contribute to pulsed operation and are synchronized.

In section 4, we report on regimes of hybrid ML in the 10GHz QD laser. Under hybrid ML, a clean electrical signal from an external source is available and thus application of a broader range of measurement equipment is possible. We present the evaluation of spectral chirp based on recorded time traces from a fast sampling oscilloscope. In order to better understand the physical mechanism behind ML in our QD devices, we have fabricated devices with three different repetition rates. In section 5, we investigate a 3GHz laser and follow similar characterization steps as mentioned in the preceding lines to highlight key features of ML in InAs/InP(100) QD lasers. The 3GHz laser is 13mm long and has, to the extent of our knowledge, the lowest repetition rate reported for a monolithic InAs/InP(100) QD laser. In section 6, we present, for the first time, the mode-locked operation of a single-section laser which incorporates our QD material. The device is 9mm long and operates at 4.5GHz repetition frequency. Discussions and conclusions are summarized in section 7, where an overview of the experimental results is given and a comparison is made with our previously reported devices. We will discuss the observed spectral splitting which is linked to the ML operation in the devices presented. We show that the power balance in the spectral lobes is affected by the cavity losses and equivalently the lasing threshold current density. Furthermore, we investigate the systematic generation of chirped pulses in our InAs/InP(100) QD ML lasers and confirm the fact that even under hybrid ML, duration of generated pulses is almost half the roundtrip time, independent of the cavity length.

2.2. Passively mode-locked 10GHz laser

In this section, we present results of characterization measurements which have been carried out on two-section Fabry-Pérot type devices. The gain medium incorporates five layers of InAs (on ultrathin GaAs interlayers) QDs. QD layers are stacked in the center of the 500nm-thick InGaAsP waveguiding layer and separated by 40nm. Details of material growth, layer stack and device fabrication are given in [8,12].

Two-section devices are operated by current injection to the SOA-section (I_{SOA}) to create the gain section. A saturable absorber (SA) section is achieved by applying reverse bias voltage (V_{SA}) on the shorter section. The two sections are electrically isolated by an isolation segment which is a 30 μ m-long 45°-tilted etch section. Fabricated devices are mounted on specially designed RF submounts which provide contact pads in ground-signal-ground (GSG) configuration for wire-bonding and applying RF signals on SA-sections. The RF submount is realized on 280 μ m-thick AlN polished substrate. The chip is first fixed and wire-bonded on the RF submount; the submount is then glued on a copper chuck. During measurements, the copper chuck is water cooled and the chip is temperature stabilized at 12°C using a thermistor and Peltier element. In order to decrease the cavity losses and operate the SOA-section at a lower injection current/gain level, we have applied a highly-reflective (HR, reflectivity>96%) coating on the absorber side of the devices. A lensed fiber which has an anti-reflection coated tip is used at the SOA-section side to collect the output light from the devices. We use an optical isolator to prevent possible back-reflection to the lasers.

Fig.2.1 shows top view of an array of 12 realized MLLDs. Their cavity length determines the round-trip frequency. The devices have different lengths of absorber section and are tested for the best ML performance. The device on which we focus in this section is 4mm long and has a 120 μ m-long absorber section, equal to 3% of the total cavity length. The device has a threshold current of 173mA to 190mA for SA reverse bias voltages of $V_{SA}=0V$ to $V_{SA}=-1V$. A single-section 4mm-long FP laser is also on the same chip. Its threshold current is 115mA. The higher threshold currents for

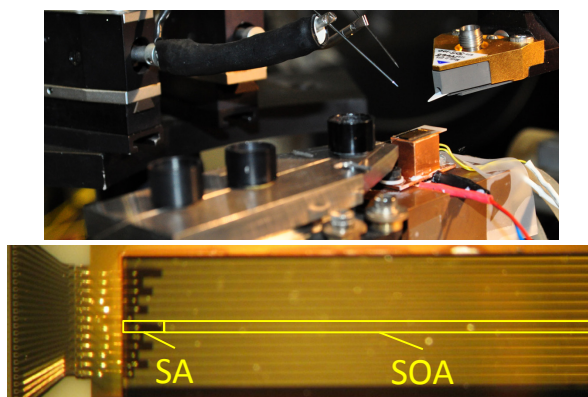


Fig.2.1. (Above) An image of the measurement setup and (below) top view of an array of 12 mode-locked lasers with different lengths of absorber section. Devices are mounted and wire-bonded on an RF submount. The RF cable is not connected. Two single-section FP structures are included as reference lasers.

the two-section devices are due to the loss introduced by the absorber section.

Passive mode locking is studied by recording the electrical power spectrum. In the ML state, the recorded traces from the electrical spectrum analyzer (ESA) show well-defined peaks at the cavity round-trip frequency, i.e. 10GHz corresponding to a 4mm-long cavity, and its higher order harmonics. The height of RF peak is related to the pulsed power and hence is an indication of stable mode-locking. Our first step to characterize the QD laser is to define an operating range in terms of the values of injected current to the SOA-section and bias voltage on the SA-section to indicate where stable ML is achieved. To determine the stable ML operating range of the MLLD, I_{SOA} is sweep-scanned and the RF spectra traces are recorded with a 50GHz ESA which is connected to a 50GHz photo diode (PD). The measurement is repeated for a range of values of bias voltage V_{SA} . The height of RF peak at the fundamental frequency over the noise floor (and lower frequency components) is then mapped as function of operating parameters. A plot is presented in Fig.2.2. The 10GHz laser operates in a stable passive ML regime from $V_{SA}=-0.1V$ (for $I_{SOA}=240-310mA$) to $V_{SA}=-1.0V$ (for $I_{SOA}=260mA-300mA$). Recorded RF peaks are up to more than 45dB in height over the noise floor of the electrical spectrum analyzer.

In the range of stable mode-locking, the 3dB width of fundamental RF peaks is in order of 110kHz to 300kHz. The width of peaks at $-20dB$ below top of the peak ranges from less than 0.5MHz to around 2.5MHz in the ML region. Contour plots of the width of RF peaks are superimposed on the map plot of Fig.2.2. Fig.2.2 shows that the decrease in peak height is accompanied by an increase of width of the peak at the fundamental frequency. This effect is expected and means that the amount of pulsed power remains relatively constant over the optimum range of stable ML.

The variation of roundtrip frequency over the operating region of stable ML is about 10MHz. The repetition frequency of a passively ML laser diode is influenced by the bias conditions due to the gain/absorption saturation effects [13]. Increasing the

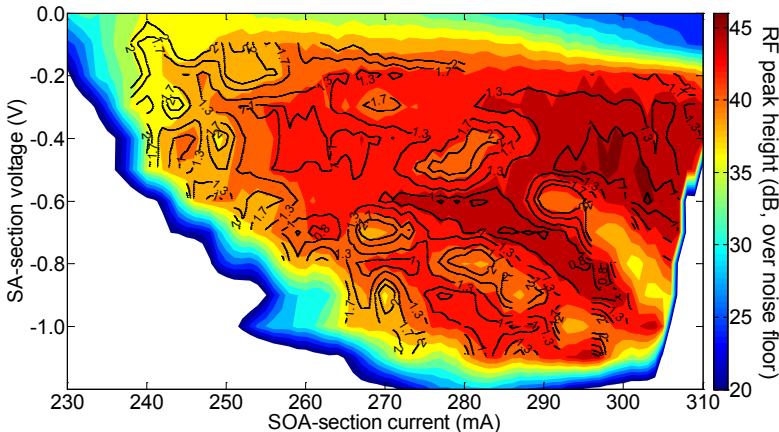


Fig.2.2. Region of mode-locking for the 10GHz laser. Height of the peak (color-coded in dB scale) at the fundamental frequency over noise floor ($-90dB$), recorded with a 50GHz electrical spectrum analyzer. The electrical bandwidth used to obtain the spectra is 50kHz. Value of full width of peak (MHz) at 20dB lower than the top of peak is superimposed on the RF power mapping.

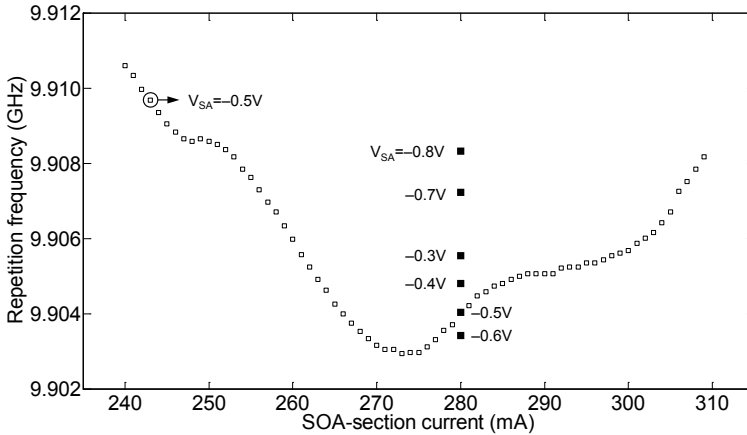


Fig.2.3. Repetition frequency tuning characteristics of the 10GHz passively mode-locked QD laser at $V_{SA}=-0.5V$ as the injection current to the SOA-section is increased (open squares). The filled black squares show the repetition frequency at $I_{SOA}=280mA$ for different values of absorber reverse bias.

injection current to the gain section, as well as reducing the reverse bias on the absorber corresponds to an increase in pulse energy and vice versa. Therefore, the repetition frequency of a passively ML semiconductor laser varies with pulse energy. Fig.2.3 shows the changes in the repetition frequency (open squares) of the 10GHz passively mode-locked QD laser as the injection current to the SOA-section is increased at $V_{SA}=-0.5V$. The filled black squares in Fig.2.3 show the repetition frequency at $I_{SOA}=280mA$ for different values of absorber reverse bias.

2.3. Dual-wavelength operation at 10GHz

Dual-wavelength synchronous ML is very attractive for application such as THz generation and nonlinear microscopy for bio-imaging, where a two-color pulse train is required. In case of Ti:sapphire ML lasers, various techniques are being studied and implemented (see for example [14] and references in [15]) to achieve dual-wavelength mode-locking. In QD lasers, simultaneous emission from ground state (GS) and excited state (ES) is a well known origin of two color emission [16,17]. In the ML state, the GS-ES emission may give rise to synchronously mode-locked dual-wavelength ML. GS-ES emission state in two-section InGaAs/GaAs laser diodes is reported in [18,19]. Apart from the conventional multi state emission in QD lasers, dual wavelength emission from a single energy state, i.e. GS, is also reported for 92.5GHz ML operation in a single-section InAs/InP QD structure [20]. Recently, similar performance was observed in a multi-section InAs/InGaAs QD laser grown on a GaAs(100) substrate [21].

2.3.1 Optical spectra

In this section, we report on optical spectra of our MLLDs in the state of passive ML. Fig.2.4 shows the evolution of optical spectra of the output light of the 10GHz laser while the SOA-section injection current is increased from above threshold over the ML

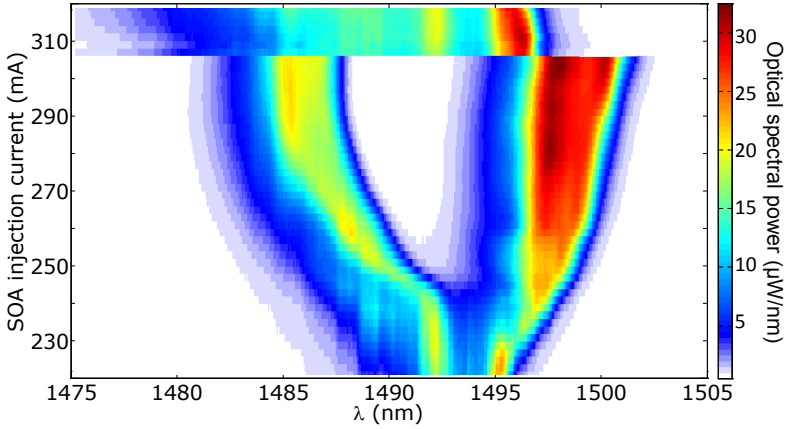


Fig.2.4. Evolution of optical spectrum (linear scale, color-coded in $\mu\text{W}/\text{nm}$) for the 4mm HR-coated QD MLLD with 120 μm -long SA-section at $V_{\text{SA}}=-0.5\text{V}$. The plot is obtained as a function injection current to the SOA-section. The optical bandwidth used is 1nm.

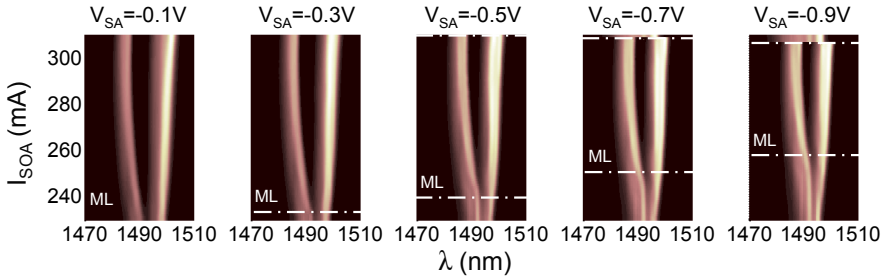


Fig.2.5. Optical spectra (linear scale, a.u.) obtained with the 10GHz QD laser as the gain section injection section is increased at different values of absorber voltage.

region. Above threshold, the laser emits in the wavelength range of 1.49 μm to 1.50 μm . Near the onset of ML, the optical spectrum splits in two parts. The two lobes get spectrally separated gradually as the injection current increases. Nevertheless, at a certain operating point, the two groups of modes suddenly jump together and form a wide spectrum. At this point the laser enters a weak Q-switched ML state.

As indicated in Fig.2.4, the double-lobe spectrum evolves slowly from a single mode group as the injection current increases and then changes suddenly back to a structure more similar to the one at lower currents. There are two reasons that the two spectral lobes belong to the same transition rather than separate emission from GS and ES. Firstly, simultaneous emission from GS and ES at higher current densities is most likely to lead to emergence of a separate spectral lobe as the injection current is increased. However one also expects then that such a structure would always be separate and stay separate. This is similar to the observations in [20,21] and is clearly not the case here. Another fact is that the measurement of optical gain of similar QD material [3] indicates that separation of GS and ES in our material is around 60nm, which is much more than the 10-15nm wavelength distance observed in Fig.2.4.

Fig.2.5 presents the optical spectra (linear scale) as a function of I_{SOA} and V_{SA} obtained with the 10GHz laser. The region of ML is indicated in each plot. The laser is mode-

locked for all current values except those above and below the dash-dotted lines. It is clear that over the whole region of ML, the optical spectrum consists of two groups of modes. For all the five values of the bias voltage shown in Fig.2.5, the short- λ side of the spectrum significantly shifts to blue as the current is increased. However, the long- λ side undergoes a minor red-shift. On the other hand, the qualitative shape of optical spectra remains similar for different values of bias voltage. Fig.2.5 will be discussed in more details in section 7.

2.3.2 Verification of ML in both mode groups

An instance of a dual-wavelength optical spectrum recorded at $I_{SOA}=280\text{mA}$ ($\sim 1.5I_{th}$) and $V_{SA}=-0.5\text{V}$ is presented in Fig.2.6(a). The two groups of modes are similar in shape and are separated by $\sim 12\text{nm}$; the width of long-wavelength group of modes is around 5nm and shows higher optical power as compared to the other lobe which has a FWHM of 3nm . The output signal in the two groups of modes is studied in more detail in order to verify pulsed operation at both spectral lobes. A tunable band-pass filter (BPF) with 1.2nm FWHM bandwidth that can be tuned over the whole optical spectrum is used to filter the MLLD output signal. The filtered signal is then amplified using a booster SOA and measured at the characterization setup. If only the SOA is used at the output of the laser, the short wavelength group is effectively filtered out due to the gain properties of the booster amplifier.

Fig.2.6(b) shows the RF spectra of the optical signals with the filter tuned at the centre of each of the two mode groups, i.e. green and red when the filter is tuned at 1486.5nm and 1498.5nm respectively. The RF spectrum from the total long wavelength mode group (LWMG) is shown in black. Clear RF peaks at the repetition frequency and higher harmonics confirm that both mode groups contribute to the pulsed operation. The recorded RF spectra with 50kHz resolution bandwidth show that the optical signals generated at the two lobes have within 0.003% similar repetition frequencies.

Another important conclusion follows by comparison of the pedestal around RF components for the three signals. In particular, the pedestal around the DC component is of importance because it corresponds to the amplitude noise. In Fig.2.6(b), the low frequency components in the RF spectrum corresponding to the total output from the LWMG are very low and in the order of the ESA noise level. However, the filtered signals, which contain only a fraction of the laser output, show significantly increased DC pedestal. This shows that the filtered signals exhibit a higher amplitude noise and that the two spectral lobes are coupled. The coupling is attributed to spectral energy exchange between optical modes. The observations are consistent with the results presented in [9].

We verify the pulsed operation of both mode groups further in the next section by investigation of time traces. For this we had to use a sampling oscilloscope system. In order to apply the sampling oscilloscope, the device is operated with the SA under an external modulation, i.e. the hybrid ML. The results are presented in following section.

2.4. Hybrid mode-locking

In hybrid ML of a two-section MLLD, a stable electrical modulating signal at a frequency close to the free spectral range of the laser cavity is applied to the absorber section. The RF signal can be applied to slightly tune the repetition rate of the pulsed

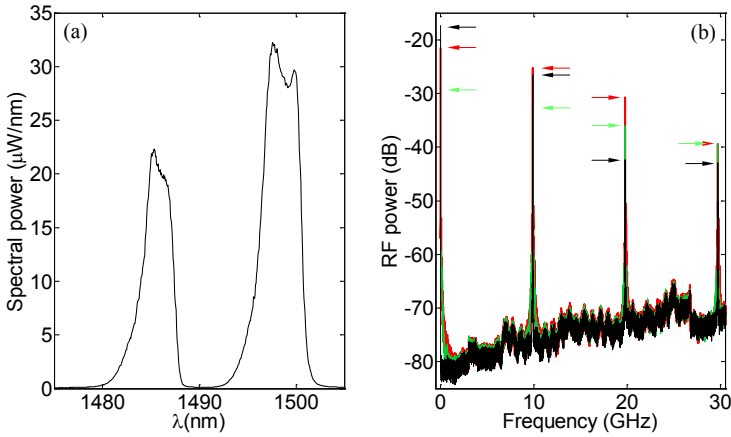


Fig.2.6. (a) Dual-wavelength optical spectrum (linear scale, μ W/nm) of the 10GHz QD laser operating at $I_{SOA}=280$ mA, $V_{SA}=-0.5$ V. (b) RF spectra of full bandwidth and filtered optical signals when BPF is tuned at the center of short-wavelength (green) and the long-wavelength (red) lobes. RF resolution bandwidth is 3MHz. The arrows on show top of RF peaks.

laser, but more importantly it reduces the timing jitter. We have previously investigated hybrid mode-locking in a 4.6GHz QD MLLD and shown that by applying an external modulating signal, it is possible to achieve timing jitter as low as 0.6ps, while the measured value of timing jitter for the passively mode-locked laser was 35-40ps [22]. Furthermore, hybrid ML enables broader range of measurement and characterization possibilities, e.g. with high-speed electrical sampling oscilloscopes, due to the availability of a clean electrical trigger. The RF source used is an Anritsu MG3691B low phase noise synthesized signal generator.

2.4.1 RF locking range

In order to define an RF locking range in terms of frequency and power of the modulating signal, we use the value of timing jitter. Timing jitter is an important parameter for practical applications and is usually referred to when evaluating the stability of optical pulses. Jitter values have been calculated by integration of the measured single sideband phase noise signal over 10kHz-80MHz offset around the fundamental RF peak.

A good operating point for the passively mode-locked (free running) 4mm-long QD MLLD is at $I_{SOA}=280$ mA and $V_{SA}=-0.5$ V with $f_{rep}=9.904$ GHz. At this point, we measure a timing jitter of 14.5ps. Fig.2.7 shows a map in which the values of timing jitter are indicated. Jitter values are measured under hybrid ML for a range of RF power levels and frequencies. Over the whole range of operating parameters, the jitter remains below 5.5ps. The value of minimum jitter measured in this range is about 1ps. At $P_{RF}=15$ dBm, a maximum locking range of ~ 22 MHz is achieved.

At any power level of the external RF signal, a certain frequency tuning range exists where the ML is stable. Detuning the modulating signal from the free-running frequency, outside the locking range (shown in Fig.2.7), results in a state of passive ML which is perturbed by the RF signal. The tuning range broadens as the modulating power is increased; however, the locking range is not symmetric around the free-

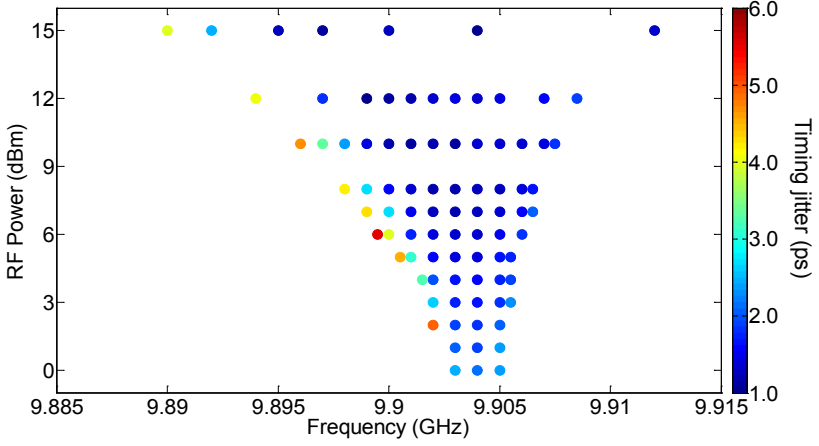


Fig.2.7. Measured values of timing jitter (color-coded in ps) determine the RF locking range vs. RF power and frequency. Jitter values are calculated by integration of single side-band phase noise signal (10kHz-80MHz) around the fundamental harmonic. The device is operated at $I_{SOA}=280\text{mA}$ and $V_{SA}=-0.5\text{V}$.

running frequency. In slow saturable absorber mode-locking the pulse repetition rate and the pulse amplitude are correlated; in other words, the repetition frequency depends nonlinearly on the laser pulse energy. In [13], the detuning parameter (difference between the repetition frequency of the passively mode-locked laser and the cavity roundtrip frequency) is expressed as a function of pulse energy and the repetition frequency tuning characteristics of a passively mode-locked laser is discussed.

The origin of the asymmetry observed in Fig.2.7 becomes clear by considering the change in repetition frequency around the operating point $I_{SOA}=280\text{mA}$ and $V_{SA}=-0.5\text{V}$ which is depicted in Fig.2.3. At this point, the repetition frequency increases by either increasing the injection current to the gain section or by decreasing the absorber bias voltage, i.e. increasing the pulse energy. On the other hand, if the injection current is reduced or the bias voltage on the absorber is increased (pulse energy decreased), the repetition frequency decreases until a certain bias parameters are reached, and then starts to increase. This behavior is in good agreement with the model presented in [13].

It follows from the observations of Fig.2.3 that, at the operating point $I_{SOA}=280\text{mA}$ and $V_{SA}=-0.5\text{V}$, the required change in the pulse energy is smaller for tuning the repetition frequency of the MLLD towards lower frequencies than towards higher frequencies. At this bias condition, the frequency tuning range around the free-running frequency is asymmetrical and is skewed towards the lower frequencies. The RF locking range, presented in Fig.2.7, accords very well with this statement. This observation is consistent with the arguments given in [23] where hybrid ML is theoretically studied using a set of delay-differential equations and compared with experiments on GaAs-based QD lasers.

2.4.2 Evaluation of chirp

To evaluate the value of chirp in devices under test, a similar approach as reported in [9] is adopted. A schematic of the measurement setup is shown in Fig.2.8(a). In this method

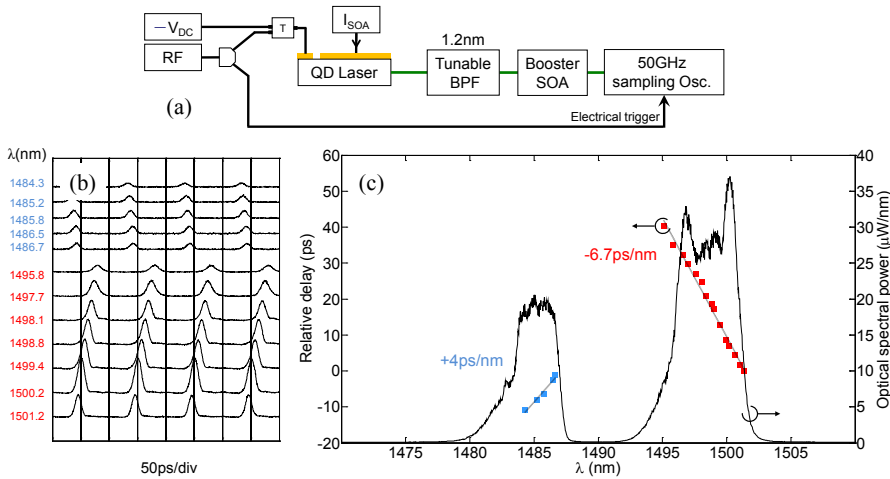


Fig.2.8. (a) Schematic of the setup used to measure relative timing difference of spectrally filtered optical pulses. (b) Typical time traces recorded with the 50GHz sampling oscilloscope. (c) Measured values of timing differences (ps, left axis) on a plot of optical spectrum (right axis, $\mu\text{W}/\text{nm}$) indicate an almost linear spectral chirp over each mode group.

the output of the hybridly mode-locked device is passed through a band-pass filter BPF which is tuned over the spectrum and oscilloscope traces are recorded. These traces are then analyzed to determine the relative time delay of the different spectral components. A 50GHz sampling oscilloscope is used to record time traces. In case of hybrid ML, the RF signal can be used as the trigger for the sampling oscilloscope. The results are shown in Fig.2.8(b) for the 10GHz QD MLLD operating at $P_{\text{RF}}=3\text{dB}$.

The recorded time traces are presented in Fig.2.8(b). It is clear that as the BPF is tuned over the spectrum, the signals in the time traces move in time accordingly. These signals also confirm that both mode groups contribute to the pulsed operation. The pulse train period for each of the signals is $\sim 100\text{ps}$ (10GHz repetition rate). The value of the linear chirp is determined to be $-6.7\text{ps}/\text{nm}$ over the long-wavelength spectral lobe. On the short-wavelength side of the spectrum, we measure a $+4.0\text{ps}/\text{nm}$ chirp. The overall time delay from all different spectral components is around 50ps which is half the roundtrip time. The autocorrelator shows approximately 43ps FWHM for the optical pulse which is consistent with the data in Fig.2.8(c). It is interesting that the spectral chirp has opposite signs over the two groups of modes. The measured chirp profile in Fig.2.8(c) indicates that leading edge of pulses in time domain consists of the short-wavelength lobe, i.e. from 1480nm to 1487nm. The spectral components to follow are from the long wavelength side, from 1502nm to 1495nm.

2.5. 3GHz mode-locked laser

2.5.1 Passive mode-locking

In order to have an overview of ML properties in QD MLLDs with different repetition rates, we have also fabricated a series of 13mm-long lasers. In this section, we present results obtained with the 3GHz laser. To the extent of our knowledge, the 3GHz mode-locked laser has the lowest repetition rate reported for a monolithic InAs/InP(100) QD

laser. The MLLD under test in this section has a 650 μm absorber section which is 3% of the total cavity length.

We follow similar measurement steps, as described in section 2, to map the region of ML in terms of operating parameters, i.e. I_{SOA} and V_{SA} . To assure a uniform current distribution to the relatively long gain section, we used two probe tips for current injection. The device operates in stable ML regime for a range of injection current $I_{\text{SOA}}=600\text{-}870\text{mA}$ at $V_{\text{SA}}=-0.2\text{V}$ and $I_{\text{SOA}}=650\text{-}900\text{mA}$ at $V_{\text{SA}}=-1.2\text{V}$. In the ML operating range, recorded ESA traces show clear RF peaks at 3GHz and higher harmonics; fundamental RF peaks are up to 55dB in height over the noise floor. The width of RF peaks at -20dB below the top of peak range from less than 200kHz to around 2MHz in this region. Variation of roundtrip frequency over the entire stable ML operating regime is about 10MHz. Fig.2.9 shows the changes in the repetition frequency (open squares) as the injection current to the SOA-section is increased at $V_{\text{SA}}=-0.8\text{V}$. The filled black in Fig.2.9 show the repetition frequency of the 3GHz passively mode-locked laser at $I_{\text{SOA}}=800\text{mA}$ for different values of absorber reverse bias.

Observations on the optical spectra show that the 3GHz laser generates a dual-wavelength spectrum, similar to the 10GHz laser. The optical spectrum spreads over approximately 20nm optical bandwidth which is larger than widths observed from the 10GHz MLLD. However, the power balance between the two spectral lobes is different. The short-wavelength group of modes contains a relatively large portion of the spectral power. The spectral components between the two main lobes are not fully suppressed as well.

To verify the opposite sign of chirp over the optical spectrum in passively mode-locked regime, we have used the setup which is schematically shown in Fig.2.10(a). We take a similar approach as mentioned in previous sections to filter the spectrum and record corresponding time traces. In case of the 3GHz laser, we can apply a 6GHz real-time oscilloscope. This allows for a study of the purely passively mode-locked state similar to the way presented in [9]. This will also allow us a comparison with (more accurate)

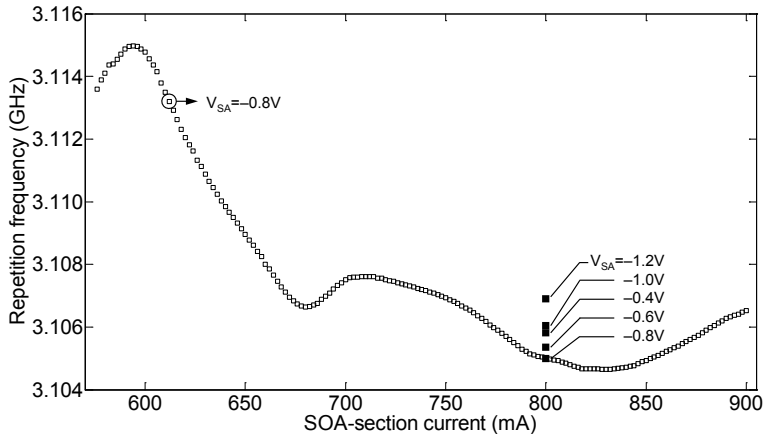


Fig.2.9. Repetition frequency tuning characteristics of the 3GHz passively mode-locked QD laser at $V_{\text{SA}}=-0.8\text{V}$ as the injection current to the SOA-section is increased (open squares). The filled black squares show the repetition frequency at $I_{\text{SOA}}=800\text{mA}$ for different values of absorber reverse bias.

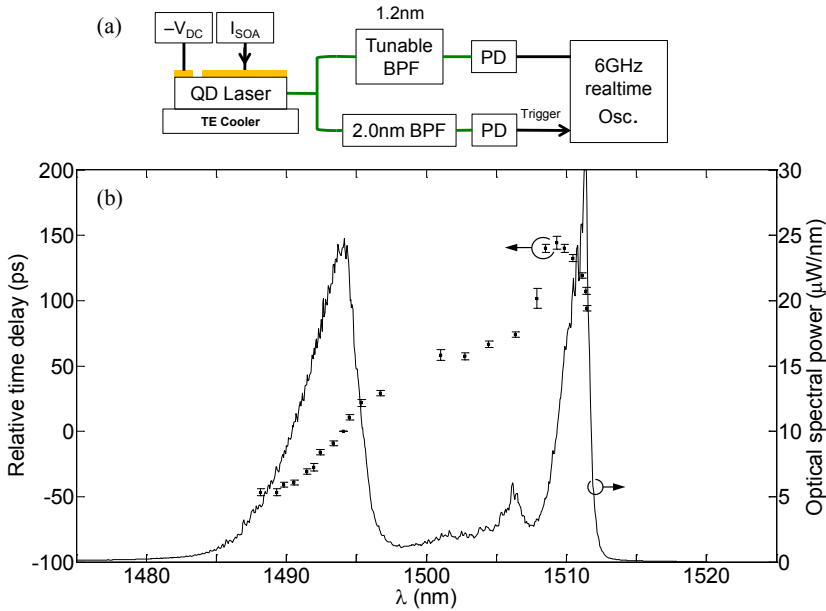


Fig.2.10. (a) Schematic of the setup used to measure relative timing difference of spectrally filtered optical pulses in passive ML regime. (b) Measured values of timing differences (ps, left axis) on a plot of optical spectrum ($\mu\text{W}/\text{nm}$, right axis).

results from hybrid mode-locking in the next section 5.2. In the passive ML regime the oscilloscope needs to be triggered on the optical pulses themselves. Therefore, the output light of the MLLD is first split using a 3dB power splitter. Each branch of the power splitter includes a tunable BPF which are connected to input channels of the real-time oscilloscope through fast PDs. The trigger signal is provided through a BPF with 2.0nm bandwidth and the central wavelength fixed at $\sim 1494\text{nm}$. The other BPF (1.2nm bandwidth) is tuned and the output is recorded by the oscilloscope. We monitor the triggering optical signal during the measurement to make sure trigger signal is stable enough and that recorded time traces are not affected by the amplitude noise of the trigger signal, as much as possible.

Fig.2.10(b) shows the relative time delays measured for the QD MLLD operating at $I_{SOA}=750\text{mA}$ and $V_{SA}=-0.6\text{V}$. A different sign of chirp value over the two spectral lobes, i.e. positive chirp over shorter wavelength and negative chirp over longer wavelength group is observed. The measurement is repeated for four operating points at different values of injection current ($I_{SOA}=750\text{mA}$, 800mA) and bias voltage ($V_{SA}=-0.6\text{V}$, -0.8V) and in all cases we observed opposite sign of chirp on the spectral lobes, where the short-wavelength spectral lobe shows a positive chirp.

2.5.2 Hybrid mode-locking

In case of the 13mm long QD MLLD, a good operating point for the free running laser is at $I_{SOA}=800\text{mA}$ and $V_{SA}=-0.8\text{V}$ with $f_{\text{rep}}=3.105\text{GHz}$. At this point the value of timing jitter for the optical pulses is measured to be 8-16ps. Fig.2.11 shows the timing jitter values measured for the hybridly mode-locked laser, over a range of RF power levels

and frequencies. The range is chosen such that the jitter remains below 3ps. The minimum jitter value achieved in this range is about 0.7ps.

At $P_{RF}=15\text{dBm}$, the tuning range is around 27MHz and is comparable to the case of 10GHz laser where we measure approximately 22MHz of locking range (see Fig.2.7). At $P_{RF}=20\text{dBm}$ a maximum locking range of $\sim 70\text{MHz}$ is achieved, which is a significant tuning range around the 3.105GHz repetition frequency of the laser. The tolerable detuning to the lower frequencies is $\Delta f=5\text{MHz}$, while a detuning of $\Delta f=65\text{MHz}$ to higher frequencies is allowed. It is clear from Fig.2.11 that the locking range is strongly asymmetrical around the free running frequency. However, unlike the case of the 10GHz laser, the locking range is skewed towards higher frequencies. This difference in shape of the RF locking range is to be expected given the data in Fig.2.9 and the operating point of the passively ML 3GHz laser in comparison with the data of the 10GHz laser in Fig.2.3. In case of the 3GHz laser, a larger tuning range is achieved towards the higher frequencies since the (passive ML) operating point lies relatively close to, and on the left side of the bias condition where the minimum repetition frequency occurs.

In order to evaluate the effect of the RF signal on the optical spectra, a number of optical spectra obtained from the 13mm-long MLLD are recorded in the regime of hybrid ML at $P_{RF}=15\text{dBm}$ and shown in Fig.2.12. Modulating the absorber voltage at frequencies lower than the free-running frequency, i.e. 3.105GHz, mostly affects the longer wavelength spectral lobe. As the modulating frequency decreases, the long-wavelength lobe shifts to the blue side ($\sim 1.2\text{nm}$ for 3MHz frequency change) and the spectral power in this lobe increases. This results in an overall reduction of the total optical bandwidth. However, if the modulating frequency is increased above the free-running frequency, the short-wavelength group undergoes a blue shift of around 6nm. Meanwhile, the long-wavelength group broadens and shifts towards the short-wavelength group ($\sim 3\text{nm}$ for 24MHz). Therefore, the total optical bandwidth is increased by approximately 3nm.

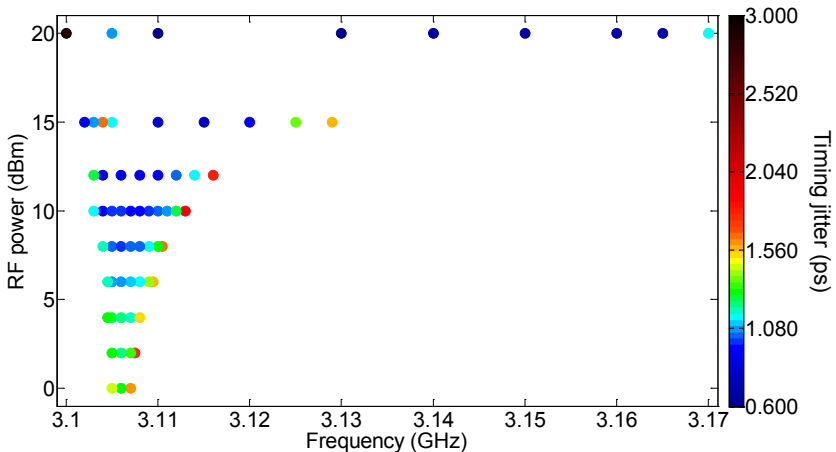


Fig.2.11. RF locking range: measured values of timing jitter at several values of RF power and frequencies for the 3GHz QD MLLD. The device is operated at $I_{SOA}=800\text{mA}$ and $V_{SA}=-0.8\text{V}$. Timing jitter in case of passively mode-locked laser is 8-16ps.

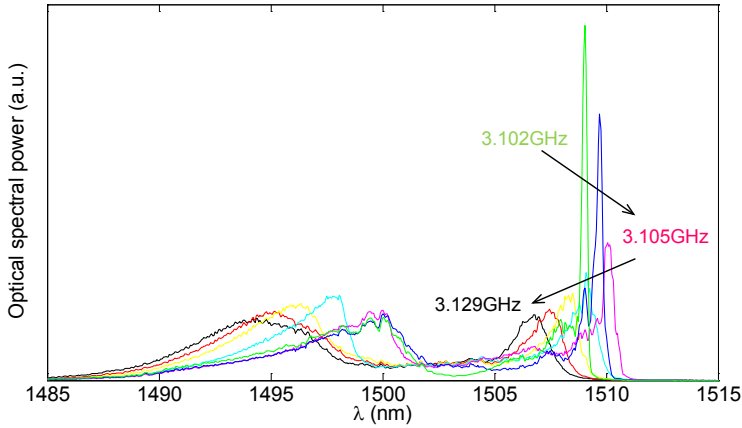


Fig.2.12. Recorded optical spectra (linear scale) obtained with the 13mm-long MLLD under hybrid ML at several RF frequencies. Modulation RF power is $P_{RF}=15\text{dBm}$. Free running frequency is $f_{rep}=3.105\text{GHz}$.

2.5.3 Chirp evaluation under hybrid mode-locking

Evaluating the chirp profile for the 3GHz QD MLLD confirms opposite sign of chirp over the spectral lobes under hybrid mode-locking. The observation is consistent with the results on the dual-wavelength 10GHz MLLD. To determine the chirp, we used the same technique. Results are shown in Fig.2.13. Fig.2.13(a) shows time traces of spectrally filtered pulses, recorded with a 30GHz sampling oscilloscope. Timing difference between different pulses is clear from the figure. The measured timing differences are shown in Fig.2.13(b) over a plot of the optical spectrum at $I_{SOA}=800\text{mA}$, $V_{SA}=-0.8\text{V}$ and $P_{RF}=19\text{dBm}$. Available RF power on the absorber is approximately 6dBm which is the maximum power available in this setup due to losses introduced by the 3dB power splitter and cables.

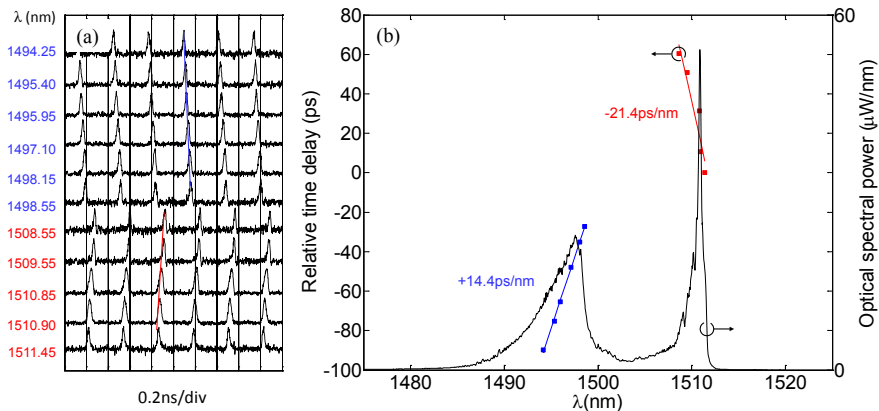


Fig.2.13. (a) Time traces of spectrally filtered optical pulses recorded by a 30GHz sampling oscilloscope. (b) Measured values of timing differences (ps, left axis) on a plot of optical spectrum at $I_{SOA}=800\text{mA}$, $V_{SA}=-0.8\text{V}$, and $P_{RF}=19\text{dBm}$ (6dBm on the SA due to RF losses).

2.6. Self mode-locked 4.5GHz QD laser

Self induced ML is already demonstrated in quantum well [24,25] as well as InP-based quantum dash material. Passive mode-locking in FP lasers was first reported in [26] for an InGaAsP laser with cavity length of 250 μ m. The effect was explained through power dependent self- and cross gain saturation. The analysis presented in [10,26] shows that four-wave mixing accompanied by nonlinear gain saturation would lead to passive mode-locking.

In this section, we present experimental results obtained from a 9mm-long, single-section FP laser. The laser has cleaved facets and lasing threshold at $I=430$ mA. Fig.2.14(a) shows the evolution of the optical spectrum as the injection current is increased. The optical spectrum splits in two (almost) separate lobes at approximately $I=600$ mA. This coincides with the onset of mode-locking at a repetition frequency of $f_{\text{rep}}\sim 4.5$ GHz. The ESA trace in Fig.2.14(b) is recorded at $I=650$ mA and shows clear RF peaks at harmonics of the repetition frequency. This is an indication of mode-locking.

As the current is increased above $I=650$ mA, a third lobe at around $\lambda=1500$ nm appears in the optical spectrum. The ML is affected by appearance of the third spectral lobe. The ESA trace in Fig.2.14(c) is recorded at $I=700$ mA and contains RF peaks at harmonics of $f_{\text{rep}}=4.5$ GHz accompanied by additional frequency components. The extra frequency components have relatively low spectral power and indicate increased amplitude modulation at 388MHz.

Following similar measurement steps as mentioned in previous sections, we confirm the synchronized pulsed operation of both spectral lobes. A BPF is tuned over the spectrum and time traces are recorded using a 6GHz real-time oscilloscope. Results are shown in Fig.2.15(a). Relative time delay between traces are then measured and mapped on a plot of spectrum in Fig.2.15(b). The measured spectral phase relation indicates different sign of chirp over the two spectral lobes, which is consistent with observations presented in the preceding sections.

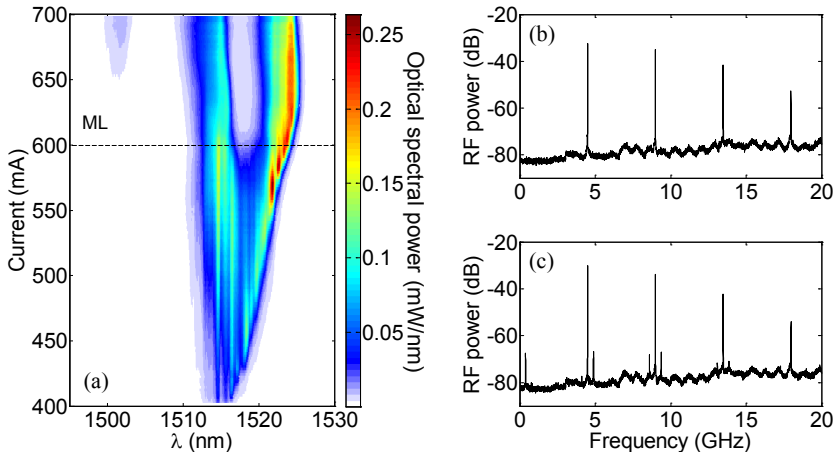


Fig.2.14. (a) Evolution of optical spectrum (mW/nm) obtained with the single-section QD laser, as the injection current is increased. Region of ML is indicated. (b) Electrical spectrum recorded at $I=650$ mA, and (c) $I=700$ mA.

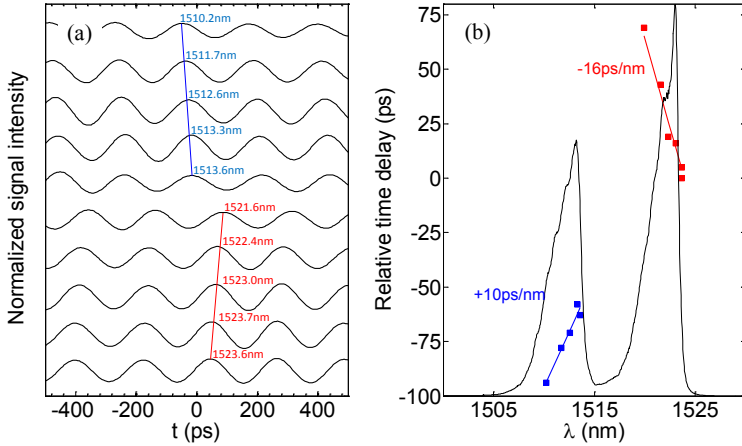


Fig.2.15. (a) Time traces of spectrally filtered optical pulses recorded with a 6GHz real time oscilloscope. (b) Measured values of timing delays on a plot of optical spectrum at $I=650\text{mA}$.

A point to mention is that we have observed the self-induced mode-locking in a single-section 10GHz (4mm-long cavity) QD laser as well. The 10GHz single-section laser operates in a dual-wavelength ML state. However, the electrical bandwidth of our real-time oscilloscope does not allow us to observe the 10GHz optical signal, thus we have not been able to evaluate the spectral chirp.

2.7. Summary and Discussion

We have fabricated and characterized InAs/InP QD-based mode-locked lasers with different repetition frequencies. The devices under test provide a larger optical bandwidth than the bulk and quantum well ML devices that we have fabricated (see for instance [27,28]). Wide coherent bandwidth which is desirable for generation of short optical pulses, together with the potential for full photonic integration are the main motivations to use InAs/InP QD mode-locked lasers as sources of optical pulses in combination with optical pulse shapers.

We have presented stabilization of the timing jitter of optical pulses in the regime of hybrid mode-locking. Furthermore, we have mapped regions of RF locking in terms of modulating power and frequency. A map of RF locking range is defined by measuring the timing jitter and is in itself of importance for practical purposes, such as in specifying the RF tuning range.

2.7.1 Spectral Splitting: dual-wavelength ML

The main feature of mode-locking in the devices presented in this chapter is the dual-wavelength pulsed operation. We have confirmed the synchronized pulsed operation of both spectral lobes by electrical spectra and recorded time traces of filtered spectral components. Furthermore, we have shown that spectral chirp has different sign over the two lobes.

In order to investigate the origin of dual-wavelength ML operation, we have recorded optical spectra at different values of operating parameters, i.e. I_{SOA} and V_{SA} . The optical

spectra obtained with the 10GHz two-section laser and the 4.5GHz single-section FP lasers are similar. In case of the 3GHz laser, the power balance between the spectral lobes is different; however, dual-wavelength operation is observed and confirmed. From the results in the previous sections, a number of conclusions can be made that are presented below.

- (a) In QD lasers, simultaneous emission from GS and ES is a well known origin of two color emission. This phenomenon is more likely to give rise to a distinct spectral lobe at higher pump levels. In the devices presented here, we observe a splitting of the output spectrum from a single lobe as the current density is increased. This means that both spectral lobes are generated from a single state.
- (b) In case of the single-section QD laser (Fig.2.14), the emission above threshold starts at GS. Optical spectrum then splits into two lobes at the onset of mode-locking. Regarding the observed similarities in case of two-section devices, we believe that our devices operate at GS.
- (c) It is clear from Fig.2.5 that as the reverse bias on the absorber is increased, the spectral splitting occurs at a higher value of current injection. While an increased absorber voltage causes a relatively higher roundtrip loss, a higher current injection brings about a higher optical gain. This suggests that the onset of spectral splitting is mostly dependent on the internal optical power.
- (d) Observation of mode-locking in the single-section QD laser reveals that processes in the gain section make our QD laser devices go into mode-locked operation. While the absorber section affects the laser behavior, it is not essential for mode-locking. The advantage of self mode-locked single-section MLLDs is that they require a single bias source and hence are operated more easily. On the other hand, for practical purposes two-section MLLDs offer several benefits such as timing jitter stabilization and tuning the repetition frequency which were mentioned in case of hybrid ML.

2.7.2 Chirped pulse generation

In [8] we have reported on a unique feature of ML operation in a 9mm-long FP-type QD MLLD. The MLLD had a repetition rate of 4.6GHz and generated very elongated pulses in spite of a relatively wide optical bandwidth. In passively ML state, the time variation of the output power was only approximately ten percent of the total power, meaning that the duration of pulses was close to the roundtrip time and pulses overlapped. We measured a nearly linear chirp of -20ps/nm over the spectrum. In hybrid ML regime [22], time duration of pulses was reduced to less than half the roundtrip time. The negative chirp was verified when the chirp was (almost) compensated for by using length sections of single mode fibers with normal dispersion.

The results presented in this chapter complement and extends the previously reported results on the 4.6GHz laser [9,22]. Comparing the chirp results of the different devices gives some insight into the dynamics when the operating current density and roundtrip losses are considered. The injection current density in the ML region for the 10GHz and 3GHz lasers is in the range of 3.1–3.9kA/cm² and 2.4–3.6kA/cm² respectively. The value of current density for the 4.6GHz two-section laser, which is reported in [9], is in the range of 4.3–5.7kA/cm². The facets of the 10GHz and the 3GHz lasers which are presented in this chapter are HR coated at the absorber side, while the 4.6GHz laser had uncoated facets. Thus, the reduction in operating current density in the devices

presented in this chapter is attributed to application of HR coating. However, the operating range in terms of absorber voltage seems to be less wide as compared with the ML region of the 4.6GHz laser. A 9mm-long single section FP laser is also presented in this chapter which operates in stable mode-locked regime for current densities in the range of 3.4–3.7kA/cm². The single-section device has non-coated facets. Its operating current densities are therefore lower than that of the two-section 4.6GHz laser which also has no coating applied but does have an absorber.

Fig.2.16 shows instances of optical spectra and spectral chirp which are obtained from the different QD MLLDs presented at an operating point of strong ML. Fig.2.16(a) and (b) correspond to the 13mm-long and 4mm-long two-section lasers respectively. The device in Fig.2.16(c) is a 9mm-long single-section laser which has un-coated facets. The device in Fig.2.16(d) is the one presented in [8] and is a 9mm-long two-section laser with un-coated facets. In Fig.2.16, the devices are arranged in order of the threshold current density from left to right. The threshold current density in the 3GHz laser is $J_{th}=1.82\text{kA/cm}^2$; this is the lowest value due to the longest gain section among the four lasers. The 4mm-long laser with HR-coating comes next with $J_{th}=2.28\text{kA/cm}^2$. The single-section 9mm-long laser has a slightly higher threshold current density. The two-section 9mm-long with the highest cavity losses has $J_{th}=3.78\text{kA/cm}^2$.

The device with the lowest operating current densities, i.e. the 3GHz laser at $J_{SOA}=3.27\text{kA/cm}^2$, shows a dual-lobe spectrum. The longer-wavelength side has a narrow lobe and the shorter wavelength side has around 80% of the spectral power. It is clear that this laser tends to operate on the shorter-wavelength side of the spectrum. In terms of the operating current densities, the 10GHz laser with an HR-coated facet and the 4.5GHz single-section laser come next in the order with $J_{SOA}=3.61\text{kA/cm}^2$. The optical spectra in case these devices consist of two clear spectral lobes with comparable amount of power. In case of the next device, i.e. the 9mm-long two-section

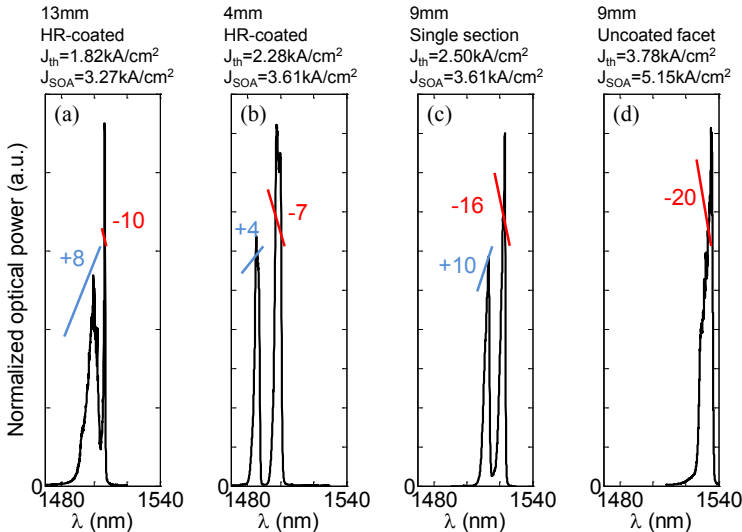


Fig.2.16. Optical spectra (linear scale, a.u.) and spectral chirp (ps/nm) obtained with (a) 3GHz laser at $J=3.27\text{kA/cm}^2$, (b) 10GHz laser at $J=3.61\text{kA/cm}^2$, (c) 4.5GHz single-section at $J=3.61\text{kA/cm}^2$, and (d) 4.6GHz two-section at $J=5.15\text{kA/cm}^2$.

laser with uncoated facets, the operating current density is $J_{\text{SOA}}=5.15\text{kA/cm}^2$. This laser operates with only a single spectral lobe in the ML region, which we believe is the long-wavelength side of the spectrum. This is consistent with the observation presented in Fig.2.4 which shows that at higher current densities, the two spectral lobes jump together to form a single-lobe spectrum.

The chirp in our devices is high and leads to elongated optical pulses. The total time differences between spectral components are 50ps, 70ps and 150ps for the 4mm, 9mm and 13mm cavity lengths. From Fig.2.16 one can clearly see that the long wavelength spectral lobe is always up-chirped and the short wavelength lobe is always down-chirped. Our results show that the chirp is driven by a robust mechanism which prevents the formation of a short pulse, i.e. locking of the phases of all spectral components to the same value. Even under hybrid ML, the pulse duration is almost half the roundtrip time, independent of the cavity length.

The question remains on the exact origin of the dynamics. We have shown that mode-locked operation in InAs/InP(100) QD MLLDs has similar properties to the state of FM locking. Theoretical discussion on details FM locking in these devices is out of scope this chapter. However, the generation of highly chirped pulses, the presence of correlated amplitude noise in our devices and the observation of self-induced mode-locking in a single section laser stress the fact that the processes in the gain section play a critical role in these devices. The inhomogeneous broadening and size distribution of quantum dots provide the wide and smooth gain spectrum in InAs/InP QD-based devices. The gain in QD material is localized in the dots which are spatially separated. The carriers providing the gain are held at the position of the dots and their mobility is significantly reduced compared to the carrier mobility in bulk or quantum well material. The low side-wall surface recombination rate observed in deeply-etched ridge waveguide QD lasers [29] confirms this effect. Therefore, dynamic gain gratings are stronger in QD materials than in quantum well systems and as a result the four-wave mixing process is more efficient which is the process that we assume to be at the basis of the laser dynamics observed [2].

References

- [1] R. Nötzel, S. Anantathanasarn, R. P. J. van Veldhoven, F. W. M. van Otten, T. J. Eijkemans, A. Trampert, B. Satpati, Y. Barbarin, E. A. J. M. Bente, Y.-S. Oei, T. de Vries, E. Geluk, B. Smalbrugge, M. K. Smit, and J. H. Wolter, "Self Assembled InAs/InP Quantum Dots for Telecom Applications in the 1.55 μm Wavelength Range: Wavelength Tuning, Stacking, Polarization Control, and Lasing," *Japanese Journal of Applied Physics* 45, pp. 6544–6549 (2006).
- [2] F. Lelarge, B. Dagens, J. Renaudier, R. Brenot, A. Accard, F. van Dijk, D. Make, O. L. Gouezigou, J.-G. Provost, F. Poingt, J. Landreau, O. Drisse, E. Derouin, B. Rousseau, F. Pommereau, and G.-H. Duan, "Recent Advances on InAs/InP Quantum Dash Based Semiconductor Lasers and Optical Amplifiers Operating at 1.55 μm ," *IEEE Journal of Selected Topics in Quantum Electronics* 13, 111-124 (2007).
- [3] B. W. Tilma, M. S. Tahvili, J. Kotani, R. Nötzel, M. K. Smit, and E. A. J. M. Bente, "Measurement and analysis of optical gain spectra in 1.6 to 1.8 μm InAs/InP (100) quantum-dot amplifiers," *Optical and Quantum Electronics* 41, 735-749 (2010).
- [4] B. W. Tilma, Y. Jiao, J. Kotani, H. P. M. M. Ambrosius, P. J. Thijs, X. J. M. Leijtens, M. K. Smit, and E. A. J. M. Bente, "Integrated tunable quantum-dot laser for optical

- coherence tomography in the 1.7 μm wavelength region," *IEEE Journal of Quantum Electronics* (2011).
- [5] X. Huang, A. Stintz, H. Li, L. F. Lester, J. Cheng, and K. J. Malloy, "Passive mode-locking in 1.3 μm two-section InAs quantum dot lasers," *Applied Physics Letters* 78, 2825-2827 (2001).
- [6] E. U. Rafailov, M. A. Cataluna, W. Sibbett, N. D. Il'inskaya, Y. M. Zadiranov, A. E. Zhukov, V. M. Ustinov, D. A. Livshits, A. R. Kovsh, and N. N. Ledentsov, "High-power picosecond and femtosecond pulse generation from a two-section mode-locked quantum-dot laser," *Applied Physics Letters* 87, 081107 (2005).
- [7] M. G. Thompson, A. R. Rae, R. V. Penty, and I. H. White, "InGaAs Quantum-Dot Mode-Locked Laser Diodes," *IEEE Journal of Selected Topics in Quantum Electronics* 15, 661-672 (2009).
- [8] M. J. R. Heck, E. A. J. M. Bente, B. Smalbrugge, Y. S. Oei, M. K. Smit, S. Anantathanasarn, and R. Nötzel, "Observation of Q-switching and mode-locking in two-section InAs/InP (100) quantum dot lasers around 1.55 μm ," *Optics express* 15, 16292-301 (2007).
- [9] M. J. R. Heck, A. Renault, E. A. J. M. Bente, M. K. Smit, K. S. E. Eikema, W. Ubachs, S. Anantathanasarn, and R. Notzel, "Passively Mode-Locked 4.6 and 10.5 GHz Quantum Dot Laser Diodes Around 1.55 μm With Large Operating Regime," *IEEE Journal of Selected Topics in Quantum Electronics* 15, 634-643 (2009).
- [10] W. M. Yee and K. A. Shore, "Multimode analysis of self locked FM operation in laser diodes," *IEE Proceedings J Optoelectronics* 140, 21 (1993).
- [11] J. P. Turrenc, A. Akrou, K. Merghem, A. Martinez, F. Lelarge, A. Shen, G. H. Duan, and A. Ramdane, "Experimental investigation of the timing jitter in self-pulsating quantum-dash lasers operating at 1.55 μm ," *Optics express* 16, 17706-13 (2008).
- [12] S. Anantathanasarn, R. Nötzel, P. J. van Veldhoven, F. W. M. van Otten, Y. Barbarin, G. Servanton, T. de Vries, E. Smalbrugge, E. J. Geluk, T. J. Eijkemans, E. a. J. M. Bente, Y. S. Oei, M. K. Smit, and J. H. Wolter, "Lasing of wavelength-tunable (1.55 μm region) InAs/InGaAsP/InP (100) quantum dots grown by metal organic vapor-phase epitaxy," *Applied Physics Letters* 89, 073115 (2006).
- [13] S. Arahira and Y. Ogawa, "Repetition – Frequency Tuning of Monolithic Passively Mode-Locked Semiconductor Lasers with Integrated Extended Cavities," *IEEE JOURNAL OF QUANTUM ELECTRONICS*, 33, 255-264 (1997).
- [14] Z. Zhang and T. Yagi, "Dual-wavelength synchronous operation of a mode-locked Ti:Sapphire laser based on self-spectrum splitting," *Optics letters* 18, 2126 (1993).
- [15] Z. Cong, D. Tang, W. De Tan, J. Zhang, C. Xu, D. Luo, X. Xu, D. Li, J. Xu, X. Zhang, and Q. Wang, "Dual-wavelength passively mode-locked Nd:LuYSiO₅ laser with SESAM," *Optics express* 19, 3984-9 (2011).
- [16] K. Veselinov, F. Grillot, C. Cornet, J. Even, A. Bekiarski, M. Gioannini, and S. Loualiche, "Analysis of the Double Laser Emission Occurring in 1.55- μm InAs–InP (113)B Quantum-Dot Lasers," *IEEE Journal of Quantum Electronics* 43, 810-816 (2007).
- [17] N. A. Naderi, F. Grillot, K. Yang, J. B. Wright, A. Gin, and L. F. Lester, "Two-color multi-section quantum dot distributed feedback laser," *Optics Express* 18, 27028 (2010).
- [18] S. Breuer, M. Rossetti, W. Elsasser, L. Drzewietzki, P. Bardella, I. Montrosset, M. Krakowski, and M. Hopkinson, "Reverse ground-state excited-state transition dynamics in two-section quantum dot semiconductor lasers: mode-locking and state-switching," in *Optical Spectra* (2010), pp. 772011-772011-10.
- [19] M. A. Cataluna, W. Sibbett, D. A. Livshits, J. Weimert, A. R. Kovsh, and E. U. Rafailov, "Stable mode locking via ground- or excited-state transitions in a two-section quantum-dot laser," *Applied Physics Letters* 89, 081124 (2006).

- [20] J. Liu, Z. Lu, S. Raymond, P. J. Poole, P. J. Barrios, and D. Poitras, "Dual-wavelength 92.5GHz self-mode-locked InP-based quantum dot laser," *Optics Letters* 33, 1702-1704 (2008).
- [21] C. Mesaritis, C. Simos, H. Simos, I. Krestnikov, and D. Syvridis, "Dual ground-state pulse generation from a passively mode-locked InAs/InGaAs quantum dot laser," *Applied Physics Letters* 99, 141109 (2011).
- [22] M. J. R. Heck, E. J. Salumbides, A. Renault, E. A. J. M. Bente, Y. S. Oei, M. K. Smit, R. van Veldhoven, R. Nötzel, K. S. E. Eikema, and W. Ubachs, "Analysis of hybrid mode-locking of two-section quantum dot lasers operating at 1.5 microm.," *Optics express* 17, 18063-75 (2009).
- [23] G. Fiol, D. Arsenijević, D. Bimberg, A. G. Vladimirov, M. Wolfrum, E. A. Viktorov, and P. Mandel, "Hybrid mode-locking in a 40 GHz monolithic quantum dot laser," *Applied Physics Letters* 96, 011104 (2010).
- [24] K. Sato, "Optical Pulse Generation Using Fabry – Pérot Lasers Under Continuous-Wave Operation," *Quantum* 9, 1288-1293 (2003).
- [25] W. Yang, N. J. Sauer, P. G. Bernasconi, and L. Zhang, "Self-mode-locked single-section Fabry-Perot semiconductor lasers at 1.56 microm.," *Applied optics* 46, 113-6 (2007).
- [26] L. F. Tiemeijer, P. I. Kuindersma, P. J. A. Thijs, and G. L. J. Rikken, "Passive FM locking in InGaAsP semiconductor lasers," *IEEE Journal of Quantum Electronics* 25, 1385-1392 (1989).
- [27] Y. Barbarin, E. A. J. M. Bente, M. J. R. Heck, Y. S. Oei, R. Nötzel, and M. K. Smit, "Characterization of a 15 GHz integrated bulk InGaAsP passively modelocked ring laser at 1.53 μm ," *Optics Express* 14, 9716 (2006).
- [28] M. S. Tahvili, Y. Barbarin, X. J. M. Leijtens, T. de Vries, E. Smalbrugge, J. Bolk, H. P. M. M. Ambrosius, M. K. Smit, and E. A. J. M. Bente, "Directional control of optical power in integrated InP/InGaAsP extended cavity mode-locked ring lasers," *Optics Letters* 36, 2462 (2011).
- [29] Y. Barbarin, S. Anantathanasarn, E. A. J. M. Bente, Y. S. Oei, M. K. Smit, and R. Nötzel, "1.55- μm Range InAs-InP (100) Quantum-Dot Fabry-Perot and Ring Lasers Using Narrow Deeply Etched Ridge Waveguides," *IEEE Photonics Technology Letters* 18, 2644-2646 (2006).

CHAPTER 3

Extended Cavity InP/InGaAsP Integrated Mode-locked Ring Laser

In this chapter, a passively mode-locked InP/InGaAsP multiple quantum well semiconductor extended cavity ring laser is presented. The laser operates at 20GHz repetition rate and around 1575nm wavelength. The device has been realized using the active-passive integration technology in a standardized photonic integration platform. We demonstrate experimentally that the relative positioning of the amplifier and absorber in a monolithically integrated ring laser can be used to control the balance of power between counter-propagating fields in the mode-locked state. The directional power balance is verified to be in agreement with a model which is previously reported.

3.1. Introduction

Monolithic Indium-phosphide based photonic integrated circuits [1] has become a subject of interest, in particular where active-passive integration technology is used [2,3]. Such a technology enables the generation, processing and detection of optical signals on a single chip where all devices on the chip utilize the same active and passive layer stack. In this framework, semiconductor mode-locked lasers (MLLs) are of particular importance as sources of stable optical pulses for optical communication and novel applications such as optical signal processing and all-optical sampling [4].

When a semiconductor optical amplifier (SOA) is integrated with a saturable absorber (SA) in a ring cavity, ML operation may be achieved. A ring laser can be located freely on a semiconductor chip to be directly integrated with other optical components and devices. Since the cavity length of a ring cavity is controlled lithographically, its repetition rate can be controlled more accurately than that of a cleaved facet ML Fabry-Pérot type structure. The use of active-passive integration technology allows for an extended cavity structure where the cavity length and relative position of gain and absorption sections can be chosen independently. A ML ring laser typically operates in a colliding pulse (CP) ML regime and supports two counter-propagating fields in the cavity. However, for many applications it is favorable to achieve unidirectional operation to have most output power into one waveguide. Previously, a theoretical study using a travelling wave model [5] as indicated that the relative position of SOA- and SA-sections in the ring cavity can be used to achieve up to 13dB contrast in output

power between the two directions. In this chapter we demonstrate this effect in an InP/InGaAsP based experimental device, i.e. a monolithic 20GHz integrated extended cavity ring laser.

3.2. Device design and operation

The 4mm-long laser ring cavity incorporates a 750 μ m-long optical amplifier section (SOA-section), a separate 40 μ m-long saturable absorber (SA) section, passive waveguide sections (shallow and deep etch) and a passive MMI-type 50% output coupler. Fabrication has been carried out in the JePPIX platform [6]. A mask layout image of the device under test is shown in Fig.3.1. The SOA- and SA-sections contain a layer structure with four quantum wells.

Parasitic internal reflections destabilize mode-locked operation. In order to minimize the unwanted reflections, deeply etched adiabatic bends, shallow-deep tapered transitions and tilted active-passive transitions are used to design the device. Furthermore, the MMI corners are cut and output waveguides (not shown in Fig.3.1) are tilted under an angle of 7° to minimize back reflections into the device.

The choice of gain material is determined by the available technology platform, in which other devices on the same chip and wafer may be realized. The quality of ML is strongly affected by the active material properties and better performing monolithic passively mode-locked devices e.g. in terms of timing jitter, can be achieved using quantum dot or dash material [7].

In the CPML regime, the clockwise (CW) and counter clockwise (CCW) propagating pulses will meet in the SA-section to saturate the absorber. The relative position of SOA and SA sections is designed such that the travel time between the center of SA-section to the right side of SOA-section (point M in Fig.3.1) for the CCW pulse is equal to the time it takes for the CW pulse to travel from the center of SA to point M. As shown in the modeling work of [5] on a similar layout, the CCW-propagating pulse will therefore enter the SOA-section just after the amplifier gain is depleted by the CW pulse. In the design presented here, the separation is 2.1mm, half the total optical cavity length. Since a roundtrip gain difference is expected for the pulses in the two directions, the asymmetrical design of the device under test was expected to lead to nearly unidirectional performance of the laser in favor of the CW-propagating pulses.

The devices are mounted on a copper chuck and are temperature stabilized at 12°C. The output light from the devices is collected by two lensed fibers with anti-reflection coated tips. Optical isolators are used to prevent back reflections into the cavity. The ring MLL is operated by current injection to the SOA-section (I_{SOA}) and reverse-biasing

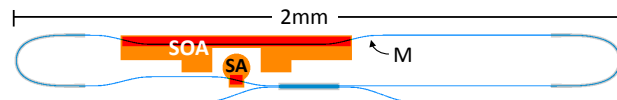


Fig.3.1. Mask layout image of the asymmetric ring laser under test. Passive waveguide sections are depicted as thin blue lines and the grey shaded areas are deeply etched regions. Active parts are illustrated as red rectangular sections and the contact pads on absorber and optical amplifier sections are seen in an orange color. Point M shows the location at the right side of the SOA where the counter-propagating pulses meet.

the SA-section (V_{SA}). The operation of the ring laser is presented first in some detail to assist with the interpretation of measurements on the balance of power in the two directions. Mode-locking of the ring laser is investigated and confirmed in three ways. By observation of RF spectra recorded by a 50GHz electrical spectrum analyzer connected to a fast photodiode, by observation of the spectrum with a high resolution ($20\text{MHz}\approx 0.16\text{pm}$) optical spectrum analyzer and with an autocorrelator.

Operating regimes of the device is shown in Fig.3.2(a) for a range of SA-section reverse bias voltage and SOA-section current. The device operates in stable ML state for $V_{SA}=-2.2\text{V}$ to -2.6V and $I_{SOA}=45\text{mA}$ to 70mA . Fig.3.2(b) shows RF spectra at $V_{SA}=-2.4\text{V}$ and for a range of injection current values from below threshold and up to over the whole range of ML. The lasing threshold is at $I_{SOA}\sim 30\text{mA}$ and the device has a complex dynamic behavior just above threshold. The electrical spectrum given at the inset of Fig.3.2(b) is recorded at $I_{SOA}=40\text{mA}$ and shows low frequency spectral

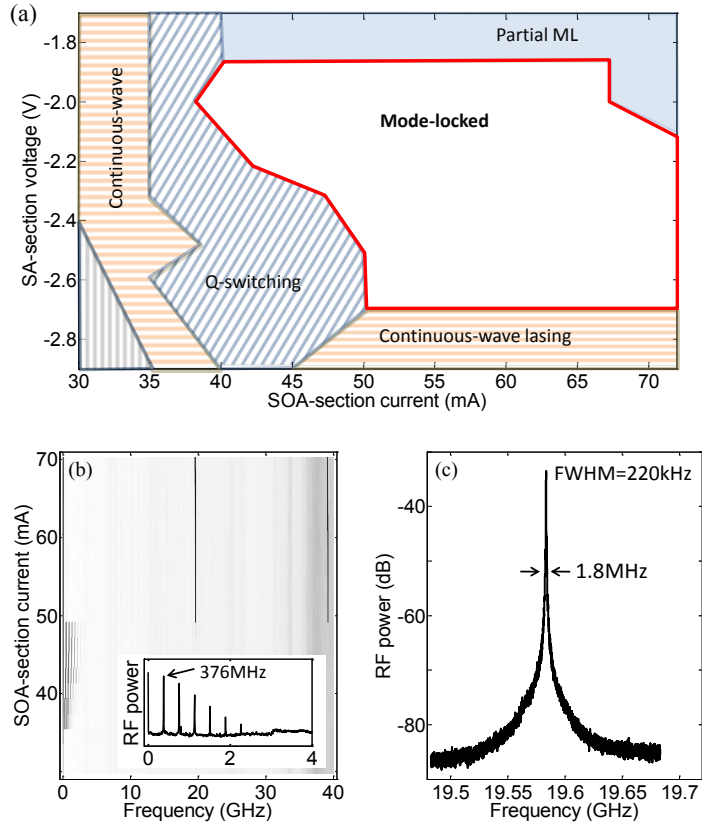


Fig.3.2. (a) Operating regimes of the device under test for a range of SA-section reverse bias voltage and SOA-section current. (b) Electrical spectra (grey-scale in dB) for a range of injection currents and at $V_{SA}=-2.4\text{V}$. The 40GHz-span RF spectra are recorded with 1MHz resolution bandwidth. Inset shows the recorded electrical spectrum at $I_{SOA}=40\text{mA}$ and indicates Q-switching. (c) Fundamental RF peak at 19.58GHz which indicates ML for the device operating at $V_{SA}=-2.4\text{V}$ and $I_{SOA}=60\text{mA}$. The resolution bandwidth used is 50kHz.

components (up to 3GHz) which is an indication of Q-switching. The device enters the locked state at approximately $I_{SOA}=50\text{mA}$. The electrical spectra show clear RF peaks at $f_{\text{rep}}\sim 19.6\text{GHz}$ (corresponding to the roundtrip time) and the second harmonic. The RF spectrum at $I_{SOA}=60\text{mA}$ is shown in Fig.3.2(c). The RF peak at the fundamental frequency is more than 50dB over the noise floor and all other spectral components at lower frequencies with a full width at half maximum (FWHM) of 220kHz. The width at 20dB below the top of the peak is 1.8MHz.

The high resolution optical spectra resulting from the same current scan as in Fig.3.2(b) are shown in Fig.3.3(a) with the reverse bias on the absorber kept at $V_{SA}=-2.4\text{V}$. Just above threshold at $I_{SOA}=30\text{mA}$ and up to $I_{SOA}=38\text{mA}$, the device operates in multi-mode continuous wave lasing. Increasing the injection current further will initiate Q-switching as can be seen in the optical spectrum which is recorded at $I_{SOA}=40\text{mA}$ and shown in the inset plot of Fig.3.3(a). The optical spectrum at this operating point shows a clear increase in the width of the laser modes to approximately half the free spectral range which is consistent with Q-switching and the electrical spectrum given in the inset of Fig.3.2(b).

At the onset of ML region ($I_{SOA}\sim 50\text{mA}$) the spectrum shifts to longer wavelengths. The increased spectral bandwidth accompanied by the emergence of well-defined modes which are spaced at free spectral range of the cavity is an indication of mode-locking. The measured full 3dB linewidth of the optical modes around 1577nm is $830\pm 70\text{MHz}$. This indicates significant instability in the spectral comb on a time scale that is longer than the round-trip time. Background free autocorrelator traces from the output from the CW lasing direction at $V_{SA}=-2.4\text{V}$ and $I_{SOA}=60\text{mA}$ show a FWHM of 5.9ps which corresponds to sech^2 pulse duration of 3.8ps. The time-bandwidth product is then calculated to be approximately 1.0 which demonstrates that pulses are chirped.

Optical spectra of the CW (black) and CCW (red) directions are given in Fig.3.3(b) for $I_{SOA}=60\text{mA}$. It is clear from Fig.3.3(b) that the total optical power in CW direction is higher ($\sim 8.9\text{dB}$) than the CCW direction as expected from the model prediction in [5].

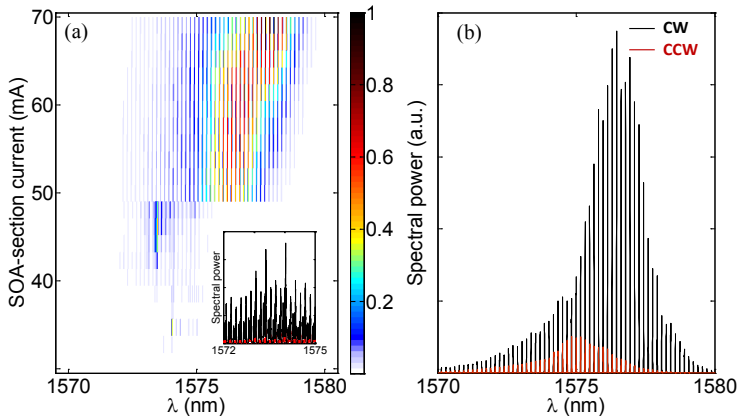


Fig.3.3. (a) High resolution optical spectra (linear scale, color-coded in μW) at $V_{SA}=-2.4\text{V}$ as I_{SOA} is increased from below threshold. (b) Optical spectra of CW (black) and CCW (red) pulses. Significantly different spectral distribution of power confirms the effect of asymmetrical cavity design.

The optical spectra for CW and CCW pulses, given in Fig.3.3(b), show that the central wavelength of the CCW pulses is approximately 1.5nm shorter than that of the CW pulses. This can be a consequence of a faster gain recovery at shorter wavelengths. It should be mentioned that the model [5] predicts 0.5nm chirp and no more than 0.1nm wavelength difference between the two directions.

3.3. Directional control of power

To investigate the power balance between counter-propagating fields, the CW and CCW optical output power as a function of gain section current was measured for the asymmetric device under test. For comparison, a ML ring laser which has a symmetrical cavity design with a 750 μm -long active section and a 15 μm -long SA located in the middle of the optical amplifier was also tested. Fig.3.4 shows the LI-curves for the asymmetrical and symmetrical devices at different values of absorber bias. The asymmetrical ring laser has a threshold current of $I_{\text{SOA}}=25\text{mA}$ at $V_{\text{SA}}=0\text{V}$. Above threshold, the absorber is saturated and the device starts lasing in a bidirectional continuous wave mode. When in continuous wave operation mode and close to threshold, the optical gain in the ring cavity is the same for the counter propagating fields. When the gain saturation in the amplifier becomes stronger the cross-gain saturation between counter propagating fields leads to bistable operation with the dominance of one direction [8]. Optical spectrum measurements reveal that the laser operates in a multi-mode regime; hence, the power switching between CW and CCW directions does not lead to a unidirectional operation. Similar continuous wave behavior is observed for the symmetrical ring laser at $V_{\text{SA}}=0\text{V}$. The symmetrical ring laser has a slightly higher threshold current compared to the asymmetrical device due to the fact that it has an approximately 60 μm shorter amplifier.

The structural design comes to play an important role when the device enters the mode-locked state as can be seen by comparing the results in Fig 4(b) and 4(d). The measured optical power in the two directions clearly show an increase in the CW output power (as

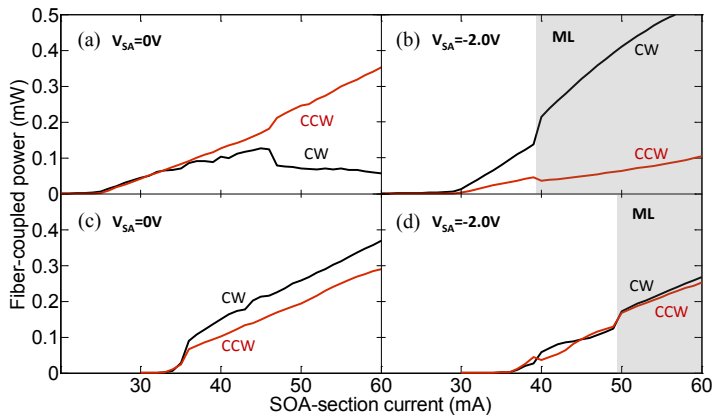


Fig.3.4. Fiber-coupled optical power (CW in black and CCW in red) as a function of SOA-section injection current for the asymmetrical (a,b) and the symmetrical (c,d) ring laser and at different values of absorber voltage. The grey areas in (b) and (d) indicate the region of ML.

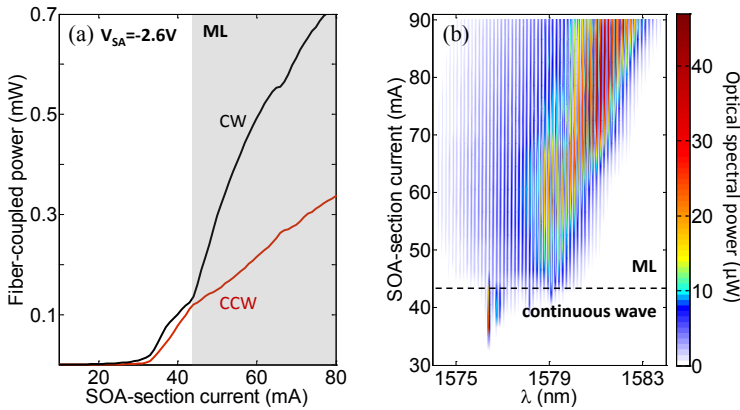


Fig.3.5. (a) LI curves (CW in black and CCW in red) for the asymmetrical ring laser with $40\mu\text{m}$ absorber section at $V_{SA}=-2.6\text{V}$. (b) Spectral evolution of optical power (CW direction) from continuous wave lasing to mode-locked operation as I_{SOA} is increased. Resolution bandwidth is 0.1nm .

expected) at the onset of ML for the asymmetrical device, i.e. $I_{SOA}=40\text{mA}$ and $V_{SA}=-2.0\text{V}$. At this bias voltage, the difference in CW and CCW power levels outside the range of ML is attributed to cross-gain saturation effects which can start close to threshold because of the higher peak power levels during Q-switching (Fig.3.2(b)). The power ratio between the counter-propagating pulses (CW/CCW) over the whole range of mode-locking for the asymmetric ring laser is 5-8dB. The highest contrast observed for the device under test is somewhat lower than the predicted value in [5]. The difference is attributed to inaccuracies in the modeling of the gain and self phase modulation.

The symmetrical ring laser (Fig.3.4(d)) operates in the mode-locked state at $V_{SA}=-2.0\text{V}$ and for injection currents above $I_{SOA}=52\text{mA}$. Below this current value the device has bidirectional (single- and multi-mode) continuous wave lasing. At the onset of ML, more optical modes are locked in phase to saturate the cavity losses and the internal optical power increases. However, unlike what is observed for the asymmetrical ring and again as expected the optical power of counter-propagating pulses increase at the same time. This is depicted by the jump in CW and CCW power level in Fig.3.4(d).

The control of the directional power was verified by testing a second asymmetrical ring laser with similar structural design. The device operates as a bidirectional continuous-wave single mode laser at $V_{SA}=-2.6\text{V}$ and for $I_{SOA}=35\text{mA}$ to 41mA . The LI curve is shown in Fig.3.5(a) which shows that outside the range of ML, the fiber-coupled output power level in the two directions is almost equal. The splitting of the two curves at $I_{SOA}=45\text{mA}$ corresponds to the onset of ML where the CW direction is favored over the CCW. Fig.3.5(b) illustrates spectral evolution of optical power from continuous wave lasing to ML operation as I_{SOA} is increased.

In conclusion, we have for the first time, demonstrated control of the directional performance of a mode-locked monolithic semiconductor ring laser by means of relative positioning of the amplifier and absorber. Observations presented in this chapter for the

two asymmetrical lasers are consistent and verify qualitatively the predictions of the model in [5].

References

- [1] J. J. G. M. van der Tol, Y. S. Oei, U. Khalique, R. Nötzel, and M. K. Smit, InP-based photonic circuits: Comparison of monolithic integration techniques, *Prog. Quantum Electron.*, vol. 34, no. 4, pp. 135–172, Jul. 2010.
- [2] Y. Barbarin, E.A.J.M. Bente, C. Marquet, E.J.S Leclère, J.J.M Binsma, and M.K. Smit, Measurement of Reflectivity of Butt-Joint Active–Passive Interfaces in Integrated Extended Cavity Lasers, *Photon. Technol. Lett.*, 17:11, 2265 — 2267 (2005).
- [3] J.S. Parker, A. Bhardwaj, P.R.A. Binetti, Y. Hung, C. Lin, L.A. Coldren, Integrated 30GHz passive ring mode-locked laser with gain flattening filter, *ISLC*, PD1, Kyoto, Japan (September 26-30, 2010)
- [4] Peter J. Delfyett, Sangyoung Gee, Myoung-Taek Choi, Hossein Izadpanah, Wangkuen Lee, Sarper Ozharar, Franklyn Quinlan, and Tolga Yilmaz, Optical Frequency Combs from Semiconductor Lasers and Applications in Ultrawideband Signal Processing and Communications, *J. Lightw. Technol.*, 24:7, 2701 — 2719 (2006).
- [5] Erwin A. J. M. Bente, Yohan Barbarin, Martijn J. R. Heck, Meint K. Smit, Modeling of integrated extended cavity InP/InGaAsP semiconductor modelocked ring lasers, *Opt. and Quantum Electron.*, 40, 131 — 148 (2008).
- [6] JePPIX: Joint European Platform for InP-based Photonic Integrated Components and Circuits www.jepix.eu.
- [7] François Lelarge, Béatrice Dagens, Jeremie Renaudier, R. Brenot, Alain Accard, Frédéric van Dijk, Dalila Make, Odile Le Gouezigou, Jean-Guy Provost, Francis Poingt, Jean Landreau, Olivier Drisse, Estelle Derouin, Benjamin Rousseau, Frédéric Pommereau, and Guang-Hua Duan, Recent Advances on InAs/InP Quantum Dash Based Semiconductor Lasers and Optical Amplifiers Operating at 1.55 μm , *IEEE J. Sel. Topics Quantum Electron.*, 13, 111 (2007).
- [8] M. Sorel, P. J. R. Laybourn, A. Scirè, S. Balle, G. Giuliani, R. Miglierina, and S. Donati, Alternate oscillations in semiconductor ring lasers, *Opt. Lett.*, 27:22, 1992 — 1994 (2002).

CHAPTER 4

Optical Pulse Shaping: Overview and Design of an InP Integrated Device

Over the past decades, several pulse shaping techniques have been developed and employed for diverse applications. Optical pulse shaping can be defined as manipulation of an (input) optical pulse to synthesize a desired (output) waveform. There are different approaches to achieve pulse shaping, the majority of which are targeted towards specific application requirements. A variety of pulse shaping techniques which were investigated prior to 1983 are reviewed in [1]. Review articles [2–4] present the progress of pulse shaping techniques and applications since then.

In this chapter an overview of technological approaches to optical pulse shaping and the design of a monolithic InP-based pulse shaper device are presented. In section 1, we begin with presenting the concept of Fourier transform pulse shaping. Special attention is given to programmable (spatial) light modulators which are currently widely in use. A brief overview of other optical pulse shaping methods is given in section 2. In section 3, we discuss control strategies for programmable pulse shapers and then briefly review the subject of line-by-line and group-of-lines pulse shaping in section 4. An overview of integrated pulse shapers is given in section 5 where several types of integrated devices and relevant applications are described. Section 6 describes the design that was made for a monolithically integrated InP-based pulse shaper. We explain the role of the application requirements in the design and discuss the possibilities of the available generic InP fabrication platform for the realization of the pulse shaper.

4.1. Fourier transform pulse shaping

The most widely adopted approach for shaping optical pulses is the so-called Fourier transform (FT) technique. FT pulse shaping relies on manipulation of the pulse in the frequency domain and is based on the concept of linear, time-invariant systems. The linear system is generally described in the time domain by its impulse response $h(t)$. If the input signal to the systems is $e_{in}(t)$, the output response is given by

$$e_{out}(t) = e_{in}(t) \otimes h(t) = \int e_{in}(\tau)h(t - \tau)d\tau \quad (4.1)$$

in which \otimes represents the convolution operation. If the input signal is a sufficiently short pulse, i.e. an approximate impulse, the output will be $h(t)$. This means that

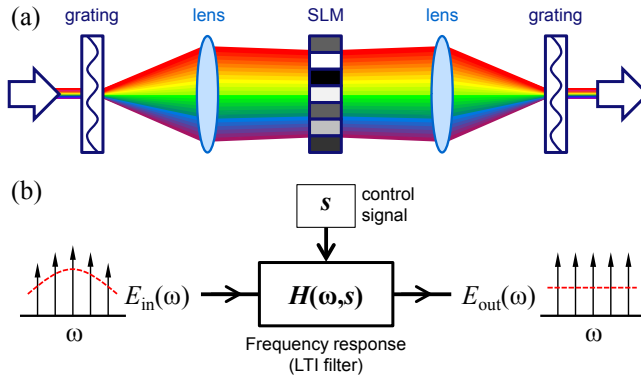


Fig.4.1. (a) Schematic representation of the Fourier transform pulse shaping. (b) Schematic diagram of a programmable pulse shaper. SLM: spatial light modulator, E : electric field, $H(\omega)$: the frequency response of the pulse shaper, s stands for the control signals which are used to program the device.

synthesizing a certain pulse shape from a short input pulse is equivalent to creating a linear optical filter with the desired impulse response.

An equivalent description of the linear system in the frequency domain is the frequency response. The frequency response which is denoted as $H(\omega)$, is the Fourier transform of the system impulse response, $H(\omega) = \mathcal{F}\{h(t)\}$, and relates the input and output signals according to

$$E_{\text{out}}(\omega) = H(\omega) \times E_{\text{in}}(\omega) \quad (4.2)$$

FT pulse shaping is most commonly described in the frequency domain. A basic pulse shaper device is schematically shown in Fig.4.1(a) to clarify the principle of FT pulse shaping. The device includes a pair of gratings and lenses, and a spatial light modulator (SLM) mask. The first grating spreads the spectral components of the incident pulse into different directions. The spread in direction of the spectral components is then turned into a well defined spatial separation and focused on the SLM by the first lens. The SLM is used to transfer the desired pattern, i.e. phase and/or amplitude, onto the signal spectrum. The second lens and grating are used to combine the patterned spectral components to form the desired pulse shape.

The SLM is either a fixed spatially patterned amplitude/phase mask or a programmable light modulator. A programmable SLM is generally preferred over a fixed mask and has the advantage of being software controlled. In this context, programmability of the SLM refers to the fact that the frequency response of the pulse shaper may be modified through control signals. A pulse shaper device is commonly combined with a mode-locked laser source which generates the input pulses and all its spectral components have a fixed phase relation. A schematic diagram of a programmable pulse shaper is shown in Fig.4.1(b).

The configuration shown in Fig.4.1(a) is generally referred to as the 4f-setup in transmission mode. Depending on the type of SLM and choice of optical elements (for instance lens vs mirror or grating vs prism) and according to the design requirements, the setup is configured in a variety of arrangements. Fig.4.2 shows some of the more commonly employed configurations based on the FT technique. In certain cases, such as

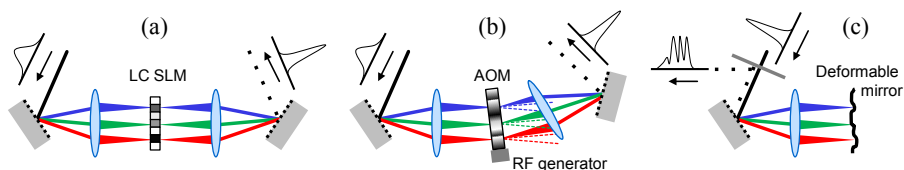


Fig.4.2. Different pulse shaper realizations based on a 4f configuration: (a) liquid crystal SLM, (b) acousto-optic SLM, (c) deformable mirror. The setups of (a) and (b) are configured in the transmission mode, whereas (c) has a reflective configuration. (Adapted from [6])

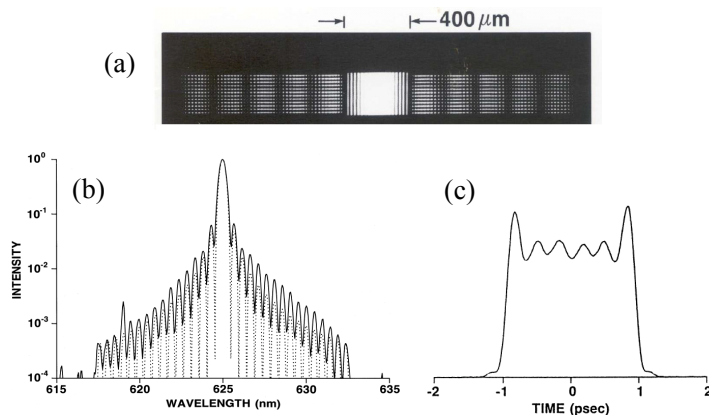


Fig.4.3. (a) Photograph of a lithographically patterned amplitude mask used for generating a square pulse. Transparent regions are bright, opaque regions are dark. (b) Power spectra for a square pulse: measured spectrum patterned by phase and amplitude masks (solid trace) and an actual sinc function (dotted trace). (c) A typical cross-correlation measurements of square pulse. The mask image does not correspond to the measured data. (Reproduced from [5])

the one shown in Fig.4.2(c), it is possible to use reflective elements which effectively fold the signal path to make the setup more compact.

4.1.1. FT pulse shaping using fixed masks

Before the emergence of programmable SLMs which are software controlled, fixed phase and amplitude masks were used for fs waveform synthesis. In early works on shaping, fixed masks that were fabricated using lithography were utilized [5]. The required phase and amplitude masks were patterned on fused silica substrates. Separate amplitude and phase masks were placed back to back at the masking plane of the pulse shaper [3]. Phase masks were fabricated by using reactive ion etching to produce a pattern on the surface of the fused silica. In this technique, the phase value at each pattern point is related to the etch depth. This technique is generally suitable for fabricating masks with two phase values (usually 0 and π) but making a mask with continuous phase changes (gray-level) is challenging.

Amplitude masks consisted of a series of fine opaque metal lines deposited onto the substrate with width and spacing varied to obtain the desired transmission. Fig.4.3(a) shows an example of a patterned amplitude mask which is used to generate a sinc-like spectrum, corresponding to a square pulse in time domain. Fig.4.3(b,c) depict the plot of the spectrum and resulting intensity profile in time. Other examples are given in [3].

4.1.2. FT pulse shaping using programmable spatial light modulators

An important feature of pulse shaping is programmability which enables generation of a variety of waveforms for different applications. Several programmable mask technologies are employed in the FT pulse shaping technique [3], [6]. Here we give a brief review of the two widely used technologies, namely liquid crystal arrays and acousto-optic modulators. There are several experimental examples based on other amplitude and phase shaping methods. These approaches include pulse shaping using movable and deformable mirrors and are usually developed according to very specific needs of some applications and thus are not so common. More details can be found in [3], [7] and references therein.

4.1.2.1. Liquid crystal SLM

Liquid crystal (LC) based pulse shaper are probably the most versatile systems which are currently in use. Arrays of LC cells are fabricated in the form of SLMs which can be used in various configurations to build pulse shapers. Fig.4.4 depicts the basic layout of a single layer LC SLM. The structure consists of a thin region of a (nematic) liquid crystal which is sandwiched between two glass plates. The inside surface of the glass is coated with a thin film of a transparent electric conductor, such as indium tin oxide (ITO). One of the glass pieces is not patterned and serves as the ground plate. The conducting film on the other glass plate is patterned to form an array of separate electrodes. Each section of the array is referred to as a device pixel. The electrodes provide the required control signals on each pixel. In a pulse shaper setup, the spatially dispersed pulse falls on the LC SLM and each pixel is used to control the corresponding portion of the spectrum.

The nematic LC has long, rod-like molecules which may easily flow (as a liquid) but

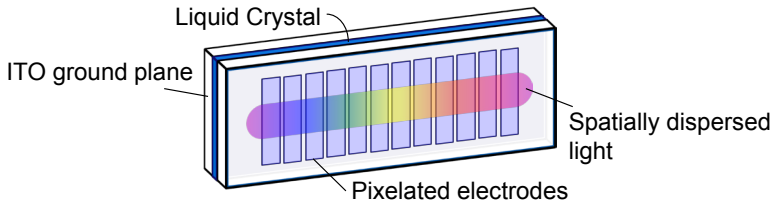


Fig.4.4. Basic layout of a typical liquid crystal SLM used for pulse shaping. The figure illustrates a single-layer, 1-dimensional SLM which may be used for phase-only pulse shaping.

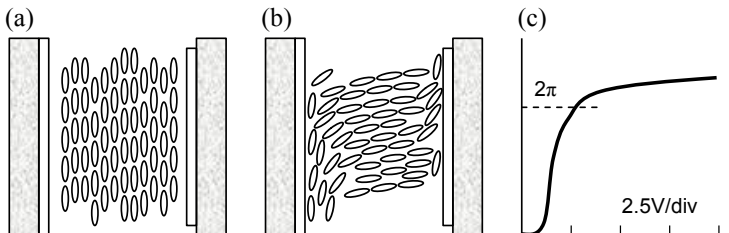


Fig.4.5. Side view of a liquid crystal pixel with (a) no electric field applied, and (b) electric field in the lateral direction. (c) A typical plot of the optical phase change versus the applied voltage.

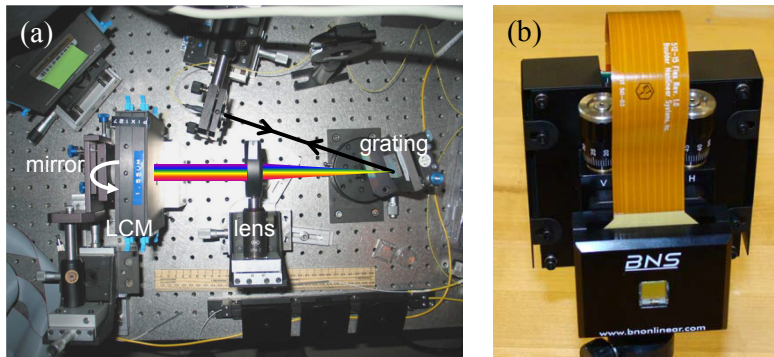


Fig.4.6. A reflective FT pulse shaping setup based on LC SLM, assembled on an optical table (adapted from [76]). The input/output pulses are in fiber. (b) A commercial LC SLM (Boulder Nonlinear Systems, series DS0909).

maintain orientational order (similar to a crystalline solid). By proper treatment during fabrication, the molecules are oriented along the desired direction. In case of LCMs, this direction is commonly chosen to be parallel to the glass plate surface. The LC molecules are not symmetric in shape, thus an external electric field can induce rotational torque on them, leading to a change of their orientation. The asymmetric shape of LC molecules has an important consequence for the optical properties as well which is the birefringence. Birefringence is a result of the way that light interacts with molecules. If the light is polarized parallel to the long axis of the LC molecule, it induces a large polarization response. Therefore, the molecules show a relatively large refractive index. If the light polarization is parallel to the short axis of the molecule, the light-matter interaction is lower due to the fact that electrons are not free to move much along the short axis. In other words, the refractive index is lower.

In practice the average orientation of LC molecules is controlled by an external (DC or low frequency) voltage signal on each device pixel. Since the phase is proportional to the refractive index, a continuous phase change may be applied by adjusting the driving voltage signal. The description given here is graphically presented in Fig.4.5. The maximum amount of phase change is determined by the birefringence of the LC and the thickness of pixels.

The single layer LC SLM is commonly used for phase-only pulse shaping. To achieve independent amplitude and phase control, a two layer SLM is employed. In this case, two layers of LC SLMs, with separate electrical controls, are aligned and attached together. The orientations of molecules in the LCM layers are originally treated to be different. Control over the relative amplitude of spectral components in such a device is achieved by adjusting the transmission through the device. Based on the polarization of the incident field, the transmission and phase change can be controlled independently.

Fig.4.6(a) shows an experimental LC SLM pulse shaper which is mounted on an optical bench and is configured in the reflection mode. The reflective configuration is more compact and easier to align, particularly when the light in free-space needs to be coupled to a fiber. Fig.4.6(b) shows a commercial LC SLM.

A typical pixel size for LCMs is in the order of $2\text{mm} \times 100\mu\text{m}$ and the pixel count is about 128-640. The number of pixels in LCMs is typically limited due to difficulties in providing electrical connections to more than a few hundred pixels in the optically

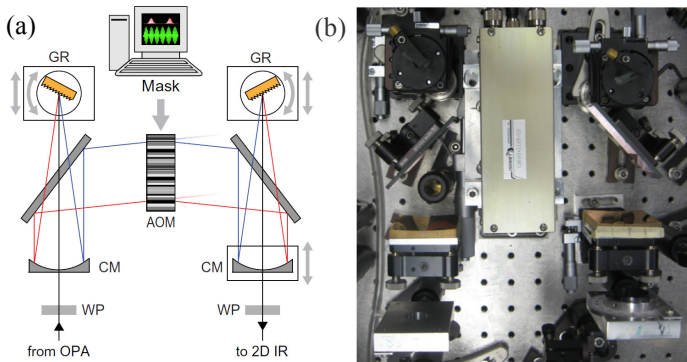


Fig.4.7. (a) Optical layout of mid infrared pulse shaper based on Germanium AOM (adapted from [77]). (b) Top down photograph of the pulse shaper setup. WP: $\lambda/2$ wave-plate, CM: cylindrical mirror, GR: diffraction grating.

active area of the LCM. An increased number of pixels can be achieved using the liquid crystal on silicon (LCoS) technology. A LCoS SLM is directly fabricated on a silicon chip which has a reflective layer deposition and provides electronic signals in a very compact format. Such SLMs are essentially reflective devices.

4.1.2.2. Acousto-optic SLM

Acousto-optic (AO) technology has also been used for FT pulse shaping for over 15 years now [8]. AO modulation is based on driving an appropriate medium, typically TeO_2 crystal (visible light) or InP (infrared), by a modulated RF signal. The crystal is attached to a piezoelectric transducer on one end. The transducer converts electric signal into acoustic waves. Propagation of the acoustic wave in the medium is a series of contractions and expansion in the medium. When the acoustic wave travels across the crystal, it induces a refractive index grating in the medium.

The schematic setup of an AO pulse shaper is shown in Fig.4.2(b). The incident light usually comes on the AOM under the Bragg angle and diffracts in different directions as a result of the AO-induced grating. The setup is optimized for a particular diffraction order for higher efficiency. However, some part of the light is inevitably lost in other diffraction orders. An experimental setup arrangement based on AOM is shown in Fig.4.7.

The RF driving signal is modulated according to the desired optical pulse shape. The modulated RF signal propagates at the speed of sound in the AOM crystals. Light travels much faster than the speed of acoustic waves in the AOM crystals. Therefore, the acoustic wave looks like a static (but modulated) diffraction grating at the moment that the optical pulse arrives. The amplitude and phase of the acoustic wave determine the diffraction efficiency and phase shift at each position along the AOM [9]. Therefore, the pulse passing through the AOM is shaped.

4.2. Other pulse shaping techniques

There are several other approaches towards optical pulse shaping which are worth a brief introduction for the sake of completeness.

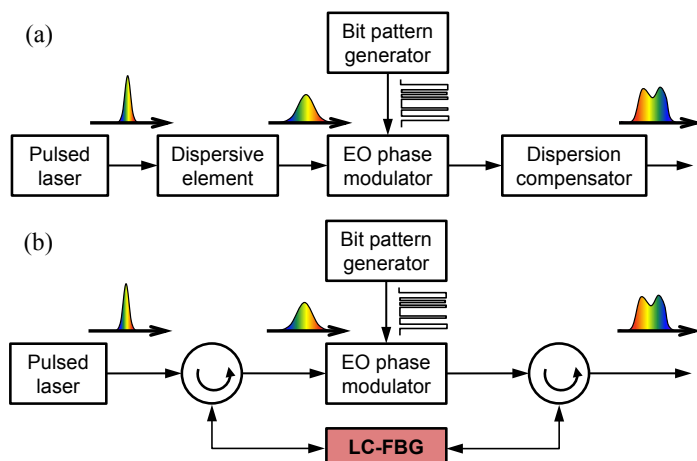


Fig.4.8 (a) Schematic diagram of the pulse shaping concept based on time-frequency mapping and exploiting a binary phase-only filtering. (b) Schematic diagram of the pulse shaping concept based on the time-frequency mapping with a single linearly chirped fiber-Bragg grating (LC-FBG) as the pre- and post-dispersive medium. (Adapted from [11])

4.2.1. All-fiber pulse shaper

The FT pulse shaping technique is in general extremely flexible and powerful. However, the experimental complexity of the free-space setup and the required high quality of the bulk optical components has motivated research on implementation of pulse shapers in using optical fibers and fiber-pigtailed components. Here, we describe a programmable all-fiber phase-only pulse shaper which is reported in [10], [11].

Unlike the FT technique in which the spectral components are spatially separated using a grating, the all-fiber system is based on time-domain filtering. The schematic setup is shown in Fig.4.8(a). The fs input pulse is first passed through a linear dispersive element which stretches the spectral components over time. This is called the frequency-time mapping. Then a properly designed temporal phase modulation is applied to the dispersed signal. This can be done by an electro-optic phase modulator. The temporal phase modulation corresponds to the required spectral phase modulation. Finally, the shaped stretched pulse is compressed back with a dispersion compensator which provides the conjugated dispersion of the first dispersive element.

A practical implementation of this system is shown in Fig.4.8(b). In this setup, a single linearly chirped fiber-Bragg grating is used as the first and second dispersive elements.

4.2.2. Acousto-optic programmable dispersive filters

Acousto-optic programmable dispersive filters (AOPDFs) [12], [13] are mainly useful as in-line pulse shaping devices for amplified ultrafast systems. These devices are particularly interesting because of their compactness. Although the term AOPDF sounds rather similar to the acousto-optic modulator, they should not be mixed with each other. Similar to an AOM, operating principle of an AOPDF is based on driving an acoustically active medium such as TeO_2 or calomel by a modulated RF signal. A transducer converts the RF signal to acoustic waves which, unlike the case of AOMs, co-propagate with and in the direction of the optical signal. Since the light travels much

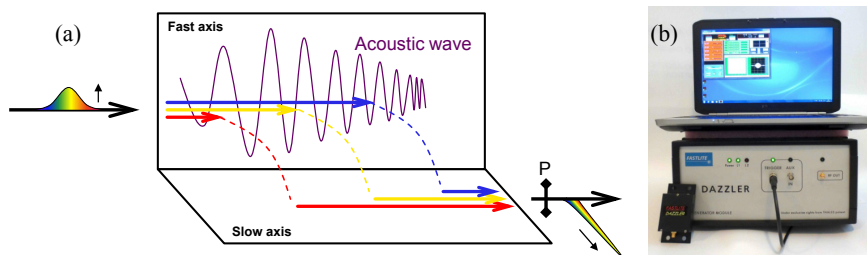


Fig.4.9 (a) Schematic illustration of pulse shaping by an acousto-optic programmable dispersive filter (AOPDF). Element P is the polarization filter. (b) The DAZZLER system which is commercially available from FASTLITE.

faster than the acoustic wave, the light pulse sees an effectively static acoustic pattern along the crystal. Under certain conditions, called phase matched conditions, the acoustic wave induces rotation of the light polarization. Phase matching condition for any given optical frequency is satisfied at a certain acoustic wave (and equivalently RF) frequency, which is essentially the basic characteristic to build an optical filter.

If RF driving signal is modulated in frequency, the aforementioned interaction is distributed over the length of the crystal and each spectral portion of the incident light meets the phase matched condition at a different point as it travels along the medium. This effect is schematically shown in Fig.4.9(a). The crucial point for pulse shaping is that the crystal is birefringent, i.e. the optical velocity is different for the two polarizations. Therefore, the total transit time through the device for each spectral portion is related to the amount of time it travels with the fast and slow velocities. It is possible to shape the pulse by controlling the modulation on the RF driving signal.

Commercial AOPDF devices cover a wide optical wavelength range of 250nm-7 μ m but their application is limited to low rep rate (tens of kHz) systems. Fig.4.9(b) shows an AOPDF module together with the driving electronic box and controlling computer. The compactness of the system, as compared with pulse shapers based on LC or AO SLMs is certainly of interest.

4.2.3. Direct space to time pulse shaping

Direct space to time (DST) technique is another pulse shaping approach which is mostly interesting for high speed parallel-to-serial conversion. In the DST pulse shaper, the impulse response is a scaled version of the applied mask whereas, in the FT technique, the impulse response is related to the inverse Fourier transform of the shaping mask [14].

The interesting feature of the DST configuration is that it could be realized as an integrated device in a relatively simple way. Except for the shaping mask, the DST setup is essentially an arrayed waveguide grating (AWG) or a modified AWG-type device. In [15] femtosecond operation of an AWG-based DST pulse shaper is demonstrated. The device is used to generate a data packet of 30 optical pulses. Operating principle of the AWG-based device is shown in Fig.4.10 [16]. In the AWG-based device, the time duration of the input optical pulse is less than the time delay increment between the arrayed waveguides, i.e. the inverse of the free spectral range.

Data packet (series of bits of 0 or 1) generation using the FT technique typically requires precise amplitude and phase control whereas in the DST configuration requires

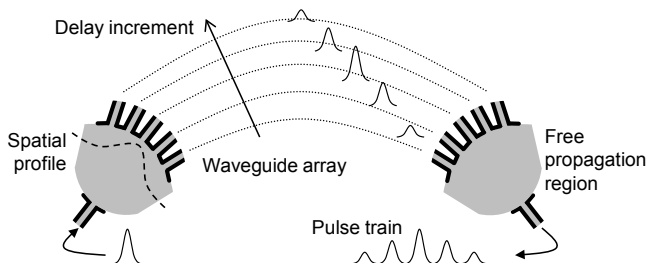


Fig.4.10. Illustration of the operating principle of a direct space to time pulse shaper based on an arrayed waveguide grating.

only intensity modulation. Intensity-only modulation is less complex to achieve if the fabrication platform allows integration of semiconductor optical amplifiers (SOAs) on chip. On passive platforms, fabrication of variable optical attenuators (such as those based upon Mach-Zehnder interferometers) can be a solution.

4.3. Control strategies for programmable pulse shaping

Optical pulse shapers can be operated either under open-loop or in an adaptive (feedback) configuration [3]. In the open-loop configuration, which is schematically shown in Fig.4.11(a), the desired output pulse shape (spectral amplitude and phase) is specified and the input pulse shape is known. Therefore, the required transfer function of the pulse shaper is calculated according to Eq.4.2. The design task is then to properly set the control signals (in case of a programmable SLM) such that the desired system transfer function is realized. Any distortion caused by the optical system (lens aberration, additional dispersion, etc.) can be included in calculation of the transfer function to be (pre-)compensated.

The open-loop configuration needs precise calibration of the SLM. In this context, calibration means to find the transfer function of the SLM and determine the effect of control signals. In general, detailed knowledge of the input pulse shape is also required. For instance, in case of pulse compression, the input pulse is initially broad and the

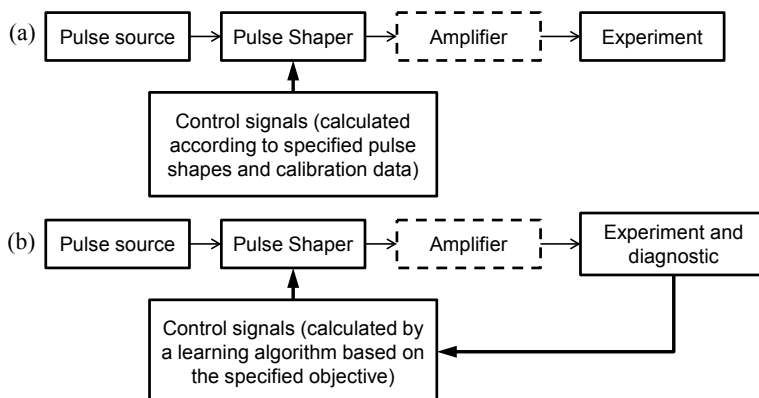


Fig.4.11. Block diagram of (a) open loop and (b) feedback (adaptive) control strategies for optical pulse shaping.

input spectral phase/amplitude profile needs to be characterized as well. However, if the input pulse is known to be sufficiently short, i.e. close to transform limited and much shorter than the shortest features of the desired output waveform, precise characterization of the input pulse is not necessary. In this case the input pulse is assumed to be an “approximate” impulse; hence the output signal is essentially the same as the transfer function of the pulse shaper.

The alternative approach for programmable pulse shapers is the adaptive loop. As it's shown in Fig.4.11(b), the adaptive control is based on a feedback loop which involves observation of an experimental outcome and iterative optimization of the control signals according to the measured observable. The adaptive approach generally relies on a learning algorithm (such as Genetic [17] or evolutionary [18] algorithms) which is capable of recognizing patterns and guides the sequence of iterations for optimization of the control signals.

The experimental observable could be an attribute of the shaped pulse, for instance the average second harmonic signal in case of pulse compression, or the outcome of an experiment. Examples of the latter case are the yield of a particular photochemical product in the field of ‘coherent control’ where laser waveforms are used to control quantum-mechanical motions [6], or the integrated CARS signal in phase-shaped CARS microscopy [19] where pulse shaping optimizes the CARS process for specific molecules. It is also possible that a pulse characterization tool is used to (fully) characterize the shaped pulse at each iteration. In this case, the measured profile is compared with the design shape and control signals are set for the next iteration. This approach is implemented in the so-called MIIPS (Multiphoton intrapulse interference phase scan) pulse shapers (see for example the commercially available product at [20]).

The adaptive control strategy is appropriate when it is difficult to fully calibrate the SLM and/or in a case where the state of the SLM depends in a complicated way on the control signals. Moreover, adaptive approach is mainly of use when the optimized waveform for a certain experiment is not known and needs to be determined. An example of this is the case of CARS experiments on rotational states in molecules.

4.4. Line-by-line vs. group-of-lines pulse shaping

Conventional pulse shapers are generally used to manipulate the spectral components of the light of a regular train of pulses in groups of several lines. This is mainly dictated by properties of the available pulsed lasers and optical components. Most of the stable mode-locked (dye, solid-state and more recently fiber) lasers have repetition frequencies of usually up to few 100s of MHz. The repetition frequency corresponds to the spacing between the spectral lines in the (optical) frequency domain; this implies that the optical spectrum of such lasers has spectral components which are close to each other. The scheme in which the pulse shaping occurs for a number of lines at a time is called the group-of-lines pulse shaping [21]. This is schematically illustrated in Fig.4.12(a). Building a pulse shaper capable of resolving and manipulating tightly-spaced lines is difficult in practice and requires large gratings (tens of cm wide) to achieve the required resolution and a large number of high quality optical elements.

In a typical LC-SLM based pulse shaper system (0.06nm channel resolution, 80MHz repetition frequency pulse source with 10nm 3dB width, around 790nm [22]) the incident pulse contains tens of thousands of lines in the spectral bandwidth and the size

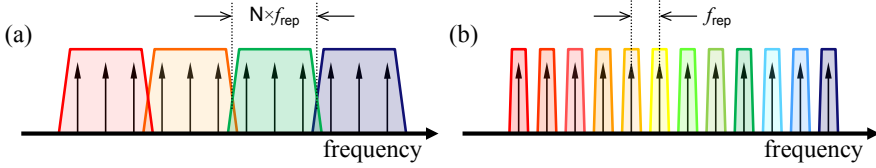


Fig.4.12. Illustration of pulse shaping under (a) group-of-lines and (b) line-by-line schemes.

of the group of lines per channel is in the order of few hundreds. The minimum number of lines per channel is determined by the resolution of the LC-SLM, i.e. the number of pixels. This pixilation in the group-of-lines pulse shaping leads to the presence of replicas of the shaped pulse in the time-domain signal. These replicas are also known as satellite pulses. In the following, several simple simulations of group-of-lines pulse shaping are presented to help illustrate the effect of the number of lines per channel. In these simulations, we assume the spectrum of the input pulse has 1000 equally-spaced lines within the 3dB width. The spectral intensity profile has a Gaussian shape and the spectral phase is flat. We set the number of lines per group to be N . The groups are fully isolated. The first case is to set a linear phase profile over the spectrum to create a time delay. For $N=4$ and $N=10$ the spectral phase profile of the shaped pulse is a staircase approximation of the specified phase profile, i.e. the phase profile in case $N=1$. $N=1$ corresponds to the line-by-line shaping scheme which is illustrated in Fig.4.12(b) and will be explained later. The repetition frequency (spacing between adjacent lines) is $f_{\text{rep}}=1$ (unit of frequency). The temporal intensity of the shaped pulses are shown in Fig.4.13(a). The pulses are delayed with respect to $t=0$ and the period of delayed pulses is $T=1/f_{\text{rep}}=1$ (unit of time). It is clear that for the cases of $N=4$ and $N=10$ weaker replicas of the shaped pulse, caused by the pixilation, are present in the time domain.

For the next case we design the pulse shaper to scramble the spectral phase, i.e. to set a single random phase value for each group which consists of N spectral lines. The input pulse is an ideal transform limited pulse train. Fig.4.13(b-d) presents the temporal intensity (linear scale, a.u.) of the shaped pulses for values of $N=10$, $N=4$ and $N=1$ respectively. For each value of N , the simulation is repeated 10 times and the results are overlaid to give an indication of the maximum pulse duration in the pulse shaper output. For $N=10$ and $N=4$, shaped pulses repeat at a period of $T=1/f_{\text{rep}}=1$ (unit of time) and the (maximum) pulse duration is approximately 0.1 and 0.2 (unit of time) respectively. In group-of-lines pulse shaping, the maximum pulse duration is inversely proportional to $N \times f_{\text{rep}}$. For $N=1$, the signal spans over the period resulting in a detailed noise like, but periodic signal due to the entirely random spectral phase.

The possibility of controlling the amplitude and phase of individual spectral lines in a coherent frequency comb leads to the line-by-line pulse shaping scheme [21]. This scheme has recently attracted much attention for application in optical arbitrary waveform generation [23], [24], ultra-high bandwidth optical communication [25] and THz and microwave photonics [26].

A major challenge in the line-by-line pulse shaping scheme is to resolve the spectral lines individually. The spectral resolution of the spectral filter has to be higher than the repetition frequency of the input pulse since the repetition frequency of the pulse is equal to the spacing between adjacent spectral lines in the frequency domain. The conventional low repetition frequency mode-locked lasers do not easily scale to

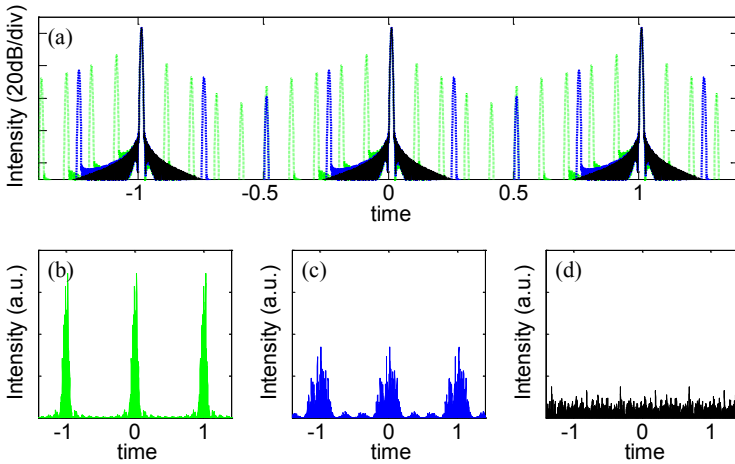


Fig.4.13. (a) Effect of pixilation on the creation of shaped satellite pulses in time domain. The size of line groups is $N=10$ (dotted green), $N=4$ (dashed blue) and $N=1$ (solid black). (b-d) Effect of group size on the temporal extent of the shaped pulse, in this case with scrambled phase with (b) $N=10$, (c) $N=4$ and (d) $N=1$.

repetition rates much beyond 1GHz. Therefore, such lasers are not convenient for line-by-line shaping as the pulse shaper would require an ultra high resolution to resolve the spectral lines. Alternatively, high repetition frequency sources, such as harmonically mode-locked fiber lasers, semiconductor mode-locked lasers, modulated continuous-wave lasers [27] and frequency combs [28] can be used.

Semiconductor mode-locked lasers cover a range of repetition frequencies from around 1GHz [29], [30] and up to 100s of GHz and even THz frequencies [31], [32]. The repetition frequency of many of the currently reported monolithic semiconductor systems is typically in the range of 5-40GHz. Apart from the repetition frequency, the total spectral bandwidth and thus the number of spectral lines generated by the source, is important. Several techniques have been investigated to broaden the lasing spectra of mode-locked semiconductor sources [33]. Among the semiconductor lasers, the quantum-dot and quantum-dash mode-locked lasers [34–40] with their wide material gain bandwidth and wide lasing spectra attract much interest.

The high spectral resolution required for line-by-line shaping is difficult to achieve in practice with conventional gratings and lenses. For instance, the free-space experimental setup described in [41] has a 10GHz harmonically mode-locked fiber laser which operates around $\sim 1542\text{nm}$. The 3ps optical pulse from the fiber laser is sent through a beam collimator and a magnifying telescope to expand the beam size to $\sim 18\text{mm}$ on the grating. The setup, which is configured in reflective configuration, includes a 1200groove/mm grating and a lens with 1000mm focal length. The spectral resolution is 2.6GHz which is sufficient for the application. These numbers indicate the scale of current pulse shaper devices for line-by-line applications.

Alternative devices which could provide the required high resolution for line-by-line shaping include grism (grating-prism) [42], [43], virtually imaged phased array (VIPA) [44] and AWGs. VIPA is similar to a Fabry-Perot etalon in structure (with $\sim 100\%$ and

~96% reflectors) and perhaps provides the highest spectral resolution (750MHz at 3GHz spacing [45]). AWGs are of particular interest for integrated pulse shapers. Silica-based AWGs generally have a better performance than their InP-based counterparts. However, the possibility of integration with fast electro-optic phase modulators as well as active components, make the InP-based devices very interesting.

4.5. Integrated optical pulse shaper devices

Photonic integration technology is capable of providing the required functionalities for building such a complex optical system as a FT optical pulse shaper. Waveguides, AWGs, phase modulators (PMs), PM-based structures such as interferometers, and SOAs are the basic components that are needed to build an integrated circuit which operates as a pulse shaper device.

In earlier works, silica-based optical circuits were used to build (partly-) integrated pulse shapers. These circuits were essentially an AWG which replaced the grating and lens in the FT pulse shaping setup. Configurations with external phase masks are reported in [46–48]. More recent attempts include the devices with integrated amplitude and phase modulators [49–52] with an AWG channel spacing down to 10GHz. The device presented in [53] consists of a pair of 64×20GHz AWGs and thermally tunable phase and amplitude modulators. In recent years, considerable effort has been directed at development of the InP-based photonic integration platforms for optical pulse shaping. In [54] an integrated tunable pulse shaper with phase-only capabilities is presented which operates at 1550nm wavelength and consists of a pair of 200GHz AWGs and an array of 20 electro-optic phase modulators. The temperature of each AWG was individually controlled to maximize their spectral overlap.

Integrated pulse shapers are of particular interest for the field of optical communication in optical code-division multiple-access (O-CDMA) systems [55] and optical arbitrary waveform generation [23], [25], [56]. In recent years, application in RF/microwave photonics [26], [57–59] has attracted attention as well. In O-CDMA systems, the spectral amplitude and phase information encoder/decoder has a similar structure as a FT pulse shaper. Furthermore, it is desirable that the pulse source/detector circuit is integrated on the transmitter/receiver chip together with the encoder/decoder. InP-based technology is currently the best candidate to realize such integrated devices, as it provides the possibility to directly integrate active devices with passive circuits.

The line-by-line pulse shaping scheme is usually referred to as optical arbitrary waveform generation (OAWG) in the context of high-speed optical communication and microwave photonics. OAWG generally starts with a stable frequency comb generator or a stabilized mode-locked laser source to provide the coherent input spectral lines. High resolution spectral filters are needed to resolve the lines individually. Each individual line is then modulated in phase and amplitude according to the specifications of the waveform or requirements of application.

There are two classes of OAWG: Static OAWG in which the modulation bandwidths of the signals on the individual spectral line are much less than the input repetition frequency, and dynamic OAWG where the modulation bandwidths are at least equal to the spectral lines spacing [25]. A static optical arbitrary waveform generator is essentially a programmable line-by-line pulse shaper. In this approach the spectral bandwidth of the output waveform cannot exceed that of the source. In dynamic

OAWG, the device applies a rapid time-varying modulation, amplitude and phase mask, to the individual spectral lines. Different approaches have been investigated for generation of arbitrary waveforms including the ‘rapid-update’ and ‘spectral-slice’ approaches [25]. In the rapid-update approach, the waveform is synthesized on a pulse-to-pulse basis by updating the modulating masks for each period of the input, whereas in spectral-slice method, the desired spectrum is synthesized by modulating the individual spectral lines and then concatenating the corresponding spectral slices.

4.5.1. Integrated spectral de-/multiplexer

The spectral de-/multiplexer is a key component in FT pulse shaping which determines a number of important attributes of the pulse shaper device. Such attributes include the total device bandwidth, number of channels and channel resolution. For monolithically integrated devices, a phased-array (arrayed waveguide) [60] or a grating-based [61–63] component can be used as the spectral de-/multiplexer. AWGs are currently the most widely used spectral filters in integrated optics, including the application of integrated pulse shapers. For sake of completeness, we first explain the basic properties of the AWG and then give an overview of issues which affect the operation of the AWG. For the pulse shaping application, the following AWG specifications are relevant:

- Central frequency (wavelength), which matches (or is close to) that of the pulse source.
- Number of channels, which is equal to the required number of device channels.
- Channel spacing, ideally matches the repetition frequency of the pulse source, which is the case for a line-by-line pulse shaper. In group-of-lines pulse shaping, the channel spacing is higher than the repetition frequency of the source.
- Free spectral range (FSR) determines the bandwidth of the device. Spectral components which are separated by the FSR fall within a single device channel and cannot be independently controlled. Therefore, the FSR has to be sufficiently large to accommodate the required bandwidth.
- Insertion loss, which is mainly caused by the loss in the coupling at the interface between the free propagation region and the arrayed waveguides, and loss of optical waveguides.
- Passband shape and channel resolution. The spectral resolution of the AWG channel determines the number of spectral lines in the channel. The passband shape of a basic AWG is (close to) a Gaussian which is described by its full width at half maximum (FWHM).

Channel width and channel spacing are generally design parameters which affect the layout of the AWG. A high resolution AWG (typically <20GHz channel width on InP) requires a large number of arrayed waveguides which makes it relatively large and hence more sensitive to fabrication imperfections due to phase errors in the arrayed waveguides. In practice, error correction techniques in the waveguide array [64], [65] are required to achieve the high-resolution AWG performance.

To achieve high spectral resolution, AWG channels are designed to be narrow and tightly spaced in spectral domain. However, a narrow Gaussian passband is not tolerant to possible misalignments between the frequency (wavelength) of the spectral line and the channel. The desired shape of AWG channel depends on the requirements of the

application, but is typically preferred to be flat within the passband with steep cut-off at either side to avoid channel overlap. A method to flatten the passband is to use parabolic tapers or multi mode interference couplers at the input waveguides [54], [66]. An alternative approach is to actively control the phase (and amplitude) of the arrayed waveguides. This method is in principle more complicated and is equivalent to building an AWG-based finite impulse response filter [24], [65].

The choice of AWG layout (box-shape, horse shoe, etc.), material layer stack, uniformity of the wafer and birefringence of the array waveguides also affect the AWG performance. The effect of birefringence, the difference in propagation constants for TE and TM, results in polarization dispersion. This means that a polarization dependent AWG shows a different spectral response to different incident polarizations; furthermore, the spectral response is affected by polarization rotation in curved sections of arrayed waveguides. Dispersion compensated AWGs do not suffer from a polarization-induced spectral sidelobes [67].

4.6. Design of an InP-based monolithically integrated pulse shaper

The design is a compromise between the requirements of the application and possibilities of the fabrication technology. Therefore, we first introduce the applications of our interest, and then describe the general design considerations of an integrated optical pulse shaper with a focus on the available generic fabrication platform. That provides a set of boundary conditions for the design framework and justifies the final design. A design in the generic platform is based on a number of defined and standardized building blocks. The wafer material layer stack and fabrication procedure are optimized for best overall performance and compatibility of its basic components.

We are interested in the development of a miniaturized laser system which can benefit two specific applications, namely metrology and CARS microscopy. Widespread use of these applications is currently hindered by the cost, complexity and vulnerability of the (bulk) laser systems involved. One issue is that typically not just a mode-locked laser source is required. Rather than that, electronic and optical systems are needed to stabilize the laser operation and to control the spectral phase/amplitude of optical pulses. In chapter 2, we have considered (partial) stabilization of mode-locked lasers through application of RF modulating signals. Manipulation of the spectral phase/amplitude was extensively addressed in this chapter and is the subject of focus for the integrated pulse shaper device.

The integrated pulse shaper device is mainly intended to be combined with our quantum dot (QD) mode-locked lasers. For both of the applications which are mentioned in the previous paragraph, the available optical bandwidth is important. The optical bandwidth is in principle a feature of the pulse source, i.e. the mode-locked laser. The QD mode-locked laser diodes have a spectral bandwidth of up to 8nm [35], [68]. The QD lasers are interesting because they provide larger gain bandwidth as compared with bulk or quantum well lasers [35], [69]. The large gain bandwidth is ideal for short pulse generation. However, our QD lasers generate chirped pulses which are elongated in time. Detailed discussions are presented in chapter 2. This means that generation of short optical pulses (ideally ~ 300 fs in case of transform limited pulses) is only possible after compensation of the spectral chirp, i.e. pulse compression. Pulse compression is a

specific case of pulse shaping where the output waveform is desired to be as short as possible and ideally a transform-limited pulse.

CARS microscopy is a non-linear detection method that generates a signal depending on the presence of certain molecules (using vibrational resonances). For short pulse excitation, many vibrational frequencies are excited at once resulting in a nonspecific response. Pulse shaping (particularly phase) has an added advantage for CARS since it allows for creation of interferences such that the integrated response is large for molecules with specific resonances but low for all others. This greatly improves the ability to detect specific molecules. In this application, an interesting feature of integrated devices is the possibility of achieving high switching speeds, i.e. up to 100kHz versus few 100Hz in conventional shapers, to achieve video rate imaging.

In [19], a case study of shaped CARS microscopy is presented in which the central wavelength of the pulse source is $\sim 806\text{nm}$ and the FWHM is 26nm . In the experiments, the spectral phase profile is characterized by 40 parameters over 66nm , which is currently within the reach of available commercial pulse shapers. The results show that for 40 parameters, the (calculated) optimal phase is defined accurately. A higher number does not significantly affect the quality of imaging, i.e. contrast ratio. The minimum number of parameters is around 20-25, which determines the minimum number of pulse shaper channels. A higher number of pulse shaper channels/elements ensures a more smooth phase profile.

4.6.1. AWG: spectral de-/multiplexer

AWGs are standard (composite) components in the available foundry technology libraries which are used as the spectral de-/multiplexer. The AWG is the core of an integrated pulse shaper. An optimized pulse shaper should cover the bandwidth of the input pulse. The FSR of the AWG must match the required pulse shaper device bandwidth. The optical spectral bandwidth of the device is determined by the number of AWG channels and the spacing between the channels.

To cover the available optical bandwidth of the QD lasers, the FSR is set to be 8nm . The minimum channel spacing which can be achieved in the current generic foundry platform is $40\text{-}50\text{GHz}$. This means that the number of independent channels in one FSR is in the order of 20-25. Ideally the channel passband is flattened such that the total AWG response efficiently covers the FSR. However, this is not provided in the current fabrication run. Highly isolated, narrowband channels are not desired either, because they are not tolerant to variations in the repetition frequency of the input pulse for the line-by-line pulse shaping scheme. Furthermore, a narrow channel passband causes significant loss of spectral power in the group-of-lines scheme. Therefore, we have chosen to increase the channel width by reducing the gap between the input/output waveguides of the free propagation region. In this case, the coupling between the waveguides is higher which makes for a higher overlap between the channels as well.

4.6.2. Modulation speed of phase and amplitude

The type of application determines the required modulation speed. For instance, a programmable pulse shaper device for compressing (sufficiently stable) chirped pulses does not typically require high modulation speeds. On the other hand a dynamic OAWG device has to provide sufficient modulation bandwidth for waveform synthesis. In silica-based platform thermo-optic modulators are commonly employed whereas in InP-

based platforms, usually electro-optic phase modulators are used. Achieving high modulation speeds is not possible through thermo-optic modulators and getting to speeds beyond 10GHz through electro-optic effect is a practical challenge which involves careful device design to avoid cross-talk, material layer-stack and doping-profile optimization to reduce high frequency losses and eventually extra fabrication steps [70], [71]. An alternative approach adopted in [71] is to incorporate optically driven modulators, in which an external light signal is used to modulate the phase of the spectral line. In case of our applications of interest, a modulation speed up to a few hundred MHz is required to enable pixel-by-pixel phase-shaped CARS imaging at video rates [72].

4.6.3. Phase-only or amplitude-and-phase pulse shaping

Phase-only pulse shapers cannot be used for arbitrary pulse shaping purposes where control over the spectral amplitude is required. Generally in silica-based devices, variable optical attenuators based on Mach-Zehnder modulators (MZMs) which are controlled through resistive heaters are used to adjust the optical loss in device channels and thus to control the relative amplitude of spectral components. A similar approach based on EO modulators is applicable to InP-based devices. Achieving extinction ratios above 20dB with simple MZM stages is challenging. If the fabrication technology allows integration of active components on chip, SOAs can be used to control spectral amplitude. An SOA provides optical gain if it is forward-biased. The optical gain depends on the amount of bias, i.e. injection current. If the SOA is biased below transparency, extra losses are induced due to absorption. Therefore, frequency components of the pulse may be effectively eliminated by reverse-biasing SOAs. Including SOAs on chip has the added advantage that the device losses may be (partially) compensated by the gain of SOAs.

4.6.4. Layout

An integrated pulse shaper could be designed in transmission mode by employing two separate AWGs for demultiplexing and multiplexing the light signal [53], [54]. Such design does not require an optical circulator; however, proper operation of devices with a pair of AWGs requires perfectly matched transmission spectra of the two AWGs. On the other hand, the reflective design requires a single AWG and the signal in each AWG channel passes through the optical elements twice. Therefore, it is more efficient, compact and tolerant to the fabrication process. A drawback of a reflective pulse shaper is the need for an optical circulator. This currently hinders the integration of the reflective pulse shaper with a pulse source on the available fabrication platforms. This is due to the fact that monolithic integration of non-reciprocal optical components, such as isolators and circulators [73], [74], on semiconductor photonic integration platforms is a technological challenge.

4.6.5. Final design

As it was mentioned in section 4.5, an integrated pulse shaper is most duly realized in the FT configuration. A schematic illustration of the functional diagram of the final device design is shown in Fig.4.14. We have chosen to configure the device in the reflection mode. In this mode, the input optical pulse passes through the AWG which decomposes it into constituent components. The spectral components pass through

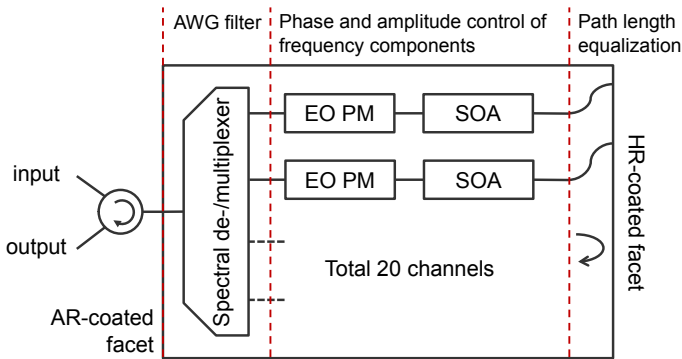


Fig.4.14. Functional diagram of ASPIC9 design, showing the working principal of the pulse compressor/shaper chip. The light will pass the SOA and the phase modulators twice making the system more compact.

electro-optic (EO) PMs and SOAs and are then reflected back from a facet with a high-reflection coating. The PMs and SOAs provide the required phase/amplitude mask and are used to manipulate the spectral phase and amplitude of the components in order to achieve the desired pulse shape. The spectral components are then recombined in the AWG and return through the input/output (I/O) waveguide. The two directions are separated by a circulator outside the chip.

In the reflective design, only a single AWG is required to demultiplex and multiplex the spectral components. This eliminates the need for the realization of two perfectly similar AWGs on the chip (such as the case of transmission mode devices) and saves the complication of tuning and aligning the two AWGs' transmission spectra. Furthermore, the optical elements, i.e. PMs and SOAs, are effectively more efficient in the reflection mode since the spectral components pass through them twice. Both of these arguments lead to a more compact device design which occupies a smaller chip area. In practice, this means that a device with a higher number of channels could fit on a certain available area on the wafer. This is particularly important in multi-user wafer runs, where the size of available cells is predefined and costs are shared per wafer area.

The design is made according to the generic integration technology which is available in the framework of European FP7 project EuroPIC [75]. The chip is designed on a $6 \times 6 \text{ mm}^2$ cell, which is currently the largest available cell size. The designed AWG has 20 channels. Each channel has a PM and an SOA. This means that the pulse shaper has 40 optical elements to be controlled in total. According to the specifications of the current platform, the SOAs must be oriented perpendicular to the wafer major flat and the PMs must be aligned parallel to the wafer major flat for higher efficiency. Therefore, 20 is the maximum number of device channels that fit on the defined cell size. An image of the mask layout is given in Fig.4.15. To compensate for path length differences on the chip and to equalize the channel lengths, extra sections of passive waveguides are included in each channel near the high-reflection coated facet. The effect of variations of the path length in different channels is discussed in chapter 6.

The FSR of the AWG is designed to be 8nm to cover the spectral bandwidth of the QD lasers, such as those presented in chapter 2. The AWG has a cyclic design which means that there is a continuous cover of the spectrum. This makes that the device can be combined with pulse sources that have different central frequencies.

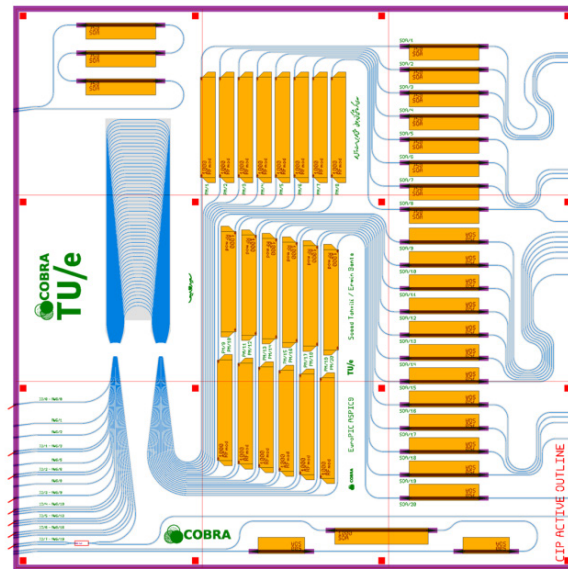


Fig.4.15. Mask layout of the monolithically integrated optical pulse shaper, which indicates the passive waveguides and the PM / SOA building blocks. The image does not include all the mask layers which are required for device fabrication

Since the number of channels is set to 20, the channel spacing is designed to be 50GHz ($\sim 0.4\text{nm}$) to cover the 8nm. The integrated device is planned to be used in the two pulse shaping schemes, i.e. line-by-line and group-of-lines. In the line-by-line scheme, the repetition frequency of the pulse source (closely) matches the AWG channel spacing. In the group-of-lines pulse shaping, the 5 and 10GHz QD lasers in particular are of interest as the pulse source. Since the channel spacing needs to be maintained at 50GHz to keep the required device bandwidth, having a high channel resolution leads to an increasing loss of the signal power due to rejection of the spectral lines in between the channels. This causes a (super-) modulation of the pulse spectrum and will cause severe pulse ringing. The 3dB width of the AWG channel is chosen to be 50GHz. In other words, the AWG channels are designed to overlap at the 3dB width. This value is a trade-off between channel cross-talk and modulation of the pulse spectrum.

References

- [1] M. V. C. Froehly, B. Colombeau, "Shaping and Analysis of Picosecond Light Pulses," *Progress in Optics*, vol. 20, pp. 63–153, 1983.
- [2] A. M. Weiner, "Femtosecond optical pulse shaping and processing," *Progress in Quantum Electronics*, vol. 19, no. 3, pp. 161–237, Jan. 1995.
- [3] A. M. Weiner, "Femtosecond pulse shaping using spatial light modulators," *Review of Scientific Instruments*, vol. 71, no. 5, p. 1929, 2000.
- [4] A. M. Weiner, "Ultrafast optical pulse shaping: A tutorial review," *Optics Communications*, vol. 284, no. 15, pp. 3669–3692, Jul. 2011.
- [5] A. M. Weiner, J. P. Heritage, and E. M. Kirschner, "High-resolution femtosecond pulse shaping," *Journal of the Optical Society of America B*, vol. 5, no. 8, p. 1563, Aug. 1988.

- [6] P. Nuernberger, G. Vogt, T. Brixner, and G. Gerber, "Femtosecond quantum control of molecular dynamics in the condensed phase," *Physical chemistry chemical physics: PCCP*, vol. 9, no. 20, pp. 2470–97, May 2007.
- [7] OKOTech, "Linear Deformable Mirrors." [Online]. Available: <http://www.okotech.com/linear>.
- [8] M. A. Dugan, J. X. Tull, and W. S. Warren, "High-resolution acousto-optic shaping of unamplified and amplified femtosecond laser pulses," *Journal of the Optical Society of America B*, vol. 14, no. 9, p. 2348, Sep. 1997.
- [9] D. Goswami, "Optical pulse shaping approaches to coherent control," *Physics Reports*, vol. 374, no. 6, pp. 385–481, Feb. 2003.
- [10] S. Thomas, A. Malacarne, F. Fresi, L. Potì, and J. Azana, "Fiber-Based Programmable Picosecond Optical Pulse Shaper," *Journal of Lightwave Technology*, vol. 28, no. 12, pp. 1832–1843, Jun. 2010.
- [11] A. Malacarne, S. Thomas, F. Fresi, L. Potì, A. Bogoni, and J. Azaña, "Programmable All-Fiber Optical Pulse Shaping," in *Frontiers in Guided Wave Optics and Optoelectronics*, no. February, B. Pal, Ed. InTech, 2010.
- [12] P. Tournois, "Acousto-optic programmable dispersive filter for adaptive compensation of group delay time dispersion in laser systems," *Optics Communications*, vol. 140, no. 4–6, pp. 245–249, Aug. 1997.
- [13] F. Verluise, V. Laude, Z. Cheng, C. Spielmann, and P. Tournois, "Amplitude and phase control of ultrashort pulses by use of an acousto-optic programmable dispersive filter: pulse compression and shaping," *Optics Letters*, vol. 25, no. 8, p. 575, Apr. 2000.
- [14] A. M. Weiner, *Ultrafast Optics*. Hoboken, NJ, USA: John Wiley & Sons, Inc., 2009.
- [15] D. E. Leaird and a M. Weiner, "Femtosecond optical packet generation by a direct space-to-time pulse shaper.," *Optics letters*, vol. 24, no. 12, pp. 853–5, Jun. 1999.
- [16] D. E. Leaird, a. M. Weiner, S. Kamei, M. Ishii, a. Sugita, and K. Okamoto, "Generation of flat-topped 500-GHz pulse bursts using loss engineered arrayed waveguide gratings," *IEEE Photonics Technology Letters*, vol. 14, no. 6, pp. 816–818, Jun. 2002.
- [17] R. Judson and H. Rabitz, "Teaching lasers to control molecules," *Physical Review Letters*, vol. 68, no. 10, pp. 1500–1503, Mar. 1992.
- [18] N. Hansen, "The CMA Evolution Strategy: A Tutorial," 2011. [Online]. Available: <http://www.lri.fr/~hansen/cmatutorial.pdf>.
- [19] A. C. W. van Rhijn, M. Jurna, A. Jafarpour, J. L. Herek, and H. L. Offerhaus, "Phase-shaping strategies for coherent anti-Stokes Raman scattering," *Journal of Raman Spectroscopy*, vol. 42, no. 10, pp. 1859–1863, Oct. 2011.
- [20] "Biophotonic Solutions Inc." [Online]. Available: <http://www.biophotonicsolutions.com/index.php>.
- [21] C.-B. Huang, Z. Jiang, D. Leaird, J. Caraquitena, and A. Weiner, "Spectral line-by-line shaping for optical and microwave arbitrary waveform generations," *Laser & Photonics Review*, vol. 2, no. 4, pp. 227–248, Aug. 2008.
- [22] S. Postma, P. van der Walle, H. L. Offerhaus, and N. F. van Hulst, "Compact high-resolution spectral phase shaper," *Review of Scientific Instruments*, vol. 76, no. 12, p. 123105, 2005.
- [23] S. T. Cundiff and A. M. Weiner, "Optical arbitrary waveform generation," *Nature Photonics*, vol. 4, no. 11, pp. 760–766, Oct. 2010.
- [24] R. P. Scott, N. K. Fontaine, J. P. Heritage, and S. J. B. Yoo, "Dynamic optical arbitrary waveform generation and measurement.," *Optics express*, vol. 18, no. 18, pp. 18655–70, Aug. 2010.
- [25] N. K. Fontaine, R. P. Scott, and S. J. B. Yoo, "Dynamic optical arbitrary waveform generation and detection in InP photonic integrated circuits for Tb/s optical communications," *Optics Communications*, vol. 284, no. 15, pp. 3693–3705, Jul. 2011.

- [26] S. J. Ben Yoo, R. P. Scott, D. J. Geisler, N. K. Fontaine, and F. M. Soares, "Terahertz Information and Signal Processing by RF-Photonics," *IEEE Transactions on Terahertz Science and Technology*, vol. 2, no. 2, pp. 167–176, Mar. 2012.
- [27] Z. Jiang, C.-B. Huang, D. E. Leaird, and A. M. Weiner, "Optical arbitrary waveform processing of more than 100 spectral comb lines," *Nature Photonics*, vol. 1, no. 8, pp. 463–467, Aug. 2007.
- [28] S. T. Cundiff, "Phase stabilization of ultrashort optical pulses," *Journal of Physics D: Applied Physics*, vol. 35, no. 8, pp. R43–R59, Apr. 2002.
- [29] M. J. R. Heck, M. L. Davenport, H. Park, D. J. Blumenthal, and J. E. Bowers, "Ultra-Long Cavity Hybrid Silicon Mode-locked Laser Diode Operating at 930 MHz," in *Optical Fiber Communication (OFC), collocated National Fiber Optic Engineers Conference*, 2010, pp. 1–3.
- [30] S. Cheung et al., "1-GHz Monolithically Integrated Hybrid Mode-Locked InP Laser," *IEEE Photonics Technology Letters*, vol. 22, no. 24, pp. 1793–1795, Dec. 2010.
- [31] S. Arahira and Y. Ogawa, "Repetition – Frequency Tuning of Monolithic Passively Mode-Locked Semiconductor Lasers with Integrated Extended Cavities," *IEEE JOURNAL OF QUANTUM ELECTRONICS*, vol. 33, no. 2, pp. 255–264, 1997.
- [32] D. A. Yanson, M. W. Street, S. D. McDougall, I. G. Thayne, J. H. Marsh, and E. a. Avrutin, "Terahertz repetition frequencies from harmonic mode-locked monolithic compound-cavity laser diodes," *Applied Physics Letters*, vol. 78, no. 23, p. 3571, 2001.
- [33] J. S. Parker, A. Bhardwaj, P. R. a. Binetti, Y.-J. Hung, and L. a. Coldren, "Monolithically Integrated Gain-Flattened Ring Mode-Locked Laser for Comb-Line Generation," *IEEE Photonics Technology Letters*, vol. 24, no. 2, pp. 131–133, Jan. 2012.
- [34] M. J. R. Heck et al., "Observation of Q-switching and mode-locking in two-section InAs/InP (100) quantum dot lasers around 1.55 μm ," *Optics express*, vol. 15, no. 25, pp. 16292–301, Dec. 2007.
- [35] M. S. Tahvili, L. Du, M. J. R. Heck, R. Nötzel, M. K. Smit, and E. A. J. M. Bente, "Dual-wavelength passive and hybrid mode-locking of 3, 4.5 and 10 GHz InAs/InP(100) quantum dot lasers," *Optics Express*, vol. 20, no. 7, p. 8117, Mar. 2012.
- [36] F. Lelarge et al., "Recent Advances on InAs/InP Quantum Dash Based Semiconductor Lasers and Optical Amplifiers Operating at 1.55 μm ," *IEEE Journal of Selected Topics in Quantum Electronics*, vol. 13, no. 1, pp. 111–124, 2007.
- [37] E. Sooudi et al., "Optical Frequency Comb Generation Using Dual-Mode Injection-Locking of Quantum-Dash Mode-Locked Lasers: Properties and Applications," *IEEE Journal of Quantum Electronics*, vol. 48, no. 10, pp. 1327–1338, Oct. 2012.
- [38] S. G. Murdoch et al., "Spectral amplitude and phase measurement of a 40 GHz free-running quantum-dash modelocked laser diode," *Optics Express*, vol. 19, no. 14, p. 13628, Jun. 2011.
- [39] S. Latkowski, R. Maldonado-Basilio, and P. Landais, "Sub-picosecond pulse generation by 40-GHz passively mode-locked quantum-dash 1-mm-long Fabry-Pérot laser diode," *Optics Express*, vol. 17, no. 21, p. 19166, Oct. 2009.
- [40] R. Rosales et al., "High performance mode locking characteristics of single section quantum dash lasers," *Optics express*, vol. 20, no. 8, pp. 8649–57, Apr. 2012.
- [41] Z. Jiang, D. E. Leaird, and A. M. Weiner, "Line-by-line pulse shaping control for optical arbitrary waveform generation," *Optics express*, vol. 13, no. 25, pp. 10431–9, Dec. 2005.
- [42] W. A. Traub, "Constant-dispersion grism spectrometer for channeled spectra," *Journal of the Optical Society of America A*, vol. 7, no. 9, p. 1779, Sep. 1990.
- [43] S. Kane and J. Squier, "Grism-pair stretcher-compressor system for simultaneous second- and third-order dispersion compensation in chirped-pulse amplification," *Journal of the Optical Society of America B*, vol. 14, no. 3, p. 661, Mar. 1997.

- [44] M. Shirasaki, "Large angular dispersion by a virtually imaged phased array and its application to a wavelength demultiplexer," *Optics letters*, vol. 21, no. 5, pp. 366–8, Mar. 1996.
- [45] A. M. Weiner, "An eight-channel hyperfine wavelength demultiplexer using a virtually imaged phased-array (VIPA)," *IEEE Photonics Technology Letters*, vol. 17, no. 2, pp. 372–374, Feb. 2005.
- [46] H. Tsuda et al., "Second- and Third-Order Dispersion Compensator Using a High-Resolution Arrayed-Waveguide Grating," *IEEE Photonics Technology Letters*, vol. 11, no. 5, pp. 569–571, 1999.
- [47] H. Tsuda et al., "Spectral encoding and decoding of 10 Gbit/s femtosecond pulses using high resolution arrayed-waveguide grating," *Electronics Letters*, vol. 35, no. 14, p. 1186, 1999.
- [48] H. Takenouchi and T. Goh, "2/spl times/40-channel dispersion-slope compensator for 40-Gbit/s WDM transmission systems covering entire C- and L-bands," *Optical Fiber Communication Conference and Exhibit*, pp. 2–4, 2001.
- [49] K. Mandai, T. Suzuki, H. Tsuda, T. Kurokawa, and T. Kawanishi, "Arbitrary optical short pulse generator using a high-resolution arrayed-waveguide grating," in *2004 IEEE International Topical Meeting on Microwave Photonics (IEEE Cat. No.04EX859)*, pp. 107–110.
- [50] K. Takiguchi, K. Okamoto, T. Kominato, H. Takahashi, and T. Shibata, "Flexible pulse waveform generation using silica-waveguide-based spectrum synthesis circuit ELECTRONICS LETTERS 29th April 2004 ELECTRONICS LETTERS 29th April 2004," *Electronics Letters*, vol. 40, no. 9, pp. 29–30, 2004.
- [51] K. Okamoto, T. Kominato, H. Yamada, and T. Goh, "Fabrication of frequency spectrum synthesiser consisting of arrayed-waveguide grating pair and thermo-optic amplitude and phase controllers," *Electronics Letters*, vol. 35, no. 9, p. 733, 1999.
- [52] R. P. Scott et al., "High-fidelity line-by-line optical waveform generation and complete characterization using FROG," *Optics Express*, vol. 15, no. 16, p. 9977, 2007.
- [53] N. K. Fontaine et al., "32 Phase X 32 amplitude optical arbitrary waveform generation.," *Optics letters*, vol. 32, no. 7, pp. 865–7, Apr. 2007.
- [54] M. J. R. Heck et al., "Design, Fabrication and Characterization of an InP-Based Tunable Integrated Optical Pulse Shaper," *IEEE Journal of Quantum Electronics*, vol. 44, no. 4, pp. 370–377, Apr. 2008.
- [55] R. G. Broeke et al., "Monolithically integrated InP-based photonic chip development for O-CDMA systems," *IEEE Journal of Selected Topics in Quantum Electronics*, vol. 11, no. 1, pp. 66–77, Jan. 2005.
- [56] T. Yilmaz, C. M. DePriest, T. Turpin, J. H. Abeles, and P. J. Delfyett, "Toward a photonic arbitrary waveform generator using a modelocked external cavity semiconductor laser," *IEEE Photonics Technology Letters*, vol. 14, no. 11, pp. 1608–1610, Nov. 2002.
- [57] J. Chou, Y. Han, and B. Jalali, "Adaptive RF-photonic arbitrary waveform generator," *IEEE Photonics Technology Letters*, vol. 15, no. 4, pp. 581–583, Apr. 2003.
- [58] I. S. Lin, J. D. McKinney, and A. M. Weiner, "Photonic synthesis of broadband microwave arbitrary waveforms applicable to ultra-wideband communication," *IEEE Microwave and Wireless Components Letters*, vol. 15, no. 4, pp. 226–228, Apr. 2005.
- [59] E. Hamidi and A. M. Weiner, "Phase-Only Matched Filtering of Ultrawideband Arbitrary Microwave Waveforms via Optical Pulse Shaping," *Journal of Lightwave Technology*, vol. 26, no. 15, pp. 2355–2363, Aug. 2008.
- [60] M. K. Smit and C. Van Dam, "PHASAR-based WDM-devices: Principles, design and applications," *IEEE Journal of Selected Topics in Quantum Electronics*, vol. 2, no. 2, pp. 236–250, Jun. 1996.

- [61] S. Janz et al., "Planar Waveguide Echelle Gratings in Silica-On-Silicon," *IEEE Photonics Technology Letters*, vol. 16, no. 2, pp. 503–505, Feb. 2004.
- [62] F. Horst, W. M. J. Green, B. J. Offrein, and Y. a. Vlasov, "Silicon-on-Insulator Echelle Grating WDM Demultiplexers With Two Stigmatic Points," *IEEE Photonics Technology Letters*, vol. 21, no. 23, pp. 1743–1745, Dec. 2009.
- [63] J. Brouckaert, W. Bogaerts, S. Selvaraja, P. Dumon, R. Baets, and D. Van Thourhout, "Planar Concave Grating Demultiplexer With High Reflective Bragg Reflector Facets," *IEEE Photonics Technology Letters*, vol. 20, no. 4, pp. 309–311, Feb. 2008.
- [64] K. Takada and S. Satoh, "Method for measuring the phase error distribution of a wideband arrayed waveguide grating in the frequency domain," *Optics Letters*, vol. 31, no. 3, p. 323, Feb. 2006.
- [65] M. C. Parker, S. D. Walker, A. Yiptong, and R. J. Mears, "Applications of active arrayed-waveguide gratings in dynamic WDM networking and routing," *Journal of Lightwave Technology*, vol. 18, no. 12, pp. 1749–1756, 2000.
- [66] P. Munoz, D. Pastor, and J. Capmany, "Analysis and design of arrayed waveguide gratings with MMI couplers," *Optics express*, vol. 9, no. 7, pp. 328–38, Sep. 2001.
- [67] E. Kleijn, P. J. Williams, N. D. Whitbread, M. J. Wale, M. K. Smit, and X. J. M. Leijtens, "Sidelobes in the response of arrayed waveguide gratings caused by polarization rotation," *Optics express*, vol. 20, no. 20, pp. 22660–8, Sep. 2012.
- [68] M. J. R. Heck et al., "Analysis of hybrid mode-locking of two-section quantum dot lasers operating at 1.5 microm," *Optics express*, vol. 17, no. 20, pp. 18063–75, Sep. 2009.
- [69] M. J. R. Heck et al., "Passively Mode-Locked 4.6 and 10.5 GHz Quantum Dot Laser Diodes Around 1.55 μm With Large Operating Regime," *IEEE Journal of Selected Topics in Quantum Electronics*, vol. 15, no. 3, pp. 634–643, 2009.
- [70] J. H. Baek et al., "10-GHz and 20-GHz Channel Spacing High-Resolution AWGs on InP," *IEEE Photonics Technology Letters*, vol. 21, no. 5, pp. 298–300, Mar. 2009.
- [71] F. M. Soares et al., "Monolithic InP 100-Channel \times 10-GHz Device for Optical Arbitrary Waveform Generation," *IEEE Photonics Journal*, vol. 3, no. 6, pp. 975–985, Dec. 2011.
- [72] H. L. Offerhaus, E. T. Garbacik, A. C. W. van Rhijn, A. L. Fussell, and J. L. Herek, "Phase aspects of (broadband) stimulated Raman scattering," *Reviews in Analytical Chemistry*, vol. 31, no. 1, pp. 1–6, Jan. 2012.
- [73] M. Lohmeyer, "Integrated optical circulator based on radiatively coupled magneto-optic waveguides," *Optical Engineering*, vol. 36, no. 3, p. 889, Mar. 1997.
- [74] T. R. Zaman, X. Guo, and R. J. Ram, "Semiconductor Waveguide Isolators," *Journal of Lightwave Technology*, vol. 26, no. 2, pp. 291–301, 2008.
- [75] "European manufacturing platform for Photonic Integrated Circuits." [Online]. Available: <http://europic.jepix.eu/>.
- [76] A. M. Weiner, "ECE 616: Ultrafast Optics," 2011. [Online]. Available: <https://nanohub.org/resources/11874>.
- [77] C. T. Middleton, A. M. Woys, S. S. Mukherjee, and M. T. Zanni, "Residue-specific structural kinetics of proteins through the union of isotope labeling, mid-IR pulse shaping, and coherent 2D IR spectroscopy," *Methods (San Diego, Calif.)*, vol. 52, no. 1, pp. 12–22, Sep. 2010.

CHAPTER 5

Full Calibration and Characterization of the InP-based Optical Pulse Shaper

For producing predictable pulse shapes with a shaping device, an accurate calibration of the effect of the device's control signals is required. In this chapter, we present the full calibration and characterization of the monolithically integrated optical pulse shaper that was presented at the end of the previous chapter. This chapter is organized as follows. In section 1, we briefly present the realization of the InP-based integrated optical pulse shaper. In section 2, we present the general mathematical description of the Fourier transform pulse shaping technique. The general description is formulated in terms of mathematical expressions which can be experimentally quantified. This serves as the basis of the calibration method. We describe how the calibration method is implemented in practice in section 3, where the measurement setups are presented in detail and the measured results are discussed. The full calibration of the device provides a complete mathematical description of the pulse shaper. This model is required for operating the device. In section 4, we round off the work on the calibration of the pulse shaper with two demonstrations. The first is a test of the interferometric method used to measure the reference states. The second demonstration shows that the pulse shaper indeed behaves as a linear system and that the system response is correctly predicted using the reference state and mask function.

5.1. Device realization

The device is fabricated in a generic integration technology platform [1] in which the design is based on certain standardized building blocks. In the generic integration platform, the wafer layer stack and fabrication process are optimized for best overall performance and are not tailored towards a specific application. This enables the possibility of multi-user fabrication runs which allow for an earlier (commercial) exploitation of the results. A key advantage of the present platform is the active-passive integration scheme which allows direct integration of active components, such as semiconductor optical amplifiers (SOAs) with passive elements on a single chip.

A microscope image of the realized chip is shown in Fig.5.1. Details of the device design were given in section 6 of chapter 4. The device includes an arrayed waveguide grating (AWG) which has 20 channels. Each channel has a phase modulator (PM) and

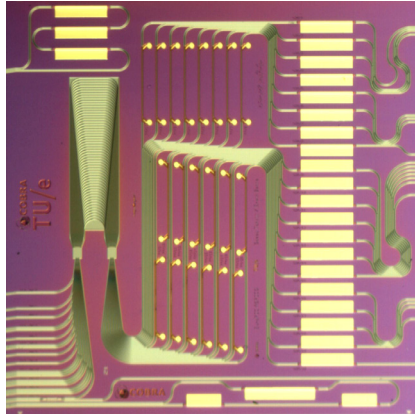


Fig.5.1. A microscope image of the realized pulse shaper chip.

an SOA. In this design, the AWG is the spectral de-/multiplexer and PMs and SOAs are used to control the phase and amplitude of the spectral components. The chip size is $6 \times 6 \text{ mm}^2$ and the substrate is thinned and has a thickness of $135 \mu\text{m}$.

The light from the optical pulse source, i.e. a mode-locked (ML) laser, is injected into the pulse shaper chip via an anti-reflection (AR) coated facet (the left hand side facet in Fig.5.1). The pulsed signal passes through the AWG which decomposes the light into its spectral components. Each component passes through electro-optic (EO) PMs and SOAs and is then reflected back from a facet with a high-reflection ($\sim 95\%$) coating (the right hand side facet in Fig.5.1). The spectral components are then recombined in the AWG and return through the input/output (I/O) waveguide. The two directions are separated by an optical circulator outside the chip.

The PMs on the pulse shaper chip are deeply-etched structures which are 1 mm -long and $1.2 \mu\text{m}$ -wide. The core of the waveguide is a multi-quantum well (MQW) structure to provide efficient electro-optic phase tuning through the quantum-confined Stark effect (QCSE). The EO efficiency is significantly increased when oriented parallel to the major flat due to the fact that the linear EO effect adds to the QCSE shift whereas it subtracts in the orthogonal direction. The QCSE is generally regarded as quadratic in nature resulting in the more nonlinear characteristic. In the current device, all the 20 PMs are parallel to the major flat. There is some wavelength dependence to both phase and loss due to the effect of proximity to the bandgap wavelength of the MQW core. This will be investigated in detail later in this chapter. PMs are operated by applying a reverse bias voltage. The SOAs are shallowly etched waveguide structures oriented orthogonal to the wafer major flat. The width of SOA waveguides is fixed at $1.9 \mu\text{m}$. The total contact resistance of SOAs is measured to be $8.5 \pm 1.2 \Omega$. The SOAs are $750 \mu\text{m}$ long and provide around 7dB total optical gain at $I_{\text{SOA}} = 40 \text{ mA}$.

5.1.1. Device mounting and cooling

The realized integrated pulse shaper requires 2×20 electrical control signals for PMs and SOAs. The fabrication platform in which the device has been realized did not provide on-chip metal routing as a standard option. As a result, the probe pads are distributed over the chip area and were not located at the edge of the chip. Therefore,

using multi-probes to provide simultaneous connection to such number of elements is not convenient and reliable.

In order to facilitate the measurements, the chip is first mounted on a subcarrier which is a 280 μm -thick polished AlN substrate. The subcarrier was lithographically patterned with thick ($>1\mu\text{m}$) gold plating to provide a common ground plane and wire-bond pads. The back side of the chip was first glued on the ground plane. A set of bonding pads on the subcarrier, which are arranged around the ground plane, were then wire bonded to metal contacts on PMs and SOAs. Metal tracks on the AlN substrate route the connections to the edge of the subcarrier, where a second set of bonding pads are patterned. These pads were wire-bonded to a printed circuit board (PCB).

The PCB has a 50-way IDC connector which is suitable for compact wiring via a flat cable. The flat cable provides connection to the controlling electronic instruments, i.e. multi channel voltage sources and current supplies. The voltage sources are the AWG100 eight-channel analog waveform generator units [2] which are used for controlling the PMs. The current supplies are Thorlabs MLC8100 modules which are used to bias the SOAs.

The subcarrier and the PCB are mounted on an aluminum mechanical block, as depicted in Fig.5.2. The aluminum block is then mounted on a water-cooled block which acts as a heat sink. The water temperature is controlled using a water cooler that stabilizes the water temperature within 0.1°C and therefore the temperature of the setup. Due to the fact that there is a thermal resistance between the device and the cooling water, the temperature of the device will depend on the amount of heat dissipated in it by the biased SOAs. The total dissipated power exceeds 1W when the SOAs are biased above 40mA. To monitor the device temperature a thermistor is located just below the device as indicated in Fig.5.2. The actual device temperature will still be somewhat higher than what the monitor will indicate, and will vary on the distance to the SOAs.

Temperature variations affect the operation of the device in two ways. The effective index of the waveguides and the current gain relationship of the amplifiers both depend on the device temperature. To have an indication of the sensitivity of the device operation and the thermal dependence of the effective index we can investigate the wavelength shift of the AWG channels versus the temperature. In order to do so, we

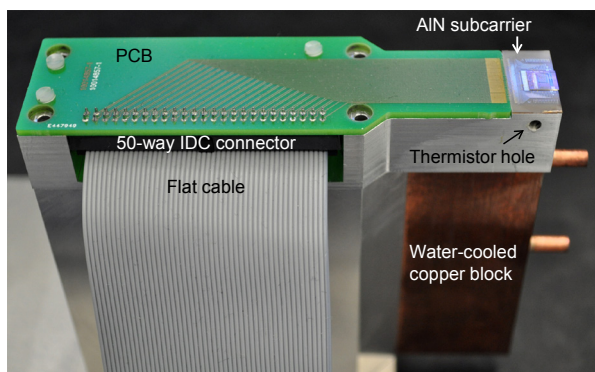


Fig.5.2. The chip is mounted and wire-bonded on an AlN subcarrier. The subcarrier is wire-bonded to a PCB which provides electrical connections to the control instruments via a 50-way IDC connector. The device temperature is stabilized by the water-cooled block.

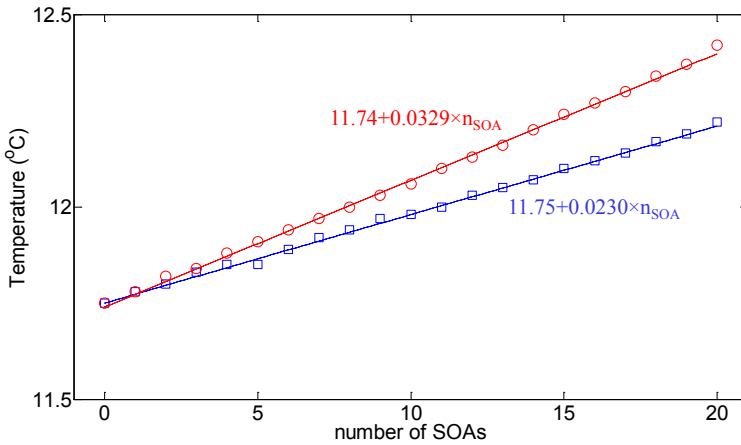


Fig.5.3. The temperature which is indicated by the thermistor versus the number of SOAs which are simultaneously biased at $I_{SOA}=30\text{mA}$ (squares) and $I_{SOA}=40\text{mA}$ (circles). The setpoint of the water cooler is at $T=10.5^\circ\text{C}$.

change the set point of the water cooler which controls the device temperature. We use a temperature sensor to monitor the device temperature and then measure the transmission spectrum of the AWG channels. The result is a $\sim 0.128\text{nm}/^\circ\text{C}$ shift of the central AWG wavelength. This is a typical value for AWGs in InP [3] and corresponds to approximately $2.5 \times 10^{-4} / ^\circ\text{C}$ temperature dependence of the effective index.

Next, we observe the effect of SOA bias on the device temperature. We fix the water cooler temperature and bias the SOAs to the operating current one by one. When the SOAs are biased, the monitor temperature starts to increase. The recorded temperature results are given in Fig.5.3. The measurements are done at $I_{SOA}=30\text{mA}$ and $I_{SOA}=40\text{mA}$ for each SOA. Fig.5.3 shows that when all the 20 SOAs on chip are biased at $I_{SOA}=30\text{-}40\text{mA}$, the device temperature increases by about $0.5\text{-}0.7^\circ\text{C}$. This corresponds to an overall temperature change of less than $0.01^\circ\text{C}/10\text{mA}$ per SOA.

The device temperature is not automatically stabilized but we operate the pulse shaper at the same constant monitor temperature; we set the water temperature such that the temperature sensor indicates $12 \pm 0.03^\circ\text{C}$ after the SOA bias values are set and the temperature is stabilized. Thus given the results in Fig.5.3, the effect of small changes of SOA current on the overall device temperature are negligible if no further correction on the water temperature is applied.

The optical path length differences between the device channels have been minimized and will in practice be limited to a few μm . Given the thermal dependence of the effective index, we estimate that the effect of temperature variations on the relative phases of the optical signal passing through the device is less than $\pm 10^{-5}$ rad. This means that this temperature effect can be neglected.

5.2. Description of the calibration method

The Fourier Transform (FT) pulse shaping technique is based on the concept of linear, time-invariant (LTI) systems. Linear systems are generally described in the time domain

by an impulse response $h(t)$, and in the frequency domain by $H(\omega)$ which is known as the frequency response. $H(\omega)$ may also be referred to as the system transfer function. $H(\omega)$ is the key to understanding the principle of the FT pulse shaping technique. In a FT pulse shaper, the shape of the output pulse, i.e. the amplitude and phase, is related to the shape of input pulse through the system response of the pulse shaper device as

$$E_{\text{out}}(\omega) = H(\omega) \times E_{\text{in}}(\omega) \quad (5.1)$$

where E denotes the pulse shape in the frequency domain which is in general complex valued. Eq.5.1 implies that the shape of the output pulse can be controlled by manipulating the frequency response of the pulse shaper device.

In a programmable pulse shaper, the frequency response of the device can be (re-)configured by applying the control signals. This implies that in order to generate predictable pulse shapes, the system requires to be calibrated. Calibration of the pulse shaper in this context is equivalent to finding the frequency response of the pulse shaper device for any condition of the control signals.

In practice, it is not convenient (even possible) to measure the transfer function of a pulse shaper for all the possible combinations of the control signals. Our approach to calibrate the pulse shaper is to identify the system in a ‘reference’ state and consider the effect of control signals separately. The reference state can be defined as any particular set of control signals. This approach is described in more details as follows.

The pulse shaper device consists of several channels. The total response of the pulse shaper is a linear summation of the frequency responses of the operating channels. If the total response of the system is H_{tot} , we have

$$H_{\text{tot}}(\omega, s) = \sum_{i=1}^N H_i(\omega, s_i) \quad (5.2)$$

in which N is the number of channels, H_i is the individual channel response of the channel number i , and s_i stands for the control signals in the corresponding channel. It is convenient to define

$$H_i(\omega, s_i) = HR_i(\omega) \times M_i(s_i) \quad (5.3)$$

in which $HR_i(\omega)$ is the channel response at the reference state of the control signals. We let the function $M_i(s_i)$ account for the effect of applied control signals on the phase and amplitude of the optical signal in each channel. This means that changes of the phase and amplitude with respect to the reference state are taken into account by the mask function M_i . The advantage of this method is that the functions HR_i and M_i can be measured separately.

HR_i and M_i are in general complex valued functions of the optical frequency, i.e. they affect the amplitude and phase of the optical signal. Therefore, evaluating these functions in practice requires measurement of the optical amplitude and phase. In the following subsections, we first explain a practical method to characterize the frequency response (amplitude and phase) of a given device. This represents the basis for measuring the frequency response of individual pulse shaper channels, i.e. HR_i . We then express the mask function, i.e. M_i , in terms of the effect of control signals on the amplitude and phase of the optical signal. The mathematical expression is formulated such that the measured data on the amplitude and phase modulators can be directly implemented in the expressions to determine the mask function.

5.2.1. Measurement of a complex transfer function: the channel response

In the following we describe an interferometric measurement method that can be employed to determine the complex transfer function of an optical device. The schematic illustration of the measurement method is presented in Fig.5.4. The setup is configured in the form of a Mach-Zehnder interferometer (MZI). In this setup, the light from an optical single frequency laser source is divided between the reference arm and the device. The device arm includes the device under test (DUT) and a time-delay element. The delay element is an additional path length difference between the reference arm and the device arm. The signals of the two arms are then combined and the optical power is recorded.

In this method, the frequency of the optical source is tuned and the optical power at the output of the MZI is measured at each frequency. The key point about the interferometric setup is that it enables measurement of the optical phase with a setup that is easy to build in practice. Measuring the phase generally requires complicated and advanced tools such as a network analyzer. In the interferometric setup, any phase change between the two MZI arms is translated into changes of the optical power, which is easily measured.

We define the electric field of the signal generated by the optical source to be

$$\mathcal{E}(t) = E_0 e^{j\omega t} \quad (5.4)$$

where E_0 is the field amplitude, j is the imaginary number, ω is the angular frequency and t is the time. Therefore, the signal in the reference arm is represented as $\mathcal{E}_1 = E_0$ in frequency domain. For convenience and without loss of generality, we have assumed a splitting ratio of unity and a zero delay in the reference arm. The electric field which has passed through the device arm is then

$$\mathcal{E}_2 = E_0 \times e^{-j\omega\tau} \times H(\omega) \quad (5.5)$$

where τ is the time delay in the device arm and $H(\omega)$ is frequency response of the DUT. If we define $H(\omega)$ in terms of the magnitude and the phase as

$$H(\omega) = \rho(\omega) e^{j\varphi(\omega)} \quad (5.6)$$

with the

$$\rho(\omega) = |H(\omega)| \quad (5.7)$$

and

$$\varphi(\omega) = \angle H(\omega) \quad (5.8)$$

The measured optical power P_{det} , can be stated as

$$P_{\text{det}}(\omega) \sim |\mathcal{E}_1 + \mathcal{E}_2|^2 = E_0^2 \left| 1 + \rho(\omega) e^{j\varphi(\omega) - j\omega\tau} \right|^2 \sim 1 + \rho^2(\omega) + 2\rho(\omega) \cos(\varphi(\omega) - \omega\tau) \quad (5.9)$$

Now we examine the measured signal in time domain.

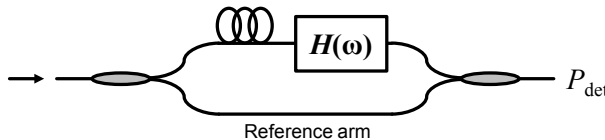


Fig.5.4. Schematic drawing of the interferometric setup in the Mach-Zehnder configuration.

$$p_{\text{det}}(t) = \mathcal{F}^{-1} \{ P_{\text{det}}(\omega) \} \sim \int_{-\infty}^{\infty} \left[1 + \rho^2(\omega) + 2\rho(\omega) \cos(\varphi(\omega) - \omega\tau) \right] e^{j\omega t} d\omega \quad (5.10)$$

Hence

$$p_{\text{det}}(t) \sim \delta(t) + \underbrace{\int_{-\infty}^{\infty} \rho^2(\omega) e^{j\omega t} d\omega}_{\text{A}} + \underbrace{\int_{-\infty}^{\infty} 2\rho(\omega) \frac{e^{j(\varphi(\omega) - \omega\tau)} + e^{-j(\varphi(\omega) - \omega\tau)}}{2} e^{j\omega t} d\omega}_{\text{B}} \quad (5.11)$$

where $\delta(t)$ is the Dirac delta and

$$\text{A} = \int_{-\infty}^{\infty} \rho^2(\omega) e^{j\omega t} d\omega = \int_{-\infty}^{\infty} |H(\omega)|^2 e^{j\omega t} d\omega = \mathcal{F}^{-1} \{ H(\omega) H^*(\omega) \} = h(t) \otimes h^*(-t) \quad (5.12)$$

$$\begin{aligned} \text{B} &= \int_{-\infty}^{\infty} 2\rho(\omega) \frac{e^{j(\varphi(\omega) - \omega\tau)} + e^{-j(\varphi(\omega) - \omega\tau)}}{2} e^{j\omega t} d\omega \\ &= \int_{-\infty}^{\infty} \rho(\omega) e^{j\varphi(\omega)} e^{j\omega(t-\tau)} d\omega + \int_{-\infty}^{\infty} \rho(\omega) e^{-j\varphi(\omega)} e^{j\omega(t+\tau)} d\omega = h(t-\tau) + h^*(-(t+\tau)) \end{aligned} \quad (5.13)$$

in which the symbol $*$ is the complex conjugate and \otimes is the convolution operation. Therefore,

$$p_{\text{det}}(t) \sim \delta(t) + h(t) \otimes h^*(-t) + h(t-\tau) + h^*(-(t+\tau)) \quad (5.14)$$

If $h(t)$ corresponds to a causal system and has a finite duration in time, the term A in Eq.5.12 is limited in time, and goes to zero for values of t larger than the duration of $h(t)$. This means that if a proper value of τ (larger than the duration of the impulse response) is chosen, the effect of the system impulse response, i.e. $h(t-\tau)$, does not temporally overlap with other terms. Therefore it is possible to filter out the part of the signal which corresponds to $h(t)$ in the time domain. This is equivalent to achieving the system frequency response through a Fourier transform $H(\omega) = \mathcal{F} \{ h(t) \}$.

The method which was described in this subsection, is a general technique which can be applied to different systems [4–6]. In case of the integrated pulse shaper which is presented in this chapter, we employ the method to characterize the complex, i.e. amplitude and phase, transfer function of the device channels. Device channels are formed by the AWG channels. We note that in this case, $h(t)$ corresponds to a physical system which is causal. Furthermore, since the AWG is essentially an FIR (finite impulse response) filter, the duration of $h(t)$ in time is limited. Therefore, the method can be conveniently applied.

5.2.2. Mathematical description the mask function: the effect of control signals

The control signals are used to tune the optical elements and hence manipulate the total system response. The complex-valued mask function M (which appears in Eq.5.3) can be written as

$$M(G, \Phi) = G e^{j\Phi} \quad (5.15)$$

to account for the gain G of the amplifiers and the phase shift Φ of the phase modulator. In an ideal pulse shaper, the amplitude and phase of the spectral components can be

modulated independently. In this case, the optical amplifiers only affect the spectral amplitude and the phase modulators only affect the phase. Therefore, G and Φ are real-valued functions of the control signals in each device channel.

In case of the integrated pulse shaper, the optical gain is provided by the SOAs and the phase modulation is achieved through PMs. In practice the PMs and SOAs do not perform independently and the G and Φ functions are complex. This is due to the fact that applying a reverse bias signal on a PM for tuning the phase, induces some absorption and affects the signal amplitude. On the other hand, changing the biasing current of the SOA affects the phase of the signal. To consider the mutual effect of the PMs and SOAs in case of the integrated device, we define

$$G = g_{\text{SOA}} \times e^{j\varphi_{\text{SOA}}} \quad (5.16)$$

$$\Phi = \varphi_{\text{PM}} + j\alpha_{\text{PM}} \quad (5.17)$$

In Eq.5.16, g_{SOA} is the optical gain and φ_{SOA} is the phase effect of the SOA section. In Eq.5.17, φ_{PM} is the phase tuning and α_{PM} is the induced loss due to the reverse bias. It is very important for the full calibration to get the information over the performance of individual optical elements as well as the mutual effect of control signals.

5.3. Experimental implementation of the calibration method

In this section we present the details on the measurement of the calibration of the pulse shaper. First the measurement of the reference state is discussed, followed by the measurement of the effect of the control signals on the phase modulators and amplifiers.

5.3.1. Measurement of the channel response in reference state

The integrated pulse shaper has a reflective geometry in which the input light signal passes through the chip and returns to the I/O port. Therefore, the interferometric setup which was explained in section 5.2.1 is easier to realize in the Michelson configuration. This configuration can be realized relatively easily in practice. We have used a cleaved fiber tip to inject light from a single frequency tunable laser to the chip. The reflection of the tip of the fiber could then be used as the reference signal; this makes the length of the reference arm zero. The loss in the optical coupling from the fiber to the chip and back is approximately 10dB higher compared to a lensed fiber coupling, but the signal strength of the return signal is sufficiently strong to obtain a clear interferogram. Furthermore, the required time delay of the device arm corresponds to the total path length (double pass) of the chip.

As it was described in the previous section, our calibration procedure requires that characterization of the device channels is done separately. The key point which enables individual channel characterization in the current device is that an SOA is included in each channel. If the SOA in the channel is not biased, it effectively absorbs the light in the corresponding channel and hence, there is no return signal to the I/O port. On the other hand, if the SOA is biased to provide enough gain, the signal which goes through the channel and returns to the I/O port where it interferes with the reflected signal from the tip of the cleaved fiber. This forms the required interference pattern which is used to analyze the channel response.

Measuring the complex channel response involves the measurement of the amplitude and phase of the frequency response according to the basic method and corresponding

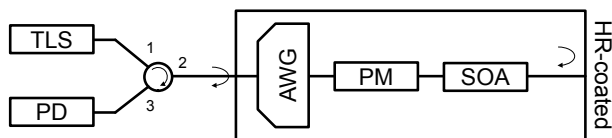


Fig.5.5. Schematic illustration of the measurement setup for characterizing the complex transfer function of the individual device channels in the reference state. A cleaved fiber tip is connected to port 2 of the circulator to inject the light to the chip. TLS: tunable laser source, PD: photo detector (optical power meter), HR: high-reflection.

calculations which were described in section 5.2.1. The schematic illustration of the measurement setup is given in Fig.5.5. We have used a continuously tunable laser source to sweep the input signal wavelength and recorded the optical power in steps of 1pm over a length of several nm to clearly cover the full channel width. The optical power of the source is kept below 3dBm to make sure nonlinear effects in SOAs, such as self-phase modulation, does not disturb the measurement by violating the LTI system assumption. We measure the interference signal in order to determine the frequency response of each channel. The reference state of control signals is chosen as $V_{PM}=0V$ and $I_{SOA}=40mA$.

A typical measurement result which shows the interference pattern is given in Fig.5.6(a). In this figure, the laser source is scanned over the wavelength range $\lambda=1544-1548nm$ and the SOA in channel 10 is biased at $I_{SOA}=40mA$. The inset is a focus on the interference fringes and shows that the wavelength step of 1pm provides sufficient sample points to resolve the fringes properly.

The magnitude of the inverse Fourier transform of the measured optical power is given in Fig.5.6(b). The signal which passes through the chip is delayed by approximately 400ps. This corresponds to the total travel time through the device length (double pass) which was denoted as the term τ in Eq.5.5-Eq.5.14. In Fig.5.6(b), the peak that appears at $t\sim 400ps$ corresponds to the retarded impulse response of the channel, i.e. $h(t-\tau)$ in Eq.5.14. The temporal peak is well separated from the other signals and well above the noise floor. The isolated peak in the time domain is then filtered out, as indicated in the inset of Fig.5.6(b). The complex frequency response of the channel is then calculated by a Fourier transform, i.e. $H(\omega)=\mathcal{F}\{h(t)\}$.

The measured transfer function, i.e. peak amplitude normalized to 1 and the spectral phase, of the device channel number 10 at $V_{PM}=0V$ and $I_{SOA}=40mA$ is given in Fig.5.7. The wavelength dependence of the channel response is caused by the filtering effect of the transmission of the AWG channels. Therefore, the magnitude of the channel response is a measurement of the transmission of the AWG channels. In order to confirm this, we have measured the power transmission through the AWG channel directly. The AWG channel was characterized by biasing the SOA in channel 10. When the SOA is turned on, it generates amplified spontaneous emission (ASE). The SOA is then used as an on-chip broad-band light source. We have then measured the optical signal at the I/O waveguide using an optical spectrum analyzer. This gives the transmission spectrum of the AWG channel. The measured power transmission spectrum of the AWG channel is presented in Fig.5.7 (squares) and it compares very well with the magnitude of the channel response.

Following the same technique, we have measured the complex response of all the individual device channels at the reference state. An overview of all results is given in

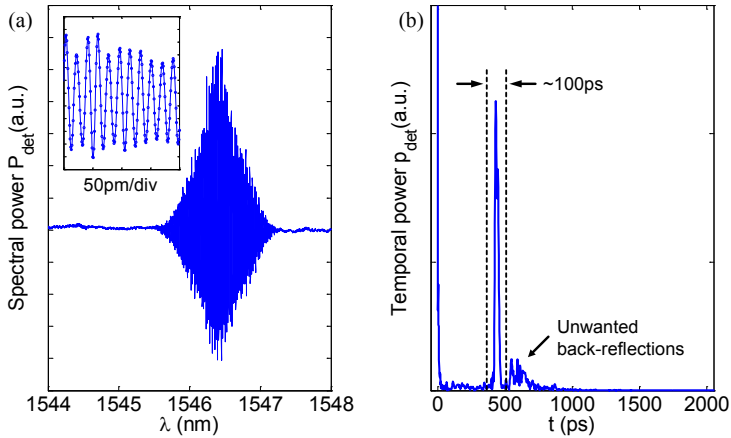


Fig.5.6. (a) A typical interferogram which is recorded for channel characterization. The inset is a zoom-in over 0.2nm range to show the number of points per fringe and the spectral resolution. (b) The magnitude of the time-domain representation of the recorded signal. The peak at $t \sim 400$ ps corresponds to the device channel. The temporal filter which is used to numerically isolate the retarded channel response $h(t)$ is ~ 100 ps wide.

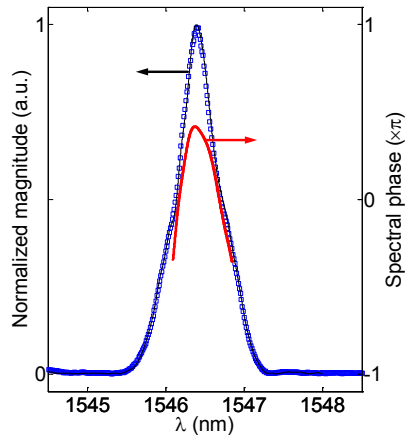


Fig.5.7. Frequency response (magnitude normalized to 1 and phase) of channel 10 at the reference state ($I_{SOA}=40$ mA, $V_{PM}=0$ V). Blue squares show the transmission spectrum of the AWG channel 10 which is measured separately.

Fig.5.8. The total system response of the shaper in the reference state can be calculated by a complex summation of these measured frequency responses. It is seen from Fig.5.8 that the frequency response for the channels 4 and 5 appear to be different from the other channels. This is caused by a short circuit problem between the contacts on the SOAs in those two channels which made that these SOAs could not be biased individually. Furthermore increasing the bias current on these two SOAs did not increase the gain in the channels. We were not able to resolve this issue.

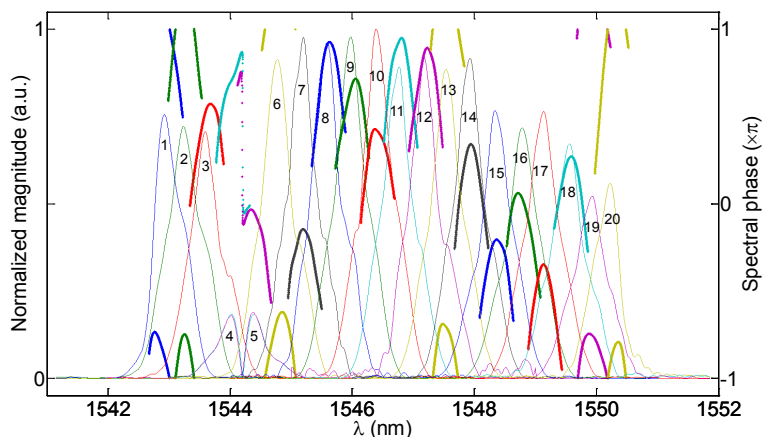


Fig.5.8. Individual channel response for the 20 device channels. Channel numbers are indicated on the plot.

The spectral phase response curves of the channels are quite similar. The shape can be approximated by a quadratic relation over the width of the channel. The spectral phase response determines the channel dispersion which is an important issue for pulse shaper devices. The effect of channel dispersion on the pulse shaper performance is discussed in section 6.5 of the next chapter. The phase offset values vary randomly over the channels. It reflects the fact that the optical path length of each channel is not controlled down to the sub-wavelength level in the manufacturing.

5.3.2. Effect of control signals

Knowledge of the performance of tuning elements, i.e. the effect of control signals on the phase and amplitude of the optical signal, is required for proper operation of the pulse shaper. For open-loop operation of the pulse shaper, it is particularly important that the device components are characterized on-chip. In section 5.2.2, we have presented the mathematical description of the mask function which includes the effect of control signals on the PMs and SOAs. The method that has been used to characterize the effect of PMs and SOAs is described in this section.

As already mentioned in the last section of the previous chapter, the width of the AWG channels in our device has been designed to be equal to the channel spacing, i.e. 50GHz. Therefore, the AWG channels overlap at the 3dB width. If a laser light signal is injected into the device, such that its wavelength is spectrally located in between two neighboring channels, the signal is effectively split between the two adjacent channels. The signal then travels in the waveguides, through corresponding PMs and SOAs. If both SOAs are switched on at the same time, the optical signals of the two neighboring channels pass through to return to the I/O waveguide. This structure forms a Michelson interferometer where the two adjacent channels form the two arms of the interferometer. This Michelson interferometer structure is formed on the chip and therefore it provides a very stable interferometer structure to measure the effect of control signals on an optical signal which is passing through the structure. The on-chip Michelson interferometer is schematically illustrated in Fig.5.9. This is the basis for characterizing the relative phase effect of PMS and SOAs.

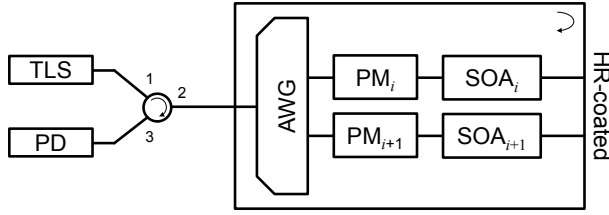


Fig.5.9. Schematic illustration of the measurement technique which is used to evaluate the effect of control signals. Two neighboring device arms form an on-chip Michelson interferometer structure. An AR-coated lensed fiber tip is connected to port 2 of the circulator to inject the light to the chip.

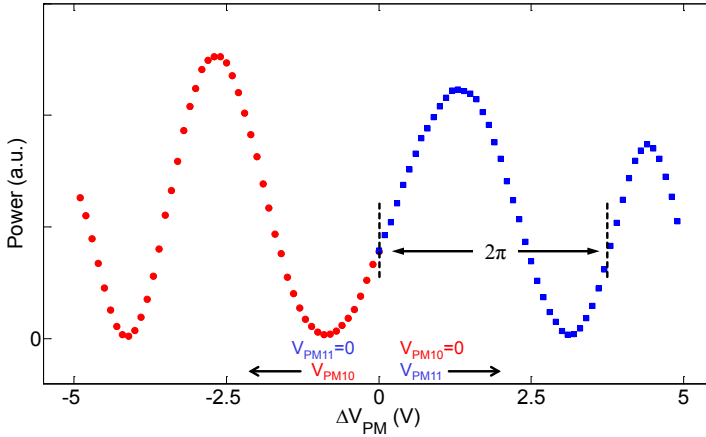


Fig.5.10. A typical interferogram which is used to measure the parameters of the PMs. In this measurement, device channels 10 (red circles) and 11 (blue squares) are biased together. The effect of additional loss of the PM at higher bias voltage is seen as the reduced modulation depth of the interference pattern.

5.3.2.1. PM: Phase tuning and induced excess loss

The contribution of the effect of PMs to the mask function is mathematically described as in Eq.5.17. This includes a phase shift as a function of the applied voltage, as well as possible excess loss which occurs due to absorption of the light in presence of the external electric field. In order to characterize the PMs, we have followed the measurement technique which was described above and illustrated in Fig.5.9. The SOAs in two neighboring channels are forward biased at the reference state, i.e. $I_{SOA}=40\text{mA}$. The voltage bias on one of the PMs is kept constant at $V_{PM}=0\text{V}$, whereas the bias voltage on the other PM is scanned. The output power is measured for each value of the voltage. Single frequency laser light is injected to the chip using an AR-coated lensed fiber tip to minimize back reflections from the tip of the fiber. A circulator is used to separate the input/output directions outside the chip. The result is an interferogram which we have used to extract the PM parameters.

A typical measurement result is given in Fig.5.10. The interference pattern is fitted to an analytical expression which is given by

$$P_{\text{int}} = f_0 + f_1^2 + [f_2 I(V)]^2 + 2f_1 f_2 I(V) \cos(\varphi(V)) \quad (5.18)$$

in which P_{int} is the measured interferogram (power), f_0 is the background signal and f_1 is the electric field amplitude in the interferometer arm with the PM that is not scanned. The signal electric field amplitude in the arm in which the PM bias is scanned is given by its maximum value f_2 and a function $l(V)$, which describes the induced voltage dependent loss in the field. The voltage dependent loss in one arm of the Michelson interferometer causes an imbalance between the signal amplitudes in the arms and reduces the modulation depth of the interferogram with increasing voltage. This effect is clearly seen in Fig.5.8 for voltage values near 5V. We have used an empirical relation to express the excess loss as a function of the bias voltage as

$$l(V) = 1 - f_3 V^3 \quad (5.19)$$

The phase tuning function, $\varphi(V)$, is phenomenologically expressed by a second order polynomial as

$$\varphi(V) = f_4 + f_5 V + f_6 V^2 \quad (5.20)$$

in which f_4 is the phase offset between the two neighboring arms, f_5 and f_6 are the linear and quadratic phase shift terms. The quadratic phase term is mainly due to the QCSE shift.

Eq.5.18-Eq.5.20 include seven fitting parameters (f_0 to f_6) in total. The nonlinear curve fitting problem is solved in the least-squares sense which is implemented in MATLAB using the 'lsqcurvefit' routine. We first present the results obtained for the phase tuning curves $\varphi(V)$. These phase tuning data have been measured for the PMs in the different channels of the pulse shaper. The data are recorded at wavelengths over one FSR of the AWG in the device around 1529nm.

The linear and quadratic terms of the fitted curves are given in Fig.5.11. As mentioned before the SOA sections in channel 4 and 5 are short circuited and cannot be controlled independently. The transmitted power through these channels at the reference state is 10dB lower than the neighboring channels. Therefore, we were not able to measure the PM performance in these two channels. The PMs in channels 1, 19 and 20 have not been measured. The data points corresponding to these channels are missing in Fig.5.11. The tuning curves for the PMs are fairly consistent below 4V. The required voltage for a 2π phase shift is $\sim 3.7V$ on average. At this value of the bias voltage, the amount of phase shift for all the PMs is $2\pi \pm 0.25\pi$. This is shown in Fig.5.12.

The values of the parameter f_3 give the voltage dependent loss of the PMs as in Eq.5.19. From the fit values, the voltage dependent power losses for the PMs were calculated. These results are presented in Fig.5.13. The excess loss of the PM in channel 9 was also measured in an independent way. This result is given in Fig.5.13 (red squares) as well for comparison. This loss curve is obtained by measuring the ASE power of the SOA in channel 9. The SOA is biased at $I_{\text{SOA}}=40\text{mA}$ and the fiber-coupled output ASE power is measured. When the reverse bias on the PM in channel 9 is increased, the measured ASE power reduces due to the absorption in the PM. The difference in the measured power level is interpreted as the excess loss of the PM section in presence of the reverse bias. This result shows that for operation of the PMs below 4V, the voltage dependent loss is described sufficiently accurate using Eq.5.19.

The measured parameters define the PM performance that is described Eq.5.17 in terms of the control voltage on the PM. The PM loss factor, α_{PM} in Eq.5.17, can then be calculated as

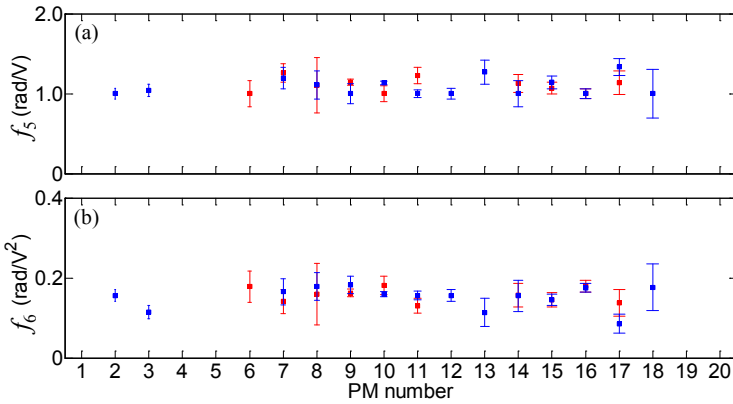


Fig.5.11. (a) Linear and (b) quadratic phase shift parameters with the 95% prediction confidence intervals. The red and blue colors indicate separate measurements. Measurement data for PMs in channels 1,4,5,19,20 are not available.

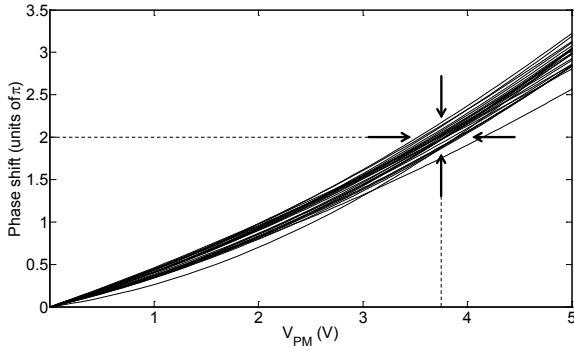


Fig.5.12. Measured phase tuning curves of the PMs. The required voltage for a 2π phase shift (double pass) is $\sim 3.7V$ on average. At this value of the bias voltage, the amount of phase shift for all the PMs is $2\pi \pm 0.25\pi$

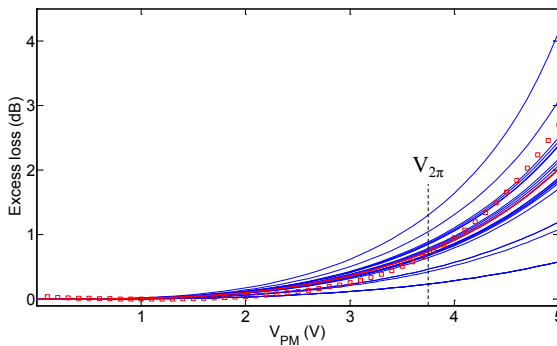


Fig.5.13. Voltage dependent loss of the PMs calculated based on the fitted parameters (solid blue). The calculated curve for channel 9 is indicated as a thick red line. The excess power loss of the same PM which is measured independently (red squares) is given for comparison.

$$\alpha_{\text{PM}} = \ln(I(V)) = \ln(1 - f_3 V_{\text{PM}}^3) \quad (5.21)$$

where \ln is the natural logarithm function. The phase shift, φ_{PM} in Eq.5.17, is directly linked to the fitted parameters (f_5 and f_6) through

$$\varphi_{\text{PM}} = f_5 V_{\text{PM}} + f_6 V_{\text{PM}}^2 \quad (5.22)$$

We note that the measured data for the PMs are obtained at different wavelengths within one FSR of the device. The fitted parameters for different PMs do not show a clear wavelength dependence over the limited range $\sim 1526\text{-}1532\text{nm}$. The PM parameters are in principle wavelength dependent for two reasons. The PM voltage changes the phase of the light by changing the optical path length through a change in refractive index. This gives a λ^{-1} dependency. The refractive index also changes with wavelength due to material dispersion and the effect of proximity to the band-gap wavelength of the MQW core. However the differences between the properties of the PMs appear larger than the wavelength dependence over the limited wavelength range.

To have an indication of the wavelength dependence of the phase tuning parameters, we present measurement results obtained with scanning the PM in channel 9 for three different wavelengths. These are three different orders of the AWG transmission spectrum that connect to channel 9. In these measurements the SOAs in the channels 8 and 9 are both biased. The PM voltage in channel 8 is kept at $V_{\text{PM}}=0\text{V}$. The same measurement and fitting method as described in the preceding paragraphs was used to find the PM parameters at different wavelengths. In this case, we have repeated the measurements at different values of SOA bias, i.e. $I_{\text{SOA}}=30\text{mA}$, 35mA and 40mA . This gives a set of 9 different measurements. The measured data are presented in Fig.5.14. The recorded data for each wavelength are indicated by a different color and the SOA bias values are given in the figure. The nine interference patterns for each wavelength presented in Fig.5.14 were fitted simultaneously to determine the PM parameters, at that wavelength, to the expressions given in Eq.5.18-Eq.5.20.

The PM parameters which govern the voltage dependent phase shift were measured at the three wavelengths. The voltage dependent phase shift can be expressed in terms of the voltage dependent change of the refractive index of the PM section according to

$$\Delta n = \frac{\varphi_{\text{PM}}}{2\pi} \frac{\lambda}{2L_{\text{PM}}} \quad (5.23)$$

in which $2L_{\text{PM}}$ is the double-pass length of the PM section. The calculated Δn versus the voltage is given in Fig.5.15. This information is used to model the phase modulators in the pulse shaper device as is discussed in chapter 6.

The term f_4 which appears in the relation between phase and voltage in Eq.5.20 is a constant phase term that is not included in the voltage dependent phase shift in Eq.5.22 which goes back in the mask function M . In our measurements, this term represents the phase difference between the arms of the Michelson interferometer when both PMs are biased at $V_{\text{PM}}=0$.

There are three main conclusions regarding the phase offset between the channels which follow from the plots of Fig.5.14. First, if a single plot with the interferograms at the three wavelengths is considered, we see that the phase offsets (at $V_{\text{PM}}=0$) are different for the different wavelengths. This means that the phase offset is wavelength dependent. Second, the phase offset also depends on the relative bias level of the SOAs. This can be

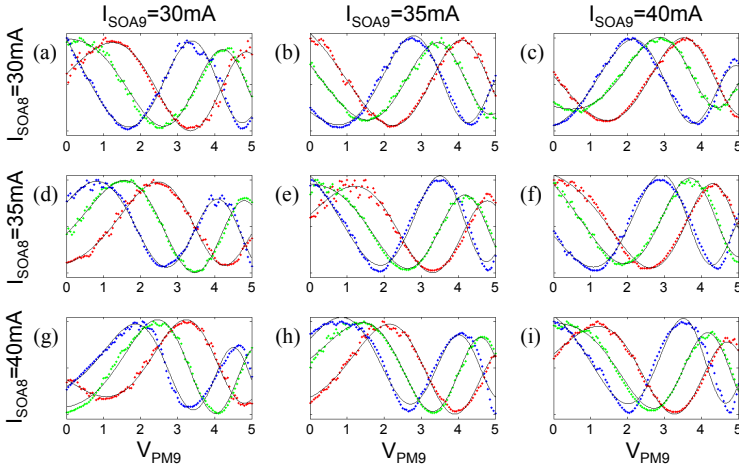


Fig.5.14. Measured interferograms (dots) with the device channels 8 and 9. Bias voltage value in channel 8 is kept constant at $V_{PM8}=0V$ and V_{PM9} is scanned. The fitted curves are shown as solid black lines. $\lambda=1551.7nm$ (red), $\lambda=1543.8nm$ (green) and $\lambda=1536.0nm$ (blue).

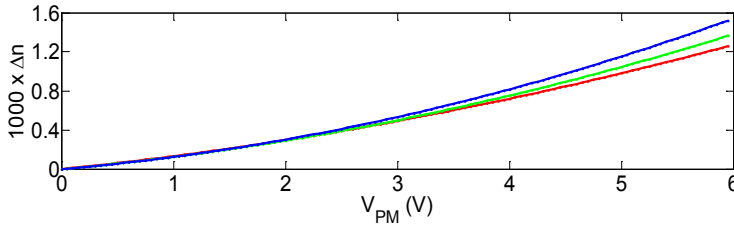


Fig.5.15. voltage dependent change of the refractive index calculated based on the measurement results given in Fig.5.14 at $\lambda=1551.7nm$ (red), $\lambda=1543.8nm$ (green) and $\lambda=1536.0nm$ (blue).

seen by considering the off-diagonal plots (Fig.5.14(b,c,d,f,g,h)) at each wavelength. This is a measure of the effect of the SOA on the phase of the signal in the channel.

The third conclusion is drawn by considering the diagonal plots, i.e. Fig.5.14(a,e,i). In this case, we observe that the phase offset remains the same when the SOA bias levels in the two arms are the same. This shows that the amount of induced phase change by an SOA bias change is, within our measurement accuracy, the same for both SOAs. The effect of SOA bias on the phase of the optical signal will be discussed in detail in the following subsection. In our calibration scheme, the phase offset between the channels appears as the difference in the phase of the frequency response of the channels. This is taken into account in the reference state, as described in section 3.1.

5.3.2.2. SOA: Optical gain and induced phase change

For the SOAs, the change from the reference point in optical gain and the change in phase as a function of injection current need to be determined. We define the relative gain, g_r , as

$$g_r = \frac{g}{g_{ref}} \quad (5.24)$$

where g is the optical gain at any bias condition, i.e. any value of I_{SOA} , and g_{ref} is the optical gain at the reference bias level. The change in optical gain can be measured in a straightforward way. The light from a single frequency continuous wave laser source is tuned to a particular device channel, is kept at a constant power level and is injected into the device via a circulator. The returning output power from the shaper is then measured as a function of the current in the SOA of the addressed channel. The ratio of the measured output power to the measured output power at the reference bias current is the value of g_r . The reference state is defined at $I_{SOA}=40\text{mA}$. The measured values for g_r as a function of current are given in Fig.5.16 for channels 8, 9 and 10. As can be seen, the gain cannot be increased much above the reference state. This is limited by reflections in the chip. The limits in gain due to unwanted reflections in a pulse shaper with reflective geometry are discussed in detail in section 2 of chapter 8. The minimum measurable relative gain is determined by the ASE from the amplifier and the total device losses. In Eq.5.16, the term g_{SOA} is equal to the square root of the relative gain.

It appeared that the amplifier behavior with respect to the relative gain was sufficiently uniform (better than 5% of the average above 35mA and within 20% overall) to have the same parameters for all amplifiers in the masking function. It can be concluded that useful range for the SOA bias current is 25 to 45mA.

As well as causing a change in optical gain, a change in injection current of the SOA affects the phase of the light in the channel. This effect is due to the change in carrier density with the changing injection current and the change of the temperature in the SOA. Since our pulse shaper is operated electrically in DC mode, we cannot separate between the two origins. It is possible to measure the overall effect of the SOA bias on the phase of the optical signal. This effect was evaluated by using the on-chip Michelson interferometer structure that was used to characterize the phase tuning performance of the PMs (see subsection 5.3.2.1). However, in this case the PM voltage is kept constant at $V_{PM}=0$ and the SOA current is scanned. The measured optical power then provides interference patterns according to phase changes induced by I_{SOA} . The interference patterns are then analyzed to obtain the phase difference between the arms versus the SOA bias current. For the 30-50mA range of applied current in Fig.5.17, the induced phase change is linear with the current and can be expressed as

$$\varphi_{SOA} = f_7 \times \Delta I_{SOA} \quad (5.25)$$

in which f_7 is the fit parameter which is determined to be 0.2704 ± 0.004 , ΔI_{SOA} is the

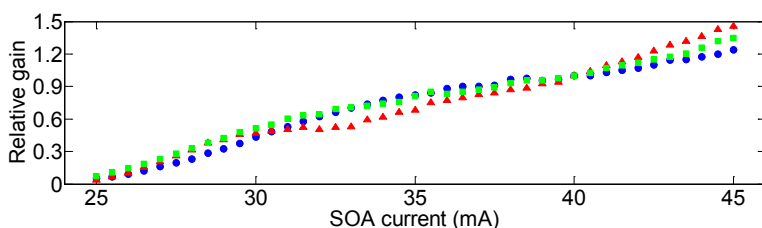


Fig.5.16. Relative gain measured with SOAs in the device channels 8 (green squares), 9 (blue circles) and 10 (red triangles).

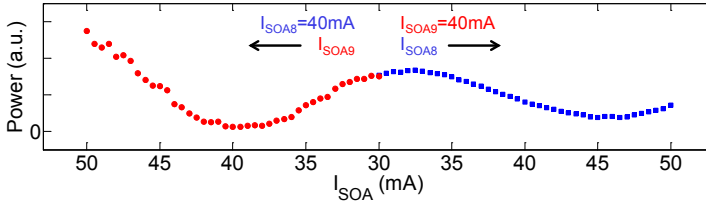


Fig.5.17. A typical interferogram which is used to measure the phase effect of the SOAs. In this measurement, device channels 8 (blue squares) and 9 (red circles) are biased together.

difference between the operating current of the SOA and I_{SOA} at the reference state, i.e. $I_{SOA}=40\text{mA}$. The term φ_{SOA} directly links to the function G that is given defined as Eq.5.16. This value was used for all the channels in the calibration.

5.4. Verification of the channel characterization method

In this section we round off the work on the calibration of the pulse shaper with two demonstrations. The first is a test of the interferometric method used to measure the reference states. The second demonstration shows that the pulse shaper indeed behaves as a linear system and that the system response is correctly predicted using the reference state and mask function.

5.4.1. Verification of the channel characterization method - SIMBA technique

We first verify the interferometric method which is used to measure the frequency response of the device. In this section, we show how the SIMBA (Spectral Interferometry using Minimum-phase Based Algorithm) method can be used to characterize a device channel. We then compare the result obtained with the SIMBA method and the one which is achieved by interferometric technique and show that the results, i.e. spectral amplitude and phase of the frequency response, match very well.

The SIMBA method [7] is a measurement technique which can be used for the complete characterization of optical pulses. The SIMBA method involves measuring the power spectrum of a sequence of optical pulses which consists of a dummy pulse and the target pulse, i.e. the optical pulse which is to be characterized. According to the theory behind the SIMBA method, if the dummy pulse is (close to) a minimum phase signal, the spectral amplitude and phase of the target pulse can be retrieved by merely measuring the power spectrum.

SIMBA is a powerful option to verify our calibration method since it is able to characterize the optical pulse which passes through the pulse shaper. Furthermore, it does not require a high optical power level and is able to operate the wavelengths of our interest. In our SIMBA setup, the optical pulse source is an FSL1010 fiber laser source which generates 150fs optical pulses at 80MHz repetition frequency. The central wavelength is around 1560nm. The optical pulse is sent through an optical circulator and a cleaved fiber tip is used to inject the pulses to the pulse shaper. A part of the signal is reflected at the tip of the fiber. This signal which is a replica of the short input pulse is the dummy (reference) pulse for SIMBA measurements. A part of the signal which is coupled to the chip passes through the operating channels and returns to the

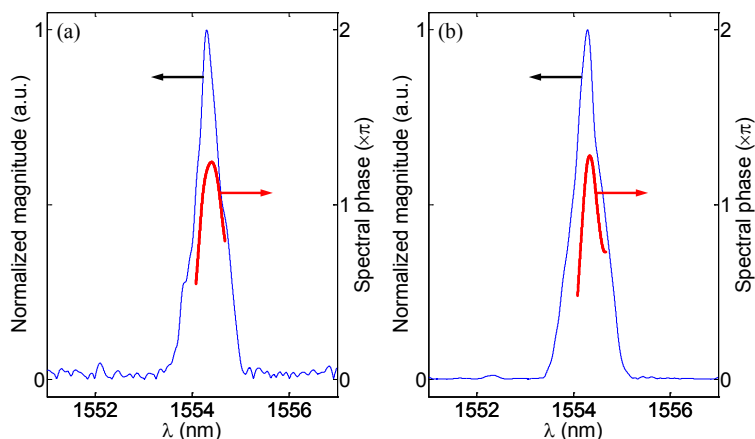


Fig.5.18. Complex frequency response (spectral amplitude and phase) of the device channel number 10, measured with (a) the SIMBA method, and (b) the interferometric method. The results are obtained at the reference state $I_{SOA}=40\text{mA}$, $V_{PM}=0\text{V}$.

I/O waveguide. This signal is the target pulse which characterizes the channel response. The sequence of the dummy and target pulses is then measured by an APEX high resolution (20MHz) optical spectrum analyzer to resolve spectral features, the interference between the pulses. The recorded spectrum is then analyzed by an iterative mathematical algorithm to retrieve spectral amplitude and phase of the target pulse.

The key point here lies in the fact that, if the input pulse has sufficiently short time duration such that it could be approximated by an impulse signal $\delta(t)$, the output pulse will, by definition, be the system impulse response $h(t)$. Therefore, by retrieving the amplitude and phase of the output signal we achieve the system frequency response. In our setup the input pulse is close to an impulse signal; hence, the target pulse approximates the frequency response of the channel.

We set the control signals in channel 10 at the reference state, i.e. $I_{SOA}=40\text{mA}$ and $V_{PM}=0\text{V}$. The measurement result obtained with the SIMBA method is given in Fig.5.18(a). The frequency response of the channel as measured with the interferometric method is given in Fig.5.18(b) for comparison. The spectral magnitude and the spectral phase of the channel match for both methods very well. This demonstrates that the measurement method that is presented in part 5.2.1 is reliable.

5.4.2. Demonstration of the control signal calibration

As a demonstration of our approach on how to control the pulse shaper we follow the steps below. For convenience, we have considered only channels 9, 10 and 11.

1- First we bias the SOA in the channels, one at a time, and measure the individual channel response at $I_{SOA}=40\text{mA}$ and $V_{PM}=0\text{V}$ using the interferometric method. This is defined as the channel response at the reference state.

2- Next, we bias the three channels together and measure the total response using the same method. The result is shown in Fig.5.19(a). Now we calculate the complex summation of the three channels at the reference state and compare it with the measured result of the three channels together. As indicated in Fig.5.19(a), we observe that the

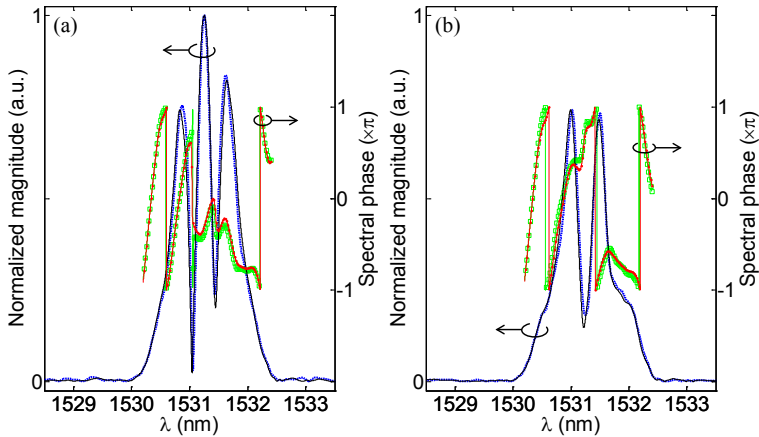


Fig.5.19. Normalized amplitude and spectral phase of the system response when the three device channels 9, 10 and 11 are considered. (a) The Measured and calculated amplitude and phase of the system response with the three device channels being switched on at the same time at $I_{SOA9,10,11}=40\text{mA}$ and $V_{PM9,10,11}=0\text{V}$. (b) The Measured and calculated system response with channels 9 and 11 at the reference state, $I_{SOA10}=40\text{mA}$ and $V_{PM10}=2.3\text{V}$. In this figure, the measured (calculated) amplitude is shown as the solid back (dashed blue) lines and the measured (calculated) spectral phase is shown with the red dot (green square) markers.

measured total response matches very well with the summation of individual channel responses. This verifies the assumption that the total channel response is a linear summation of individual channel responses.

3- Then we consider the effect of a control signal. For instance, we apply a reverse bias on the PM in channel 10 of $V_{PM10}=2.3\text{V}$. This corresponds to a π phase change in channel 10. We then put this phase change in the mask function and multiply it with the reference state response of channel 10 to calculate the response of channel 10 at this operating point (Eq.5.3). The total system response is again calculated by a summation of the channel responses (Eq.5.2). The calculated result is shown in Fig.5.19(b). The total system response with the channels 9 and 11 at the reference state and $V_{PM10}=2.3\text{V}$ is measured separately and given for comparison. The agreement between the measured and calculated results is clear and confirms the proposed calibration method.

References

- [1] M. Smit et al., "Generic foundry model for InP-based photonics," *IET Optoelectronics*, vol. 5, no. 5, p. 187, 2011.
- [2] TUEDOCS, "AWG100 8 Channel 100MHz Analog Waveform Generator." [Online] http://www.tuedacs.nl/Manual/TUEdACS/HTML_Manual/TUEdACS/AWG100/AWG100_dir_description.html.
- [3] X. J. M. Leijtens, B. Kuhlow, and M. K. Smit, "Arrayed Waveguide Gratings," in *Wavelength filters in fiber optics*, H. Venghau., Berlin: Springer, 2006, pp. 125–187.
- [4] M. Froggatt et al., "Optical frequency domain characterization (OFDC) of dispersion in optical fiber Bragg gratings," pp. 176–178, 1999.

- [5] B. J. Soller, D. K. Gifford, M. S. Wolfe, and M. E. Froggatt, "High resolution optical frequency domain reflectometry for characterization of components and assemblies," *Optics Express*, vol. 13, no. 2, p. 666, 2005.
- [6] E. D. Moore and R. R. McLeod, "Correction of sampling errors due to laser tuning rate fluctuations in swept-wavelength interferometry.," *Optics express*, vol. 16, no. 17, pp. 13139–49, Aug. 2008.
- [7] A. Ozcan, *Non-destructive optical characterization tools: spectral interferometry using minimum-phase functions*. VDM Verlag Dr. Mueller e.K., 2008, p. 272.

CHAPTER 6

Modeling Performance of the Integrated Pulse Shaper Device

We have devised a model to simulate the effect on an optical pulse which passes through our pulse-shaper device with its 20 channels at 50GHz spacing using the actual calibration data. The first goal of this modeling of the pulse shaper is to give insight into the performance of the integrated device and to simulate the effect of practical issues which disturb the pulse shaping performance. The second goal is to use the model to demonstrate how the required control signals can be calculated in order to achieve specific output pulse properties given an input pulse shape.

In this model we first focus on the group-of-line pulse shaping scheme. For this purpose, we consider only the phase control capabilities of the pulse shaper. Thus we do not consider amplitude control per channel and ignore any spectrally independent device loss. In particular, we investigate the effect of device dispersion. The group-of-lines scheme is relevant since the repetition frequency of our quantum dot mode-locked (ML) lasers is typically in the range of 5-20GHz which is lower than the resolution of the pulse shaper channels which is designed to be 50GHz. We show that dispersion within the channels is the actual limiting effect for pulse shaping. In case of our device, the channel dispersion is dominated by the dispersion of the AWG channel.

We then focus on the device operation in the line-by-line shaping scheme. In this case, we extend our model to incorporate amplitude shaping capability for each channel as well. We give some practical examples and show that the device dispersion is not an issue for operation of the device in the line-by-line shaping scheme.

6.1. Description of the pulse shaper model

Since we are dealing with a Fourier transform (FT) pulse shaper, calculations are most conveniently carried out in the frequency domain. In this case, the effect of device components on the input optical pulse is to multiply the frequency domain electric field by the transfer function of each component. In the model, we first define the spectral amplitudes and phases of the input signal. We also bring in the device parameters such as waveguide length, channel width, PM tuning characteristics, etc. We then specify a desired output pulse shape according to which the control signals (voltage values) on the PMs have to be calculated for a “best” match.

6.1.1. Input and output pulse shapes

The model assumes an ideal ML laser as an input source. In the frequency domain, the input spectrum to the shaper thus consists of a number of lines, i.e. frequency components that are equally spaced in frequency and with a fixed phase relationship between them. The input signal described by its electric field envelope in time domain is expressed as

$$e_{in}(t) = \sum_{k=1}^K a_k \cdot e^{j[\Delta\omega(k-k_c)t + \varphi_k]} \quad (6.1)$$

where t is the time, e_{in} represents the electric field in the time domain, a_k is the spectral amplitude, k is the corresponding line number ($k=0\dots K$) and K is the total number of lines. $\Delta\omega=2\pi f_{rep}$ with f_{rep} being the frequency spacing between the spectral lines which equals the repetition frequency of the source, k_c is the line number at the center of the spectrum and φ_k is the phase of the line number k . So the input field is described in terms of the (real valued) amplitudes a_k and the phases φ_k . For convenience and without loss of generality, we set the amplitudes of the spectral lines to follow a Gaussian profile with the central line located at wavelength $\lambda=1550\text{nm}$. Furthermore, the spectral phase of the lines can be defined arbitrarily, e.g. to express a chirped input.

Since the input pulses are typically generated by a ML laser of some sort, the spectral phase values of the spectral lines will not be random, but the closely spaced spectral lines will typically have only a small slowly varying difference in the spectral phase. It is practical to describe the spectral input phases in a polynomial using only a few terms. The phase φ_k of each spectral component in the input can be described as

$$\varphi_k = \theta_0 + \frac{\theta_1}{1!} \cdot (k - k_c) \cdot \Delta\omega + \frac{\theta_2}{2!} \cdot (k - k_c)^2 \cdot \Delta\omega^2 + \frac{\theta_3}{3!} \cdot (k - k_c)^3 \cdot \Delta\omega^3 + \dots \quad (6.2)$$

In Eq.6.2, the given terms $\theta_0, \theta_1, \theta_2$, etc. are constant values which describe the spectral phase in terms that are in practice convenient to link to the optical properties of phase offset, group delay, group velocity dispersion, etc. respectively.

The effect of the pulse shaper on the input pulse can be described by the effect it has on the amplitudes and phases of the input spectral lines. This will define the output pulse as

$$e_{out}(t) = \sum_{k=1}^K H_k \cdot a_k \cdot e^{j[\Delta\omega(k-k_c)t + \varphi_k]} \quad (6.3)$$

in which H_k is a complex number that is given by

$$H_k = \sum_{i=1}^N HR_{i,k} \cdot M_{i,k} \quad (6.4)$$

In Eq.6.4, i the device channel number, N is the total number of the channels, HR is the effect of the device in the reference state of the control signals, and $M_{i,k}$ is the mask function which includes the effect of control signals. The term $HR_{i,k} \cdot M_{i,k}$ gives the effect of the device on line k which passes through channel i . The summation in Eq.6.4 then accounts for the total effect of all device channels. The output pulse, as given in Eq.6.3, can be expressed as

$$e_{out}(t) = \sum_{k=1}^K b_k \cdot e^{j[\Delta\omega(k-k_c)t + \psi_k]} \quad (6.5)$$

where $b_k = a_k \cdot |H_k|$ and $\psi_k = \varphi_k + \arg(H_k)$.

Since our model involves a linear pulse shaper, the spectral position of the lines (line numbers) in the output pulse is given by the input pulse. The effect of the device on the spectral lines is discussed in the next part.

6.1.2. Device model components

The pulse shaper device is modeled as a set of 20 parallel spectral filters which are connected to waveguide sections and phase modulators. The spectral filters have a Gaussian shape and represent the device channel spectral response. The filters are arranged with a spacing of 50GHz and are used as a simple model for the 20 channel arrayed waveguide grating (AWG) on the chip.

Each device channel is modeled by a ~15mm-long passive waveguide. The phase change due to optical path length of a waveguide is calculated by

$$\Delta\varphi = \frac{n_{eff}\omega}{c} L \quad (6.6)$$

where n_{eff} is the effective index, c is speed of the light in vacuum and L is the length of the waveguide section.

Device dispersion is an important issue which distinguishes the integrated pulse shaper from its free-space bulk counterparts. In general, the integrated device, unlike the FT-configuration pulse shaper, is not dispersion free. The two main contributions to the device dispersion are the effect of passive waveguide sections and that of the AWG filter. Waveguide dispersion arises from the material dispersion (wavelength-dependent refractive index) and the effect of waveguide geometry. Waveguide dispersion is inherent to integrated devices, whereas the AWG is theoretically a linear phase filter which is dispersion-less in the passband. In practice however, design inaccuracies (such as the paraxial approximation) and/or fabrication variations lead to imaging errors in the AWG [1], [2]. These affect the actual passband shape and cause dispersion within a channel of the AWG.

Device dispersion is not desirable, particularly for the group-of-lines pulse shaping scheme. In this scheme, the constituent spectral lines of the laser source are not resolved individually by the AWG and each filtered portion of the spectrum undergoes a single phase change after passing through the device channel. Therefore, the spectral phase profile within a single group of lines cannot be fully controlled. This also means that the device channel dispersion cannot be compensated.

The waveguide dispersion is taken into account in the model through the wavelength dependence of the group index. The InP pulse shaper device incorporates deeply etched passive waveguides. To have a value for the dispersion we have simulated the waveguide structure using the PhoeniX FieldDesigner mode solver. The waveguide geometry and material indices used are taken from [3]. The group index, n_g , is then calculated according to

$$n_g(\lambda) = n_{eff}(\lambda) - \lambda \frac{dn_{eff}(\lambda)}{d\lambda} \quad (6.7)$$

in which λ is the wavelength. The result is given in Fig.6.1 for the wavelength range of $\lambda=1530-1560\text{nm}$. Over this range the group index of the passive waveguide at each line number, k , is approximated as a linear function given by

$$n_g = n_0 + n_1(k - k_c)\Delta\omega \quad (6.8)$$

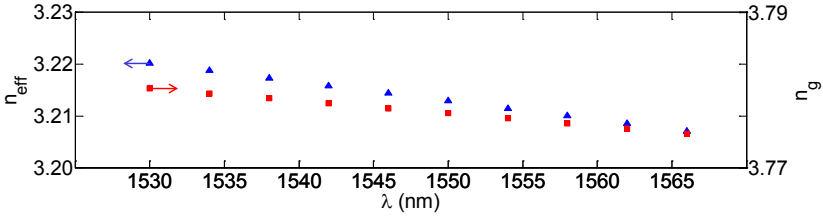


Fig.6.1. Effective index (blue triangles, left axis) and group index (red squares, right axis) of the waveguide structures, calculated with the Phoenix FieldDesigner.

in which $n_0=3.777$, $n_1=6\times 10^{-7}$ in units of per Grad/s and following Eq.6.1, k_c is the line number at the center of the spectrum.

Our experimental results (given in chapter 5) show that the AWG gives the main contribution to the device dispersion due to imaging errors in the AWG. In case of our device, the AWG channel dispersion is dominated by defocusing of the star coupler [2]. We include the effect of AWG channel dispersion in our model by defining a spectral phase profile over the passband of individual Gaussian filters.

Each device channel includes a 1mm-long phase modulator (PM). The phase shift in each PM is controlled by a voltage signal that changes the effective index of the PM section. The voltage dependent group index of the PM sections is given by

$$n_{\text{PM}} = n_g + \eta_1 V_{\text{PM}} + \eta_2 V_{\text{PM}}^2 \quad (6.9)$$

in which n_g is the waveguide group index that is given in Eq.6.7 and V_{PM} is the control signal on the PM. The values $\eta_1=1.16\times 10^{-4} \text{ V}^{-1}$ and $\eta_2=3.59\times 10^{-5} \text{ V}^{-2}$ are used to describe the voltage dependence of all PMs. The linear and quadratic terms (η_1 and η_2) are the same for the effective and group indices. The index change terms are calculated based on the measurement results for the wavelength around 1550nm which was presented in section 3 of chapter 5.

In the model the effect of optical amplifiers in the channels for amplitude control can be included by a simple multiplication of $M_{i,k}$ for a single channel by a (real valued) gain factor for all values of k . This is used only in the last example on line-by-line shaping. The passive losses and backscattering in the waveguides are not included in the model.

6.1.3. Calculation of control signals

Our approach to describe the calibration of the pulse shaper device is to express the total transfer function of the device as a linear summation of the frequency response of the individual channels. The frequency response of each channel is expressed in terms of a transfer function at the reference state of the control signals, and mask function which consider the effect of control signals. In this approach, the mask function was defined to account for the effect of the control signals. The experimental implementation of this approach was explained in detail in chapter 5.

In our model, the desired output pulse is specified, and is described in terms of the amplitude and phase of the spectral lines. The desired output pulse in time domain can be expressed as

$$e_{\text{des}}(t) = \sum_{k=1}^K B_k \cdot e^{j[\Delta\omega(k-k_c)t + \Psi_k]} \quad (6.10)$$

where B_k and Ψ_k are the amplitude and phase of each line. Mathematically, the problem of determining optimal control settings is to calculate the required control signals such that the output pulse, as given by Eq.6.5, approximates the particular desired pulse shape, as given by Eq.6.10. Not every output pulse shape can be constructed with a given input and the capabilities of our pulse shaper. Finding the optimal control signals is therefore essentially a fitting problem. In general, the complexity of such a fitting problem depends on the number of spectral lines, the number of device channels, the mathematical complexity of the relationship which describes the connection between the amplitude/phase change and the control signals, etc. Furthermore, the fit criterion depends on the application requirements.

In case of a phase-only pulse shaper, we have minimized the difference between the calculated output phase values and the specified output phase profile. The voltage signals on the PMs are then the fit parameters in the minimization. We have used the 'lsqcurvefit' non-linear minimization routine of MATLAB to find the required signals.

6.2. Group-of-lines shaping: 10GHz input

To demonstrate the effect of the waveguide and AWG dispersion in the group-of-lines pulse shaping scheme we are presenting a number of simulations. We assume the repetition frequency of the input source is $f_{\text{rep}} \sim 10\text{GHz}$. We set the total number of lines to be $K=201$ and a FWHM spectral bandwidth of 83 lines. For modeling purposes, the bandwidth is chosen such that 16 device channels cover the FWHM of the input spectrum. In the following simulations, the cyclic nature of the AWG is not taken into account. In this section we consider a phase-only system. In the group-of-lines scheme, it is not possible to manipulate the phase of spectral lines individually. We define a relatively simple and straight forward pulse shaping design task as a start. It should be noted that the total phase of spectral lines in each channel is affected by neighboring channels as well due to the overlap between the channels.

In the group-of-lines scheme, the signal within each device channel is time variant. This is due to the presence of several spectral lines in each channel. In our model, we assume the possible nonlinear effects from e.g. an SOA which change the spectral content in the channel are negligible. This assumption is justified in practice by keeping the optical power levels below the onset of nonlinear effects. This is not a particularly demanding requirement because the power into a single channel is a fraction of the optical input power to the device. Also the bandwidth of the time dependent optical signal in a channel is limited by the width of the channel which in turn limits any relevant non-linear response.

In the following, we start with the simplest model and develop it in three steps. We first consider the effect of waveguide dispersion. Then, we consider the effect of channel length variation, and at last include the effect of AWG channel dispersion. In each step, we assume the input signal is a transform limited Gaussian pulse which is given in Fig.6.2(a). The input pulse has a Gaussian spectrum with equal phase for each line.

6.2.1. Waveguide dispersion

We assume the device channels are equal in length and that only waveguide dispersion is present. The AWG is assumed to be dispersion-less. This case represents an ideal integrated pulse shaper. We then specify the output pulse to have a flat phase as well.

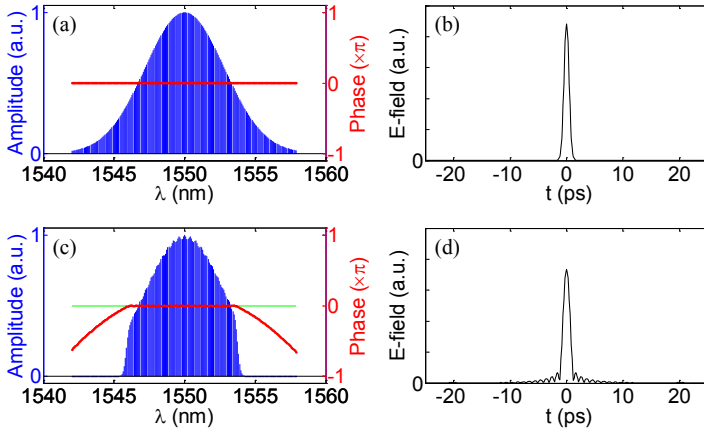


Fig.6.2. (a) Spectral amplitude (blue, left axis) and phase (red dots, right axis) of the input pulse. (b) The input electric field in time domain. (c) Spectral amplitude (blue, left axis) and phase (red dots, right axis) of the pulse at the output of the pulse shaper device. The control signals are optimized to achieve the target phase profile (green). (d) The output electric field in time domain.

This means that the control signals are calculated and the pulse shaper is configured to compensate its own dispersion. Fig.6.2(b) depicts the corresponding simulation result. The input spectrum is chosen to be wider than the bandwidth of the pulse shaper. Because of this the spectrum of the light at the output of the pulse shaper has a smaller bandwidth as compared with the input pulse. Consequently the output pulse has lower power and is longer. The output spectrum has a small ($<0.2\text{dB}$) modulation due to filtering effect of the pulse shaper channels. The spectral phase of the output is relatively flat around 0. These phase variations translate to a higher pulse pedestal in time domain. Fig.6.2 shows that the waveguide dispersion in our device can be effectively compensated. The deviations in the phase of the spectral lines from the targeted value are less than 0.002rad . The device operation in this case is comparable to conventional pulse shapers which are dispersionless.

In our design, we have included passive waveguide sections to compensate for (physical) path length differences as much as possible. In practice, differences in optical channel length are unavoidable due to design inaccuracies (straight vs curved waveguides, etc.) or processing and epitaxial layer growth variations. For a properly designed device, optical path length differences are mostly a result of waveguide bends with different radii, etch depth variations and wafer uniformities. Such variations are essentially random. Using our model we studied these effects by including random deviations in the lengths of the 20 device channels. We run simulations on devices with channel length variations that are randomly distributed between $+\Delta L$ and $-\Delta L$. The average channel length is thus kept constant at $\sim 3\text{cm}$ (in double-pass). A series of simulations was done in which the value of ΔL was increased from 0 to $200\mu\text{m}$. In each simulation there is an optimization to a flat output phase profile, similar to what was described above. Then for each of the simulation results we record the peak power of the output pulse and the total energy in the output of the pulse shaper which falls in between the pulses and outside the -10dB width of the peaks. The results are given in Fig.6.3.

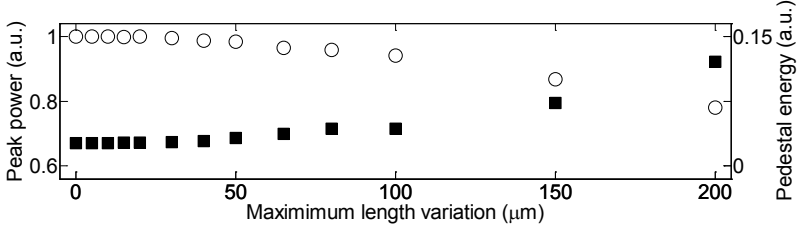


Fig.6.3. Relative peak power (open circles, left axis) and relative pedestal energy (squares, right axis) versus the maximum value of random channel length variations.

The peak power is normalized to the peak power level of the output pulse when there is no length variation $\Delta L=0$. From Fig.6.3 we can see that $\pm 50\mu\text{m}$ maximum length variation reduces the achievable peak power by less than 2%. The pedestal energy in this case is $\sim 3\%$. We have defined the pedestal energy as the ratio of the energy which is not bound within the -10dB width of the pulse to the total energy of the pulse. For such a length variation, the variation of the optimized spectral phases of the output signal (using the PMs) is within 0.03π . It is not difficult to realize a $\pm 50\mu\text{m}$ path length equalization on chip.

6.2.2. AWG channel dispersion

As mentioned before, in the group-of-lines scheme, the actual limiting factor for pulse shaping is that of the phase profile within a group of lines. In this respect, the device channel dispersion is the most perturbing parameter. In our integrated device, the AWG is responsible for a major part of the channel dispersion. This is due to AWG imaging errors (mainly related to defocus of the star coupler) and amplitude/phase errors in the arrayed waveguides. Here we consider the effect of the AWG channel dispersion by including a phase profile over the passband of the spectral filters in our model. The parameters used for modeling the device are based on our measurements of the pulse shaper. We express the phase profile (Φ) over each device channel as

$$\Phi_{i,k} = \Phi_{0i} - \frac{2\pi}{\Delta^2}(k - k_i)^2 \quad (6.11)$$

in which k is the spectral line number, i is the number of the channel, k_i is the line number at the center of the of the device channel, Φ_{0i} is the phase at the central line of the current channel, and Δ defines the phase profile. The phase offset was implemented in the model set for the different channels at a random value between 0 and 2π since in real devices it is in practice also random. We assume the device channels have a similar dispersion and set $\Delta=100$ according to the measurement results presented in chapter 5. We have included a $\Delta L=\pm 10\mu\text{m}$ random variation of the (physical) length of the channels as a realistic estimate.

We first take an input that is transform limited. For pulse shaping, it is essential that the device is able to compensate its dispersion. Therefore, we specify the output pulse to have a flat phase profile as well. The optimized output pulse achieved is given in Fig.6.4.

Fig.6.4 shows that the phase offsets (Φ_0) between the centre lines in the channels are indeed compensated. But the full spectral phase does not follow the desired profile entirely due to the channel dispersion. The spectral amplitude is also modulated due to

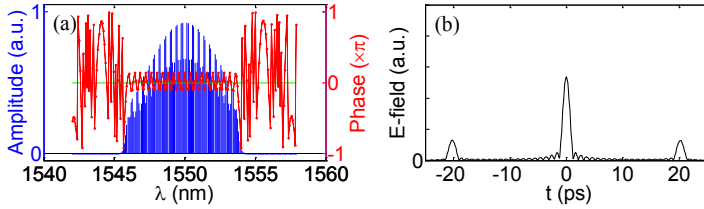


Fig.6.4. (a) Spectral amplitude (blue, left axis) and phase (red dots, right axis) of the output pulse. The control signals are optimized to achieve the target phase profile (green). The input pulse is a transform limited Gaussian pulse as given in Fig.6.2(a). (b) The output electric field in time domain.

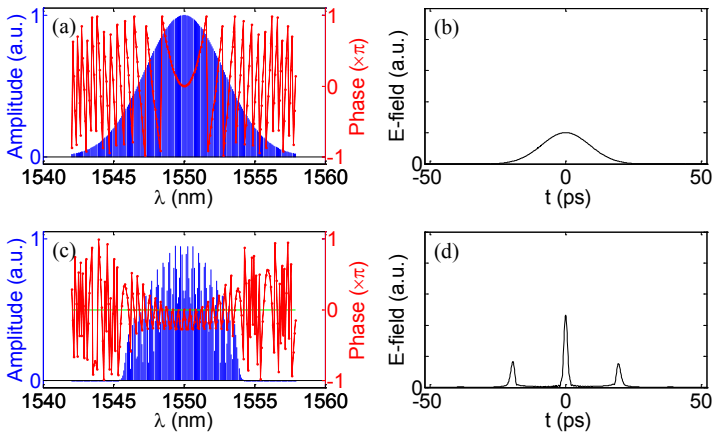


Fig.6.5. (a) Spectral amplitude and phase of the input pulse which has a $\theta_2=4\text{ps}^2$ quadratic phase profile. (b) The input electric field in time domain. (c) Spectral amplitude and phase of the pulse at the output of the pulse shaper device. The control signals are optimized to achieve the target phase profile (green). (d) The output electric field in time domain.

interference between the lines passing through the neighboring channels. The amplitude modulation of the spectrum gives rise to the appearance of satellite pulses in the time domain. Satellite pulses appear at $t=20\text{ps}$ which corresponds to the channel spacing of the device, i.e. 50GHz. The results show that the channel dispersion is dominated by the dispersion in the AWG.

We conclude this section by giving an indication of the capability of the integrated device for pulse compression when it is used with our quantum dot lasers. The QD lasers, presented in chapter 2, generate highly chirped pulses with dispersion values in the order of $D=4\text{-}20\text{ps/nm}$ [4], [5]. For reference, the dispersion of a 1km-long single mode fiber SMF-28 is $\sim 17\text{ps/nm}$ at $\lambda=1550\text{nm}$. The dispersion in the QD laser output is modeled by using the quadratic spectral phase term in Eq.6.2, in our model. In order to compress the input pulses, we calculate the control signals such that the phase profile of the pulses is as flat as possible at the output. The simulation results for three typical values of chirped input and a repetition frequency of 10GHz are given in Fig.6.5-7.

In Fig.6.5 the input pulse has a $\theta_2=4\text{ps}^2$ quadratic phase profile (corresponding to a $\sim 3\text{ps/nm}$ dispersion). The input pulse is broad, it has a time duration of 20.7ps FWHM.

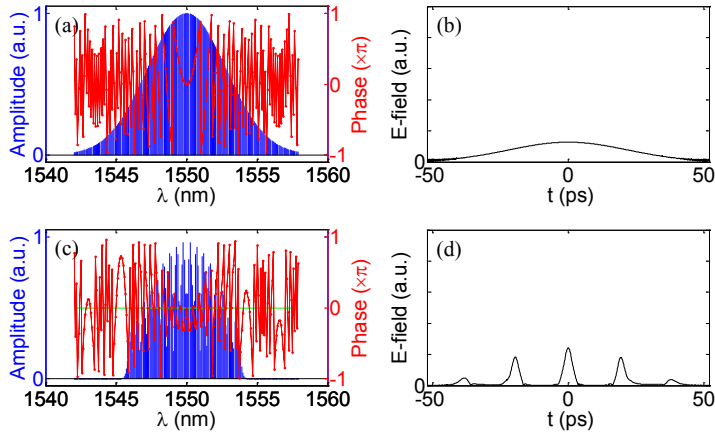


Fig.6.6. (a) Spectral amplitude and phase of the input pulse which has a $\theta_2=10\text{ps}^2$ quadratic phase profile. (b) The input electric field in time domain. (c) Spectral amplitude and phase of the pulse at the output of the pulse shaper device. The control signals are optimized to achieve the target phase profile (green). (d) The output electric field in time domain.

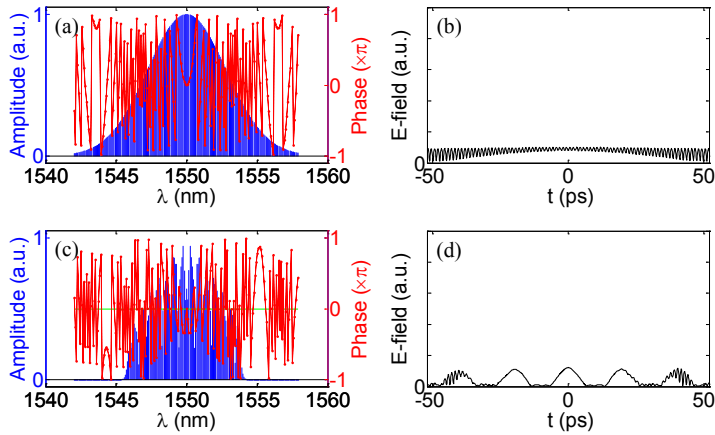


Fig.6.7. (a) Spectral amplitude and phase of the input pulse which has a $\theta_2=20\text{ps}^2$ quadratic phase profile. (b) The input electric field in time domain. (c) Spectral amplitude and phase of the pulse at the output of the pulse shaper device. The control signals are optimized to achieve the target phase profile (green). (d) The output electric field in time domain.

After passing through the device, the output pulse is compressed to $\sim 1.7\text{ps}$ FWHM. However, the spectrum is modulated and satellite pulses appear in the time domain. The duration of output pulse is comparable to that of the result given in Fig.6.3 which is obtained with a transform limited input pulse.

In Fig.6.6, the input pulse is assumed to have a $\theta_2=10\text{ps}^2$ quadratic phase profile, i.e. $\sim 7.8\text{ps/nm}$ dispersion. In the time domain, the pulse is very broad and extends over almost the whole period of the pulse train. In this case, the output pulse train includes multiple peaks within one 100ps period. In Fig.6.7, the input has a $\theta_2=20\text{ps}^2$ quadratic

phase profile, i.e. $\sim 15.6\text{ps/nm}$ dispersion. In this case, the input pulse is so highly chirped that no pulse structure is visible in time domain. The device is clearly not able to compensate for the spectral chirp. The residual chirp on the spectrum is a result of the channel dispersion which is the fundamental limit of the group-of-lines pulse shaping.

6.3. Line-by-line shaping: 50GHz input

So far we developed a phase-only device model to consider the practical effects which influence the performance of the integrated device in the group-of-lines pulse shaping scheme. We have shown that the most perturbing effect for the pulse shaper device is the channel dispersion. In this section we investigate the performance of the device in the line-by-line shaping scheme.

When the repetition frequency of the input laser signal matches the channel spacing of the pulse shaper, it is possible to manipulate all the spectral lines individually. In the line-by-line pulse shaping scheme, the fitting problem to calculate the required control signals (as described in section 6.1.3) reduces to a set of independent and consistent linear equations.

In the line-by-line scheme, if the resolution of the spectral filters is sufficiently high to select a single line per channel and reject the neighboring lines, the spectral lines can be controlled independently. Otherwise, the effect of overlap between the channels will influence the control signals for any specified pulse shape. In such a system, the device dispersion can be fully compensated. The practical limit of a phase-only system, such as the one which was used in the previous section, is the overlap between the channels. This leads to self interference of spectral lines which pass through multiple channels and hence causes a modulation over the spectral amplitude, which is not desirable.

The channel width in our device is designed to be 50GHz. In practice, due to phase errors in the waveguide array a measured FWHM of $\sim 60\text{-}65\text{GHz}$ is achieved. In order to show the effect of channel width and overlap between the channels, we give the following example. This is a practical situation of pulse compression, where the input pulse is highly chirped. We assume the input pulse has a $\theta_2=25\text{ps}^2$ quadratic phase profile. This corresponds to more than 20ps/nm group velocity dispersion which is the highest dispersion we have measured from our quantum dot ML lasers. The parameters used for modeling the device are as described in section 6.2.2. We now assume the laser source has a repetition frequency $f_{\text{rep}}=50\text{GHz}$ which matches the channel spacing of the integrated device.

The input pulse is presented in Fig.6.8(a,b). In the time domain, no clear pulse structure is visible due to the high chirp. To illustrate the effect of overlapping channels we first study the compression with a pulse shaper that has a channel width of 40GHz FWHM. This means the channels are effectively decoupled and the overlap between the channels is negligible. In this case, it is possible to fully compensate the chirp, flatten the phase profile and compress the signal to a transform limited pulse. The result is given in Fig.6.8(c,d). The amplitude spectrum over the device bandwidth ($\lambda=1546\text{-}1554\text{nm}$) is similar to that of the input spectrum. The amplitude spectrum of the output pulse has truncated tails due to the device bandwidth. This leads to relatively high signal oscillations in between the pulses in the time domain. This can be seen in Fig.6.8(d).

Next we set the channel width to 65GHz, the measured width of AWG channels. Again we calculate the required bias values of PMs such that the spectral chirp of the input

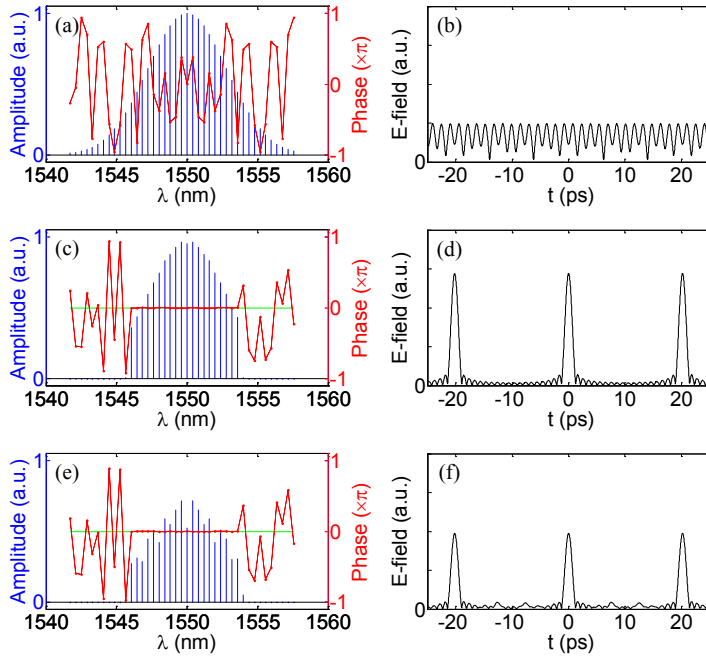


Fig.6.8. (a) Spectral amplitude and phase of the input pulse which has a $\theta_2=25\text{ps}^2$ quadratic phase profile. (b) The input electric field in time domain. Spectral amplitude and phase of the pulse at the output of the pulse shaper device with a channel width of (c) 40GHz and (e) 65GHz are given. The target phase profile (green) is given as well. (d,f) The output electric field in time domain.

pulse is compensated and the pulse is compressed. It is seen from Fig.6.8(e) that the spectral phase of the output pulse is flat, as expected. However, phase shaping affects the spectral amplitude as well due to the channel overlap. The amplitude modulation over the spectrum is observed in Fig.6.8(e). In the time domain, the pulse is clearly compressed, but has somewhat lower power and shows an increased background energy level as compared to the result given in Fig.6.8(d).

6.3.1. Phase and amplitude shaping

As shown above, the overlap between the device channels disturbs the amplitude spectrum in a phase-only pulse shaper. In order to overcome this effect, the device should provide the ability to manipulate the spectral amplitude besides the phase shaping capability. In the following simulations, we extended our device model to incorporate the amplitude control capability. A controllable optical gain is included in each device channel. Therefore, for any specified pulse shape, a set of 40 (phase and amplitude) equations are solved to find the required control signals on the 20 channels. To demonstrate the added advantage of the phase/amplitude pulse shaper, we repeat the case of pulse compression with the highly chirped input pulse which was given in Fig.6.8(a,b). Again, we specify the output pulse to have a flat phase profile. The amplitude spectrum can be shaped at will. In Fig.6.9 two examples of possible spectrum

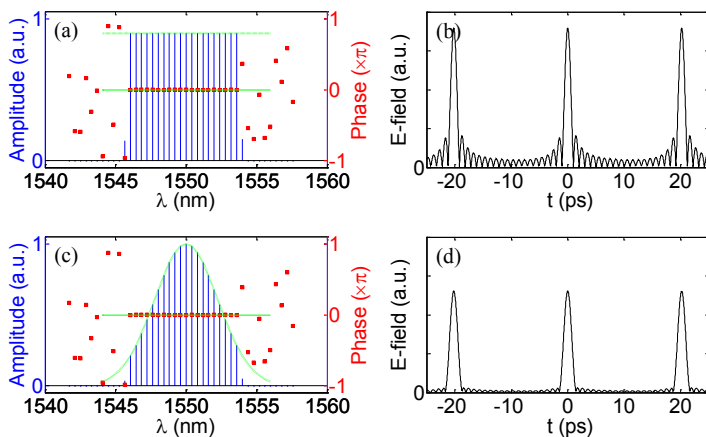


Fig.6.9. Spectral amplitude (blue) and phase (red) of the pulse at the output of the pulse shaper device with amplitude and phase shaping capability. The target shape is (a) flat spectral amplitude (dashed green) and flat phase profile (solid green) and (b) Gaussian spectral amplitude and flat phase profile. The input pulse has a $\theta_2=25\text{ps}^2$ quadratic phase profile as given in Fig.6.8(a). The channel width is 65GHz.

shapes that can be achieved using amplitude control are presented. The first spectral shape has near equal spectral amplitudes for all the lines at the output. This gives rise to sinc-like pulses in the time domain. The second spectral shape is a Gaussian shaped spectrum which leads to Gaussian shaped pulses in the time domain. In both cases a perfectly flat spectral phase is achieved.

References

- [1] A. Klekamp and R. Münzner, "Calculation of imaging errors of awg," *Journal of Lightwave Technology*, vol. 21, no. 9, pp. 1978–1986, Sep. 2003.
- [2] A. Klekamp and R. Münzner, "Imaging errors in arrayed waveguide gratings," *Optical and Quantum Electronics*, vol. 35, no. 4/5, pp. 333–345, Mar. 2003.
- [3] N. Whitbread, A. Ward, I. Knight, P. Williams, and N. Grote, "NMP Framework 7 programme: CP-TP 228839-2 EuroPIC Deliverable Report (WP4, D4.1): Initial definition of building blocks, process features and test structures of the generic process."
- [4] M. S. Tahvili, L. Du, M. J. R. Heck, R. Nötzel, M. K. Smit, and E. A. J. M. Bente, "Dual-wavelength passive and hybrid mode-locking of 3, 4.5 and 10 GHz InAs/InP(100) quantum dot lasers," *Optics Express*, vol. 20, no. 7, p. 8117, Mar. 2012.
- [5] M. J. R. Heck et al., "Analysis of hybrid mode-locking of two-section quantum dot lasers operating at 1.5 microm.," *Optics express*, vol. 17, no. 20, pp. 18063–75, Sep. 2009.

CHAPTER 7

Demonstration of Chirp Compensation for Optical Pulse Compression

We demonstrate dispersion compensation for highly chirped optical pulses with an ultracompact optical pulse shaper. The device integrates a 20-channel arrayed waveguide grating with 20 phase modulators and 20 SOAs on a single chip of $6 \times 6 \text{ mm}^2$. The chip has been realized in an InP-based generic photonic foundry process which enables a significant reduction in design effort using standardized building blocks.

7.1. Introduction

The concept of optical pulse shaping is an active subject of research which has significant applications in ultrafast optics [1], high speed optical communications [2] and coherent anti-stokes Raman scattering (CARS) microscopy [3]. In recent years, several pulse shaping techniques are adopted and different technologies are exploited to build laser systems which enable generation of arbitrarily yet specifically shaped optical pulses. A commonly used method is the so-called Fourier transform optical pulse shaping technique. In this approach, a spectrally dispersive element is used to decompose the incident optical pulse into its constituent spectral components. The phase and amplitude of the spectral components are then controlled by a spatial mask which is patterned according to the desired synthesized pulse shape. An optical grating is then used to combine the spectral components to form the shaped pulse.

Photonic integration technology is capable of providing the required functionalities for building such complex systems on an optical chip. This offers the benefits of compactness, cost effectiveness and possibility of further integration with semiconductor laser sources. In this letter, we present fabrication and characterization of a monolithically integrated optical pulse shaper. Chip fabrication has been carried out in a standardized generic photonic integration platform. A key capability of this platform is the active-passive integration scheme which allows direct integration of active components such as semiconductor optical amplifiers (SOAs) and photo detectors, with passive elements such as waveguides, arrayed waveguide gratings (AWGs) and phase modulators on a single photonic chip.

In order to demonstrate the functionality of the pulse shaper chip, the device is tested using a mode-locked (ML) quantum dash laser diode which generates heavily chirped

optical pulses. By optimizing the control signals on the integrated pulse shaper, we were able to compress the optical pulses and obtain a nearly flat chirp profile.

7.2. Design and fabrication

7.2.1 Generic integration technology

In the generic photonic integration approach [4], a set of components are defined as building blocks. The building blocks provide basic optical functions such as light transmission, phase modulation and amplitude manipulation. A wide range of functionalities may then be realized by combining the standardized building blocks to make complex photonic circuits. The integrated pulse shaper presented in this paper is fabricated in a multi-project foundry run in which multiple designs, aimed for different applications, are combined together and processed in a single fabrication procedure. This will significantly reduce the fabrication costs and design efforts involved. Some specifications of basic building blocks which are used to design the current photonic chip are summarized in Table I.

7.2.2 Device design and characterization

The pulse shaper device is designed with a reflective geometry. The light from the optical pulse source, i.e. a ML laser, is injected into the pulse shaper chip via an anti-reflection (AR) coated facet. The pulsed signal passes through an AWG which decomposes the light into its spectral components. Each component passes through electro-optic (EO) phase modulators (PMs) and SOAs and is then reflected back from a facet with a high-reflection (~95%) coating. The PMs and SOAs are used to manipulate the spectral phase and amplitude of the components in order to achieve the desired pulse shape. The spectral components are then recombined in the AWG and return through the input/output (I/O) waveguide. The two directions are separated by a circulator outside the chip. Fig.7.1 shows a microscope image of the realized chip.

An integrated pulse shaper in transmission mode, in which two separate AWGs are used for demultiplexing and multiplexing the light signal, does not require an optical circulator; however, proper operation of a device with a pair of AWGs, requires perfectly matched transmission spectra of the two AWGs. This is in practice challenging, considering the surface area of the device, wafer nonuniformities and fabrication imperfections. AWG-pair devices demand a tolerant design and require a

TABLE I
BUILDING BLOCKS AND BASIC COMPONENTS

Element	Specification
Passive waveguide	width=1.5 μ m, minimum bending radius=150 μ m, total length~ 9.2mm, deeply etched (5-6dB/cm loss)
AWG	size=1 \times 3.5 mm ² , FSR=8nm (~1THz), 20 channels, 50GHz spacing
EO PM	width=1.2 μ m, length=1mm, V_{π} =3.6-4V, orientation parallel to the wafer major flat
SOA	width=1.9 μ m, length=750 μ m, shallowly etched, orientation perpendicular to the wafer major flat
Transition elements	shallow-deep taper, active passive transition

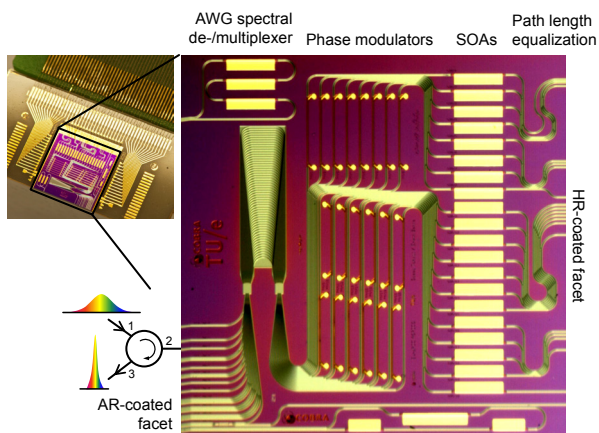


Fig.7.1. Microscope image of the realized pulse shaper. The chip is mounted on a subcarrier which is connected to a printed circuit board and provides the control signals. AR: anti-reflection, HR: high-reflection.

dedicated fabrication process and tailored wafer layer stack [2]. Such devices are operated by some means of individual control on each AWG, such as temperature tuning, to match the transmission spectra of the AWGs [5]. On the other hand, the reflective design requires a single AWG and the signal in each AWG channel passes through the optical elements twice. Therefore, it is more efficient, compact and tolerant to the fabrication process, and hence, attractive for realization in a generic integration platform. The total size of the device under test is $6 \times 6 \text{ mm}^2$.

An important issue in the performance of a pulse shaper in reflective mode is the effect of unwanted reflections from on-chip components and the facet, leading to detailed spectral features that will affect the shaped pulse. To minimize the back reflections in the current device, the I/O waveguides are angled, the I/O facet is AR-coated and tapered elements at the shallow-deep waveguide junctions are used. Roughness-induced backscattering, which is largely incoherent feedback, for similar (deep-etched) waveguides is measured to be in the order of -40 dB/mm . In case of the device under test, the total unwanted reflection level is measured to be at least 21 dB lower than the signal. Furthermore, the lensed fiber tip which is used to inject the pulsed signal to the chip and collect the return signal is AR-coated. A drawback of a reflective pulse shaper is the need for an optical circulator. Although different approaches for integration of non-reciprocal optical components on semiconductor platforms are proposed, fabrication of such elements remains a technological challenge [6,7]. This hinders the integration of the (reflective) pulse shaper with a pulse source on the current fabrication platform.

The current design includes a total number of 20 SOAs as well as 20 PMs. Extra sections of waveguides are included in each AWG channel to compensate for the path length differences. Total on-chip loss (double-pass, excluding gain of SOAs) is $\sim 20 \text{ dB}$. The fiber-chip coupling loss is below 4 dB . The SOAs are $750 \mu\text{m}$ long and are biased up to 40 mA to provide around 7 dB double-pass optical gain and low amplified spontaneous emission (ASE) power levels. If an SOA is biased below transparency, extra losses are induced due to absorption. A frequency component of the pulse may be

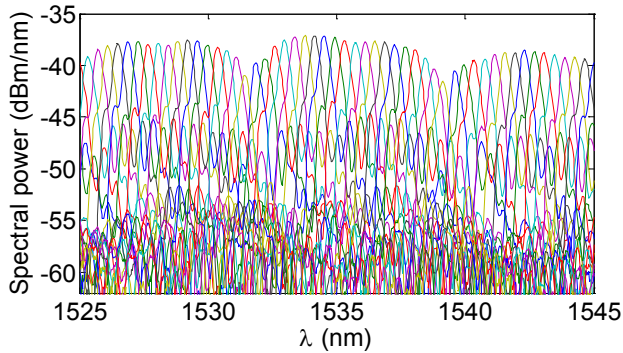


Fig.7.2. Fiber-coupled optical spectral power. SOA 9 is biased at $I_{SOA}=30\text{mA}$ and the ASE power is recorded at I/O waveguides. AWG has a cyclic design and the free spectral range is $\text{FSR}=8\text{nm}$.

effectively eliminated by reverse-biasing the SOA. The threshold voltage is approximately 0.8V and the total contact resistance of SOAs is measured to be $8.5\pm 1.2\Omega$ on average.

The AWG has a cyclic design with 20 channels at 50GHz spacing. The free spectral range is 8nm . The AWG transmission spectrum is flat within 3dB and the insertion loss is approximately 5dB . In order to characterize the spectral transmission through the AWG, the SOA in channel 9 was biased at $I_{SOA}=30\text{mA}$ and the generated ASE power is measured at the I/O waveguides. Fig.7.2 shows the spectra of the fiber-coupled optical power and indicates the shape of AWG channels. The full width at half maximum (FWHM) spectral width of AWG channels is designed to be 50GHz whereas measurements show a FWHM of $\sim 65\text{GHz}$ which is attributed to phase errors in the AWG arms. The increased overlap between channels is disturbing for some applications such as optical arbitrary waveform generation based on the line-by-line shaping scheme and can be compensated by phase error correction techniques.

The chip is mounted on a subcarrier which provides wire-bond pads for connection to the control instruments via a printed circuit board. The subcarrier is then mounted on a water-cooled copper block which is used to stabilize the operating temperature. A thermistor is used to monitor the temperature. The actual device temperature depends on power dissipation in SOA sections as well. When all the SOAs on chip are biased at $I_{SOA}=30\text{--}40\text{mA}$, the sensor indicates about $0.5\text{--}0.7^\circ\text{C}$ increase in temperature. This corresponds to a temperature change of less than $0.01^\circ\text{C}/10\text{mA}$. A 0.5°C increase in the temperature shifts the AWG spectrum to longer wavelengths by approximately 8GHz . Therefore, the effect of small changes in I_{SOA} on operating conditions of the device is negligible. The results presented here are obtained at $T=12^\circ\text{C}$.

The PMs on the pulse shaper chip are 1mm long. They are operated by reverse bias voltage and are used to apply certain phase masks on the spectral components of the input pulse. To increase the phase shifting efficiency, the PMs are oriented parallel to the wafer major flat. In this direction the linear EO effect adds to the quantum-confined Stark effect. The dark current is measured to be 2.5nA to 4nA for reverse bias $V_{PM}=0$ to $V_{PM}=-5\text{V}$. When the corresponding SOA in the channel is biased at $I_{SOA}=30\text{mA}$, the current through the PM is $I_{PM}=2\mu\text{A}$ at $V_{PM}=0\text{V}$ and increases to $I_{PM}=21\mu\text{A}$ at $V_{PM}=-5\text{V}$.

The increased reverse current is caused by higher light absorption in presence of the external electric field. The amount of excess loss induced by the reverse-biased PMs is lower than 1dB for $|V_{PM}| < 4V$. The required voltage for a 2π phase change (double-pass) is about 3.6-4V for a range of $\lambda \sim 1530-1550\text{nm}$.

7.3. Demonstration of chirp compensation

Spectral phase control of optical pulses is often required to generate short pulses, and an important application of the pulse shaper chip is spectral chirp/dispersion (pre-) compensation. To demonstrate the functionality of the device under test, we have used a 40GHz passively ML quantum dash laser which generates highly chirped optical pulses. The measurement setup is schematically shown in Fig.7.3. Optical pulses are characterized in time-domain using the stepped heterodyne technique [8]. This technique is a linear measurement method which is particularly useful in spectral and temporal phase characterization of passively ML lasers, where no external electronic clock is available. In this technique, the optical pulse is combined with the light from a continuous-wave tunable laser source (TLS) using a power combiner and then put on a photodiode. The TLS is tuned over the spectrum of the optical pulse. A real-time oscilloscope (with sufficient bandwidth) is used to record beat frequencies between the TLS light and two neighboring optical modes as well as the beat tone at the repetition frequency of the ML laser. We have used a 45GHz real-time oscilloscope (LeCroy LabMaster 9 Zi) to directly record the time traces (single shot, no signal averaging/integration). Recorded data are then post processed to retrieve the temporal amplitude and phase (and equivalently chirp) of the optical pulses.

The ML laser is a single-section, 1mm-long, quantum dash Fabry-Pérot device [9]. It is operated at 375mA (with no external modulating signal applied) and at $T=18^\circ\text{C}$. The total power at the output of the laser is 3dBm. We have first excluded the pulse shaper chip from the setup to characterize the optical pulse which is generated by the ML laser

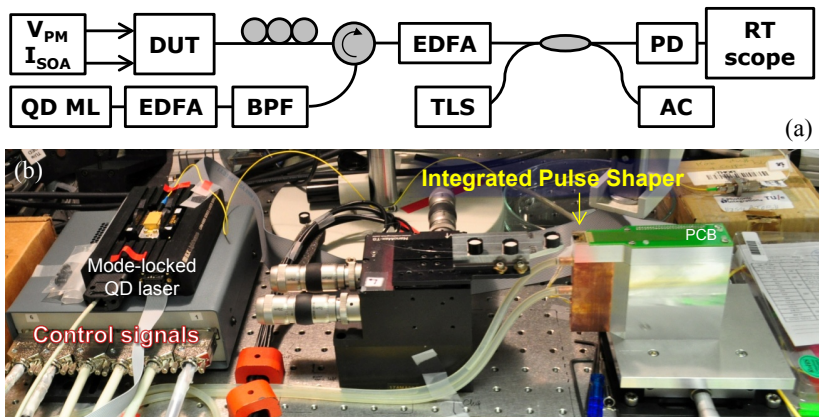


Fig.7.3. (a) Schematic drawing of the measurement setup. DUT: device under test, QD ML: quantum dash mode-locked laser diode, BPF: 6nm band-pass filter, TLS: tunable laser source, PD: 50GHz fast photo-diode, RT scope: 45GHz real-time oscilloscope, AC: autocorrelator. (b) Pulse shaper, signals control box and the quantum dash mode-locked laser source on the optical table.

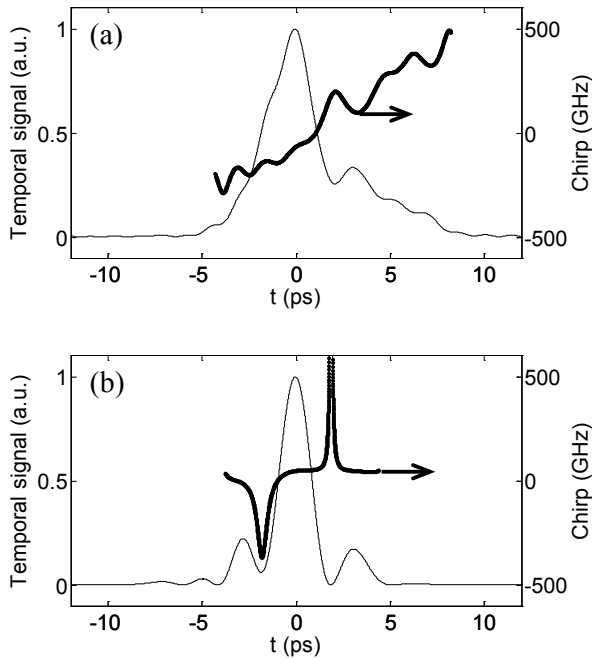


Fig.7.4. Normalized temporal amplitude (left axis) and chirp (right axis) of the optical pulse (a) generated by the quantum dash laser, and (b) passed through the pulse shaper chip for chirp compensation.

and passed through our measurement setup. In order to reliably measure the signal with the real-time oscilloscope, Erbium-doped fiber amplifiers (EDFAs) are used to boost the signal level. Oscilloscope traces are then analyzed to characterize the pulse shape. The result is shown in Fig.7.4(a) and it is clear that the pulse has a chirp profile that is not linear. The pulse has FWHM of 3ps with an asymmetric temporal shape which spans over 6.6ps at 6dB below the top of peak. It must be mentioned that the laser operates around $\lambda=1529\text{nm}$ and hence a part of the optical spectrum which falls outside the EDFA gain bandwidth is suppressed. Therefore, the results are effectively obtained for 4nm spectral bandwidth.

Next, the optical pulse is characterized after passing through the pulse shaper. In principle, the required control signals, i.e. values of bias voltage on PMs and current of SOAs, can be calculated by considering the spectral phase and amplitude of the incident pulse and the shape of the desired pulse to synthesize, which is in this case an ideal transform-limited optical pulse. Tuning the control signals on PMs affects the spectral phase profile and changes the pulse shape. We have found and optimized the phase settings by monitoring the autocorrelation signal to maximize the peak power and reduce the time duration. The SOA sections in all the operating channels are biased at $I_{\text{SOA}}=40\text{mA}$. Fig.7.4(b) shows the temporal signal and chirp of the output pulse. It is clear that the chirp profile over the duration of the optical pulse is nearly flat and the trailing edge is significantly suppressed. The FWHM of the pulse is 2.17ps and the width at 6dB below the top of the peak has reduced to 2.9ps.

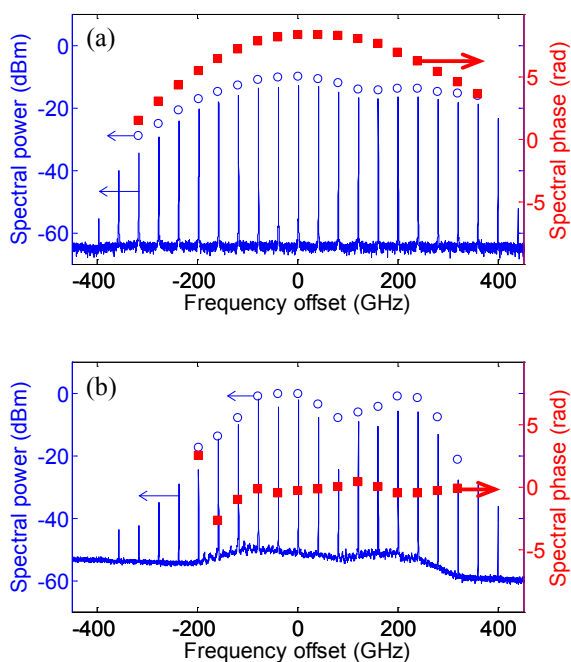


Fig.7.5. Spectral power (left axis, dBm) and phase (right axis, radians) of the optical pulse (a) generated by the quantum dash laser and passed through the measurement setup only, and (b) with the pulse shaper chip included. High resolution spectra (solid line) show the laser modes. Open circles represent the normalized power spectrum retrieved from the stepped heterodyne technique. In (a) the circles are offset by -10dB for better visibility.

The pulsed intensity contrast ratio (ICR), i.e. the ratio of the peak of the temporal signal to the background level, gives an indication of the quality of the pulsed signal. The ICR for the optical pulse before compression is 22.9dB. In case of the compressed pulse, ICR is measured to be 24.6dB which is only slightly improved due to the mismatch between the repetition frequency of the ML laser and the channel spacing of the pulse shaper. The limited contrast is attributed to the limited number of optical modes.

Functionality of the device is further verified by investigating the optical pulses in the frequency domain. This provides a clear insight on the Fourier transform shaping capability of the device. The spectral phase is measured using the stepped heterodyne technique. In order to clearly visualize the spectral lines, i.e. the frequency components, a high resolution (20MHz) optical spectrum analyzer is used to record the power spectrum as reference.

Fig.7.5(a) shows the measured spectral power (open circles, normalized and offset by -10dB for better visibility) and phase (filled squares) of the optical pulse generated by the ML source and passed through the measurement setup, excluding the pulse shaper. The high resolution power spectrum (solid line) is given and indicates the optical lines which are separated by 40GHz, i.e. the ML repetition frequency.

Fig.7.5(b) corresponds to the optical pulse when the pulse shaper chip is included in the measurement setup. The spectral phase profile is nearly flat for 11 optical lines at the

higher frequency side of the spectrum. However, it is clear that the chirp is not fully compensated and the power spectrum is not flat due to the mismatch between the repetition frequency of the source and the channel spacing of the device. In Fig. 7.5, the spectral power measured with the stepped heterodyne technique (open circles) shows a good agreement with the recorded power spectrum measured with the high resolution optical spectrum analyzer (solid line). This verifies the reliability of the measurement method and indicates that the pulse train from the laser is sufficiently stable.

7.4. Conclusions

We have designed and fabricated an integrated pulse shaper chip in an InP-based generic integration platform. The chip is characterized and operated at optimized conditions to compensate the chirp of a passively mode-locked quantum dash laser. Optical pulses are characterized in the time domain using the stepped heterodyne technique. The results show a nearly flat chirp profile over the duration of the optical pulse, and suppressed trailing features owing to chirp compensation which lead to a factor of two reduction in pulse width. Demonstration of functionality of such an integrated optical chip reveals the advance of generic photonic foundry technology.

References

- [1] A. M. Weiner, "Ultrafast optical pulse shaping: A tutorial review," *Optics Communications*, vol. 284, no. 15, pp. 3669–3692, Jul. 2011.
- [2] N. K. Fontaine, R. P. Scott, and S. J. B. Yoo, "Dynamic optical arbitrary waveform generation and detection in InP photonic integrated circuits for Tb/s optical communications," *Optics Communications*, vol. 284, no. 15, pp. 3693–3705, Jul. 2011.
- [3] A. C. W. van Rhijn, M. Jurna, A. Jafarpour, J. L. Herek, and H. L. Offerhaus, "Phase-shaping strategies for coherent anti-Stokes Raman scattering," *Journal of Raman Spectroscopy*, vol. 42, no. 10, pp. 1859–1863, Oct. 2011.
- [4] M. Smit et al., "Generic foundry model for InP-based photonics," *IET Optoelectronics*, vol. 5, no. 5, p. 187–194, 2011.
- [5] M. J. R. Heck et al., "Design, Fabrication and Characterization of an InP-Based Tunable Integrated Optical Pulse Shaper," *IEEE Journal of Quantum Electronics*, vol. 44, no. 4, pp. 370–377, Apr. 2008.
- [6] T. R. Zaman, X. Guo, and R. J. Ram, "Semiconductor Waveguide Isolators," *Journal of Lightwave Technology*, vol. 26, no. 2, pp. 291–301, 2008.
- [7] L. Bi et al., "On-chip optical isolation in monolithically integrated non-reciprocal optical resonators," *Nature Photonics*, vol. 5, no. 12, pp. 758–672, 2011.
- [8] D. A. Reid, S. G. Murdoch, and L. P. Barry, "Stepped-heterodyne optical complex spectrum analyzer," *Optics express*, vol. 18, no. 19, pp. 19724–31, Sep. 2010.
- [9] R. Maldonado-Basilio, J. Parra-Cetina, S. Latkowski, and P. Landais, "Timing-jitter, optical, and mode-beating linewidths analysis on subpicosecond optical pulses generated by a quantum-dash passively mode-locked semiconductor laser," *Optics Letters*, vol. 35, no. 8, p. 1184, Apr. 2010.

CHAPTER 8

Design and Components of a Hybrid Integrated Optical Pulse Shaper

In this chapter, we explore the possibility of realizing a hybrid integrated pulse shaper which combines the capabilities of the TriPleX¹ and InP integrated photonics technology platforms. This scheme is particularly interesting for opening up the possibility of achieving phase/amplitude manipulation in InP in combination with a multi channel TriPleX spectral de-/multiplexer. In this scheme the TriPleX device is used to decompose the incident pulse into its spectral components. The spectral components are then coupled to the InP device which includes an array of phase/amplitude modulators. The motivation for using the TriPleX technology in this context is the possibility of cascading several ring filters with low loss to create a spectral de-/multiplexer which has individually tunable channels. This is very interesting for the pulse shaping application since such a spectral filter makes the pulse shaper device to some extent flexible with respect to the repetition rate of the pulse source, i.e. a mode-locked (ML) laser diode. In practice, this is important since it is difficult to fabricate ML laser diodes with accurately determined repetition rates, e.g. 20MHz accuracy on 10GHz.

TriPleX waveguide technology is based on alternating layers of silicon oxide (SiO_2) and silicon nitride (Si_3N_4). The basic idea in this technology is to arrange layers of these two dielectric media with different thickness and refractive index to achieve the desired waveguide properties which suit the requirements of different applications. This is enabled by material growth by low pressure chemical vapor deposition and is typically done by designing the waveguide geometry [1]. An important aspect of the TriPleX technology is the possibility to design high index contrast waveguides which in turn leads to the possibility of integrating tight bends and compact optical ring waveguide structures. The optical ring waveguide structure is a main building block in the TriPleX technology and is used to build different components such as ring resonators and tunable filters. Such components are interesting for wavelength conversion [2], beam-forming [3] and in particular the lab-on-a-chip systems [4].

However, TriPleX material is inherently passive and does not provide optical amplification and efficient electro-optic phase modulation. Building an entire

¹ TriPleX is the trademark of the waveguide technology developed at LioniX B.V.

monolithic pulse shaper in the TriPleX platform is only possible through integration of thermally tunable phase/amplitude control elements, i.e. phase shifters and variable optical attenuator, with the ring filters. The switching speed of such elements is typically limited to a few kHz. An important advantage of the hybrid integration scheme incorporating a TriPleX de-/multiplexer is that light pulses with at least two orders of magnitude higher peak power can be transported in the TriPleX waveguides (compared to InP/InGaAsP waveguides). This is owing to the fact that the (nonlinear) losses in the TriPleX technology are considerably lower than those in the semiconductor material. In this scheme, the InP amplifiers and phase modulator advantages are still available and the optical power in the InP waveguides is much lower than the peak power of the pulse.

The rest of this chapter is organized as follows. In section 8.1 we present the hybrid integration scheme to combine the InP and TriPleX chips. We consider the practical challenge of efficient coupling between the chips and tackle the problem by the optical coupling interface, i.e. setting a common waveguide pitch, angle and spot size at the interface of the InP and TriPleX chips. We then focus on the design and characterization of the two devices independently. In section 8.2, a description of the TriPleX de-/multiplexer device as designed by XioPhotonics and the related design criteria are presented. Experimental results on the performance of the TriPleX spectral de-/multiplexer are then given in section 8.3. We present the design of the InP chip in section 8.4. The InP chip includes a dense array of spot size converters (SSCs) which expand the standard waveguide mode size to $\sim 3\mu\text{m}$. Detailed design procedure and characterization of the SSCs are presented as well.

8.1. Hybrid integration scheme

InP technology platforms enable the fabrication of complex photonic integrated circuits (PICs) since both active and passive components can be integrated. Monolithic integration provides the greatest reliability and cost benefits when the largest possible number of components is integrated into a single device. In recent years, heterogeneous and hybrid integration platforms have attracted attention as well. Heterogeneous integration [5–7] particularly involves integration of III-V semiconductors onto silicon-on-insulator substrates or silicon chips. Hybrid integration [8–10] is generally based on assembling multiple photonic chips and components together to form a compound optical module. The hybrid integration has the advantage that the functionality of different optical platforms may be merged.

A technological challenge in the hybrid integration scheme is the assembly of the optical devices. This mainly involves a stable and reliable mounting of the devices and low loss coupling between the chips. In this chapter, we explore the possibility of realizing a hybrid integrated pulse shaper which combines the functionality of a TriPleX spectral de-/multiplexer and an InP phase modulator array. The approach we are taking is to position the two chips opposite each other and directly couple the TriPleX and InP waveguides. In this case, efficient coupling between the devices requires that at least one of the devices is mounted on a 6-axis stage. This is schematically illustrated in Fig.8.1. Once the interface between the two chips is defined, the chips can be designed independently. The interface is defined on three main points which are discussed in detail in the following subsections.

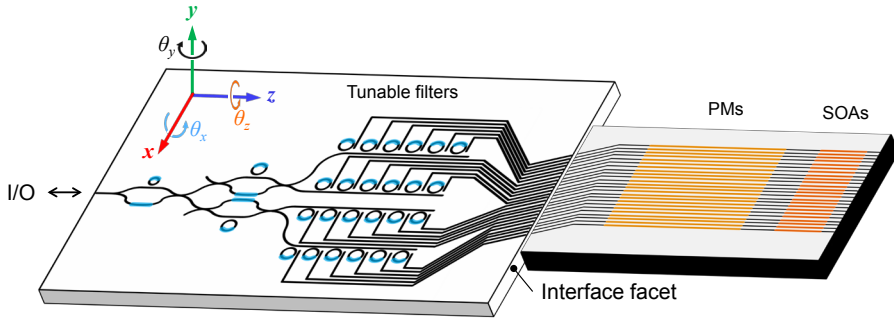


Fig.8.1. Schematic illustration of the hybrid integrated pulse shaper. The six degrees of freedom for alignment of the two optical chips are shown. I/O: input/output, PM: phase modulator, SOA: semiconductor optical amplifier.

8.1.1. Waveguide pitch

The first issue to be discussed concerns the spacing between the waveguides at the interface. This needs to be minimized for a number of reasons. The main reason is related to the alignment between the two chips. The wafer stack of both chips involved incorporates multiple epitaxial layers of different materials. The stress between the film layers causes the chip to become slightly bent. If the waveguides are located over a large length at the edge of the chip, the bow on the chip surface causes the waveguides to get misaligned in the vertical direction. To minimize the effect of surface unevenness, it is required to set the waveguide pitch as small as possible.

The minimum distance between the waveguides is determined by the amount of directional coupling. The minimum pitch for the TriPleX waveguides is $20\mu\text{m}$. The smallest distance between two (shallow) waveguides on the InP is $\sim 10\mu\text{m}$. The minimum pitch between contacted phase modulators in InP is $25\mu\text{m}$. We have decided to set the waveguide pitch at the interface to be $25\mu\text{m}$ so that the simplest useable InP chip is a series of parallel waveguides.

There is a significant difference in the thermal expansion coefficient of the TriPleX (e.g. for Si, $\alpha_{L,\text{Si}}=2.60\times 10^{-6}/^\circ\text{C}$) and InP ($\alpha_{L,\text{InP}}=4.60\times 10^{-6}/^\circ\text{C}$). For an extreme case of 50 waveguides at $25\mu\text{m}$ pitch, a 10°C temperature difference results in a relative (horizontal) shift of 25nm . The required alignment accuracy is determined by the tolerable (coupling) loss and the mode size, which is investigated in the following subsection.

8.1.2. Optical mode size

The coupling loss between two waveguides is determined by the relative alignment and the optical mode mismatch. Mode mismatch is the difference between the optical mode profiles (in the lateral and vertical directions) of the waveguides. The power coupling efficiency between an incident electric field (E_{inc}) and (the fundamental mode of) an optical waveguide (E_{wg}) is given by the overlap integral as [11]

$$\eta = \frac{\left| \iint E_{\text{inc}}(x, y, 0) E_{\text{wg}}^*(x, y) dx dy \right|^2}{\iint |E_{\text{inc}}(x, y, 0)|^2 dx dy \iint |E_{\text{wg}}(x, y)|^2 dx dy} \quad (8.1)$$

where E_{inc} is the incident electric field (possibly coming out of another waveguide), E_{wg} is the fundamental mode of the optical waveguide, x and y represent the lateral and vertical directions, and the waveguide facet is chosen to be at $z=0$ along the propagation axis.

The mode profile of waveguides depends on the waveguide structure and the constituent material stack. The mode profile can be simulated using mode solver tools and the coupling efficiency is calculated numerically. However, the mode profile can be in general reasonably well approximated by a Gaussian spot which is described as

$$E_{wg}(x, y) = E_0 e^{-4 \left(\frac{x^2}{MFD_x^2} + \frac{y^2}{MFD_y^2} \right)} \quad (8.2)$$

where E_0 is a constant which is related to the optical power, and MFD is the mode field diameter. MFD is defined as the distance over which the intensity of the optical mode is higher than $1/e^2$ of the peak intensity. In general, the Gaussian “spot size” refers to the MFD. For Gaussian spots, the mode mismatch loss (dB) of the butt-coupled waveguides is given by

$$L_{mismatch} \approx 4 \frac{MFD_{x,InP} MFD_{x,TriPleX} MFD_{y,InP} MFD_{y,TriPleX}}{(MFD_{x,InP}^2 + MFD_{x,TriPleX}^2)(MFD_{y,InP}^2 + MFD_{y,TriPleX}^2)} \quad (8.3)$$

The 1dB alignment accuracy, i.e. the required displacement to induce 1dB excess coupling loss, in the lateral and vertical direction is expressed as

$$\Delta x_{1dB} = \sqrt{\frac{\ln(10)}{80} (MFD_{x,InP}^2 + MFD_{x,TriPleX}^2)} \quad (8.4)$$

$$\Delta y_{1dB} = \sqrt{\frac{\ln(10)}{80} (MFD_{y,InP}^2 + MFD_{y,TriPleX}^2)} \quad (8.5)$$

The fundamental mode of the standard (COBRA) shallowly etched InP waveguide is elliptical with MFD of $1.84 \times 0.97 \mu\text{m}^2$ ($x \times y$). The mode profile for the TriPleX waveguides has not been standardized and depends very much on the waveguide geometry and the thickness of the layers. In practice, the waveguide geometry is determined according to the requirements of the application, i.e. polarization dependence, propagation loss, minimum bend radius, etc. [1], and then the thickness of the layers near the chip edge is designed to get the required spot size.

In order to relax the alignment tolerances, we have decided to have a $3 \mu\text{m}$ spot at the edge of the TriPleX chip. The mode-mismatch loss and alignment tolerance for coupling between a $3 \mu\text{m}$ spot and an arbitrary Gaussian field is plotted in Fig.8.2.

For a $3 \mu\text{m}$ spot size on the TriPleX chip and the standard InP waveguide mode size, the butt-coupling loss between the waveguides is $\sim 2.8\text{dB}$. The alignment accuracy for 1dB tolerance is $\Delta x \sim 597\text{nm}$ and $\Delta y \sim 534\text{nm}$. To reduce the coupling loss between the two chips, we have decided to integrate SSCs on the InP chip to expand the mode to a $3 \mu\text{m}$ circular spot. In the ideal case of perfect $3 \mu\text{m}$ circular spots, the butt-coupling is lossless and the 1dB alignment tolerance is $\Delta x, y \sim 720\text{nm}$.

In practice it is possible that the two chips are not perfectly butt-coupled hence, there is a gap between the waveguides. When the light travels in the free space gap, the spot size expands. This causes a mismatch between the waveguide mode and the field which induces extra coupling loss. If we assume the waveguides have similar MFD and they

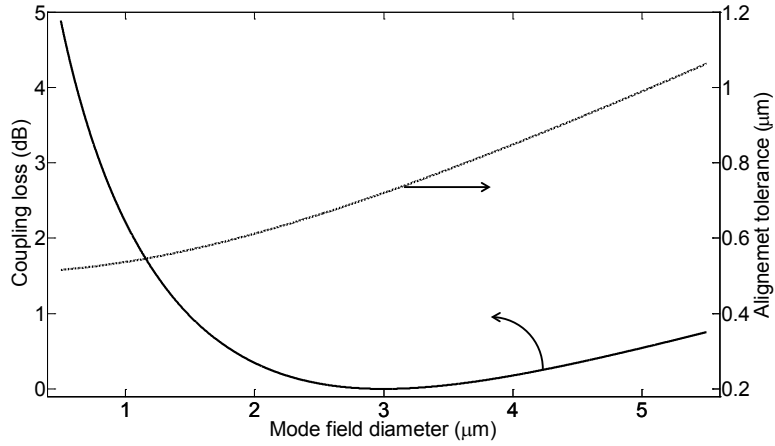


Fig.8.2. Mode-mismatch coupling loss (left axis, solid line) and 1dB alignment tolerance (right axis, dot-dashed line) between a $3\mu\text{m}$ Gaussian spot and a (circular) spot with mode field diameter as a parameter (horizontal axis).

are perfectly aligned, the amount of loss due to the gap between the waveguides is given by

$$L_{\Delta z} = \frac{1}{1 + \left(\frac{\Delta z}{2z_0}\right)^2} \quad (8.6)$$

where z_0 is the Rayleigh length given by

$$z_0 \equiv \frac{\pi \text{MFD}^2}{4\lambda} \quad (8.7)$$

In Eq.8.6, Δz is the gap along the propagation direction, and λ is the wavelength. This indicates that achieving a low coupling loss requires that the separation between the two waveguides (with similar mode size) is much smaller than the Rayleigh length. For reference, the Rayleigh length for a $3\mu\text{m}$ spot at $\lambda=1550\text{nm}$ is $4.56\mu\text{m}$.

8.1.3. Tilted waveguides

Back reflections from the interface into the waveguide limit the maximum allowable gain of optical amplifiers on the InP chip. Since one facet of the InP chip has to be highly reflective (HR) to return the signal to the input, the back reflection of the interface facet has to be as low as possible. Otherwise, the signal transmission through the chip is strongly wavelength dependent. To have an indication of the required facet reflectivity, we consider a 5mm-long structure in InP which includes an optical gain section. The effect of facet reflection and amplifier gain on modulation depth in the optical spectrum of the transmitted signal is presented in Fig.8.3. The modulation depth is defined as the ratio of the difference to the sum of maximum and minimum transmitted powers.

In order to minimize the unwanted back reflections the waveguides are angled at the interface facet. The reflection coefficient at the facet is dependent on the waveguide structure, width and angle. The typical optimized angle for the standard (COBRA)

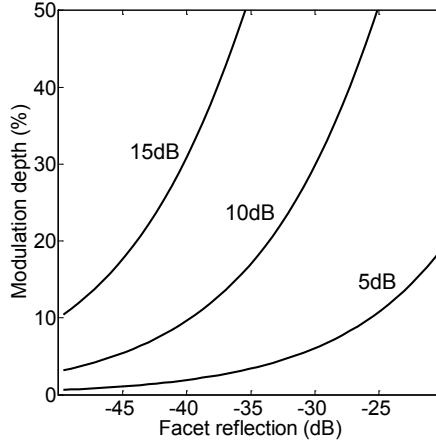


Fig.8.3. The relation between the facet reflection and the wavelength-dependent power transmission through an InP device channel. The device channels include passive waveguide sections as well as a gain section. We assume the passive loss is 4dB/cm and the reflectivity of the HR-coated facet is 0.95. The single pass optical gain of the amplifier section is shown on the curves.

shallow InP waveguide is 7° from the facet normal. In this case, the angle in air is $\sim 23^\circ$. The SSC waveguide has a different structure; therefore, the propagation angle in air is slightly different. For angles larger than 7° , the back reflected power is lower; however, collecting or launching light with a lensed fiber (or microscope objective) becomes increasingly difficult due to the large angle of refraction in air.

In order to have efficient coupling between the chips, the angular misalignment must be minimized. In order to do so, we have set the propagation angle at 23° . This means the waveguides tilt at the facet for InP and TriPleX is 7° and 15° respectively. With this value the back reflection for the InP chip can be kept below -40dB. This means for an optical gain up to 10dB (single pass) of the amplifier on the InP chip, the spectral dependence of the transmitted power, i.e. modulation depth, is below 10%. A 10dB optical gain on the standard COBRA platform is easily obtained by a 2mm-long amplifier operated at $\sim 11.5/\text{cm}$ gain. Typical maximum values of the small signal gain are at 50-60/cm. The reflectivity of the facet can be further reduced by application of an anti-reflection coating.

Now we assume that the waveguides have circular mode profiles with similar MFD, but there is an axial offset and angular misalignment. In this case, the coupling loss is given by

$$L_{\Delta z, \Delta \theta} = \frac{1}{1 + \left(\frac{\Delta z}{2z_0}\right)^2} \exp \left[- \left(\frac{1 + \frac{\Delta z^2}{2z_0^2}}{1 + \left(\frac{\Delta z}{2z_0}\right)^2} \right) \left(\frac{\Delta \theta}{\theta_0} \right)^2 \right] \quad (8.8)$$

where $\Delta \theta$ is the angular misalignment and θ_0 (numerical aperture) is defined as

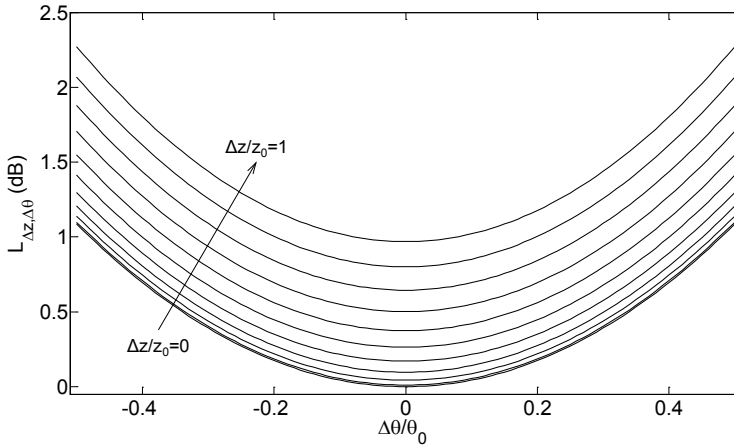


Fig.8.4. Coupling loss between two similar waveguides due to axial offset (Δz) and angular misalignment ($\Delta \theta$). The waveguides are assumed to have circular Gaussian modes of MFD= $3\mu\text{m}$ at $\lambda=1.55\mu\text{m}$.

$$\theta_0 \equiv \frac{2\lambda}{\pi\text{MFD}} \quad (8.9)$$

Eq.8.9 indicates that the numerical aperture (θ_0) is inversely proportional to the MFD. The coupling loss due to angular misalignment is minimized when $\Delta \theta$ is much smaller than θ_0 . This means that the angular alignment is more critical for a bigger mode size, which can be interpreted as the cost of relaxing the vertical and lateral positioning tolerances. The effect of angular misalignment and axial offset is shown in Fig.8.4.

The numerical aperture for a $3\mu\text{m}$ spot at $\lambda=1550\text{nm}$ is 18.8° . In this case, the maximum misalignment of the azimuth angle to achieve better than 0.1dB coupling loss is 1.3° . In practice, the angular misalignment in the plane of chips is restricted due to the restricted deviation of the chip facets from the parallel interface. A 1% obliqueness of chip facets with respect to each other, i.e. $10\mu\text{m}$ deviation of the separation gap over 1mm length, is equal to 0.5° misalignment which has a negligible effect. This also means that deviation from the propagation angle in air (which is set to 23°) due to uncertainty of the waveguides effective index ($<2\%$) is not critical.

8.2. TriPleX device: spectral de-/multiplexer

In this section, we present a brief description of the functional design of the TriPleX device. The device is a planar light wave circuit which is designed at XiO Photonics BV and operates as a multi-channel tunable filter. In principle, the filter chip functions as the spectral dispersive element in a Fourier transform pulse shaping setup.

The chip is designed according to the following application requirements and practical considerations.

- The filter should be able to spatially separate the multiple spectral components of an incident laser pulse and cover the spectral bandwidth of the laser. The spectral range of the filter is chosen to be 8nm , since this is the maximum available bandwidth of our semiconductor mode-locked laser.

- The filter channels are individually tunable. Hence, it is possible to vary the channel spacing over a certain range. This is particularly beneficial to match the channel spacing to (a multiple of) the repetition frequency of the laser source. In the current platform, resistive heaters are used to locally change the temperature and hence control the channel characteristics. The heaters are driven by electrical control signals.
- The number of channels is desired to be as high as possible. This provides control over a higher number of spectral lines which is ideal for (arbitrary) pulse shaping. In practice, the number of channels is determined by the resolution achievable for a single channel, the available chip area, fabrication uniformity and practical considerations regarding the control of electrical/optical elements. The number of channels is chosen to be 24. This keeps the number of control signals practically manageable and is about the minimum number of channels which is of use for CARS experiments (details on the application requirement are given in chapter 4).
- In the current platform, thermally-tunable ring structures are available. Therefore, the filter operation is based on micro ring resonators (MRs). Channel characteristics, such as width and crosstalk, are determined by the type of MRs. In the current design, first-order MRs are used to create the channels. The minimum inter-channel crosstalk in this case is chosen to be -10dB to provide sufficient isolation between the channels. This value is a compromise between the limit of the technology and the complexity of the circuit. A lower crosstalk value can be achieved by using multiple-ring structures in series. However this will significantly increase the complexity of the circuit and nearly double the number of required control signals per channel.

8.2.1. Ring resonator

A micro ring resonator consists of a ring structure which is coupled to a waveguide. A four-port MR configuration, which is schematically shown in Fig.8.5, is a wavelength-selective element and serves as the basic constituent part of the filter chip. The electric field transmission through the “DROP” port of the ring filter is described by [12]

$$\frac{E_{\text{DROP}}}{E_{\text{IN}}} = \frac{-\kappa_1 \kappa_2 \sqrt{\chi_r} \cdot e^{-j\varphi_r/2}}{1 - \mu_1 \mu_2 \chi_r \cdot e^{-j\varphi_r}} \quad (8.10)$$

in which κ_1 is the field coupling coefficients from the input waveguide to the ring, κ_2 is the field coupling coefficients from the ring to the output waveguide. The fraction of the field which is not coupled is given by

$$\mu = \sqrt{1 - \kappa^2} \quad (8.11)$$

In Eq.8.10, χ_r is the roundtrip loss factor of the ring which is defined as

$$\chi_r = 10^{-\frac{\alpha_r}{20}} \quad (8.12)$$

with α_r being the roundtrip power loss of the resonator in dB. φ_r is the roundtrip phase

$$\varphi_r = \frac{4\pi^2}{\lambda} n_{\text{eff}} R \quad (8.13)$$

in which λ is the wavelength, n_{eff} is the effective index and R is the ring radius. The free spectral range (FSR) of the resonator is defined as the spectral distance between two consecutive resonance peaks and is given by Eq.8.14 in which λ_0 is the central wavelength and n_g is the group index.

$$FSR \approx \frac{\lambda_0^2}{2\pi n_g R} \quad (8.14)$$

The “THROUGH” port response of the MR is expressed as

$$\frac{E_{THROUGH}}{E_{IN}} = \frac{\mu_1 - \mu_2 \chi_r \cdot e^{-j\phi_r}}{1 - \mu_1 \mu_2 \chi_r \cdot e^{-j\phi_r}} \quad (8.15)$$

The drop- and through-port response of a typical ring resonator with $800\mu\text{m}$ circumference, $\alpha_r=1\text{dB/cm}$ and $n_g=1.5$ are presented in Fig.8.6. The FSR in this case is 2nm .

The resonant wavelength of the MR can be shifted (tuned) by changing the optical roundtrip path length of the resonator. The optical path length is changed by changing the index of (a part of) the resonator waveguide. This will change the effective index which, in turn, will alter the roundtrip phase of the light in the resonator and therefore the wavelength for which it achieves maximum resonance.

In principle, an array of MRs which are coupled to a single (input) waveguide makes a multi-channel filter device in which, the drop port of each MR makes a single device channel. The total bandwidth of the device in this construction is limited to the

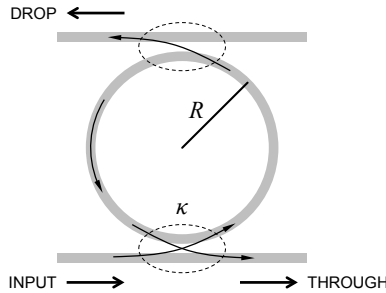


Fig.8.5. Schematic drawing of a four-port ring resonator which shows the drop and through ports. The ring-waveguide coupler is indicated by the dashed lines. κ is the electric field coupling coefficient and R is radius of the ring resonator.

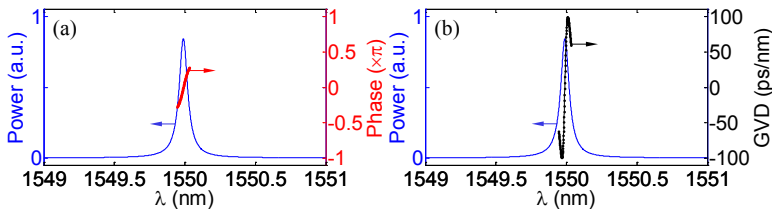


Fig.8.6. Drop port response of a micro ring resonator showing the transmitted power (left axis) and (a) spectral phase (units of π , right axis), (b) group velocity dispersion (GVD, ps/nm). The ring has a circumference of $800\mu\text{m}$, $\alpha_r=1\text{dB/cm}$, $n_g=1.5$ and coupling coefficient $\kappa^2=0.1$.

(minimum) FSR of the rings. The refractive index contrast of the available TriPleX waveguide technology, limits the FSR of the ring resonators to a maximum of 4nm. This is due to the minimum bending radius of curved waveguides which does not allow fabrication of sufficiently small rings. Since the required bandwidth for the pulse shaper device is 8nm, a single MR cannot be directly used to create an independent channel over full bandwidth. Therefore, a multi-stage approach is employed to first divide the 8nm bandwidth into smaller subbands. The spectral subbands are generated by frequency slicer stages which include interleaver filters.

8.2.2. Interleaver filter

In the current design, the 8nm bandwidth is first split in two equal subbands of about 4nm. Therefore, the first stage of the spectral filter circuit is a frequency slicer. The slicer stage is based on a ring loaded Mach-Zehnder interferometer (MZI) of which the transmission spectrum is characterized by a flattened passband with a sharp transition. Fig.8.7 illustrates a schematic drawing of a ring loaded MZI. The ring loaded MZI was first proposed in [13] and consists of an asymmetric (unbalanced) MZI which has a ring resonator coupled to its shorter arm. This structure can operate as an optical filter with a flat response or as an interleaver [14] depending on the length of the ring and path length difference at the upper and lower MZI branches.

As a frequency slicer, the ring resonator length is chosen to be twice the path length difference (ΔL). The FSR of the filter is then given by

$$\text{FSR} \approx \frac{\lambda_0^2}{n_g \Delta L} \quad (8.16)$$

The flatness of the passband depends on the coupling coefficient between the ring and the waveguide. This is shown in Fig.8.8. A higher coupling value results in a flatter passband whereas the band edge transmission becomes less sharp. When the ring-waveguide coupling coefficient approaches 1, the transmission spectrum become similar to an asymmetric MZI. The sharpness of the band edge is generally indicated by the width of the passband at 1dB below the maximum, i.e. at 90% transmission. The ring-waveguide coupling coefficient, κ_r , is a design parameter which is chosen for a compromise between the flatness of the passband and the sharpness of the transition edge, i.e. 1dB band width.

Submicron length variations in the MZI arms and the ring resonator, accompanied by fabrication imperfections which affect the phase of the signal, disturb the proper operation of the interleaver filter. This effect is represented in Fig.8.9, where an unwanted phase difference is included between the MZI arms. It is seen from Fig.8.9 that an extra π phase difference shifts the transmission spectrum by half the FSR, i.e. shifts the passband over to the wavelength range where the stopband is designed to be. In practice, a phase shifter section is included in the (longer) MZI arm to compensate for unwanted phase contributions. Furthermore, the ring resonator is made to be a tunable ring which includes a phase section for fine tuning purposes. This has the added advantage that by adjusting the two phase sections in the MZI and the ring, the passband of the interleaver can be tuned over the FSR. This is important for full tunability of the device.

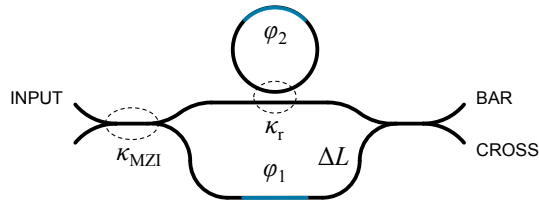


Fig.8.7. Schematic illustration of a ring loaded Mach-Zehnder interferometer with possible phase tuning elements.

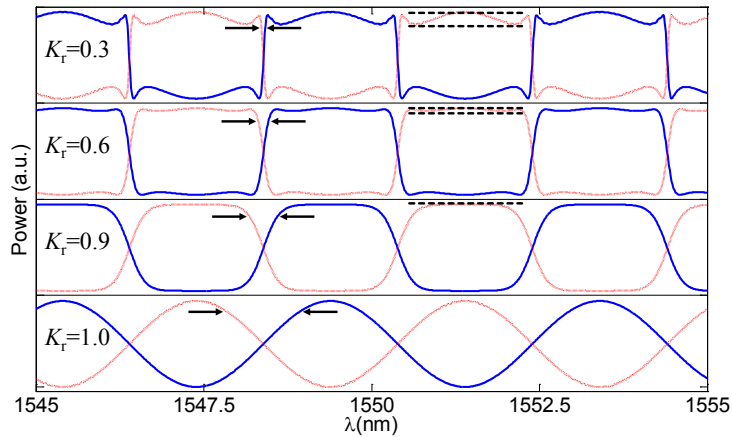


Fig.8.8. Bar-port (solid) and cross-port (dotted) response of a ring-loaded MZI interleaver for several values of ring-waveguide power coupling coefficient, and MZI power coupling coefficient $K_{MZI}=0.5$. $K_r=1$ corresponds to an asymmetric MZI. ($\varphi_1=\pi/2$ and $\varphi_2=0$)

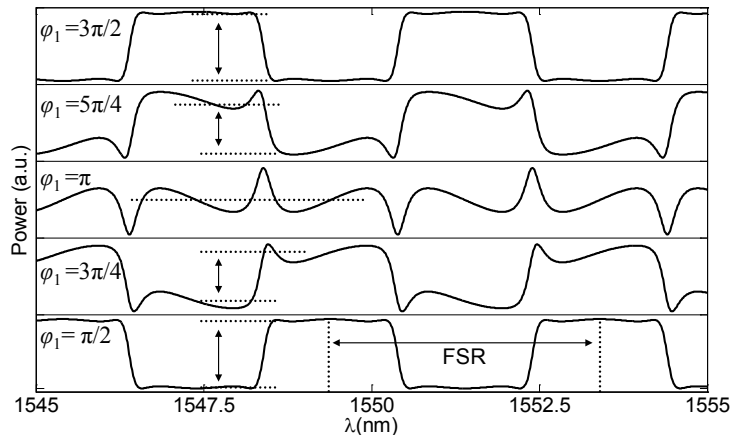


Fig.8.9. Bar-port response of a ring-loaded MZI interleaver for several values of (possibly unwanted) phase difference between the MZI arms. The phase differences are expressed in terms of φ_1 (and $\varphi_2=0$). The ring-waveguide power coupling coefficient is $K_r=0.6$, MZI power coupling coefficient $K_{MZI}=0.5$.

8.2.3. Tunable coupler

The extinction ratio is an important parameter of the interleaver filter which is determined by the coupling coefficient of the MZI couplers. For any value of the ring-waveguide coupling coefficient, the highest extinction ratio is achieved at a power coupling coefficient $K_{\text{MZI}}=0.5$. This is shown in Fig.8.10.

In practice, the MZI coupling coefficient may deviate from the designed value due to fabrication variations. Therefore tunable couplers are used instead of fixed directional couplers. The structure chosen for the tunable coupler is a symmetric MZI with phase tuning elements in one arm. In this structure, which is schematically shown in Fig.8.11, the effective electric field coupling coefficient κ_{eff} , i.e. from the input- to the output-port, can be controlled by changing the phase difference ($\Delta\phi$) between the two arms of the MZI according to

$$\kappa_{\text{eff}}^2 = 4\kappa_{\text{MZI}}^2(1 - \kappa_{\text{MZI}}^2) \cos^2(\Delta\phi/2) \quad (8.17)$$

In Eq.8.17, κ_{MZI} is the (electric field) coupling coefficient of the directional coupler of the MZI.

8.2.4. Device design

As mentioned earlier, the TriPleX device is a multi-channel spectral de-/multiplexer. The application requires that the device has 8nm bandwidth. However, a single MR in the current technology platform cannot be directly used to create an independent channel over the required bandwidth. This is due to the limited FSR of a single ring resonator. Therefore, a multi-stage approach is employed to first divide the 8nm bandwidth into smaller subbands. The ring resonators are then used within these

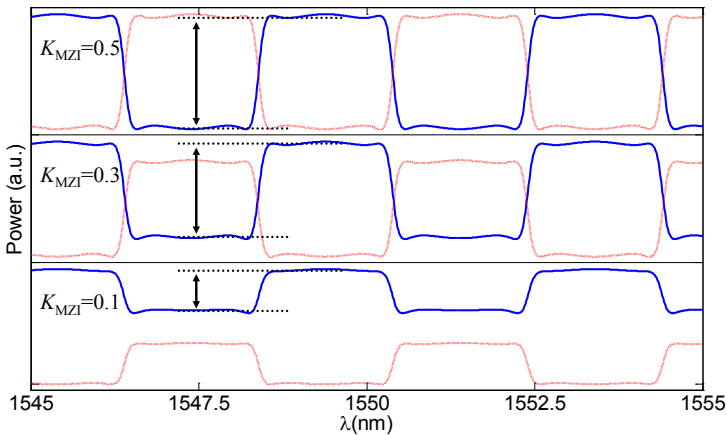


Fig.8.10. Bar-port (solid) and cross-port (dotted) response of a ring-loaded MZI interleaver for several values of MZI power coupling coefficient. The ring-waveguide power coupling coefficient is $K_r=1$.

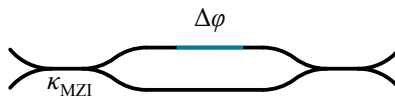


Fig.8.11. Schematic illustration of a MZ-based tunable coupler with two phase tuning elements.

subbands to filter out the channels.

The subbands are generated by flattened interleaver filters. Therefore, the first stage is a “slicer stage”. When the slicer is set to have a passband ripple less than 0.5dB and stopband suppression larger than 15dB, the band gap between the two subbands is 28.5GHz. This means that the frequency spacing between two neighboring channels must be larger than 28.5GHz. Therefore we set a minimum channel spacing of 30GHz. According to the chosen channel spacing, the FWHM of the MRs should be smaller than 25GHz to be able to achieve inter-channel crosstalk levels lower than -10 dB. This means that the power coupling coefficients of the MRs must be much lower than 0.1. However, such values are difficult to realize reliably due to fabrication variations. Therefore, the desired crosstalk level between the channels is achieved through reduction in the FSR of the MRs to below the 4nm maximum value, instead of lowering the coupling coefficients.

Since, the FSR of the MRs is required to be smaller than 4nm, a second stage of slicer is needed such that each MR can create an independent channel within the 8nm spectral bandwidth. By using two slicer stages, the spectral bandwidth is divided in four subbands. Therefore, MRs with an FSR of 2nm can be used to create the channels in the subbands. The power coupling coefficient of MRs is chosen to be 0.1 to achieve an inter-channel crosstalk lower than -10 dB.

Fig.8.12 shows the functional diagram of the device. The positions of the band gaps can be adjusted by tuning the slicers to match different channel spacings. When the maximum channel spacing of 40GHz is used, up to 24 independent channels can be created over an 8nm wavelength range. A simulated transmission spectrum of the TriPleX device with the filters tuned for covering the 8nm spectrum is illustrated in Fig.8.13. The dispersion of the two slicer stages in series is given in Fig.8.13(a) for one of the subbands (black line). This dispersion is to be compared to that of the ring resonators given in Fig.8.6(b). It shows that the total single device channel dispersion is dominated by the ring resonator in the third stage.

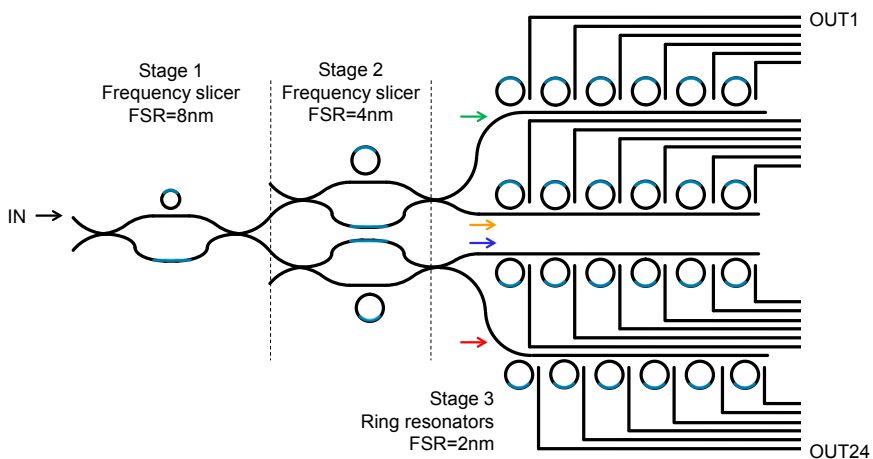


Fig.8.12. A Schematic illustration of TriPleX de-/multiplexer device.

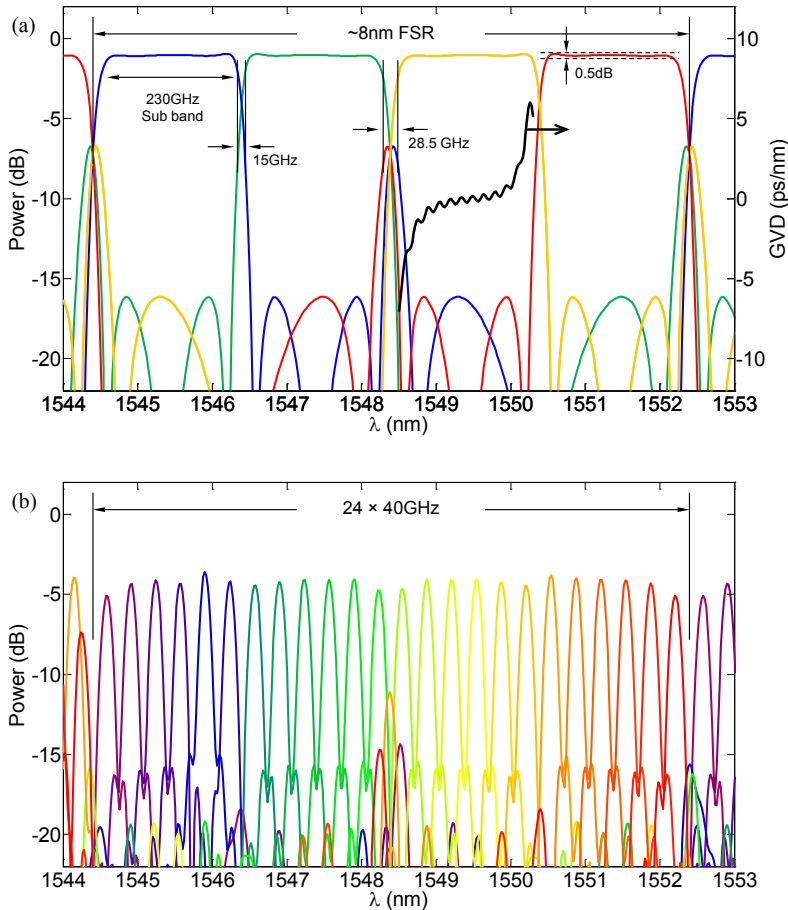


Fig.8.13. (a) Power transmission (left axis) through the first and second slicer stages when both stages are properly tuned to generate four subbands. The group velocity dispersion (GVD) over one of the subbands is given (right axis). (b) 24 device channels when the all the tuning elements are adjusted to generate 40GHz channel spacing. The results are simulated in Phoenix Aurora.

The path length difference of the asymmetric MZI for the first and second slicer stages is set to $200\mu\text{m}$ and $400\mu\text{m}$ respectively. The ring-waveguide power coupling coefficient is designed to be 0.6 to achieve 0.5dB passband ripple and -15dB stopband suppression. To be able to shift the power transfer of the slicer along the frequency axis, two tuning elements are required to change the phases of the ring resonator and the longer branch of the MZI, respectively. Including the tunable couplers, each slicer requires a total number of four tuning elements as is illustrated in Fig.8.14.

The rings and phase shifters are tuned through resistive heaters. When the heaters are driven, the dissipated electric power generates heat which causes a local change of temperature on the waveguide structure and modifies its effective index. This affects the phase of the optical signal in a phase shifter and shifts the resonance peak of a ring

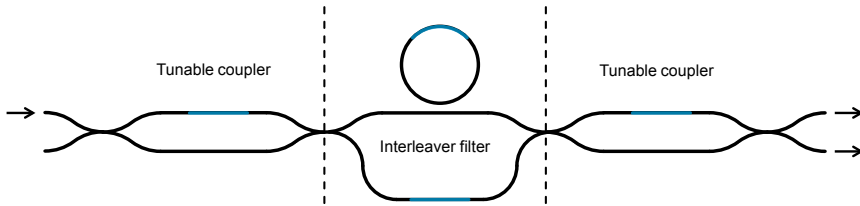


Fig.8.14. Schematic illustration of the frequency slicer stage based on a ring-loaded MZI interleaver filter with tunable couplers. The frequency slicer has 4 tuning elements.

structure. The generated heat travels from the top of the waveguide structures to the substrate which is mounted on a water-cooled block and acts as a heat sink. The circuit contains two slicer stages, i.e. three ring loaded MZIs structures with tunable couplers, and 4×6 ring resonators. Therefore, the total number of tuning elements is 36.

8.3. Experimental characterization of the TriPleX device

The TriPleX device is fabricated by LioniX BV with the double stripe (“=” shaped) waveguide technology. The double strip layout is an optimized structure to minimize the radius of curvature and has a strong polarization birefringence [4]. The device is designed for TE polarization. Fig.8.15 shows a microscope image of the realized device. The device has five main waveguides on the left side which are separated by a pitch of $250\mu\text{m}$. The center waveguide (labeled as IN) is the actual input of the device and is connected to the first slicer stage. The two waveguides (AUX1,2) directly above and below the input waveguide are inputs to the slicers at the second stage. These waveguides can be used as auxiliary inputs to bypass the first slicer stage and tune the second slicer stages and MRs for test purposes. The two outermost waveguides (T1,2) do not pass through the ring structures and can be used for alignment purposes when coupling the TriPleX device to the InP chip. At the right hand side of the device there are 28 waveguides. 24 waveguides in the middle (OUT) are the device channels. These waveguides are the drop ports of the MR filters at the third stage. The output waveguides are 15° tilted and are placed at a pitch of $25\mu\text{m}$ (to match the waveguide

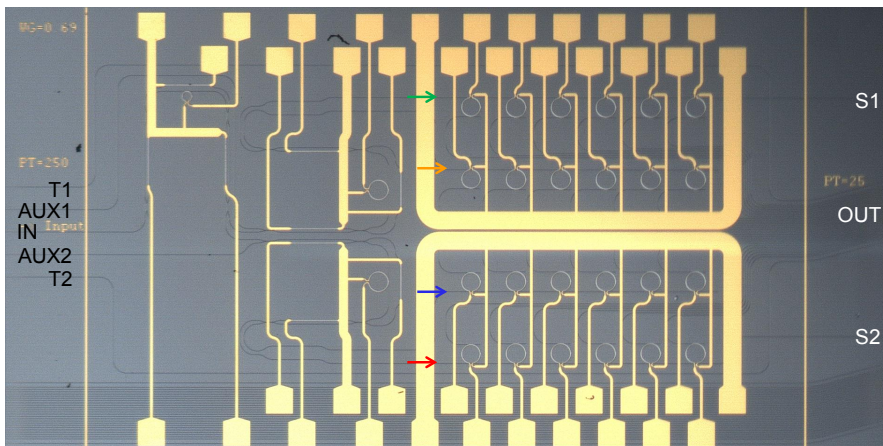


Fig.8.15. Microscope image of the realized TriPleX de-/multiplexer device.

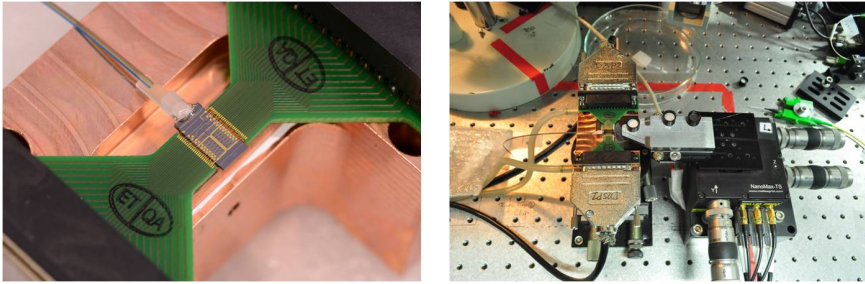


Fig.8.16. A snapshot of the TriPleX device mounted on the copper block and wire bonded to the PCBs (left) with the input fiber pigtail and A picture of the measurement setup (right).

pitch at the InP side). The two alignment waveguides are placed close to the output waveguides at a pitch of $50\mu\text{m}$. Moreover, there are two straight output waveguides (S1,2) which are connected to the through ports of two of the MR arrays (the upper and lower in the Fig.8.15). These waveguides can be used for test and tuning purposes.

The device has a fiber pigtail at the input side and is mounted on a copper block which is temperature stabilized ($T=16^\circ\text{C}$) by a water cooler. The metal pads on each side of the chip are wire-bonded to printed circuit boards (PCBs) which provide connections via SubD25 connectors. A pair of multi-core cables are connected to the SubD25 connectors. The cable wires are then redistributed to five SubD9 connectors. The SubD9 connectors are connected to current supply modules. The first slicer stage is controlled by two 2-channel Keithley source-meters; for the rest of the device, we have used four 8-channel laser driver (Thorlabs MLC8100) current supply modules. Images of the mounted device and the measurement setup are given in Fig.8.16.

In the following parts, we present the experimental characterization of the TriPleX de-/multiplexer. In the current design, the bandwidth of the input signal is first divided into four subbands of 2nm when it passes through the slicer stages. Each subband is then fed to a series of six tunable ring resonators which create the device channels. The procedure for tuning the slicer stages which is described in the following subsection, is an important step in operating the TriPleX spectral de-/multiplexer which assures generation of independent channels over the entire bandwidth of the device, i.e. 8nm . Experimental data on the device loss are presented in 8.3.2 and wavelength tuning properties of the heater elements are characterized in 8.3.3. In 8.3.4 the investigations on the operation of the multiple device channels is presented.

8.3.1. Slicer stages

As was discussed in section 8.2, the first two stages of the current device are frequency slicers which have an FSR of 8nm and 4nm in total. The third stage includes the MRs with 2nm FSR. Each frequency slicer has four tuning elements. These elements include two phase shifters in the tunable couplers, a phase shifter in the longer arm of the asymmetric MZI, and a phase tuning section in the ring resonator. Proper operation of the slicer stage requires correct combination of the four control elements.

To operate the slicer stage, the phase shifter in the asymmetric MZI arm is first tuned to adjust the bandpass shape of the interleaver filter, i.e. clear passband and stopband. The tunable couplers are then tuned to adjust the 3dB splitting/coupling ratio such that the highest extinction ratio between the passband and the stopband are achieved. The MZI

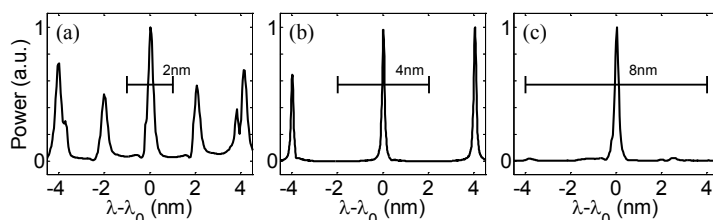


Fig.8.17. Spectral power (normalized, linear scale) measurement of a single device channel which shows the functionality of slicer stages. (a) Slicer stages are intentionally detuned. (b) Only the second stage is tuned. (c) Both slicer stages are properly tuned. The effective device FSR is indicated in each case.

ring (together with the longer arm) is then tuned to shift the passband over the required wavelength range. Since the output of the slicer stages is not directly accessible, adjusting the bandpass shape is done by measuring the transmission through a series of neighboring channels, i.e. the MRs of the third device stage.

In order to demonstrate the functionality of the slicer stages, we measure the transmission spectrum of a single device channel. The fiber pigtailed optical input of the chip is connected to an Erbium-doped fiber amplifier (EDFA) broadband light source. The output light is collected at the output waveguide with an AR-coated lensed fiber tip. Fig.8.17 shows the (normalized) optical power measured by an optical spectrum analyzer over the 8nm FSR of the whole device. In Fig.8.17(a) the slicer stages are not properly tuned. The spectral peaks are separated by 2nm and correspond to the FSR of the MRs in the third stage. The variation in relative height of the peaks is caused by the transmission shape slicer stages which are not tuned well.

The FSR of the second slicer stage is 4nm, i.e. a 2nm passband and a 2nm stopband. Therefore, when this stage is tuned, every other spectral peak of the MRs (which falls within the stopband) is suppressed. This is shown in Fig.8.17(b) where the spectral spacing between the peaks is increased to 4nm. To achieve independent channels over 8nm which is the desired device FSR, the first stage should be properly tuned as well. The results is shown Fig.8.17(c) where a single spectral peak exists over 8nm range.

In order to confirm the functionality of the slicer stages, the extinction ratio between the pass- and stopband was measured. The output ports of the slicer stages are connected in the device circuit and so we always observe the combined effect of a single slicer and ring filter. It is possible to get an impression of the band shape and extinction ratio though. Fig.8.18 shows a measured spectrum in dB scale. In this is figure, the first slicer stage was bypassed, the input signal is directly connected to the second stage. Hence transmission peaks appear at 4nm spacing. The spectral peak represents a device channel near $\lambda \sim 1556\text{nm}$ with a FWHM of $\sim 15\text{GHz}$, which is in agreement with the design and simulation results. The pedestal around the sharp peak is formed by the bandpass of the second slicer stage. The top of the peak is 15dB higher than the pedestal. The spectral features near 1554nm and 1558nm are the adjacent resonance peaks (2nm spacing) of the MR which are suppressed at the stopband of the slicer stage.

8.3.2. Loss measurement

The passive waveguide loss in the current TriPleX technology is specified at $\sim 1\text{dB/cm}$. To have an estimate of the device loss, we first measure the spectrum of the input

source over the wavelength range of our interest. Next, we connect the light source to the auxiliary input waveguide which is merely a ~ 11.7 mm-long passive waveguide running from the input- to the output-facet. The passive loss, including the loss of connectors and fiber-chip coupling, is measured to be in the order of 12dB. This is presented in Fig.8.18. The input waveguide is fiber pigtailed and the output is measured using a lensed fiber tip.

Then, we consider the spectrum of the device channel which is shown in Fig.8.18. The total transmission loss through a device channel at the central wavelength (including connectors and fiber-chip coupling loss) is approximately 17dB. This means that the excess loss of the optical de-/multiplexer circuit (the second slicer and a single ring) is ~ 5 dB. We assume the coupling loss between the lensed fiber and the chip is approximately 4-5dB. Therefore, we estimate the total device loss to be in the order of 6-9dB at a peak of the transmission spectrum (assuming a coupling loss between the chip and the pigtail fiber of 1-3dB). The simulation presented in Fig.8.13 suggests that the device loss (per channel) is around 5dB. The higher measured loss is probably due to a higher (than the specified 1dB/cm) waveguide loss, or additional loss induced by the metallic thin film heaters.

For the pulse shaping application with the hybrid scheme that was presented in section 8.1, the optical signal passes through the de-/multiplexer channels twice. The maximum tolerable loss is determined by the total available gain of amplifiers on the InP chip and unwanted back reflections at the interface facet. As was discussed in section 8.1, a 10dB total gain (single pass) is acceptable for the amplifiers on the standard COBRA platform. This means that 10dB of single pass loss for the de-/multiplexer device including the coupling loss between the chips is acceptable since a lossless pulse shaper can then be achieved. The measured TriPleX device loss (6-9dB) complies well with the requirements. It is noteworthy that the loss of an AWG in InP with a comparable number of channels and performance comparable to a MR with 15GHz minimum resolution and is in the order of 20dB, i.e. 10 times higher [15]. This shows the advantage of the low loss platform for the hybrid integrated pulse shaper.

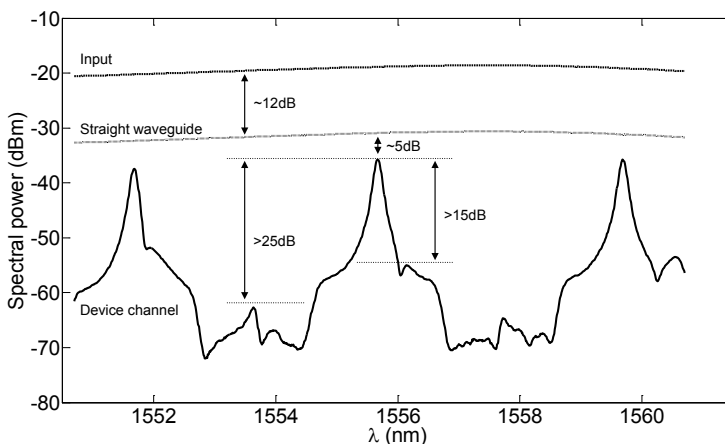


Fig.8.18. Spectral power measurement of the input signal (dashed), the signal transmitted through a passive waveguide (dotted), and the signal through a device channel (solid).

8.3.3. Wavelength tuning

The wavelength tuning method is via phase modulators in interferometric structures that are tuned thermally. The phase sections are tuned via a control signal which drives a thin film resistive heater on top of the waveguide structure. The dissipated power in the heater changes the local temperature and in turn the effective index to change. The change in the effective index changes the phase of the light signal. In the ring resonators, tuning the phase section causes the resonance peak to shift over the FSR. An important advantage of the device under test as a spectral de-/multiplexer, is that the channels are individually tunable. Each tunable MR in the third stage (in total 24) corresponds to a single device channel.

In Fig.8.19 a series of spectra are presented which were obtained by driving the ring filter at $I_{\text{ring}}=0\text{--}40\text{mA}$ and observing the ASE from an EDFA at the input. At $I_{\text{ring}}=0\text{mA}$, the spectral peak is located near $\lambda=1558.5\text{nm}$. Increasing the driving current leads to a higher local temperature; this shifts the resonance peak towards longer wavelengths. For the results shown in Fig.8.19, the peak reaches the edge of the passband (of the second stage slicer filter) at $I_{\text{ring}}\sim 20\text{mA}$. The height of the peak at the longer wavelength side decreases due to the suppression of the stopband. However, a spectral peak at the shorter-wavelength side around $\lambda\sim 1556.5\text{nm}$ appears. This corresponds to the 2nm FSR of the ring filter. The peak continues the red-shift and covers a 2nm range at $I_{\text{ring}}\sim 40\text{mA}$. Tuning the ring filters in a range of 2nm corresponds to a full FSR tuning of the MR for the current device.

It is clear from Fig.8.19 that the wavelength shift is not linear with respect to the driving current. We observe a shift of $\Delta\lambda=0.5\text{nm}$ for current values up to $I_{\text{ring}}\sim 20\text{mA}$, whereas a wavelength shift of $\Delta\lambda=1.5\text{nm}$ is recorded for the range $I_{\text{ring}}=20\text{--}40\text{mA}$. Fig.8.20(a) shows the measured wavelength shift versus the driver current. The measured data points are fitted by a quadratic curve which is expected, since we assume the wavelength shift is linear with the dissipated power/heat. Fig.8.20(b) shows the voltage

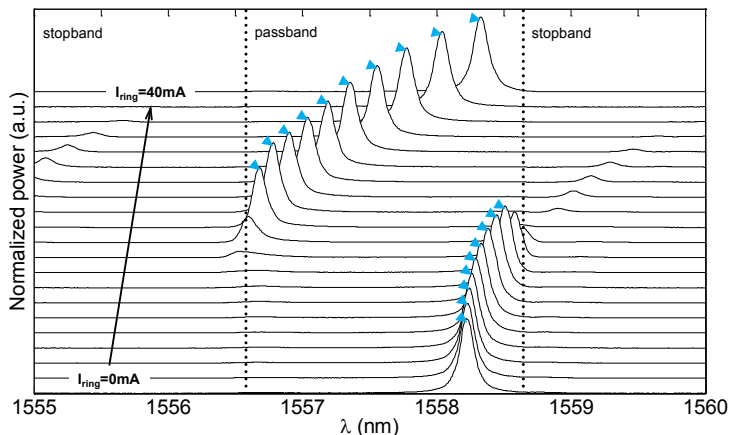


Fig.8.19. Demonstration of wavelength tuning of a single device channel. The driving current of the resistive heater is increased from $I_{\text{ring}}=0\text{mA}$ to $I_{\text{ring}}=40\text{mA}$ to achieve a full 2nm wavelength shift. The triangles indicate the top of the channel transmission at each current value.

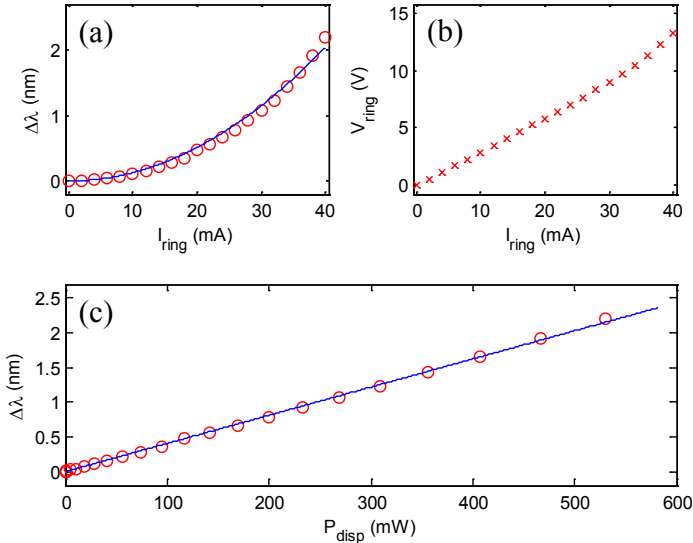


Fig.8.20. (a) Measured (circles) and fitted (line) wavelength shift versus the driving current. (b) Measured voltage across the resistive heater which shows a nonlinear behavior above 30mA. (c) Measured (circles) and fitted (line) wavelength shift versus the dissipated power.

across the heater versus the current. The resistance appears to be constant $R=310\Omega$ for current values up to $I=30\text{mA}$. Above this value, the voltage increases nonlinearly due to the temperature-induced increase of the heaters resistance. In principle this can lead to thermal runaway and burning the heater if it is current driven.

In Fig.8.20(c), the wavelength tuning versus the dissipated power ($P_{\text{disp}}=I\times V$) is presented. The measured data points fit nicely to a line and indicate that for a wavelength shift of $\Delta\lambda=2\text{nm}$, over 500mW power is required. This corresponds to $\sim 4.1\text{pm/mW}$ wavelength shift which is equivalent to a phase change of $4.1\pi/W$. The thermal efficiency of the phase modulators appears to be lower than specified and the measured heater resistance (310Ω for the MRs) is higher than the expected (100-200 Ω) value. With such values, operating the third stage, i.e. tuning the 24 rings, requires $\sim 5\text{W}$ of electrical power. The actual power consumption of the slicer stages depends on the amount of tuning which is required to compensate for unwanted phase variations (this is discussed in section 8.3 of this chapter) but is expected to be in the order of 1W. For the current device, the total dissipated power in the first and second stages is around 900mW.

8.3.4. Operating multiple channels

In the preceding parts, we described the tuning procedure of the slicer stages and presented the experimental data which are required for being able to tune the device channels. Adjusting the passband shape and extinction ratio of each frequency slicer requires tuning of the interleaver filter and tunable couplers. The phase shifter in the longer arm of the MZI in the interleaver filter is used to compensate unwanted phase difference between the MZI. The directional couplers are all similar and are designed to

have a 50% power coupling/splitting ratio. In practice, the coupling ratio can vary due to the fabrication variations. The phase shifters in the tunable couplers are used to achieve 3dB splitting/coupling ratio at the input/output of the interleaver filters. Once the slicer stages have been properly tuned, the MRs in the third stage can be tuned to create the de-/multiplexer device channels.

To demonstrate this, we have operated a single slicer from the second stage and all 12 channels coupled to that stage. The use of half the demultiplexer channels was related to two issues. The first issue is that the heater that controlled the passband shape in the first slicer stage failed at 30mA. This is probably due to a overheating at a weak point in the heater. Because of this we had to use the inputs to the second slicer stage. The second issue is also related to the heater elements. The phase tuning elements on the MRs were planned to be 200Ω heaters controlled via multi-channel current supplies (Thorlabs MLC8100). These modules have a compliance voltage of $V_{\text{comp}}\sim 6\text{V}$. In practice, this means we can only drive the heaters ($R=310\Omega$) up to a maximum current of $I_{\text{max}}\sim 20\text{mA}$. This corresponds to $\Delta\lambda=0.5\text{nm}$ wavelength shift which is not sufficient to achieve the full wavelength tuning over the FSR of the MRs, i.e. 2nm.

In order to demonstrate the functionality of the device, we replaced a number of current supply modules by alternative supplies and managed to drive 12 channels to cover a wavelength range of 4nm, i.e. half the total device bandwidth. The measured transmission spectrum of the device is presented in Fig.8.21. The transmission spectrum contains 12 spectral peaks which correspond to the device channels. There are two groups of 6 peaks which correspond to a series of six ring resonators.

The first group is located around $\lambda=1560\text{nm}$ and they are indicated by dashed lines in Fig.8.21. The ring resonators which correspond to this group are controlled by the MLC8100 current supply module (6V limit). We have chosen to spectrally distribute these 6 channels over a 0.5nm range, i.e. 12.5GHz channel spacing. The second group of channels, indicated by solid lines in Fig.8.21, are tuned around $\lambda=1558\text{nm}$ over a 2 nm range with a channel spacing of 37GHz. This demonstrates it is possible that to fully and freely tune each single ring.

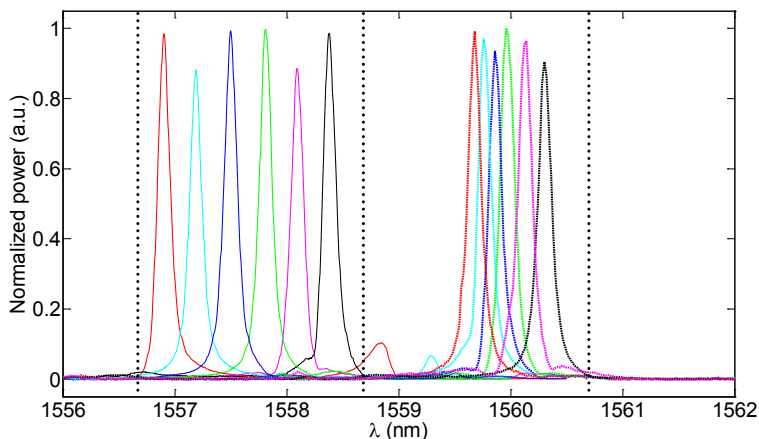


Fig.8.21. Spectral transmission of 12 channels of the TriPLeX device. Six MRs are tuned to create six channels at 37GHz spacing (solid) and the other six are tuned at 12.5GHz channel spacing (dashed). The two subbands of 2nm width are indicated by the dotted lines.

The measured spectra which are given in Fig.8.21 also confirm that a slicer stage can be properly tuned such that the ring filters create independent channels over the required wavelength range. For the group of channels which are located around $\lambda=1558\text{nm}$ (37GHz channel spacing), the crosstalk is below 10dB.

With the results given in this section, we have shown that simultaneous operation of multiple device channels is possible. We have explained the procedure for tuning the two slicer stages and verified that the passband shape of the interleaver filters can be adjusted to achieve an entire 8nm bandwidth. Furthermore, we have derived the phase tuning characteristics of the heater elements. This is particularly used to individually tune the ring resonators which create the device channels. We have measured the optical loss of the device to be $\sim 6\text{-}9\text{dB}$. This is higher than expected, i.e. 5dB; nevertheless, it is acceptable in the hybrid integration scheme for combination with an InP chip. Operating the current TriPleX de-multiplexer requires $\sim 6\text{W}$ of electrical power.

8.4. InP device: phase modulator array

In the hybrid integrated optical pulse shaper, the InP device incorporates the phase and amplitude manipulation functions. The technical challenge in the hybrid integration scheme is the coupling between the two chips. In order to focus on this issue, we have designed an InP device which does not include optical amplifiers. In this case, the simplest design is an array of 24 parallel phase modulators (PMs) and spot size converters (SSCs). The mask layout of the device is given in Fig.8.22. The PMs are 3mm long and are connected to wire-bond pads near the edge of the chip. The total length of the device is $\sim 5\text{mm}$ of which $\sim 1.5\text{mm}$ is dedicated to the SSC array.

The key point in fabrication of the InP device is the integration of a dense, i.e. $25\mu\text{m}$ pitch, array of SSCs with PMS. For incorporation of SSCs on the chip, the standard COBRA layer stack is modified. Although the current device design does not include optical amplifiers, the modified wafer layer stack is compatible with active-passive integration. This is important to ensure the possibility of integration of SSCs with active components in future. In this section we focus on design and characterization of SSCs on InP.

A spot size converter is an optical element which is used to modify the spot size, i.e. the size of the optical mode, in the waveguide. Including SSCs on integrated III-V devices was first introduced for reduction of coupling losses between the chip and optical fibers.

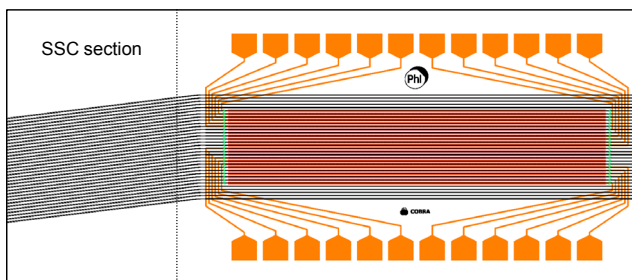


Fig.8.22. Mask layout of the designed InP chip. The device integrates an array of 24 phase modulators and spot size converters. For better visibility, the actual mask layers are simplified and/or not shown.

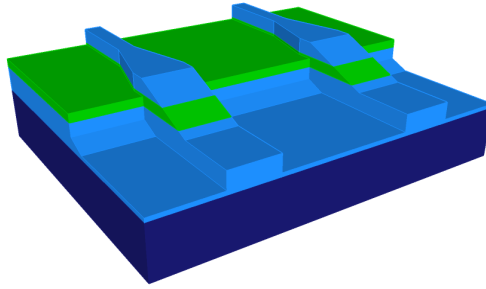


Fig.8.23. Schematic drawing of a spot size converter structure.

Later, the concept was implemented for chip to chip coupling as well. Another important reason to incorporate SSCs is to expand the optical mode at the input/output edge of the integrated device to relax alignment tolerances while coupling the light in/from the chip.

SSCs are generally fabricated by incorporating lateral and vertical waveguide tapers [16]. A schematic drawing of a possible structure is shown in Fig.8.23. In this structure, two types of waveguide are present, namely the high-confinement (HC) and mode-expanded (ME) waveguides. The HC waveguide supports a relatively small optical mode that is typical for the ‘standard’ ridge waveguide on chip. The ME waveguide is specifically designed to have a larger mode size and is employed at the chip edge to facilitate the coupling between the chip and a fiber or other chip.

Near the facet of the chip, the light is adiabatically transferred between the HC and ME waveguides. The taper structure has independent lateral and vertical sections to expand the mode size in both lateral and vertical directions. Lateral waveguide tapering is easily achieved by lithography. However, fabrication of vertical tapers is challenging and requires a so-called grey-mask lithography step which is usually accomplished by using a “grey” mask, i.e. a sliding raster mask.

8.4.1. Layer stack modification

For our application, the InP chip includes phase modulators which are shallow waveguide structures. The HC waveguide is a standard COBRA shallowly-etched structure. To be able to incorporate the ME waveguide on the same chip, the standard COBRA wafer layer stack needs to be modified. The layer stack modification involves adaptation of the bottom cladding (BC) layer.

The ME waveguide is essentially a ridge waveguide structure in the BC layer (Fig.8.23) which is formed by etching the BC layer. In such a structure, the optical confinement in the lateral direction is achieved by the index contrast between the ridge, i.e. the BC material, and the surrounding medium, i.e. typically air or the planarization polymer. The size of the optical mode in the lateral direction is mainly influenced by the ME waveguide width and the etch depth. The waveguide width is a design parameter which is lithographically defined in the fabrication. The etch depth is determined by the fabrication process flow.

The vertical spot size is determined by the thickness of the BC layer and the index contrast between the BC and the substrate. The thickness of the BC layer in the standard COBRA stack is $1.5\mu\text{m}$, which is not sufficient for incorporation of SSCs. Therefore,

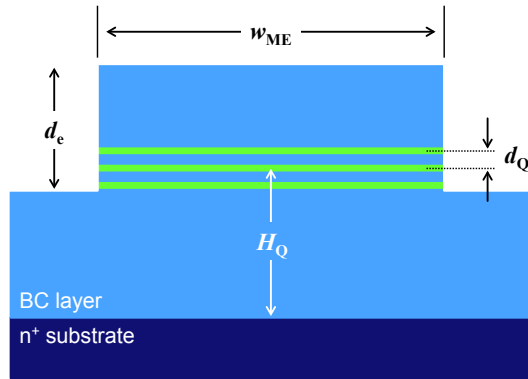


Fig.8.24. A schematic illustration of the cross section of the diluted waveguide.

the thickness of the BC layers needs to be increased. A possible approach to control the index contrast between the substrate and the BC layer is to design the doping levels. The substrate doping (n-type) is usually predefined by the manufacturer and is given within a certain tolerance range. For the COBRA platform we assume variations between $1\text{--}4 \times 10^{18} \text{cm}^{-3}$. Since we require that the wafer layer stack is compatible with fabrication of active components and in order to maintain the electrical conductivity of the structure, the doping level of the BC layer should be at least $5 \times 10^{17} \text{cm}^{-3}$, which corresponds to a refractive index of $n \sim 3.1654$ [17]. At such doping levels, the refractive index of the substrate is greatly affected by the variations of the doping level. This approach is investigated in [18] where it is shown to be practically very limited and sensitive to fabrication process. A more robust approach to confine the mode in the ME waveguide is to implement the so-called diluted waveguide structure by including few thin layers with higher refractive index in the BC layer [19], [20].

The layer stack is modified by an increase in thickness of the BC layer to $3 \mu\text{m}$. In practice, a layer thickness above $3 \mu\text{m}$ is not desirable due to costs of the material growth and increased defect density. The n-doping level in the BC is designed to be $5 \times 10^{17} \text{cm}^{-3}$. This is the minimum value determined by the resistivity requirement of the stack. In this case, the contact resistance of a 1mm -long amplifier with a $2 \mu\text{m}$ ridge waveguide structure is less than 2.5Ω . Using this doping value keeps the optical loss at a minimum. To achieve vertical mode confinement, we have chosen to incorporate thin film layers with the same composition as the HC core layer (Q1.25) in the BC. This increases the effective index contrast in the vertical direction and leads to a higher tolerance against doping level variations in the substrate. We have used three 30nm -thick Q layers. Schematic cross section of the ME waveguide is shown in Fig.8.24.

8.4.2. Waveguide geometry

Two main considerations are taken into account in determining the waveguide geometry. The first consideration is the mode profile of the ME waveguide. The mode profile should be close to a $3 \mu\text{m}$ Gaussian spot such that the InP-TriPleX chip coupling loss due to mode mismatch is minimized. This is discussed in section 8.2. The second criterion is the length of the taper sections which transfer the optical mode between the HC and ME waveguides. The geometrical parameters which need to be designed are the position of the thin Q layers, the spacing between them, the width of the waveguide and

the etch depth into the BC layer. The resulting mode profile is affected by the combination of these parameters; hence finding an optimum solution is a design task based on a series of simulations.

In the fabrication process, the ME ridge is (lithographically) defined together with the shallow waveguides. This eliminates the need for an extra lithography step and a highly accurate alignment of HC waveguides to the ME ridge. Therefore, the etch depth into the BC layer is determined by the standard passive shallow waveguide, i.e. $1.5\mu\text{m}$.

The next parameter is the waveguide width which mainly controls the mode size in the lateral direction. The waveguide width can be accurately defined in a standard lithography step. The most important parameter to control the mode size in the vertical direction is the separation between the Q layers. The index contrast on the diluted waveguide structure in the vertical direction is mainly provided by these Q layers.

Simulations of the ME waveguide optical mode profile in Phoenix FieldDesigner mode solver show that it is possible to achieve a loss due to mode mismatch below 0.5dB between the ME waveguide with a width of $w_{\text{ME}}=3\text{-}5\mu\text{m}$ and a Q-layer spacing $d_{\text{Q}}=0.2\text{-}0.4\mu\text{m}$ and a circular $3\mu\text{m}$ spot. The position of the central Q-layer above the substrate was varied in the range $H_{\text{Q}}=1.5\text{-}1.8\mu\text{m}$. These values indicate the acceptable tolerance in thickness of the layers. The lowest coupling loss value of $\sim 0.2\text{dB}$ is achieved at waveguide width $4\mu\text{m}$.

The final consideration is the length of the taper section. The length of (the vertical) taper is essentially determined by the thickness of the HC core layer and the vertical position of the optical mode of the ME waveguide relative to the HC waveguide mode. If the center of the ME waveguide mode is chosen to be close to the HC mode, the taper can be short without inducing additional loss due to a non-adiabatic transfer of the mode. Based on 2D BPM (beam propagation method) simulations, we have chosen the vertical taper length to be as short as $400\mu\text{m}$. The spacing between Q layers and the position of the central Q-layer is $d_{\text{Q}}=0.3\mu\text{m}$ and $H_{\text{Q}}=1.7\mu\text{m}$ respectively.

Fig.8.25 shows the simulated optical mode profile of the ME waveguide with $w_{\text{ME}}=4\mu\text{m}$, $d_{\text{Q}}=0.3\mu\text{m}$, $H_{\text{Q}}=1.7\mu\text{m}$ and an etch depth of $d_{\text{e}}=1.5\mu\text{m}$. The Gaussian approximation of the calculated mode profile is given for comparison. The MFD of the fitted (95% overlap) Gaussian mode is $3.2\mu\text{m}\times 2.7\mu\text{m}$. The loss due to mode mismatch between the simulated waveguide mode and a $3\mu\text{m}$ circular spot is calculated numerically and is $\sim 0.2\text{dB}$. It is seen from Fig.8.25 that the optical mode is mostly confined by the Q layers near the center of the BC layer. In the vertical direction, the tail of the mode which extends to the substrate contains less than 5% of the total power. If the mode is not well confined in the BC layer, propagation of the tail of the mode in the substrate induces extra SSC loss.

8.4.3. Characterization of SSCs

Fabrication of the InP chip which includes SSCs has been carried out in the framework of EU FP7 PARADIGM project. The layer stack for the chip was designed on the basis of the calculations and considerations presented above. Details of the fabrication are given in [21]. Prior to the device fabrication, we have measured the layer stack of the wafer. The measured stack shows deviations in thickness of the layers with respect to the design values. The deviations are tolerable. The design values and the measured stack are given in Table 8.1.

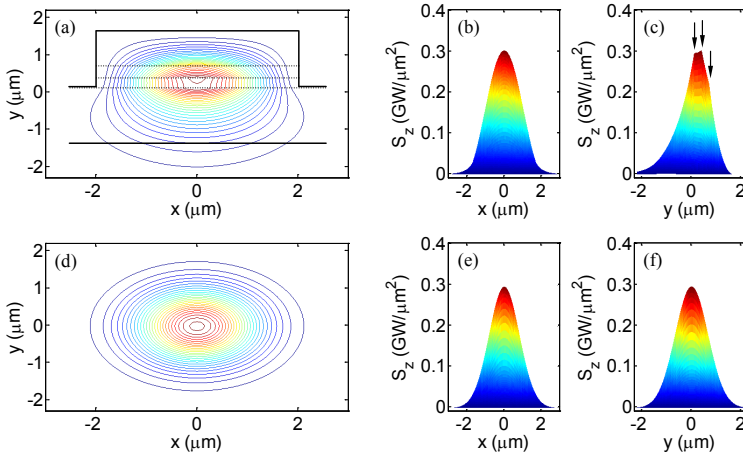


Fig.8.25. The mode (intensity) profile of the diluted ME waveguide calculated with Phoenix FieldDesigner (a-c) and the fitted Gaussian approximation (d-f). In (a) the cross section of the waveguide is shown. The arrows in (c) indicate the effect of mode confinement in the thin Q layers. x is the lateral direction, y is the vertical direction, and z is direction of propagation.

Table 8.1. The modified layer stack for integration of spot size converters with phase modulators and the measured thickness of layers.

	Designed Layer Stack				Measured Layer Stack			
	Layer	Material	Doping (cm ⁻³)	Thickness (nm)	Color code	Thickness (nm)	Deviation%	
cap	R4	i-InP	n.i.d.	20		NA	NA	
contact	R3	p-InGaAs	1.5×10 ¹⁹	280				
	R2	p-Q1.4	7.2×10 ¹⁸	10		253	-15.67	
	R1	p-Q1.2	4.7×10 ¹⁸	10				
top cladding	F13	p-InP	1×10 ¹⁸	1000		1495	15	
	F12	p-InP	5×10 ¹⁷	300				
	etch stop	F11	Q1.25	n.i.d.	20		15	-25
		F10	i-InP	n.i.d.	200		245	22.5
core	F9	i-Q1.25	n.i.d.	500		545	9	
bottom cladding	Q-layer	F8	n-InP	5×10 ¹⁷	970		1100	13.4
		F7	i-Q1.25	n.i.d.	30		30	0
		F6	n-InP	5×10 ¹⁷	270		310	14.81
	Q-layer	F5	i-Q1.25	n.i.d.	30		40	33.33
		F4	n-InP	5×10 ¹⁷	270		310	14.81
	Q-layer	F3	i-Q1.25	n.i.d.	30		35	16.67
	F2	n-InP	5×10 ¹⁷	1400		NA	NA	
substrate	F1	n-InP	2×10 ¹⁸	NA		NA	NA	

Fig.8.26 shows scanning electron microscope (SEM) images of the standard shallow HC and the ME SSC waveguides. The three Q-layers in the BC layer are clearly visible. The ME waveguide shown in Fig.8.26 appear to have a cleave defect on the facet, but the Q-layers are well positioned according to the measured wafer material stack.

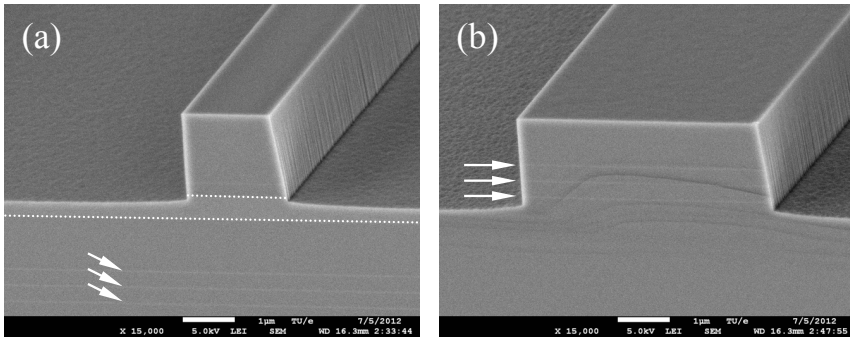


Fig.8.26. Scanning electron microscope image of the (a) standard shallowly etched, i.e. HC waveguide, and (b) the diluted, i.e. the ME, waveguide structure. In (a) the core layer is indicated by the dotted lines. The arrows in (a) and (b) point to the thin Q layers.

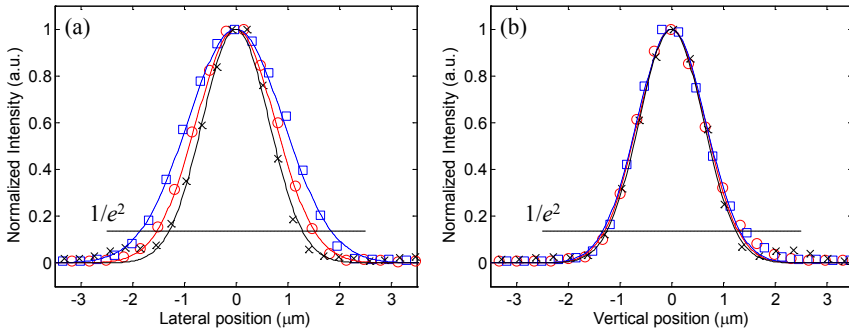


Fig.8.27. Measured optical spot of a lensed fiber tip (black, cross), the 4 μm -wide SSC waveguide (red, circle) and 5 μm -wide SSC waveguide (blue, square) in the (a) lateral and (b) vertical directions.

The spot size at the facet of a ME waveguide is characterized using a camera-based beam profiling technique. The light from a laser source is coupled into the waveguide using an objective lens. The spot at the facet of the ME waveguide is projected on an infrared camera. The two dimensional array of pixels in the infrared camera record the optical pattern which impinges the camera surface. The intensity distribution of the beam is recorded pixel by pixel; therefore, the resolution of this method is limited by the size of a camera pixel. We use a magnifying lens to increase the beam size and overcome the resolution limit. In order to calibrate the measurements, we use the same setup to measure the spot size of a lensed fiber which has a 2.5 μm MFD. The results are demonstrated in Fig.8.27. The 4 μm - and 5 μm -wide ME waveguides have MFDs (lateral \times vertical) of 3.0 \times 2.6 μm and 3.7 \times 2.7 μm respectively. The measured spots are not perfectly circular and the resulting coupling loss (due to mode mismatch) to a 3 μm Gaussian spot is 0.2dB and 0.3dB for the 4 μm - and 5 μm -wide ME waveguides respectively.

We have used a conventional Fabry-Pérot setup to determine the optical losses of the realized structure. The optical loss of the HC waveguides is measured to be as low as 1dB/cm. This is somewhat lower than the typical propagation loss specified for the COBRA platform. A possible reason for this is that the measured thickness of the core

layer (545nm) is larger than the standard core thickness, i.e. 500nm. Furthermore, the top cladding layer is thicker (1495nm instead of 1300nm). The propagation loss of the ME waveguide is measured to be 4.3dB/cm and 3.9dB/cm for a waveguide width of 4 μ m and 5 μ m respectively. We have also measured the excess optical loss which is induced by the taper sections. This is done by measuring the total loss of the structures which include SSCs and compare the results with the results obtained with the ME waveguide. Measurements show that the excess loss of 850 μ m-long tapers is approximately 0.45dB whereas the excess loss for 700 μ m and 600 μ m tapers is 0.45 \pm 0.2dB and 0.65 \pm 0.2dB respectively. In case of 400 μ m-long tapers, the excess loss increases to 1.2 \pm 1dB.

Based on the measurements and calculation which are given above, the optimal SSC structure with the current layer stack is \sim 1mm-long (700-800 μ m vertical taper) and includes a ME waveguide with a width of 5 μ m. In this case, the propagation loss in the structure is \sim 1dB and the coupling loss due to mode mismatch to an ideal 3 μ m Gaussian spot is 0.2dB. The 1dB alignment tolerance (details are given in section 8.1.2) for such structure is \sim 700nm.

8.5. Summary and conclusions

We have described a hybrid integrated optical pulse shaper in which a TriPleX spectral de-/multiplexer device is combined with an InP chip with phase/amplitude manipulation capability. In this scheme the chips are coupled at a common interface. The interface is defined and the required tolerances for efficient coupling between the devices are specified. The design, characterization results and tuning procedure of the TriPleX device are presented in detail. The fabrication and characterization of spot size converters (SSCs) on InP are given as well.

The current TriPleX device includes SSCs which are designed to transform the waveguide mode to a 3 μ m circular spot (93.5% Gaussian fit overlap) at the interface facet. This has been done by reducing the thickness of the Nitride layer near the chip facet. With such a mode size at the TriPleX side, the coupling loss to the InP angled waveguide (including only a lateral taper) on the standard COBRA platform is calculated to be around 2.5dB. In this case, the total (butt-)coupling loss between the chips is below 3dB and the 1dB alignment tolerance in the vertical direction is \sim 500nm. Including SSCs on the InP device reduces the coupling loss by \sim 1.8dB and increases the required alignment accuracy by \sim 200nm. From the technological point of view, it is a reasonable choice to include SSCs only on the TriPleX chip.

The single pass gain of amplifiers on the InP chip has to be kept below 10dB due to the back reflections at the interface facet. The single pass loss of the hybrid system includes 6dB for the TriPleX device, 1.2dB (3dB) coupling with (without) SSCs on InP and 2dB passive loss of the InP device. Therefore, the gain of amplifiers on the InP chip is nearly sufficient to compensate the total losses.

The channel dispersion in the TriPleX device is strongly wavelength dependent and is dominated by the dispersion of the ring filters. With the current design a change in the frequency of an incident spectral line is of 10GHz leads to 0.5 π phase change. Instabilities in the laser mode frequencies thus translate into instabilities in the output pulse shape. Specific requirements on the pulse shape properties in the application can therefore lead to stringent frequency stability requirements.

The current TriPLeX design has the possibility to be adopted such that it includes additional (thermo-optic) phase shifters in each channel. In this way, the device turns into a fully integrated phase-only pulse shaper. This is interesting for conventional CARS experiments where $<1\text{kHz}$ phase modulation speed is sufficient. The important issue is then to increase the bandwidth of the device. For certain applications where a high phase switching bandwidth is necessary, an alternative approach is the heterogeneous integration scheme where the InP phase modulators (and possibly SOAs) are bonded on the TriPLeX de-/multiplexer. A potential application that demands a high switching speed of the shaper is the broadband phase shaped CARS [22]. This technique is particularly interesting for highly selective imaging of multiple complex substances. As an indication, we consider an experiment with a mixture of four different substances to be selectively imaged in 1s at 512×512 pixels. In this case, the required modulation speed for pixel by pixel phase shaped imaging is in the order of 1-10MHz. The required speed is obviously higher for video rate imaging in which case the use of semiconductor material for phase and amplitude control becomes a necessity.

References

- [1] F. Morichetti et al., "Box-Shaped Dielectric Waveguides: A New Concept in Integrated Optics?," *Journal of Lightwave Technology*, vol. 25, no. 9, pp. 2579–2589, Sep. 2007.
- [2] C. Stamatidis et al., "Fabrication and Experimental Demonstration of a Four-Channel $\times 40$ Gb/s TriPLeX All-Optical Wavelength Conversion Platform," *Journal of Lightwave Technology*, vol. 29, no. 12, pp. 1886–1891, Jun. 2011.
- [3] A. Meijerink et al., "Novel Ring Resonator-Based Integrated Photonic Beamformer for Broadband Phased Array Receive Antennas — Part I: Design and Performance Analysis," vol. 28, no. 1, pp. 3–18, 2010.
- [4] R. Heideman, M. Hoekman, and E. Schreuder, "TriPLeX-Based Integrated Optical Ring Resonators for Lab-on-a-Chip and Environmental Detection," *IEEE Journal of Selected Topics in Quantum Electronics*, vol. 18, no. 5, pp. 1583–1596, Sep. 2012.
- [5] G. Roelkens et al., "III-V/silicon photonics for on-chip and intra-chip optical interconnects," *Laser & Photonics Reviews*, vol. 4, no. 6, pp. 751–779, Nov. 2010.
- [6] J. van der Tol et al., "Photonic integration in indium-phosphide membranes on silicon," *IET Optoelectronics*, vol. 5, no. 5, p. 218, 2011.
- [7] D. Liang, G. Roelkens, R. Baets, and J. E. Bowers, "Hybrid Integrated Platforms for Silicon Photonics," *Materials*, vol. 3, no. 3, pp. 1782–1802, Mar. 2010.
- [8] G. Maxwell et al., "Hybrid integration of monolithic semiconductor optical amplifier arrays using passive assembly," *Proceedings Electronic Components and Technology, 2005. ECTC '05.*, vol. 2, pp. 1349–1352, 2005.
- [9] A. Poustie, "Hybrid integration for advanced photonic devices," 2008, vol. 7135, pp. 713502–713502–10.
- [10] G. T. Kanellos et al., "All-Optical 3R Burst-Mode Reception at 40 Gb/s Using Four Integrated MZI Switches," *Journal of Lightwave Technology*, vol. 25, no. 1, pp. 184–192, Jan. 2007.
- [11] C. R. Pollock and M. Lipson, *Integrated photonics*. Boston: Kluwer Academic, 2003.
- [12] E. J. Klein, "Densely Integrated Microring Resonator based Components for Fiber to the Home Application," Universiteit Twente, 2007.
- [13] K. Oda, N. Takato, H. Toba, and K. Nosu, "A wide-band guided-wave periodic multi/demultiplexer with a ring resonator for optical FDM transmission systems," *Journal of Lightwave Technology*, vol. 6, no. 6, pp. 1016–1023, Jun. 1988.

- [14] R. M. De Ridder and C. G. H. Roeloffzen, "Wavelength Filters in Fibre Optics," in *Springer Series in Optical Sciences*, 2006th ed., vol. 123, Springer, 2006, pp. 381–432.
- [15] J. H. Baek et al., "10-GHz and 20-GHz Channel Spacing High-Resolution AWGs on InP," *IEEE Photonics Technology Letters*, vol. 21, no. 5, pp. 298–300, Mar. 2009.
- [16] I. Moerman, P. P. Van Daele, and P. M. Demeester, "A review on fabrication technologies for the monolithic integration of tapers with III-V semiconductor devices," *IEEE Journal of Selected Topics in Quantum Electronics*, vol. 3, no. 6, pp. 1308–1320, 1997.
- [17] F. Fiedler and a Schlachetzki, "Optical parameters of InP-based waveguides," *Solid-State Electronics*, vol. 30, no. 1, pp. 73–83, Jan. 1987.
- [18] L. M. Augustin, "Polarization handling in photonic integrated circuits," Technische Universiteit Eindhoven, 2008.
- [19] J. Stulemeijer, A. F. Bakker, I. Moerman, F. H. Groen, and M. K. Smit, "InP-based spotsize converter for integration with switching devices," *IEEE Photonics Technology Letters*, vol. 11, no. 1, pp. 81–83, Jan. 1999.
- [20] F. Abdelmalek, W. Aroua, and H. Bouchriha, "Spot-size conversion effect on integrated photonic devices," *Optical and Quantum Electronics*, vol. 35, no. 14, pp. 1257–1268, Nov. 2003.
- [21] D. D'Agostino, E. Kleijn, R. Santos, H. P. M. M. Ambrosius, and M. K. Smit, "A Dense Spot Size Converter Array Fabricated in a Generic Process on InP," in *SPIE Microtechnologies*, 2013.
- [22] H. L. Offerhaus, E. T. Garbacik, A. C. W. van Rhijn, A. L. Fussell, and J. L. Herek, "Phase aspects of (broadband) stimulated Raman scattering," *Reviews in Analytical Chemistry*, vol. 31, no. 1, pp. 1–6, Jan. 2012.

APPENDIX A1

Stepped Heterodyne Technique for Complex Spectrum Analysis

In this appendix, the stepped heterodyne technique is described. This method has been used to measure the complex spectra of optical pulses, as presented in chapter 7. The description given here is mainly adopted from [1].

The stepped heterodyne technique is designed to measure the complex field of periodic signals. The spectrum of a periodic signal consists of a series of discrete spectral modes spaced at multiples of the repetition frequency. The stepped heterodyne technique works by measuring the amplitude of each mode and the phase difference between adjacent modes. Once the amplitude and phase of spectral components is measured, it is straightforward to reconstruct the signal in time or frequency domain.

The electric field of the signal which is to be measured can be written as

$$e_{sig}(t) = \sum_{k=-K}^K a_k \cdot \exp(jk\Omega t + j\varphi_k) \cdot \exp(j\omega_s t + j\varphi_s(t)) \quad (A1.1)$$

in which $2\pi/\Omega$ is the period of the signal, a_k is the amplitude of the k^{th} spectral mode, φ_k is the spectral phase of the k^{th} mode, ω_s is the optical frequency of the signal and $\varphi_s(t)$ is the phase noise of the optical carrier.

The signal is combined with the light from a continuous-wave tunable laser source (TLS) which is expressed as

$$e_{TLS}(t) = a_{TLS} \cdot \exp(j\omega_{TLS}t + j\varphi_{TLS}(t)) \quad (A1.2)$$

In Eq.A1.2 a_{TLS} , ω_{TLS} and $\varphi_{TLS}(t)$ are the amplitude, optical frequency and phase noise of the laser source. The frequency of the TLS light is tuned such that the spacing between the k^{th} mode of the signal and the laser light is δ . The measurement requires that the detuning δ is less than $\Omega/2$.

The combined signal is then mixed and detected on a photodiode and recorded with a real-time oscilloscope. The detected signal can be written as

$$\begin{aligned} V(t) \propto & a_{TLS} \cdot a_k \cdot \cos(\delta t + \varphi_{TLS}(t) - \varphi_s(t) - \varphi_k) \\ & + a_{TLS} \cdot a_{k+1} \cdot \cos((\Omega - \delta)t - \varphi_{TLS}(t) + \varphi_s(t) + \varphi_{k+1}) \\ & + \sum_{m=-K}^K a_m \cdot a_{m+1} \cdot \cos(\Omega t + \varphi_{m+1} - \varphi_m) \\ & + \text{DC terms} + \text{frequencies higher than } \Omega \end{aligned} \quad (A1.3)$$

provided that the bandwidth of the detection system (photodiode and oscilloscope) is larger than Ω . The first and second terms in Eq.A1.3 represents the beating between the TLS light and the k^{th} and $(k+1)^{\text{th}}$ modes of the optical signal. These terms appear as cosine waves at frequency δ and $\Omega-\delta$ respectively. The third term is the sum of all the beat signals between the adjacent modes of the signal and can be expressed as a single cosine wave $A \cdot \cos(\Omega t + \psi)$ which appears at frequency Ω .

The recorded signal $V(t)$ is then digitally analyzed to obtain the complex spectrum of the signal, a_k and φ_k . $V(t)$ is first transformed to the frequency domain. The components at δ and $\Omega-\delta$ are filtered separately. The filtered components are transferred back to the time domain and then multiplied to generate a signal which contains the sum $s(t)$ and difference $d(t)$ terms as

$$\underbrace{\cos(\Omega t + \varphi_{k+1} - \varphi_k)}_{s(t)} + \underbrace{\cos((\Omega - 2\delta)t - 2\varphi_{\text{TLS}}(t) + 2\varphi_s(t) + \varphi_{k+1} + \varphi_k)}_{d(t)} \quad (\text{A1.4})$$

The term $s(t)$ appears at frequency Ω and can be again filtered out. $s(t)$ is then multiplied by $A \cdot \cos(\Omega t + \psi)$, i.e. the third term in Eq.A1.3 and is obtained by filtering $V(t)$ at frequency Ω . This allows for extraction of the phase difference

$$d\varphi = \varphi_{k+1} - \varphi_k - \psi \quad (\text{A1.5})$$

with complete cancellation of the phase noise of both the periodic signal and the TLS. Eq.A1.5 implies that the absolute value of the spectral phase is not determined by the stepped heterodyne technique. Yet, the phase values are measured to a constant phase offset ψ .

To measure the complete complex spectrum of the signal, the TLS is tuned across all the spectral modes of the signal. The measurement steps, as described above, are repeated for each spectral mode. The relative amplitude of each spectral mode is directly determined by calculating the amplitude of the filtered signal at δ . The phase difference at each point is calculated from the mean of $d\varphi$. The effect of the constant phase offset, i.e. ψ in Eq.A1.5, is not a significant issue for reconstruction of the pulse shape and appears as a temporal shift of the pulse in the time domain.

For the measurement results given in chapter 7, the optical pulse train had a repetition frequency of $\Omega \sim 40\text{GHz}$. The single shot real time traces were recorded using a 50GHz u^2t photodiode and a 45GHz oscilloscope LeCroy LabMaster 9 Zi at sampling rate 120GS/s, i.e. 1.2 million data points for $10\mu\text{s}$ span. The 45GHz detection bandwidth allows for direct measurement of all the required components given in Eq.A1.3. The tunable laser source was an Agilent 81600B module.

RF spectrum of a typical recorded time trace is presented in Fig.A1.1. In this figure, the components of interest at δ , $\Omega-\delta$ and Ω are indicated. The additional peaks in the spectrum appear due to the artifact of the digital bandwidth interleaving [2] in the real-time oscilloscope. Appearance of the unwanted peaks in the RF spectrum shows unwanted frequency components are present in the time trace. This is in principle not a significant issue, since the signals which are of interest for the analysis are spectrally filtered. In practice, care must be taken in choosing the frequency detuning between the TLS light and the spectral mode of the optical pulse such that the beating signals at frequency δ and $\Omega-\delta$ do not overlap with the spurious peaks.

The other important point for proper analysis is the bandwidth of the digital filters which are used to extract the required signals from $V(t)$. The spectral width of the

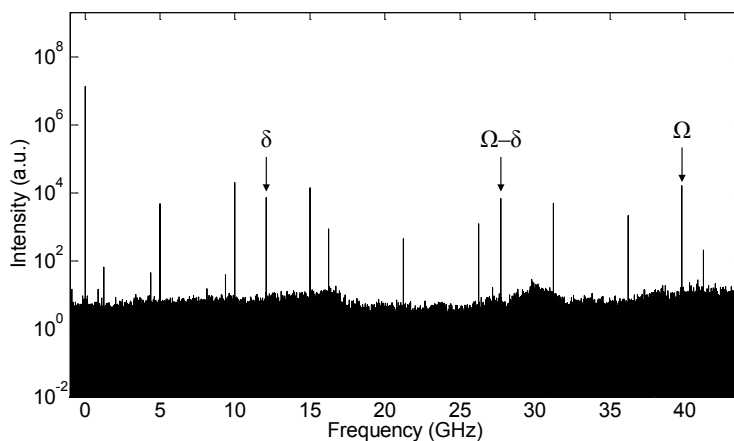


Fig.A1.1. RF spectrum of a typical real-time trace. The beat signals required by the stepped heterodyne technique are indicated by the arrows. $\Omega \sim 40\text{GHz}$ is the repetition frequency of the pulse train and δ is the detuning between the TLS light and the spectral mode in this particular measurement.

signals at δ , $\Omega - \delta$ and Ω are set by the phase noise of both the signal under test and the TLS. In order to obtain an optimum reconstruction of the complex spectrum, the filter width must be chosen such that the spectral information of interest is not clipped. For this reason, we have used a flattop raised-cosine bandpass filter with a width of 50MHz, which is sufficient to extract the required spectral information while rejecting the unwanted spectral content.

References

- [1] D. A. Reid, S. G. Murdoch, and L. P. Barry, "Stepped-heterodyne optical complex spectrum analyzer.," *Optics express*, vol. 18, no. 19, pp. 19724–31, Sep. 2010.
- [2] P. Pupalaiakis, "Digital Bandwidth Interleaving," Technical Brief, 2010. [Online]. Available: http://cdn.teledynelecroy.com/files/whitepapers/dbi_explained_15april10.pdf.

List of Abbreviations

AO	Acousto-optic
AOPDF	Acousto-optic programmable dispersive filter
AR	Anti-reflection
ASE	Amplified spontaneous emission
AWG	Arrayed waveguide grating
BB	Building block
BC	Bottom cladding
BPF	Band-pass filter
BPM	Beam propagation method
CARS	Coherent Anti-Stokes Raman Spectroscopy
CCW	Counter clockwise
CP	Colliding pulse
CW	Clockwise
DST	Direct space to time
DUT	Device under test
EDFA	Erbium-doped fiber amplifier
EO	Electro-optic
ES	Excited state
ESA	Electrical spectrum analyzer
FIR	Finite impulse response
fs	Femtosecond
FSR	Free spectral range
FT	Fourier transform
FWHM	Full width at half maximum
GaAs	Gallium arsenide
GS	Ground state
GSG	Ground-signal-ground
HC	High-confinement
HR	Highly-reflective

I/O	Input/output
ICR	Intensity contrast ratio
InAs	Indium arsenide
InP	Indium phosphide
ITO	indium tin oxide
LC	Liquid crystal
LCoS	Liquid crystal on silicon
LTI	Linear time-invariant
LWMG	Long wavelength mode group
ME	Mode-expanded
MIIPS	Multiphoton intrapulse interference phase scan
ML	Mode-ocked
MLLD	Mode-locked laser diode
MQW	Multi-quantum well
MR	Micro-ring resonator
MZI	Mach-Zehnder interferometer
MZM	Mach-Zehnder modulator
OAWG	Optical arbitrary waveform generation
O-CDMA	Optical code-division multiple-access
PCB	printed circuit board
PD	Photo diode
PIC	Photonic integrated circuit
PM	Phase modulator
QCSE	Quantum-confined Stark effect
QD	Quantum dot
SA	Saturable absorber
SEM	Scanning electron microscope
SIMBA	Spectral Interferometry using Minimum-phase Based Algorithm
SLM	spatial light modulator
SOA	Semiconductor optical amplifier
SSC	Spot size converter
TLS	Tunable laser source
VIPA	Virtually imaged phased array

SUMMARY

Photonic Integrated Circuits for Shaped Pulse Laser Systems

The research presented in this thesis concerns the development and demonstration of an integrated semiconductor shaped pulse laser system. Such a system typically includes a mode-locked (ML) laser light source for generation of optical pulses and a “pulse shaper” which is used to manipulate the shape of the optical pulses. The pulse shaper unit consists of spectral filters and a series of optical elements to control the phase and amplitude of the different optical frequencies in the light pulses. These systems are commonly used for bio-photonic imaging and microscopy applications. The goal of this research was to show that the photonic integration technology is capable of providing the required functionalities for building such complex laser systems.

The research has been divided in two major parts. In the first part, the focus was on development of an integrated optical pulse source. In this respect, two types of semiconductor ML laser diodes were investigated. The first type of lasers were based on InAs/InP(100) quantum dot (QD) gain material. This material has a peak gain in the wavelength range of 1500-1600nm and provides a wide coherent bandwidth for ML laser operation. Furthermore, it is compatible with the InP-based generic photonic integration technology at the COBRA Research Institute.

The dynamical behavior of QD ML lasers was studied in detail. A regime of dual-wavelength ML operation, in which the optical spectrum shows two distinct lobes, was investigated. It was confirmed that the two lobes provide a coherent bandwidth and lead to two synchronized optical pulses. Measurements on several InAs/InP(100) QD ML lasers with different geometrical parameters show a systematic behavior. Indications are that a single mechanism in the gain material leads to the generation of highly chirped pulses, the presence of correlated amplitude noise and self-induced mode-locking in a single section laser. The pulse duration is almost half the roundtrip time, independent of the cavity length. Stabilization of the repetition frequency of the QD lasers has been achieved by application of radio frequency modulation on a section of the laser. The locking range for this process was studied and presented in terms of the timing jitter which is of particular interest in practice.

Passively ML InP/InGaAsP multiple quantum well ring lasers were investigated as well. A number of devices with varying relative positions of the saturable absorbers and amplifiers have been realized using the active-passive integration technology in a

standardized optical integration platform. The operating regimes of an asymmetrical ring laser were investigated to demonstrate the control of power between counter-propagating light pulses. Pulse width below 4ps was achieved and a directional power contrast up to 9dB was measured. The power balance was verified to be in agreement with predictions of a theoretical model that was used to design the devices.

In the second part, integrated optical pulse shaper devices were investigated and two technologies were exploited. The first option was an InP-based monolithically integrated circuit. The device has been realized in a standardized photonic integration platform which provides shared-user foundry fabrication runs. The photonic circuit includes an arrayed waveguide grating (AWG), electro-optic phase modulators and optical amplifiers. The AWG which is the spectral filter in this circuit has 20 channels in total and covers 8nm of bandwidth. The phase modulators and amplifiers are controlled to tailor the shape of the optical pulse which passes through the device. Special attention was given to the calibration of the phase modulator and amplifier settings. A mathematical description of the integrated device was first developed and a set of experiments was then carried out to characterize the components on the chip. Total on-chip loss is around 20dB and the available gain of amplifiers is up to 7dB.

The pulse shaper has been used to compress the optical pulses generated by a quantum dash ML laser. This has been achieved by operating the device at the optimum conditions to compensate the nonlinear spectral chirp of the quantum dash laser.

Using the actual calibration data, a model has been devised to simulate the effects on the shape of an optical pulse which passes through the pulse shaper device. The modeling gives insight into the performance of the integrated device and was used to demonstrate how the required control signals can be calculated in order to achieve specific output pulse properties given an input pulse shape. It was shown that the total device dispersion is dominated by the dispersion in the AWG channels.

The second option for the pulse shaper was the hybrid integration of a TriPleX spectral filter chip and an InP-based chip for phase and amplitude control. The hybrid integrated pulse shaper was designed and the required components were characterized. In order to achieve efficient coupling between the chips, design, fabrication and the use of optical spot size converters (SSCs) on the InP chip and TriPleX chips was investigated. It was concluded that a good solution is to include SSCs only on the TriPleX chip.

The TriPleX device includes 24 channels and incorporates ring wavelength filters which are individually tunable via heater elements. The total bandwidth of the TriPleX device is 8nm. The phase tuning characteristics of the heater elements were derived. The procedure for proper tuning of the device was explored and verified. The design of the TriPleX device can be readily modified to turn it into a phase-only pulse shaper.

Pulse shaper devices with 40-50 channels are well suitable for applications such as CARS imaging. The monolithic semiconductor ML lasers that were investigated do not provide the coherent bandwidth and output power which is required for such applications. In this case a fiber ML laser can be employed as the pulse source. The knowledge which is obtained within the framework of this research shows that there is no fundamental limitation to proceed to a prototype/commercial development of integrated optical pulse shaper devices.

Acknowledgements

I look back upon the past four years with delight and gratitude. Writing this last bit of the thesis is a great pleasure because it means a lot has been achieved. I would like to thank all those who have contributed to this work by any means.

First of all Erwin, my direct supervisor. Working with you has been a valuable experience for me. I am grateful for your attitude towards research, your availability for our regular meetings as well as spontaneous discussions, the balance you provided between the supervisory guidance and student's independence, and of course your casual jokes. Special thanks for your time and care during the preparation of the thesis.

Then I would like to thank Meint, my promoter and the PhI group leader, for his trust and support during the past years. Meint, I admire your spirit, efforts and contributions to the Photonic Integration and the ecosystem of PICs!

Xaveer, I believe the mask library is much more user-friendly and efficient! Thank you for the help with the design and simulation tools. Jos, I was not a chess player; but we had a good run in vOEDbal. Huub, thanks for your MegaEffort for the NanoLab!

Barry, you have a magic connection with metal strings, either playing your guitar or wire-bonding the chips. Tjibbe, Erik Jan, Jeroen, thanks for your help in the cleanroom and realizing JeppiX/COBRA devices, also for the Walhalla 'borreltijd', the best resource for actual weather conditions in Eindhoven and the nice 'sportive' events.

Bauke, my first measurements on 'real' samples were on your QD devices. Fortunately, I did not blow up too many of them and everything worked out very well! I enjoyed a lot working with you and wish you success and happiness.

My PhI generation friends, Jing, Yuqing and Ray, shie-shie! It was nice that I shared the 'thesis-writing' office for some months with you Jing. Good luck with Prep & Landing! Yuqing, thank you for the nice chip photos :)

Antonio, I am keen to enjoy the on-board flight entertainment enabled by your chips.

Valentina, make the pulsed lasers designer-friendly (even more). Emil, thanks for your time on the AWG simulations. Domenico, I appreciate your work on the SSCs.

Hadi, it was a nice opportunity for me to have a fellow countryman in the group, Merci.

Sylwester, special thanks to you for those after-hours and weekend measurements.

Giovanni, you handle the hotness of Salsa act very well on stage, managing thermal crosstalk on the chips is sure not a problem! Rui and Dominik, good luck with the process control and 'cool' lasers. Luc, thanks for the help with the COBRA/Smart runs.

Josselin, Elton, Kasia, Staszek, Manuela, 2×Dima, Srivathsa, Deepak, Victor, Aura,

Longfei, Weiming and Alonso, it was a pleasure to work with you. I had the privilege to be contacted from time to time for OLA-related inquiries and I am pleased with that. I wish you all the best with your research projects.

I have to thank the students who spent their internship period at OED/PhI in Eindhoven and contributed to this work. Lin, Eric, Sébastien, Christophe, Aurélien, 2×Adrien and Kokila, I hope you have achieved what you had hoped for and wish you success with your studies and career.

Jolanda, Yvonne, Audrey, José and Susan, thank you for taking care of the administrative stuff and letting us worry only about the research tasks.

I am also thankful to the former members of OED/PhI. Hans, thank you for the ICT support and more in my early days at TU/e. Jose, we were office mates for two years and you are still my good friend! Martijn, thanks for the QD samples and the scientific and fun brainwaves. Boudewijn, I have a feeling that we will meet more often in future! Milan, Ling, Pietro, Tim, Fouad, Siang and Yucai it was nice to work with you.

As a member of COBRA, I would like to thank my colleagues and friends from the ECO and PSN research groups, especially Oded, Nicola, Chigo, Patty, Piet, Johan, Prof. Andrea Fiore, Margriet van Doorne, Leonardo, Döndü, Sartoon and Rosalinda.

The IOP Frequency Comb was a successful collaboration between the project partners. Wim, Kjeld, Edcel and Tjeerd, thanks for the comb generation experiments. Edwin and Douwe thank you for the TriPLeX chip. I thank René and Peter for wafer material growth, Herman for discussions on the pulse shaper application and Wilhelm Kaenders for providing the TOPTICA lasers. I am also grateful to the members of the supervisory committee for their comments and contribution. I appreciate the wonderful collaboration within EuroPIC; thank you Mike and Dave.

I express my sincere gratitude to the members of my defense committee, Prof. Wim Ubachs, Prof. Richard Nötzel, Dr. Pascal Landais, Dr. Huug de Waardt and Dr. Peter Harmsma, for their time and care to evaluate my thesis and provide valuable feedback.

I am grateful to all my teachers from whom I have learnt word by word. My special gratitude to Dr. Sheikhi who played a significant role in introducing the world of photonics to me. Ik wil dan ook Ellie, Leonie en Pauline van harte bedanken die mij hebben geholpen met de cursus Nederlands. Zonder jullie was het niet zo leuk!

Life is ongoing outside the office environment and good friends are essential part of that. I thank Pooyan & Ellaheh, Hossein & Samaneh, Salman & Leila, Shahram & Masoumeh, Amin & Elham, Hooman & Negar, Majid & Vajiheh, Ali & Erfaneh, Mahmoud & Fahimeh, Hamid & Azar and many other dear friends, for their company, joyful gatherings, memorable trips and more.

I find no words to thank my family whom I have missed a lot while living abroad. My special thanks go to Baba, Maman and Sahar for their endless love, sacrifice and support, and to beloved Madar for her everlasting prayers. A big hug for Kia, Amir and Mehdi. I appreciate the valuable support and encouragement that I have received from my in-laws, especially my late father-in-law.

Last but certainly not least, my lovely wife. Saeedeh, we have shared happy and sad moments; every moment we spend together makes me love you more. Thank you for always being there for me. And that leaves me with just a kiss for the little one...

Saeed Tahvili
Eindhoven, May 2013

List of Publications

Journal publications

- M.S. Tahvili, M.K. Smit, E.A.J.M. Bente, "**Complete calibration of an InP-based monolithically integrated optical pulse shaper,**" in preparation for submission to IEEE Photonics Journal.
- S. Tahvili, S. Latkowski, B. Smalbrugge, X.J.M. Leijtens, P.J. Williams, M.J. Wale, J. Parra-Cetina, R. Maldonado-Basilio, P. Landais, M.K. Smit, and E.A.J.M. Bente, "**InP-Based Integrated Optical Pulse Shaper: Demonstration of Chirp Compensation,**" IEEE Photonics Technology Letters, vol. 25, no. 5, pp. 450–453, Mar. 2013.
- T.J. Pinkert, E.J. Salumbides, M.S. Tahvili, W. Ubachs, E.A.J.M. Bente, and K.S.E. Eikema, "**Frequency comb generation by CW laser injection into a quantum-dot mode-locked laser,**" Optics Express, vol. 20, no. 19, pp. 21357–21371, 2012.
- M.S. Tahvili, L. Du, M.J.R. Heck, R. Nötzel, M.K. Smit, and E.A.J.M. Bente, "**Dual-wavelength passive and hybrid mode-locking of 3, 4.5 and 10 GHz InAs/InP(100) quantum dot lasers,**" Optics Express, vol. 20, no. 7, pp. 8117–8135, March 2012.
- M.S. Tahvili, Y. Barbarin, X.J.M. Leijtens, T. de Vries, E. Smalbrugge, J. Bolk, H.P.M.M. Ambrosius, M.K. Smit, and E.A.J.M. Bente, "**Directional Control of Optical Power in Integrated InP/InGaAsP Extended Cavity Mode-locked Ring Lasers,**" Optics Letters, vol. 36, no. 13, pp. 2462–2464, July 2011.
- B.W. Tilma, M.S. Tahvili, J. Kotani, R. Nötzel, M.K. Smit, E.A.J.M. Bente, "**Measurement and analysis of optical gain spectra in 1.6 to 1.8 μm InAs/InP(100) quantum-dot amplifiers,**" Optical and Quantum Electronics, 41(10), pp. 735–749, April 2010.

International conferences

- M.S. Tahvili, S. Latkowski, X.J.M. Leijtens, M.J. Wale, P. Landais, M.K. Smit, and E.A.J.M. Bente, "Monolithically Integrated InP-based Optical Pulse Shaper," in proc. Lasers and Electro-Optics Europe (CLEO), Munich- Germany, May 2013.

- Erwin Bente, Saeed Tahvili, Valentina Moskalenko, Sylwester Latkowski, Mike Wale, Julien Javaloyes, Pascal Landais, Meint Smit, “Integrated InP based modelocked lasers and pulse shapers,” (Invited) in proc. SPIE Photonics West, 8627-14, San Francisco | CA USA, Feb 2013.
- E.A.J.M. Bente, M.S. Tahvili, X.J.M. Leijtens, M.J. Wale, E. Klein, and M.K. Smit, “Integrated optical pulse shaping devices for mode-locked lasers in the 1.5 μ m region,” in proc. 14th International conference on Transparent Optical Networks (ICTON 2012), 2-5 July, 2012, Coventry, UK. (IEEE Photonics Technology Letters, pp. Th.A4.1-4). Piscataway: IEEE.
- M.S. Tahvili, X.J.M. Leijtens, P.J. Williams, M.J. Wale, M.K. Smit, and E.A.J.M. Bente, “Design and Fabrication of a Monolithically Integrated AWG-based Optical Pulse Shaper,” in proc. European Conference on Integrated Optics, pp., Sitges-Barcelona, Spain, April. 2012.
- M.S. Tahvili, M.J.R. Heck, R. Nötzel, M.K. Smit, and E.A.J.M. Bente, “Dual Wavelength Mode-Locking of InAs/InP Quantum Dot Laser Diodes at 1.5 μ m,” in proc. IEEE Photonics 2011, pp. 111-112, Arlington, VA|USA, Oct. 2011.
- M.S. Tahvili, Y. Barbarin, X.J.M. Leijtens, T. de Vries, E. Smalbrugge, J. Bolk, H.P.M.M. Ambrosius, M.K. Smit, and E.A.J.M. Bente, “An Asymmetric Integrated Extended Cavity 20GHz Mode-locked Quantum Well Ring Laser Fabricated in the JePPIX Technology Platform,” in proc. Lasers and Electro-Optics Europe (CLEO), Munich- Germany, May 2011.
- M.S. Tahvili, L. Du, M.J.R. Heck, R. Nötzel, M.K. Smit, and E.A.J.M. Bente, "Investigation of hybrid mode-locking in a 3.1GHz InAs/InP(100) Quantum Dot Mode-locked Laser Diode," in proc. European Semiconductor Laser Workshop, ESLW2010, Pavia-Italy, Sep 2010.
- M.S. Tahvili, L. Du, M.J.R. Heck, R. Nötzel, M.K. Smit, and E.A.J.M. Bente, "Passive Mode-locking Dynamics in a 3.1GHz Quantum Dot Laser Diode Operating around 1.5 μ m," in proc. 36th European Conference and Exhibition on Optical Communication, ECOC2010, Turin-Italy, Sep 2010.
- M.S. Tahvili, M.J.R. Heck, R. Nötzel, M.K. Smit, and E.A.J.M. Bente, "Dual Wavelength Passive and Hybrid Mode-Locking of a 10GHz Quantum Dot Laser Diode at 1.5 μ m," in proc. 15th European Conference on Integrated Optics, ECIO2010, Cambridge-UK, April 2010.
- B.W. Tilma, M.S. Tahvili, J. Kotani, R. Nötzel, M.K. Smit, E.A.J.M. Bente, “Observation and modeling of long-wavelength InAs/InP(100) quantum dot amplifier small signal gain spectra,” in proc. European Semiconductor Laser Workshop (ELSW), pp. 6-6, Vienna-Austria, September 2009.
- M.J.R. Heck, M.S. Tahvili, S. Anantathanasarn, M.K. Smit, R. Nötzel, E.A.J.M. Bente, “Observation of dynamics in a 5GHz passively Mode-locked InAs/InP (100) Quantum Dot Ring Laser at 1.5 μ m,” in proc. CLEO-EQEC Europe 2009, Munich-Germany, June 2009.

Local Conferences and Events

- M.S. Tahvili, "Photonic Integrated Circuits for Shaped Pulse Laser Systems," Fotonica Evenement 2013, Veldhoven, the Netherlands, April 2013.
- M.S. Tahvili, X.J.M. Leijtens, P.J. Williams, M.J. Wale, M.K. Smit, and E.A.J.M. Bente, "Design and Fabrication of a Monolithically Integrated AWG-based Optical Pulse Shaper," in proc. IEEE Photonics Society Benelux Chapter, pp. 57-60, Gent, Belgium, Dec. 2011.
- M.S. Tahvili, Y. Barbarin, X.J.M. Leijtens, T. de Vries, E. Smalbrugge, J. Bolk, H.P.M.M. Ambrosius, M.K. Smit, and E.A.J.M. Bente, "A Monolithic 20GHz Integrated Extended Cavity Mode-locked Quantum Well Ring Laser at 1.58 μ m Fabricated in the JEPPIX Platform," in proc. 15th Annual Symposium of IEEE Photonics Benelux Chapter, pp. 69-72, Delft, the Netherlands, November 2010.
- M.S. Tahvili, M.J.R. Heck, R. Nötzel, M.K. Smit, and E.A.J.M. Bente, "Operating Regime and Stability of Mode-Locking in 10GHz Quantum Dot Laser Diodes around 1.5 μ m," in proc. 14th Annual Symposium of IEEE Photonics Benelux Chapter, pp. 229-232, Brussels-Belgium, November 2009.
- B.W. Tilma, M.S. Tahvili, J. Kotani, R. Nötzel, M.K. Smit, M.K., E.A.J.M. Bente, "Observation and modeling of long-wavelength InAs/InP (100) quantum dot amplifier small signal gain spectra," in proc. 14th Annual Symposium of the IEEE Photonics Benelux Chapter, pp. 169-172, Brussels-Belgium, November 2009.

Curriculum vitae

Saeed Tahvili was born in Shiraz, Iran in 1983. He received his BSc and MSc degrees in Electrical Engineering from Shiraz University in 2005 and 2007 respectively. The subject of his MSc thesis was investigation of optical bistability which involved theoretical study of distributed feedback semiconductor optical amplifiers with nonuniform gratings. He was with the Nanotechnology Research Institute of Shiraz University in 2007-2008. He started as a PhD candidate at the Photonic Integration (formerly Opto-Electronic Devices) group of the COBRA Research Institute, Technical University of Eindhoven in Dec. 2008 where he has been involved in research on development of integrated semiconductor mode-locked lasers and pulse shaping devices.